NOTE TO USERS

In Situ Stresses and Capacity of Driven Piles in Sand

Mohab Sabry

A Thesis

in

The Department

of

Building, Civil and Environmental Engineering

Presented in Partial Fulfillment of the Requirements

For the Degree of Doctor of Philosophy at

Concordia University

Montreal, Quebec, Canada

September 2005

Your file Votre référence
ISBN: 0-494-09966-6
Our file Notre référence
ISBN: 0-494-09966-6

ABSTRACT

Insitu Stresses and Capacity of Driven Piles in Sand

Mohab Sabry, Ph.D.
Concordia University, 2005

Pile foundations are used extensively around the world to support both inland and offshore structures, including important structures such as nuclear plants and oil drilling platforms. Pile foundations are known to resist higher compression and uplift loading as compared to shallow foundations. The common factor in resisting the compression and the tensile loading is the friction, which takes place between the pile and the soil.

Pile foundations can be categorized as bored and driven piles. Bored piles installed in sand are known to provide relatively low capacity as compared to driven piles under the same condition. This is due the effect of the pile driving process.

The estimation of the shaft resistance of driven piles remains empirical at best. The changes in the insitu stress levels as a result of pile installation are quite often overestimated/underestimated leading to unsafe/uneconomic design of the foundations. The objective of this study is to examine the changes in the insitu stresses during the pile driving process, and accordingly to predict the pile capacity. In order to achieve these objectives, numerical model is developed to simulate the process of pile installation and link the cavity expansion to the pile installation and pile diameter. During this research program the changes in the soil mass due to pile installation will be recorded. Furthermore, the changes of the OCR around the pile will be examined and its effects on the earth pressure acting on the pile's shaft will be evaluated. Based on the results of the

present investigation, design theory is proposed to account for the effect of pile diameter during installation in dry sand.

In order to achieve these objectives, a numerical model utilizing the finite element method of analysis combined with the theory of cavity expansion is developed. This model is capable of predicting the magnitude and the distribution of the coefficient earth pressure acting on the pile's shaft and accordingly the overconsolidation ratio. Based on the result obtained from the numerical model, an analytical model was developed to incorporate the findings observed from the numerical model. The analytical model will be then presented in the form of design procedure and design charts for practical use. The theories developed herein compared well with the available laboratory and field experimental data.

ACKNOWLEDGEMENTS

The author gratefully acknowledges the valuable guidance, understanding and cooperation of Professor Adel Hanna, under his supervision this research work was carried out. Foremost, I am indebted to Dr. Hanna for forging my geotechnical background during the years I spent under his supervision during my Master and Ph.D. programs. His assistance, patience and valuable encouragement throughout the research is greatly appreciated.

The author wish to thank Dr Tahar Ayadat for the valuable discussions and helpful advice and comments received during the completion of this research.

The financial support from the Natural Science and Engineering Research Council of Canada (NSERC), General Consulate of Egypt Bureau of Cultural and Educational Affairs in Canada and the department of Building, Civil and Environmental Engineering at Concordia University are gratefully acknowledged.

I wish to thank my wife for bearing with me the long and tough student life and for her kindness and continuous encouragement; I could not have done it without her love and patience.

Last but not least, I wish to express my sincere gratitude to my parents for their kindness, love, and support throughout the course of my graduate studies in Canada. Special thanks to my father (Professor Mamdouh Sabry) for his technical advice and valuable help during the development of this thesis.

The support of my father in law, the honourable Dr. Hassan Younes the Minister of Electricity and Energy of Egypt, which is highly appreciated.

To My Family:

My wife Mona, my daughter Bassant

and my son Aly

TABLE OF CONTENTS

LIST OF FIGURES

Page

LIST OF TABLES

LIST OF SYMBOLS

A_s = Cross section area of pile shaft

A_t = Cross section of pile tip

D = Pile diameter

E' = Young's modulus

K_o = Coefficient of earth pressure at rest

K_p = Coefficient of passive earth pressure

K_s = Coefficient of earth pressure

K_{av} = average coefficient of passive earth pressure

L = Pile length

R = pile radius

OCR = Overconsolidation ratio

Q_u = Ultimate bearing capacity of pile

r_o = Initial cavity radius

r_i = radius of the logarithmic spiral

Δr = amount of displacement applied

δ = Interface angle of friction

ϕ = Soil angle of shearing resistance

γ = soil unit weight

ν' = Effective Poisson's ratio

σ_y = Confining pressure

σ_1 & σ_3 = Principle stresses

τ_{max} = Maximum value of shear stress

ψ = Angle of dilatation

q = deviatoric stress

e_c = Confining pressure

σ_r = Radial stresses

σ_R = horizontal stresses on the pile shaft

σ_v = vertical stresses

$\Delta\sigma_r$ = Increase of horizontal stresses

q_u = unit pile bearing capacity

τ_{rel} = Relative shear stress

a_i, b_i = Constants

π = pi (≈ 3.14)

θ = failure surface angle

α = radial angle

z = distance from the ground surface

x = distance from the pile axis

Q_t = pile tip capacity

Q_s = pile shaft capacity

Q_g = ultimate pile group capacity

X_i = horizontal distance from the pile axis to the zone of influence plane

P_{si} = earth pressure in different stress zones

β = angle of inclination of the sand surface to the horizontal

λ = angle of inclination of the pile to the vertical

L_i = vertical distance from the ground surface to the end of each stress zone

ω = radial angle on the logarithmic spiral

F = horizontal component of the shearing resistance on the rupture surface

θ' = angle of rotation around the pile axis

ρ = radius of curvature of rupture surface

C = integration constant

W_i = weight of soil wedge

W_s = total weight causing surcharge pressure

V_i = volume of soil wedge

P_{sav} = average earth pressure on the pile shaft

N_q = bearing capacity factor

q_o = effective vertical stress at the pile tip level

CHAPTER 1
INTRODUCTION

1.1 General

Pile foundations are used extensively around the world to support both inland and offshore structures, including important structures such as nuclear plants and oil drilling platforms. Pile foundations are known to resist higher compression and uplift loading as compared to shallow foundations. The common factor in resisting the compression and the tensile loading is friction, which takes place between the pile and the soil.

The estimation of the capacity of vertical pile driven into sand involves considerable uncertainty and simplifying assumptions. Quite often the design does not follow the physical process of the pile installation. The current practice in evaluating the shaft resistance, considers the pile length, angle of shearing resistance of the sand, and the angle of friction between the pile's shaft and the soil as the only governing parameters. The pile shaft resistance is also affected by the method of installation whether it is hammered or jacked into the soil. Furthermore, the soil state (normally consolidated or over consolidated) is also a major factor in determining the shaft resistance of these piles.

In the literature, several simplifying assumptions were introduced to develop analytical and empirical methods for the design of driven piles. Theories developed based on laboratory test results assume that the soil is normally consolidated, while most of the soil prepared in laboratories are in the state of overconsolidation. Furthermore, in numerical modeling for driven piles, the pile is placed in the soil as if it is a bored pile.

1.2 Purpose and Scope of Thesis

It is evident that additional research is needed in several key areas dealing with piles driven in cohesionless soil. Particular attention should be paid to the effect of pile installation and the level of overconsolidation of the soil on the initial stress level in the surrounding soil medium, and accordingly on the pile capacity.

The objectives of the present investigation are:

a) To conduct a literature review and to prepare the state of the art report on the subject matter. Special emphasis will be placed on the limitations and the basic assumptions used in developing bearing capacity theories for piles in sand.

b) To develop a numerical model to simulate the process of pile installation, and to establish the stress condition before and after pile installation. More specifically, the distribution of the earth pressure during the installation process, and accordingly the change in the level of the soil overconsolidation.

c) To develop a analytical model capable of incorporating the effect of pile installation on the pile capacity. Furthermore, to develop design procedure and chart, which can be used in practice.

1.3 Organization of Thesis

A literature review of the subject is presented in chapter 2. Chapter 3 presents the numerical model, while chapter 4 presents the analytical model. A section on the validity of the proposed models with full-scale load test results is also presented in Chapter 4.A practical design procedure for estimating bearing capacity of single piles driven in sand is

included in Chapter 4. Conclusions drawn from the present study and recommendations for future study are given in chapter 5.

CHAPTER 2
LITERATURE REVIEW

2.1 Pile Capacity

There are two conventional approaches in calculating the ultimate bearing capacity of single pile: The static approach, which relates the measured soil properties and the pile properties to the pile load capacity; and a dynamic approach, which estimates the load capacity of a driven pile from the analysis of its installation data. Only the static approach is reviewed herein because it is related to the present study.

The ultimate bearing capacity of a single pile driven in sand is generated from two components: The pile shaft resistance and the tip resistance. (Fig. 2.1)

Hence:

$$Q_u = Q_s + Q_t \qquad (2.1)$$

Where:

Q_u = Ultimate bearing capacity of pile

Q_s = Shaft resistance

Q_t = tip resistance

Conceptually, the prediction of the ultimate pile capacity using Eq. (2.1) depends heavily on the estimation of Q_s and Q_t.

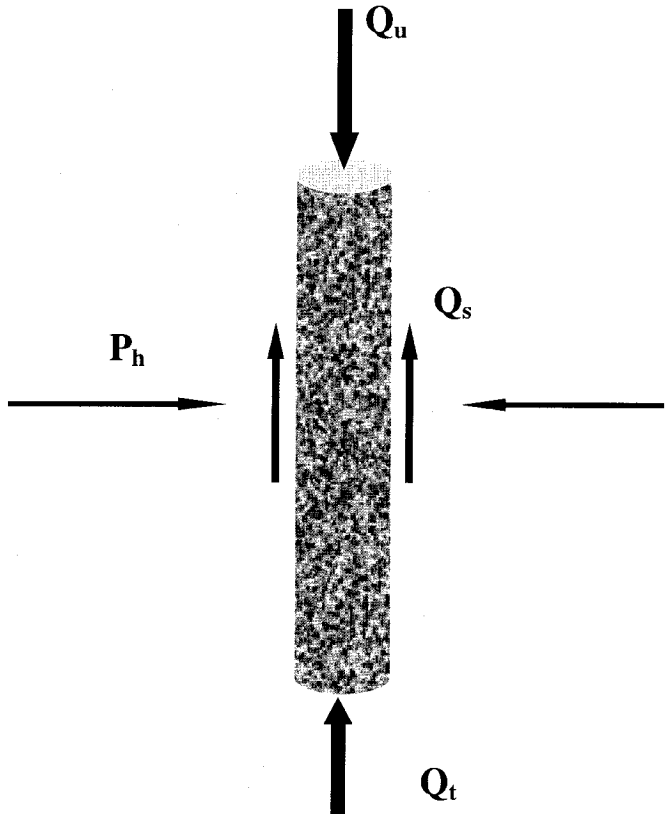

Figure 2.1 Single pile under axial load.

2.1.1 Shaft Resistance, Q_s

The shaft resistance is usually evaluated by integrating the pile – sand shear stress. τ_f at any depth is assumed to be a function of the effective normal stress σ'_n exerted on the pile by the surrounding sand at the same depth.

Thus:

$$\tau_f = \sigma'_n \tan \delta_z \qquad (2.2)$$

Where

δ_z = angle of friction between the pile and the sand at depth z.

The effective normal stress σ'_n is a function of the effective vertical stress σ'_z as:

$$\sigma'_n = K_z \sigma'_z \qquad (2.3)$$

Where

K_z = Coefficient of lateral earth pressure at depth z.

By substituting Eq. (2.3) in Eq. (2.2)

$$\tau_f = K_z \sigma'_z \tan \delta_z \qquad (2.4)$$

By integrating over the pile depth L, Q_s can be obtained:

$$Q_s = \int_o^L (\pi D)(\tau_f)(dz)$$

$$Q_s = \pi D \int_o^L \sigma'_z K_z \tan \delta_z \text{ (dz)} \qquad (2.5)$$

Where:

D = pile's diameter

L = pile embedment length

The parameters K_z and δ_z are not easy to evaluate given the soil/pile conditions (Kraft, 1991). In fact these parameters depend on the soil characteristics, pile characteristics, method of pile installation and the type of loading, beside the testing technique and the procedure used for predicting these values (Hanna and Saad, 2001).

Due to the difficulties in evaluating the values of these parameters, numerous recommendations are given in the literature and are listed in Table 2.1. It can be noted from this table that a wide range of the angle (δ) and the coefficient (K) are used for design purposes. Another concern in selecting the coefficient (K) is that the coefficient of lateral earth pressure depends further on the initial value of the coefficient of earth pressure at rest, K_o. Accordingly, it can be reported herein that researchers had ignored some governing parameters in order to simplify the calculation.

Bolton (1986) studied the effect of sand dilatancy on the shaft resistance and how it affects the angle of shearing resistance of the soil. Hanna and Tan (1973) and Feda (1976) studied the effect of residual stresses on the pile, which is generated from the method of installation. Das (1989) studied the shaft resistance in different sand types (loose, medium and dense). Some other researchers presented the factors that affect the shaft resistance; nevertheless they did not incorporate them in a design formula or procedure (Tsien, 1986 Mochtar and Edil, 1988 and Leland, 1991). It is evident that combining these governing parameters in one single theory is not an easy task, which explains the wide discrepancies noted among design theories.

2.1.2 Tip Resistance

The ultimate tip resistance of an axially loaded vertical pile in sand is conventionally evaluated by:

Table 2.1 Methods for predicting the pile shaft resistance.

Investigator No.	Reference	Side Friction	Pile Type	K	δ
1	Poulos- Davis, (1980)	F_w ($K_s$tan $\sigma'_{\infty o}$)	HP Others	0.8 0.4	30 30
2	Bustamante, Van Impe 1986	$\alpha_s q_c R_t/N_o$	—	------	
3	Tomlinson, 1967	$(K/K_o)K_{oz}$ tan $(\delta/\phi)\phi_z\sigma'_{vo}$	HP Pipe Slurry Cased	$K_o$pmt 0.5$K_o$pmt .67$K_o$pmt .67$K_o$pmt	2/3 ϕ spt 2/3 ϕ spt 0.8 ϕ spt 2/3 ϕ spt
4	Mayerhof, 1956	K' σ'_{vo}tan δ	Driven Drilled	1.5-2.3 1	40-44.5 40-46
5	Mosher, 1984	f-z curve	-------	------	
6	Kulhawy, 1983	K σ_{vo} tan δ CPT correlation	--------	------	
7	Meyerhof, 1976	N/50	------	------	
8	Meyerhof, 1976	K σ'_{vo} tanδ	HP Pipe Slurry Cased	0.5 0.57 0.45 0.5	35
9	Be Beer, 1976	CPT correlation	----		
10	API, RP2A, 1987	K σ_{vo} tan δ	HP Pipe	0.8 0.9	15-35
11	Nottingham, 1975	Limiting f_s	Driven Drilled	1 1	24.6 30
12	Nordlund, 1980	K (sin (w + δ)/cos w)σ'_{vo}	HP Pipe Drilled	$K_o$pmt $K_o$pmt 0.4	26 24 37
13	Rees – O'Neill, 1988	βσ'_{vo}	------	------	------
14	Coyl – Castello, 1981	K σ'_{vo} tan δ (pipe) fs(HP)	Pipe	0.7	30.4-31.2
15	Can. Foun. Eng. Manual	βσ'_{vo}	Driven	------	------
16	Denis – Olson, 1983	CPT f_s	------	------	------

δ = Mobilized angle of friction along the side of the pile
α = Empirical factor
pmt = Pressure Meter Test
K = Coefficient of earth pressure
K_o = Coefficient of earth pressure at rst
σ'_{vo} = Normal effective stress
ϕ = Angle of shearing resistance of the sand
β = Empirical factor
fs = Friction
F_w =Vertical force

$$Q_p = (\sigma'_o N_q) A_p \quad (2.6)$$

Where

σ'_o = effective vertical stress at the pile tip level

N_q = Bearing capacity factor

A_p = cross-sectional area of pile tip

Figure 2.2 presents the theoretical values of (N_q) as produced by different researchers, where wide discrepancies can be observed. These discrepancies can be attributed to lack of ability to evaluate the state of stresses in the surrounding sand after pile installation.

Armale and Esail (1987) introduced an empirical scheme for simulating the non-linear point resistance response of single piles in cohesionless soils. The pile-soil interaction was idealized by using a one dimensional finite element technique. It was reported that the proposed method is very complicated and contains several variables and constants that do not provide practical procedure to evaluate the response of axially loaded piles. The one-dimensional finite element technique is substituted by two-dimensional finite element that gives more accurate results and reliability. Abu Keefa (1998) developed a general regression neural network (GRNN) to predict the tip, shaft and total pile capacity. He used a database that includes full-scale and laboratory test results. Abu Keefa limited the input data to the pile length, cross-sectional area and the angle of shearing resistance of the sand, while he ignored the other key factors such as the pile/sand angle of friction and the coefficient of earth pressure, which had led to errors in the predictions.

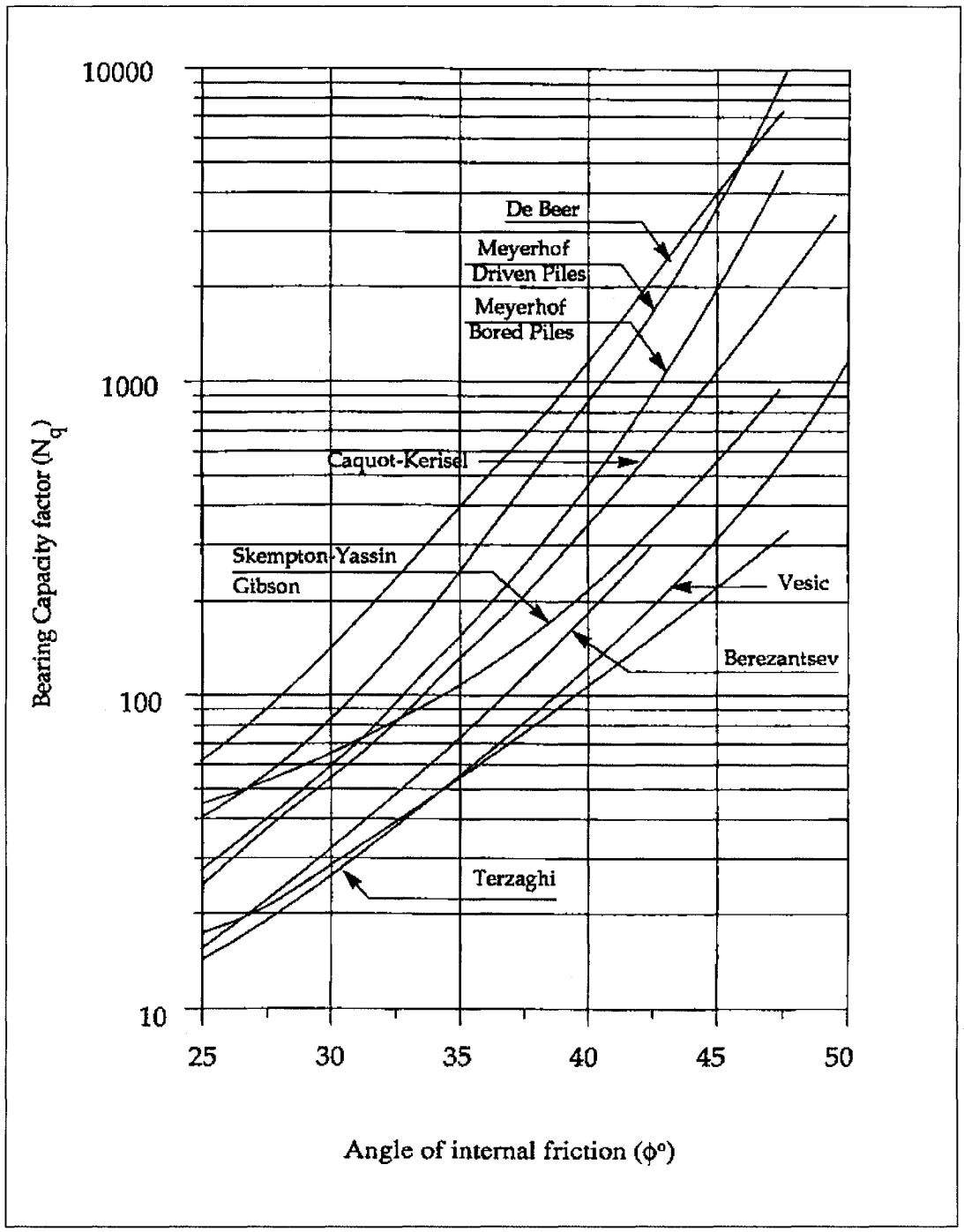

Figure 2.2 Theoretical bearing capacity factor (N_q) for deep foundation; after Poulos and Davis, (1980).

Some researchers attempted to evaluate the tip resistance using the field test results of the Standard Penetration Tests (SPT) and the Cone Penetration Test (CPT), (De Beer 1972, Been et al 1986). It should be made clear herein while the SPT and the CPT can predict the soil condition; they do not provide any information about the installation effect and the pile characteristics.

2.2 Pile Driving Simulation

The effect of pile installation remained an outstanding problem in the evaluation of the capacity. Vesic (1972) presented a solution for driven piles using the expansion of spherical and cylindrical cavities in a soil possessing both cohesion and friction. He took into account the effects of volume change in the plastic region around the pile's shaft. He presented the following Equation:

$$\frac{\partial \sigma_r}{\partial r} + 2\frac{\sigma_r - \sigma_\theta}{r} = 0 \qquad (2.7)$$

Where:

σ_r = radial normal stress

σ_θ = circumferential normal stress

r = the distance of an element to the center of the cavity.

The condition of rupture, according to Mohr-Coulomb criteria, becomes

$$(\sigma_r - \sigma_\theta) = (\sigma_r + \sigma_\theta) \sin \phi + 2c \cos \phi \qquad (2.8)$$

Substituting Eq. (2.7) into (2.8) and applying the limit equilibrium analysis: Thus

$$\frac{\sigma_\theta + c\cot\phi}{\sigma_r + c\cot\phi} = \frac{1-\sin\phi}{1+\sin\phi} \qquad (2.9)$$

$\sigma_r = p_u$ for $r = R_u$, the following solution of the differential Eq. (2.7) can be obtained

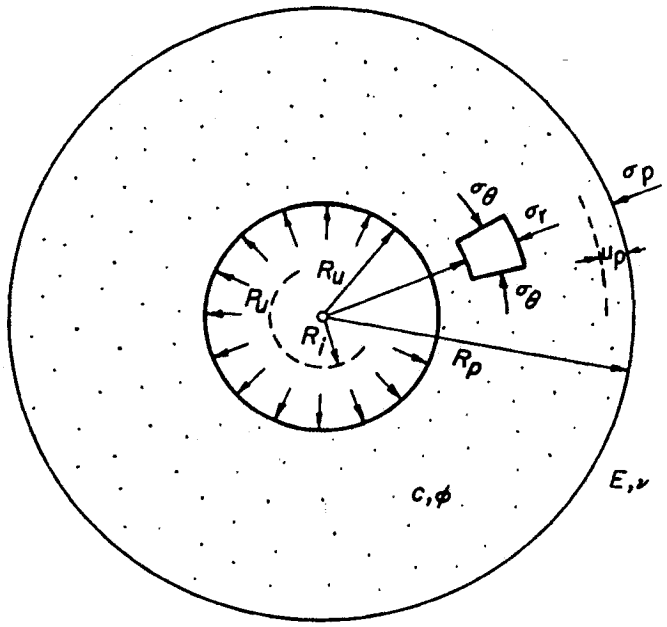

Figure 2.3 Cylindrical cavity expansion; after Vesic, (1972).

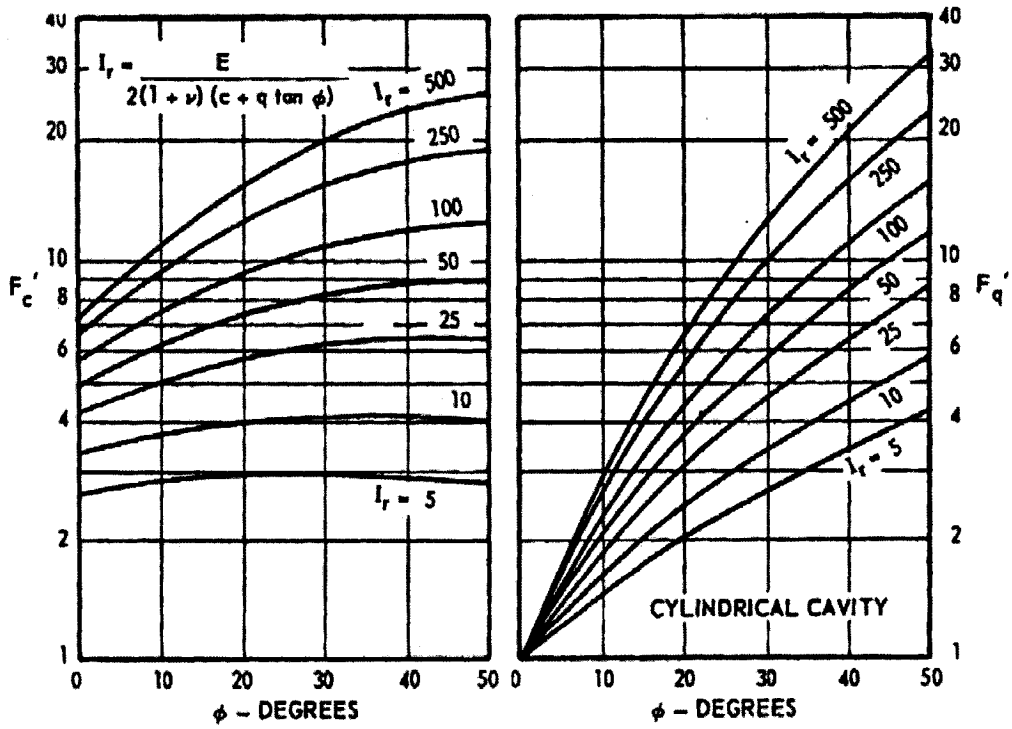

Figure 2.4 Cylindrical cavity expansion factors; after Vesic, (1972).

$$\sigma_r = (p_u + c \cot \phi)\left(\frac{R_u}{r}\right)^{4\sin\phi/(1+\sin\phi)} - c\cot\phi \quad (2.10)$$

Where:

c = cohesion of soil

p_u = the ultimate pressure,

R_p = the radius of the plastic zone.

These parameters were determined based on the assumption that the change of volume of the cavity is equal to the change of volume of the elastic and plastic zones. Thus:

$$\frac{R_p}{R_u} = \sqrt[3]{I_{rr}} \quad (2.11)$$

Furthermore:

$$I_{rr} = \frac{I_r}{1 + I_r \Delta} = \zeta_v I_r \quad (2.12)$$

$I_r = G/s$

Where:

G = shear modulus of soil

I_r= rigidity index

s = initial shear strength s = c+q tan ϕ

ζ_v = volume change factor

I_{rr} was then calculated and presented in tables. Knowing the ratio R_p/R_u, the ultimate cavity pressure can be computed. The result is presented in this form.

$P_u = cF_c + qF_q$ (2.13)

Where F_c and F_q are dimensionless spherical cavity expansion factors; presented in the form of charts in Figure 2.4. In case of cylindrical cavity:

$$\frac{R_p}{R_u} = \sqrt{I'_{rr} \sec\phi} \tag{2.14}$$

Where I'_{rr} = the reducing rigidity index

$$I'_{rr} = \zeta'_v I_r \tag{2.15}$$

ζ_v = the volume change for a cylindrical cavity

The ultimate cavity pressure, p_u, can be computed from Eq. (2.13) using the cylindrical cavity expansion factors F'_q, F'_c , which can be obtained from Figure 2.4. The average volumetric strain was introduced as a known quantity, while it is a function of the stress conditions in the plastic zone.

Alsiny et al. (1992) performed a series of experimental tests in which the cavity of a thick-walled hollow cylindrical sand specimen was inflated under volume-controlled plane strain conditions. The study was made to evaluate the localized and diffused deformation modes in the dry sand. From these tests it was found that both diffused and localized deformation modes occur in dense sand when the specimen of an aspect ratio of 1/10 is inflated under constant external pressure. The mechanical response of the tested sand is modeled by incremental elastoplastic constitutive equations. These constitutive equations involve an incrementally linear Hook's law, a linear Mohr-Coulomb yield condition, and a non-associative potential flow rule. The general form of the constitutive equations for axisymetric, plane–strain, rectilinear cavity expansion are

$$\Delta\sigma_{rr} = L_{rr\theta\theta}\,\Delta\varepsilon_{\theta\theta} + L_{rrrr}\,\Delta\varepsilon_{rr} \tag{2.16}$$

$$\Delta\sigma_{\theta\theta} = L_{\theta\theta\theta\theta}\,\Delta\varepsilon_{\theta\theta} + L_{\theta\theta rr}\,\Delta\varepsilon_{rr} \tag{2.17}$$

$$\Delta\varepsilon_{rr} = A_1\beta_1\rho^{\beta_1-1} + A_2\beta_2\rho^{\beta 2-1} \tag{2.18}$$

$$\Delta\varepsilon_{\theta\theta} = A_1\rho^{\beta_1-1} + A_2\rho^{\beta 2-1} \tag{2.19}$$

Where

$L_{rr\theta\theta}$, L_{rrrr}, $L_{\theta\theta\theta\theta}$, $L_{\theta\theta rr}$ = Components of the elastoplastic stiffness matrix.

$\Delta\varepsilon_{rr}$, $\Delta\varepsilon_{\theta\theta}$ = strain increments in polar co-ordinates

From Eq. (2.16) to (2.19) the incremental radial and circumferential stress were expressed as:

$$\Delta\sigma_{rr} = A_1\rho^{\beta_1-1}(L_{rr\theta\theta} + L_{rrrr}\beta_1) + A_2\rho^{\beta 2-1}(L_{rr\theta\theta} + L_{rrrr}\beta_2) \tag{2.20}$$

$$\Delta\sigma_{\theta\theta} = A_1\rho^{\beta_1-1}(L_{\theta\theta\theta\theta} + L_{\theta\theta rr}\beta_1) + A_2\rho^{\beta 2-1}(L_{\theta\theta\theta\theta} + L_{\theta\theta rr}\beta_2) \tag{2.21}$$

Alsiny et al. indicated that the integration constants A_1 and A_2 could not be determined directly from the boundary conditions because the exponent β_1 and β_2 are functions of the r coordinate. The authors conducted equilibrium bifurcation analysis for elements of each ring, which was determined by dividing the cylinder into a collection of separate rings, each being uniform under axisymmetric stress and strain state. It was stated that deformation localization might occur when the hardening modulus h_1, which is a parameter used to evaluate the components of the elastoplastic stiffness matrix when it reaches a critical value

$$h_1 = \frac{G(\mu-\beta)^2}{8s(1-\nu)} \tag{2.22}$$

μ = mobilized friction factor

β = mobilized dilatancy factor

ν = Poisson's ratio

s = mean stress

The measurement techniques used in the tests did not allow accurate detection of either the onset or the growth of the deformation modes. Furthermore, it can be noted from the differential cavity pressure versus cavity volume change curves that the axisymmetric deformations can be reproduced by means of a simple elastoplastic hardening/softening constitutive model.

Collins et al. (1992) presented theoretical solutions for the expansion of cylindrical and spherical cavities in sand. The paper concentrated on large strain conditions for cavities expanding from initial radius of zero in cohesionless elastic/plastic materials. One of the basic assumptions used in this theory is the existence of a critical state at which the sand deforms without any plastic volume change; accordingly, the dilation angle is zero. The authors divided the cavity expansion into two regions; namely the elastic and the elastic/plastic regions. A formula was presented to calculate the radial strain and stress for each zone. Thus for the elastic region the displacement is given as follows:

$$u = \varepsilon_R \left(\frac{R}{r}\right)^k R \qquad (2.23)$$

Where

ε_R= is the circumferential strain at the elastic/plastic boundary (r = R).

R = radius of the elastic/plastic boundary

The radial and circumferential stress components are given by

$$\sigma_r = p_o + 2Gk\varepsilon_R(R/r)^{k+1};\ \sigma_\theta = p_o - 2G\varepsilon_r(R/r)^{k+1} \qquad (2.24)$$

Where:

p_o = existing isotropic stress state

k = 1, for the cylindrical cavity and 2 for the spherical cavity

Accordingly, the mean pressure, and hence the state parameterξ, are both unaltered by the elastic deformation. At the elastic/plastic boundary $\sigma_r/\sigma_\theta = N_o$ where $N_o = N(\xi_o)$ corresponds to the initial value of ξ, so that from Eq. (2.24) the following Equation can be produced:

$$\varepsilon_R = (N_o - 1)p_o/(N_o + k)2G \qquad (2.25)$$

Furthermore, the radial stress at the elastic/plastic boundary is given as:

$$\sigma_R = (1 + k)N_o p_o/(N_o+k) \qquad (2.26)$$

The authors concluded that the material elements at the cavity wall are always at the critical state. Even if the sand is initially at a critical condition, it will compact and end up at a denser critical state. From the results presented, it was found that the value of the ratio of the cavity wall pressure to the initial effective stress, which corresponds to the normalized tip resistance in a cone penetrometer test, depends not only on the initial values of the state parameter, but also on the initial values of the void ratio. In this investigation, the sand initial state was not taken into consideration; in addition, neglecting the dilation effect will lead to unrealistic results as the soil can go beyond the critical state.

Mabsout and Tassoulas (1992) and Mabsout et al.(1995) conducted analysis of pile driving using finite element technique taking into account the non-linear behaviour of undrained clayey soil and tracing the penetration of the pile into soil. The main interest behind this paper was the dynamic modeling of pile driving. They have developed a three dimensional model, which was simplified to a two-dimensional analysis due to the axisymmetric nature of the problem. The author expected that the soil in the vicinity of

the pile would undergo large deformation as a result of the pile penetration. Accordingly, a non-linear analysis was incorporated in the finite element model. An assumption was made that the path in the strain space is straight, and the constitutive equations can be integrated along this path, leading to an incremental linearized form. During the analysis of a load increment, the variables are updated in the problem configuration upon the completion of the analysis for the step. The pile was modeled such that it will have a little deformation during the process of pile driving and remains in the elastic range. Special absorbing boundaries at the soil were incorporated; the role of such boundaries was to transmit the incident waves resulting from the driving process, and, therefore, prevent their reflection, thus avoiding a spurious response. The boundary conditions follow the one-dimensional wave equation formulation for rods:

$$\frac{\partial u}{\partial x} = -\frac{1}{c}\frac{\partial u}{\partial t} \tag{2.27}$$

$$\sigma_x = -\rho c \dot{u} \tag{2.28}$$

Where:

ρ = density of the rod

c = pressure-wave velocity of the rod

The pile-soil interface used in this investigation was modeled such that it permits large relative sliding between the pile and the soil, and allows separation if tension occurs along the interface. The analysis was applied on a pile having a diameter of 0.5m and length of 20m (L/D = 40). The tip was taken as parabolic in shape (Figure 2.5) to facilitate the numerical model procedure. The compressive strength of concrete f'_c is

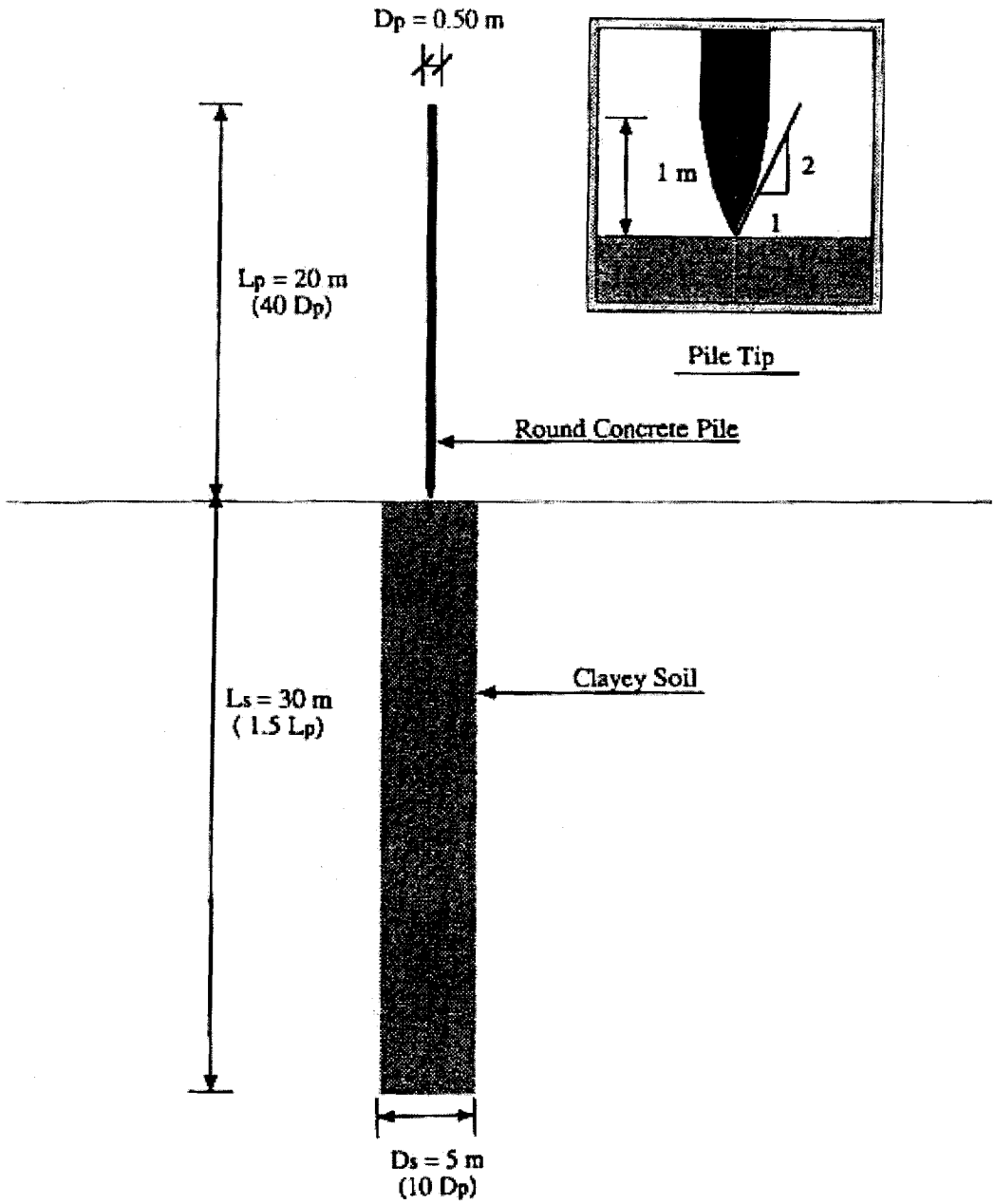

Figure 2.5 Description of the pile-driving problem; after Mabsout et al., (1995)

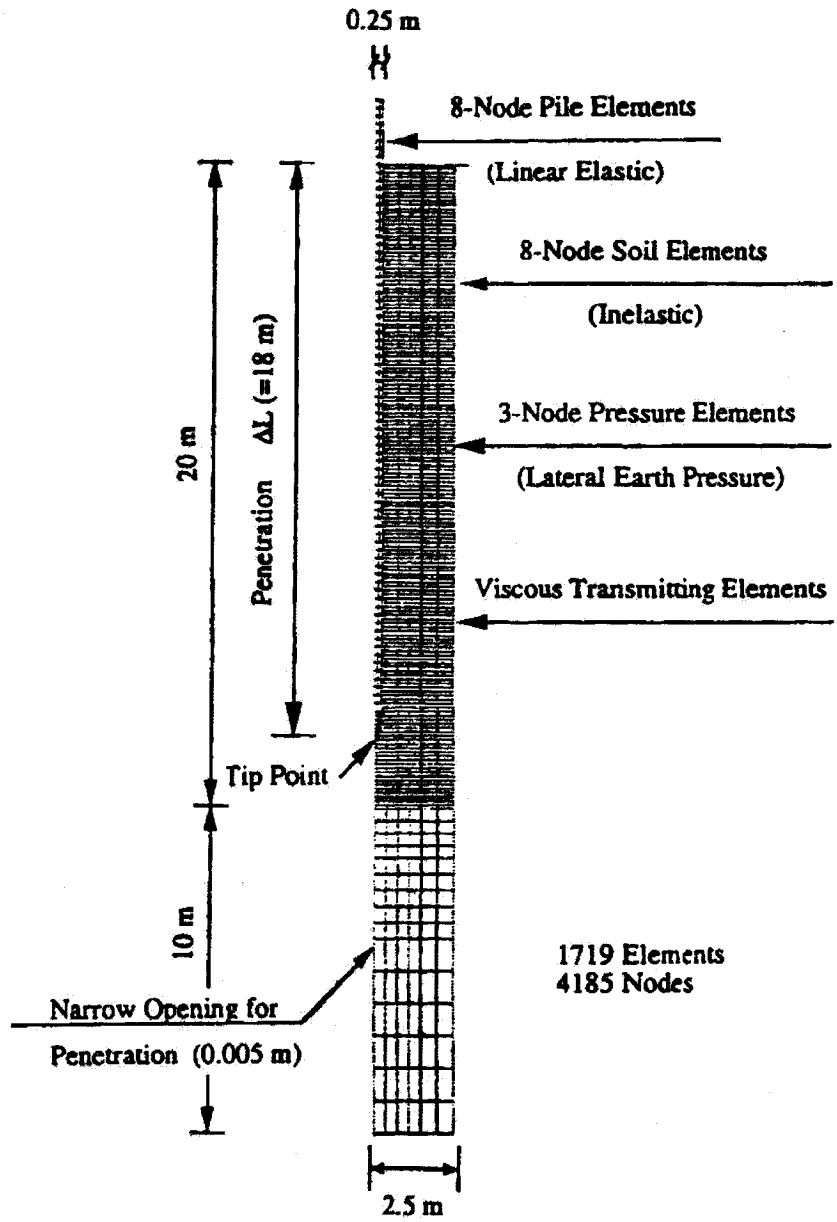

Figure 2.6 Finite element discretization of the pile-driving system; after Mabsout et al., (1996).

taken as 27500 kPa. The modulus of elasticity E_c was therefore computed as 24.8 x 10^6 kPa. Poisson's ratio of concrete ν is set equal to 0.2 and its density ρ_c equal to 2.4 x 10^3 Kg/m^3. The damping ratio of the concrete pile at the natural frequency was estimated as 0.03; considering the pile was fixed at the tip.

The voids ratio was assumed constant over the soil profile and equal to 0.63, and the soil specific gravity S_G as 2.6. It was also assumed that the coefficient of lateral earth pressure is equal to unity. Therefore, at a depth Z below the surface of the soil, the initial effective radial and hoop stress, $\sigma_r(Z)$ and $\sigma_q(Z)$, are equal to the effective vertical stress $\sigma_z(Z)$. The axisymmetric finite element mesh employed in discretizing the pile-soil system is shown in Figure (2.6). It consists of 1719 elements (including pressure, viscous transmitting, and contact elements) and 4185 nodes. The pre-bored pile is shown at a penetrated depth ΔL of 18m. A narrow opening (hole) below the tip of the pile was provided to facilitate the computational penetration of the pile upon driving. The diameter of this hole was taken as 1% of the diameter of the pile. The hammer blows on the pile were represented by a forcing function applied at the top of the pile as shown in Figure 2.7. The study was limited to deal with undrained conditions under which the soil matrix is fully saturated. The simulation tests were carried for both compression and extension at various levels of the overconsolidation ratio (OCR). The analysis was mainly base on one hammer blow on the pile head. The effect of the pre-boring level was investigated, and it was ascertained that more resistance to driving is encountered at deeper pre-bored levels, in the stronger soil strata. A case was selected where several consecutive blows were applied to the pile and the corresponding responses were

compared. This study was limited to clay; however, it can be extended to cover the case of sand.

Salgado and Jamiolkowski (1997) presented a theory, based on cavity expansion and stress relation analyses for computing the cone penetration resistance of sand. The theory developed was based on the analysis of calibration chamber tests. As presented in Figure 2.8 the authors described the stress increase that takes place around the expanding cavity by three distinct zones depending on the induced strain levels. In the linear elastic zone the strains are so small that the soil behaves as a linear-elastic material. In the nonlinear elastic zone the material has yielded, moving into the nonlinear stress-strain range, but the stresses are not large enough to produce a failure state. Finally, in the plastic zone the stresses are large enough to cause failure. The stress field established around the expanding cavity is characterized by the radial normal stress σ_r, which is the major principle stress, and the circumferential normal stress σ_θ, which is the minor principle stress in all cases, at each point in the elastic and the plastic zones. The strain was accordingly described by ε_r and ε_θ.

Salgado and Jamiolkowski (1997) assumed that the cavity expansion takes place under plane strain condition i.e. there is no normal strain in the vertical direction ($\varepsilon_z = 0$). The analysis done to the elastic zone was taken from a region between radius R and outer radius B (see Figure 2.8). This region is subjected to an internal pressure that has increased from p_o to the current radial normal stress σ_r at r = R. The strain-displacement relations and the equilibrium equation at a point distant r from the cavity axis become, respectively:

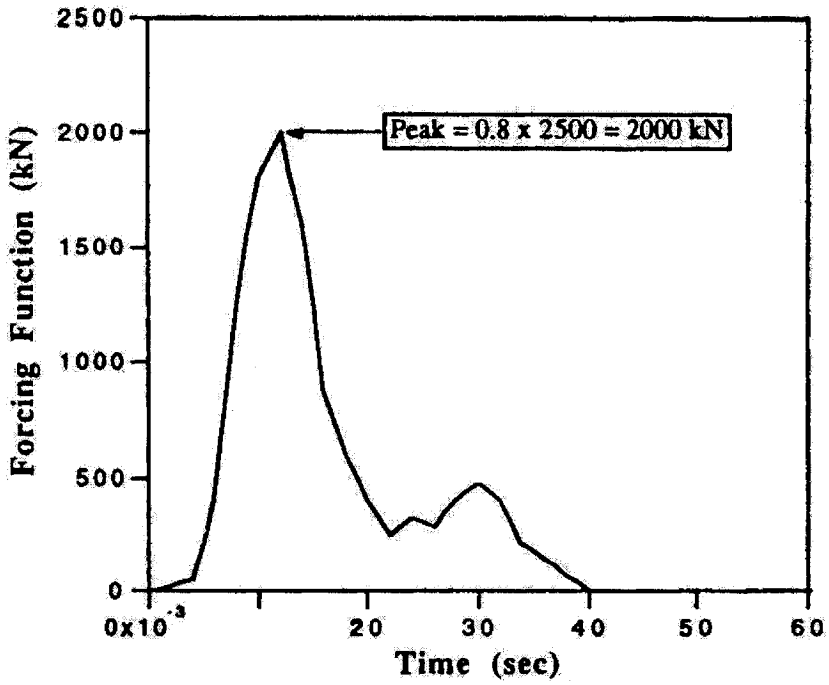

Figure 2.7 Assumed forcing function simulating a hammer blow; after Mabsout et al., (1996).

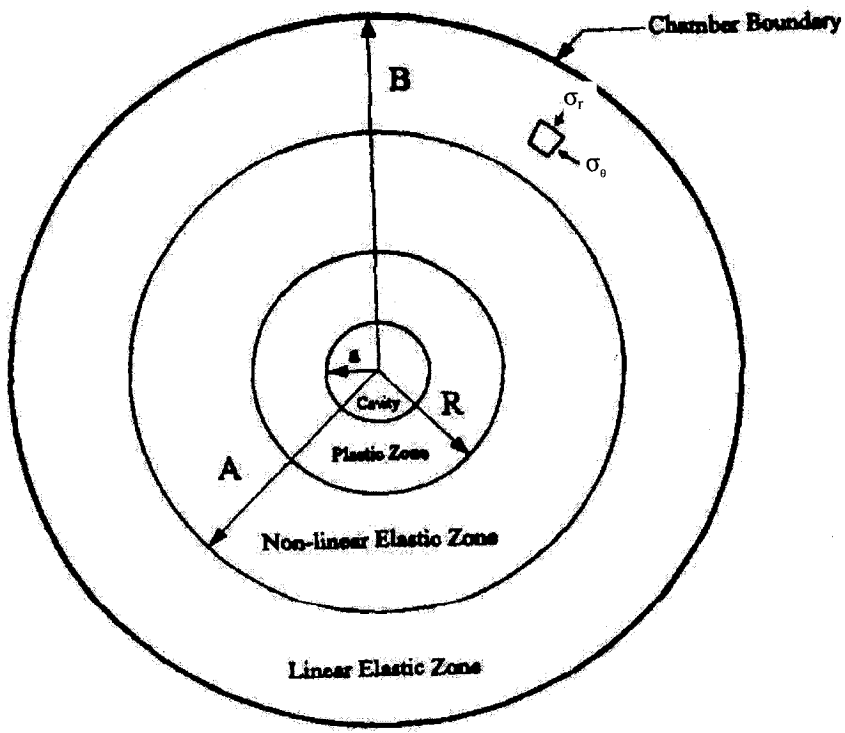

Figure 2.8 Cylindrical cavity expansion model proposed by Salgado and Jamiolkowski 1997.

$$\varepsilon_r = -\frac{du}{dr}; \qquad \varepsilon_\theta = -\frac{u}{r} \tag{2.29}$$

From (2.29)

$$\varepsilon_r = \frac{d(r\varepsilon_\theta)}{dr} \tag{2.30}$$

At the elastic-plastic interface (r = R), the radial normal stress σ_r and the circumferential strain ε_θ can be expressed as

$$\sigma_R - p_o = \frac{2N_p}{N_p + 1} \frac{1}{1 + \gamma\left(\frac{R}{B}\right)^2} \tag{2.31}$$

Where:

$N_p = \tan^2(45 + \phi_p/2)$

ϕ_p = the peak friction angle

$$\gamma = \frac{N_p - 1}{N_p + 1}$$

And

$$\varepsilon_\theta = -\varepsilon_\tau = \frac{N_p - 1}{N_p + 1} \frac{p_o}{2G} \frac{1 + \delta\left(\frac{R}{B}\right)^2}{1 + \gamma\left(\frac{R}{B}\right)^2} \tag{2.32}$$

Where δ = constant that depends on the boundary conditions, given by

$-1 < \delta < 1-2\nu$

ν = Poisson's ratio

The authors didn't provide a method to determine the value of the shear modulus "G". He left it up to the judgment and the experience of the designer and the boundary

conditions of the problem. In the plastic zone the author provided a relation between the radial and circumferential stresses in the plastic range, as follows:

$\sigma_r - \sigma_\theta = (\sigma_r - \sigma_\theta) \sin \phi_s$

Where ϕ_s was assumed to be any value between the critical ϕ_c and the peak ϕ_p.

The mean effective stress p' is given by

$$p' = \frac{1}{3}\left[1+\mu\left(1+\frac{1}{N}\right)\right]\sigma_r \qquad (2.33)$$

Where μ parameter used to compute the normal stress perpendicular to the deformation plane in plane-strain case.

$$\mu = \frac{1}{2}(1+\sin\phi\sin\psi)$$

$\phi = \phi_c + 0.8\psi$

ψ = angle of dialation

It was defined that if all operative values of the friction angle ϕ and elements flow number N exist for the plastic zone, then the cavity pressure can be formulated as:

$$p = \sigma_R\left(\frac{R}{a}\right)^{(N-1)/N} \qquad (2.34)$$

Verification was done by using 400 calibration chamber tests. The factor taken into account in this study is the relative density, horizontal stress and the boundary conditions. It was noted that the OCR was not taken into account and the vertical stresses were not applied in analytical modeling. The use of cavity expansion in predicting the pile penetration was not clearly presented.

Ladanyi and Foriero (1998) developed a numerical solution of spherical and cylindrical expansion problem in sand. The proposed theory developed was based on the following assumptions:

1- The media is homogeneous, isotropic, infinite and weightless.

2- The effect of the rate of strain is neglected, and it is assumed that in every point of the medium affected by the expansion of the cavity, the medium has the same stress-shear strain-volume strain characteristics as those obtained in drained triaxial compression tests.

3- Before cavity expansion, the state of stress in the medium is isotropic.

4- The cavity expansion took place from zero-radius under the drained condition.

The theory developed was based on four cases of simulation, performed by changing the consolidation porosity on two spherical cavities and two cylindrical cavities.

The author applied compatibility and equilibrium equation to the cavity expansion problem. The compatibility condition is enforced by observing the distortion of γ planes initially inclined at 45° from the principle planes of stress (see Figure 2.9)

Accordingly:

$$\tan\left(\frac{\pi}{4}+\frac{\gamma}{2}\right)=\frac{\rho_2+\rho_1}{\rho_2-\rho_1}\left(\frac{d\alpha}{2}\right) \tag{2.35}$$

Where ρ is the distance of an arbitrary point from the centre of the cavity after a radius expansion from $\rho = 0$ to $\rho = r$, and $d\alpha$ is an infinitesimal angle marking the summit of a pyramid defining the elementary volume. The authors developed a formula to determine the radial displacement at any arbitrary point once the distortion γ is determined.

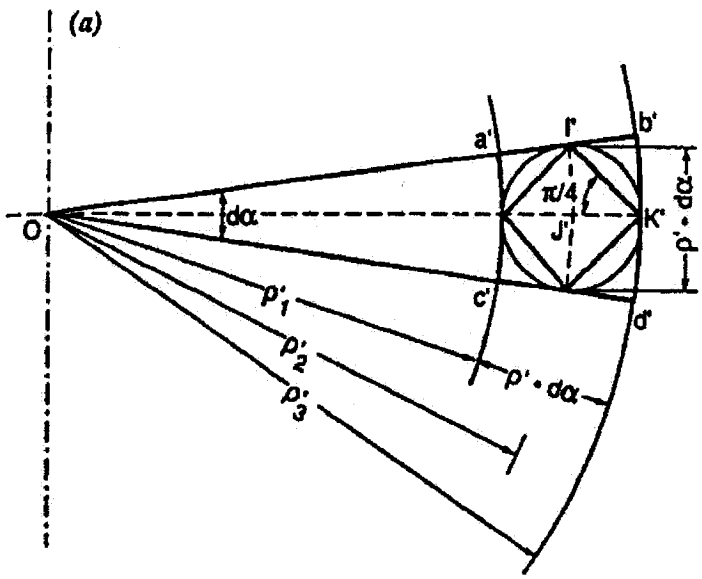

(a) The state before cavity expansion.

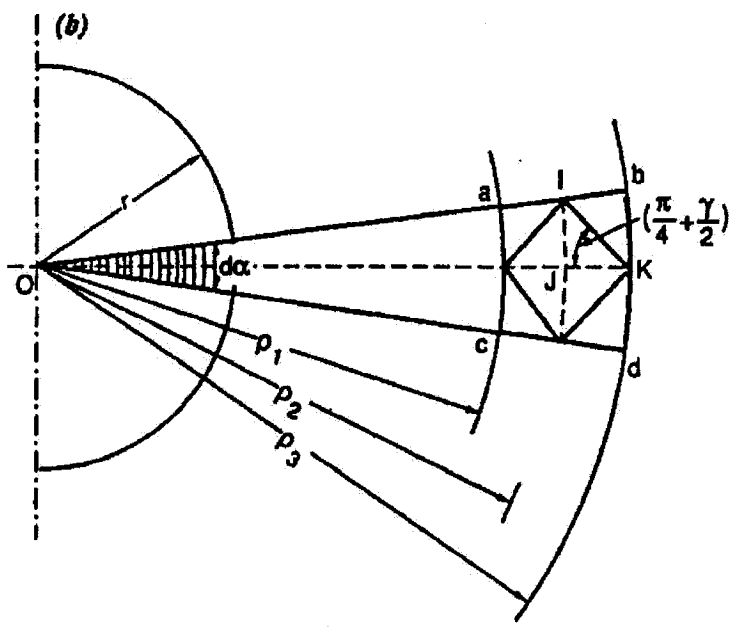

(b) The state after cavity expansion.

Figure 2.9 Diagram utilized in the calculation of the distortion; after Ladanyi and Foriero, (1998).

$$\frac{u_p}{r} = \frac{\rho}{r}\left(1 - \frac{2\tan\left(\frac{\gamma}{2}\right)}{1+\tan\left(\frac{\gamma}{2}\right)}\right)^{1/(c+1)} \tag{2.36}$$

Where:

c = is taken as 2 for spherical and 1 for cylindrical cavity expansions.

u_p = displacement in the radial direction of a point lying at a distance ρ from the line of symmetry of the cavity expansion.

r = cavity radius

Computer implementation was used to determine the strain field presented by the relation between the volumetric stain and the shear strain. It was also used to determine the stress field with the aid of the experimentally obtained drained triaxial test results.

The solution obtained by using an appropriate interpolation method for finding the values in between the experimental data takes into account the combined effects of no linearity of stress-strain curves up to the critical state, no linearity of the failure envelope, and pressure-dependent volumetric-strain due to compression and dilation of the sand. Being based on experimental stress-strain curves, the solution did not explicitly define the "elastic" and "plastic" zones around the cavity, but implies a continuity of mobilization of shear strength of sand as a function of cavity-expansion-induced shear strain.

Mabsout et al. (1999) conducted a numerical investigation to simulate the pile driving by using the cavity expansion theory. The objective of this study was to develop an alternative method proposed by Ladanyi and Foriero (1998) to simulate the pile driving process. The authors reported that their previous model was not practical for day-

to-day use. Two models were created the first one the pile was installed at a predetermined depth by hammering and the second model was installing the pile to the same depth by cavity expansion. The soil used in the investigation was modeled as plastic, isotropic, cohesive soils. The total stress in saturated $\dot{\sigma}_{ij}^{t}$ clays was obtained by adding the pore-water pressure $\dot{u}$ to the effective stress $\dot{\sigma}_{ij}$ so that:

$$\dot{\sigma}_{ij}^{t} = \dot{\sigma}_{ij} + \dot{u}\delta_{ij} \tag{2.37}$$

Where δ_{ij} is the Kronecker delta

The pile-driving model refers to the axisymmetric finite-element mesh described in Figure (2.6), where the pile was pre-bored at 18m; the discretization was based on the conventional eight-node isoperimetric elements. A 50 cm cylindrical concrete pile and 20m long and its parabolic tip extend over a depth of 1 m. The pile material was assumed to behave as linear elastic. For the driving procedure was similar to the authors' previous work on the subject matter (Mabsout and Tassoulas 1992). Results of pile response, and soil resistance and behaviour, were compared to the expansion procedure as an alternative model for pile driving.

Koltz and Taylor (2002) performed a series of centrifuge tests on an instrumented model pile driven in carbonated sands and quartz sands. The objective of this study was to demonstrate that the current pile design practices are not applicable to all type of sands and further; there is no relationship between the pile capacity and the relative density of the sand. They reported that the design methods when applied to quartz sand it leads to a very conservative design while in carbonate sands the pile capacity can be over predicted. It was found that normalization using a straight critical

state line and either a stress state parameters R_s or a volume parameter ψ gave good correlation with the bearing capacity factor N_q.

2.3 Discussion and Scope of Present Research

It can be noticed that most of the theories developed for driven piles are based on a factor used to reflect the increase in the value of the coefficient of earth pressure, which was originally developed for bored piles. The factor used is mainly based on practical or experimental experience, ignoring the factors that affect the piles during installation. On the other hand theoretical investigations were developed for the study of cavity expansions, nevertheless, the results were not incorporated in the calculation of piles capacity. Limited number of investigations was developed to study the change of the stresses around the pile's shaft during the installation process, and how it affects its capacity. Driven piles are highly influenced by the diameter of the pile not only by increasing the shaft area of the pile but also increasing the passive earth pressure acting on the shaft.

The objective of this study is to develop a numerical model to simulate pile installation utilizing the cavity expansion technique. Furthermore, the changes in the soil mass during pile installation will be monitored in order to establish the role of the governing parameters in the produced pile capacity. The changes in the OCR values along the pile will be examined during the installation process. The contribution of the diameter of the pile to the increase of the insitu stresses will be reported.

CHAPTER 3
NUMERICAL MODEL

3.1 General

In this chapter, a numerical model is developed to simulate the driving process of a single pile in sand. The objective of this model is to study the effect of the pile installation process on both the passive earth pressure developed on the pile's shaft and the overconsolidation ratio in the sand mass and, hence, on the ultimate pile capacity. A procedure was developed to simulate the driving process in the sand using the cavity expansion technique and the finite element approach. The effects on the ultimate capacity of the pile will be presented in terms of the variation of the coefficient of earth pressure "K_s" for the shaft resistance and the bearing capacity factor "N_q" for the tip resistance. Based on the results of this analysis, it was possible to define the strain field variation around the pile's shaft during pile installation and loading stages. These findings have been used to develop a guideline for the spacing of piles in a group in order to avoid overlap of stresses. Furthermore, the results of this study will define the contribution of the driving process to the pile capacity as compared to bored piles. The stress and strain fields generated around the pile's shaft and tip would constitute the base for the analytical model presented later in Chapter 4.

3.2 Numerical Model

The numerical model developed in the present investigation was constructed using the non-linear elasto-plastic finite element approach. The model was developed to idealize

the installation process through a cavity expansion and the loading process of driven piles. To be able to generate the model the computer program "Plaxis" is used in these analyses. Plaxis began in 1987 at the Technical University of Delft as an initiative of the Dutch Department of Public Work and Water Management. It is specially intended for the analysis of deformation and stability in geotechnical engineering projects. There are a number of soil models available that can be used to perform a non-linear analysis of a problem using the finite element technique.

3.2.1 Finite Element Idealization

The configuration of the finite element mesh is dependent on the size of the pile and the range of deformations expected through the analysis. The region of interest of the stress and strain fields is limited to a few diameters around the pile. Axisymmetric finite element analysis using a mesh with its axis coincides with the axis of the pile was employed to idealize the problem. In order to develop and design the appropriate finite element mesh capable of simulating all the construction activities, preliminary tests were performed using a relatively coarse mesh to establish the stress concentrations zones. This information was used to create a refined finite element model. The nodes of the vertical boundary were fixed against displacement in horizontal direction; yet remain free to move vertically. The nodes constituting the bottom of the mesh were fixed against displacement in both horizontal and vertical directions. The interface medium between the pile shaft and the surrounding soil continuum was idealized using special type interface elements to simulate the friction and to allow for slip between the pile and the surrounding soil.

To simulate the pile installation process, a prescribed displacement, equivalent to

the pile's diameter was applied to the soil along the perimeter of the pile as shown in Figure 3.1. A hole of 0.08m in diameter was first created as the initial size of the cavity to facilitate the computational process and to allow the axis of symmetry to be free from nodes. Figure 3.2 shows the developed finite element mesh, where the boundaries were chosen at a distance of 50 times the pile radius in the horizontal direction and 1.5 times the pile length in the vertical direction (Randolph, 1977) in order to avoid the effects of the mesh boundaries on the stress and strain through the zone of interest around the pile shaft and beneath the pile tip.

Through the analyses, both the soil and the pile were simulated utilizing the 15-nodes triangle elements with a quadratic displacement function. Two different constitutive models were used to simulate the stress strain behavior of both the concrete piles and the surrounding soil. Linear elastic constitutive model was utilized to simulate the stress-strain behavior of the concrete piles since the maximum stresses generated on the pile during installation and loading would not exceed the yielding limit of the pile material. The parameters used for the concrete piles constitutive model are shown in Table 3.1. The subsurface condition through the analyses was chosen as a homogeneous isotropic sandy soil. The elastic-perfectly plastic Mohr Coulomb constitutive model was used to update the sandy soil stress strain behaviour. Sand is assumed dry and homogenous. Table 3.2 presents different parameters used for the sandy soil constitutive model at different relative densities ranging from loose to dense state.

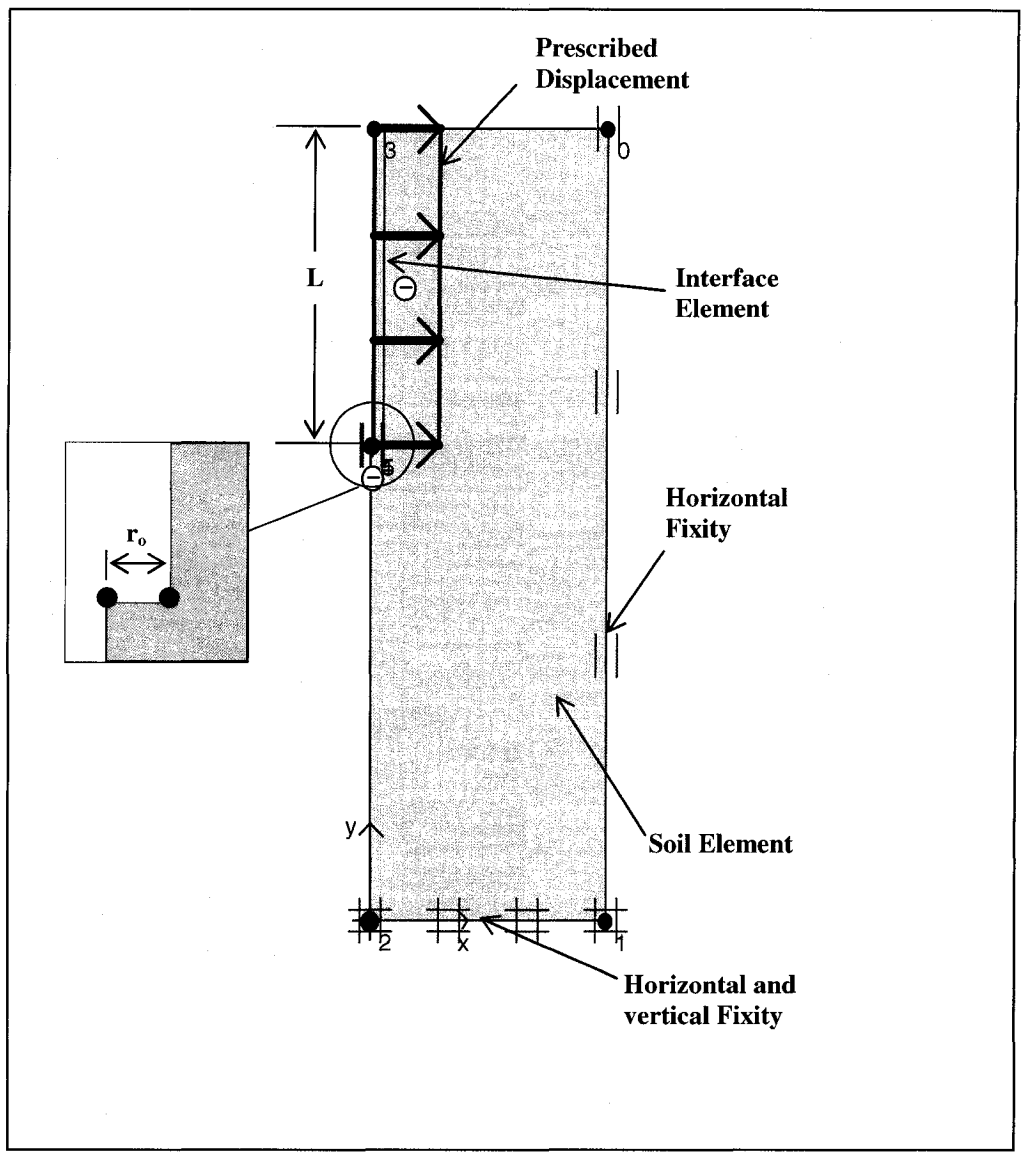

Figure 3.1 Layout of the numerical model.

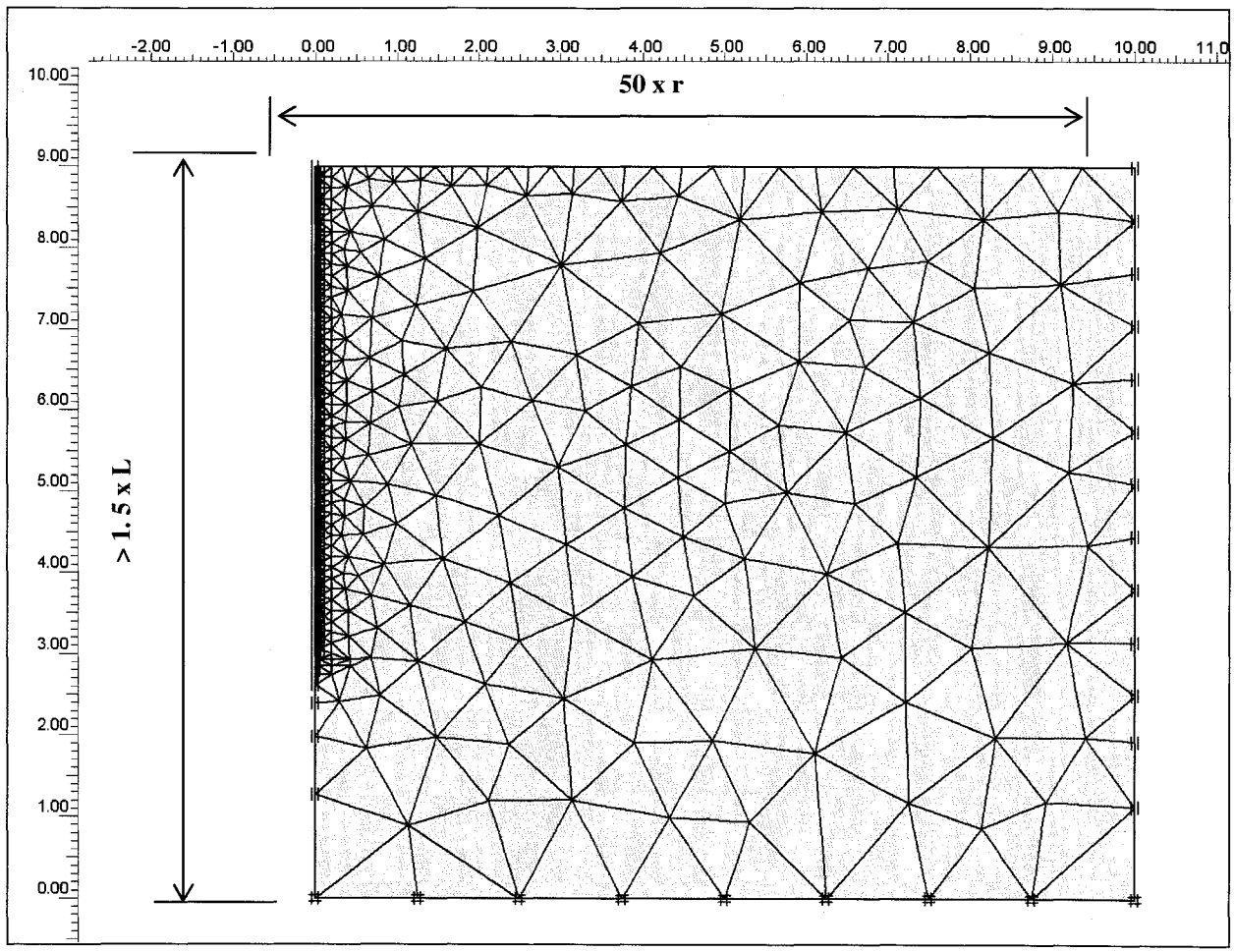

Figure 3.2 Finite element mesh.

Table 3.1 Typical data input for modeling the pile material

Parameter	Symbol	Value
Young's modulus	E'	$3*10^7$ kN/m^2
Unit weight	γ	24 kN/m^3
Poisson's ratio	ν'	0.2
Interface angle of friction	δ	$2/3\phi - 1/3\phi$

Table 3.2 Typical Input Data for the Sand.

Parameter	Loose Sand*	Medium Sand*	Dense Sand*	Unit
Dry unit weight, γ	17	18	19	kN/m^3
Young's modulus, E^{ref}	$2*10^4$	$4*10^4$	$6*10^4$	kN/m^2
Poisson's ratio, ν_{ur}	0.3	0.3	0.3	-
Angle of shearing Resistance, ϕ	30	35	40	Degrees
Angle of dilatation, ψ**	1	5	10	Degrees

* Kolar and Nemec (1989)
* * Bolton (1986)

3.2.2 Pile Installation Simulation

In order to simulate the driving process of a single pile in sand, the model must be capable of measuring the insitu stresses developed around the pile's shaft. To achieve this objective, the pile's driving process was divided into three stages as illustrated in Figure 3.3.

In the first stage, an initial opening of a value of (r_o) was first created in the sand mass; the interface elements were then placed along the opening walls to represent the pile/sand interface. To simulate the insertion of the pile in the sand mass, a prescribed displacement was generated progressively along the pile's perimeter and in the axisymmetrical direction. This prescribed displacement, will act as a cylindrical cavity in the surrounding sand continuum. The amount of the displacement (Δr) has been taken place progressively with a maximum value equal to the pile diameter (D) where:

$$D = 2*(r_o + \Delta r) \tag{3.1}$$

In the second stage, the pile elements were introduced to fill up the produced cavity. This stage acts as a transition stage between the pile installation process and the loading process where the insitu stresses are adjusted due to the pile presence and the removing of the prescribed displacement force. In this stage the residual stresses generated during the pile installation process were considered as the initial loading condition on the pile and carried over to the loading stage.

In the third stage, the pile was loaded up to the failure point, and the load-settlement characteristics were recorded. The results produced in the third stage would show the changes in the insitu stresses generated in the soil mass after installation up to the failure point.

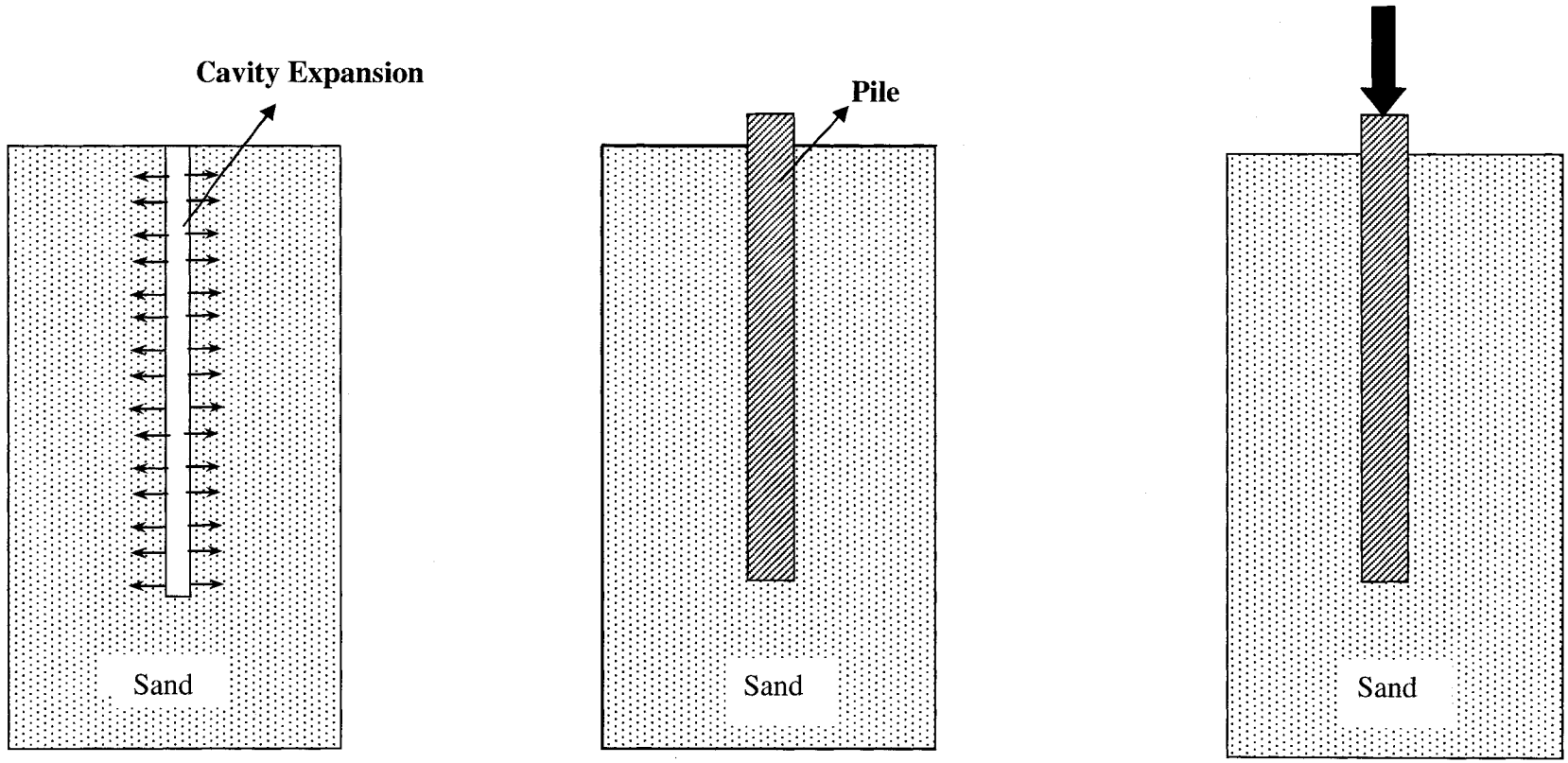

Stage 1
Cavity Expansion

Stage 2
Pile in Place

Stage 3
Pile Loading

Figure 3.3 Stages of pile driving process model.

3.3 Model Validation

The proposed model was validated by the laboratory test results (Hanna and Nguyen, 2002). The layout of the set-up for the experimental investigation is shown in Figure 3. 4. The experimental set-up comprises a 1.22m x 2.13m x 2.13m steel frame-testing tank, designed for testing piles up to 1.7m long and 0.076m in diameter. The placement of sand in the testing tank was carried out by depositing sand through a distributing hopper installed on carriage traveling back and forth over the test tank. Provisions were made to permit regulating the flow rate of sand, the speed of carriage travel and dropping distance of the sand. Once the tank is filled, the model pile can be pushed into the sand deposit by a strain-controlled screw jack attached to the loading column.

Piles were tested vertically under compression. The piles used in that investigation were 0.076m and 0.038m in outside diameter. The model piles were made of steel. Their surface was made rough by gluing sandpaper on the pile, in order to simulate the condition of concrete piles. The unit weight of the sand (γ) was 15.6KN/m^3 with $\phi = 43^\circ$. The results of the validation are presented in Table 3.3. It can be noted by comparing the numerical results with the experimental results that there is a good agreement between both data. Additional validation of the numerical model with full scale pile load test will be presented in Chapter 4 of this thesis.

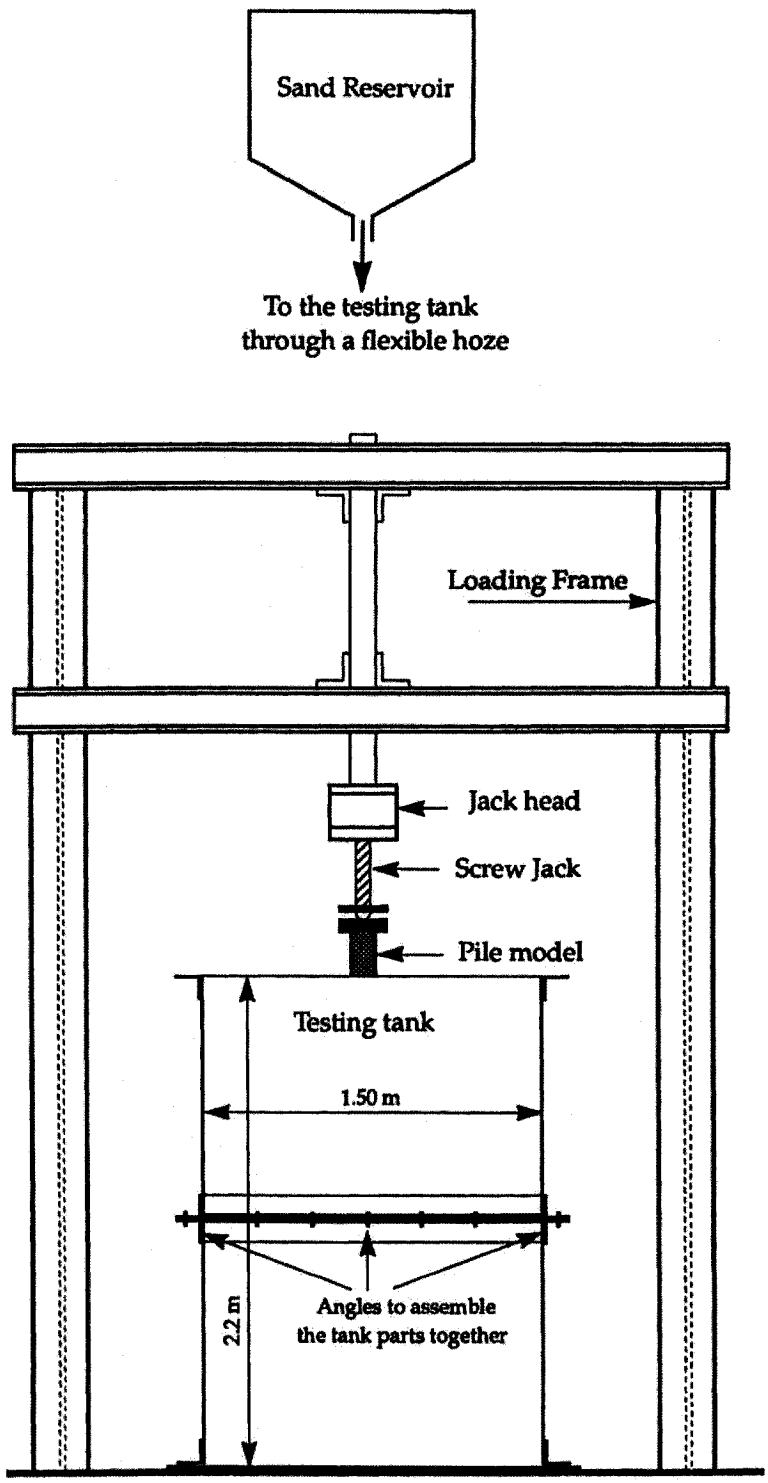

Figure 3.4 Schematic diagram of the experimental set-up; after Hanna and Nguyen (2002).

Table 3.3 Results of Model Validation

Type of Model Pile	L (mm)	L/D	Q_t (kN)	
			Numerical	Experimental
76mm Diameter	1525	20	16.65	18.24
38mm Diameter	1525	40	8.60	9.79
	1143	30	2.89	3.56
	762	20	1.60	1.78
	381	10	6.00	5.34

3.4 Study and Analysis of Numerical Model Results

The results of this investigation produced in the form of undeformed/deformed mesh, horizontal stresses, vertical stresses, shear stresses, horizontal strain, vertical strain and the rupture surface in the sand mass. Typical plots and study of these results are presented in the following sections.

3.4.1 Load Settlement Relationship

Figure 3.5 presents typical load-settlement curves for the 6m pile with different diameters driven in sand. It can be noted from this Figure that the capacity of the pile increases due to an increase of its diameter. Thus it should be made clear here that pile diameter contributes significantly to the driven pile capacity in three different ways; increasing the pile's shaft and hence the area subjected to skin friction, increasing the tip area of the pile and further increasing the passive earth pressure acting on the pile's shaft.

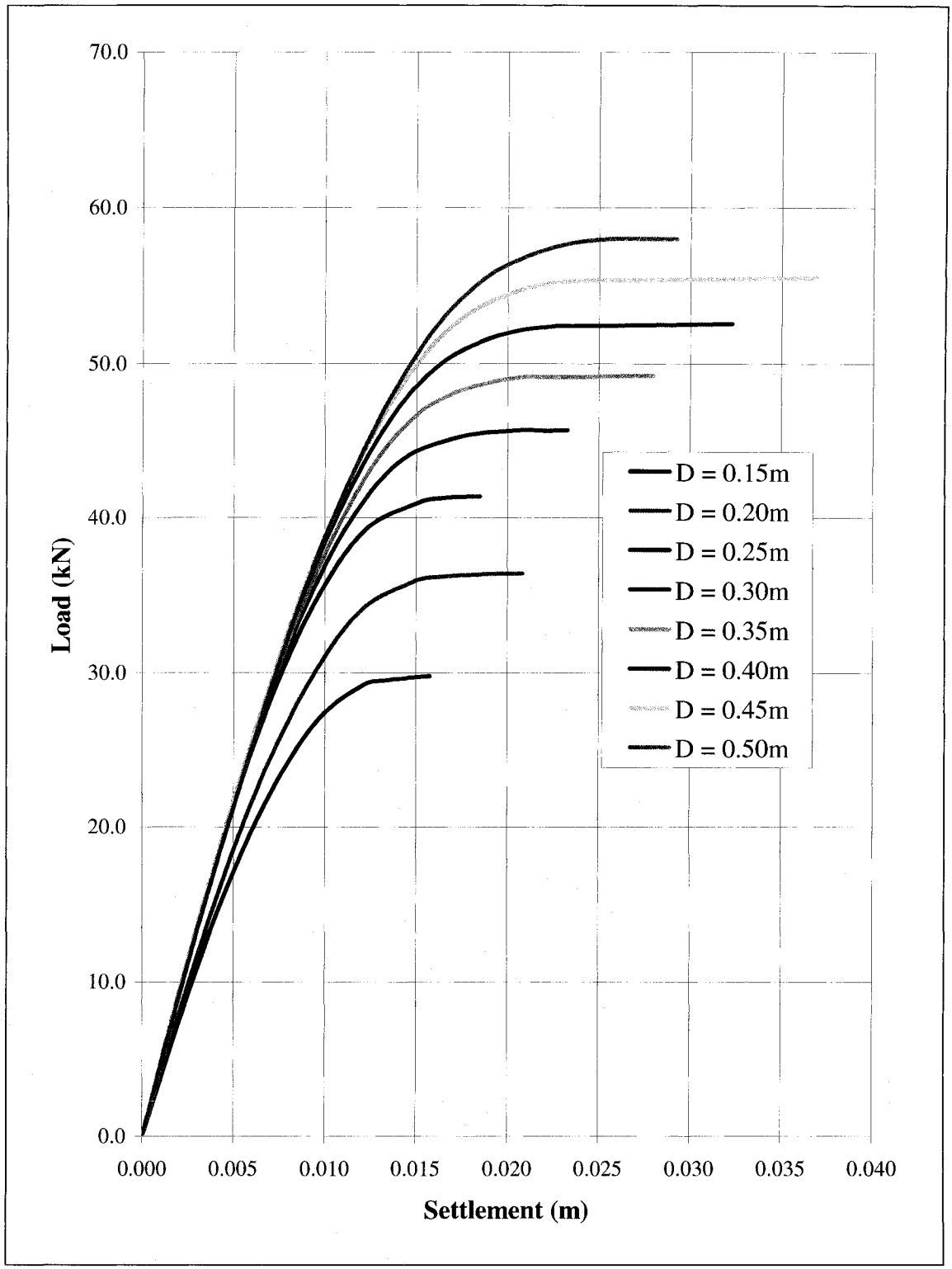

Figure 3.5 Typical load/settlement curves for the 6m pile driven in loose sand.

3.4.2 Stresses Variation Around and Beneath the Pile

Figure 3.6 presents the undeformed/deformed mesh in the displaced elements due to the cavity expansion developed along the pile length. In this figure, the pile elements were introduced in the cavity to simulate the pile material.

Figure 3.7 (a and b) presents typical horizontal and vertical stresses in the sand mass. It can be noted from these Figures that the majority of the horizontal stresses were developed during the cavity expansion stage, and accordingly, the increase in the earth pressure acting on the pile's shaft. On the other hand, the vertical stresses are mainly generated during the loading stage of the pile and accordingly, the vertical stresses increase around the pile's tip.

Figure 3.8 presents the shear stresses on the interface element along the pile's shaft. The shear stresses results are of great importance to monitor the level of mobilization of the shaft resistance. In the present investigation the pile will continue loading until full mobilization of friction on the pile shaft.

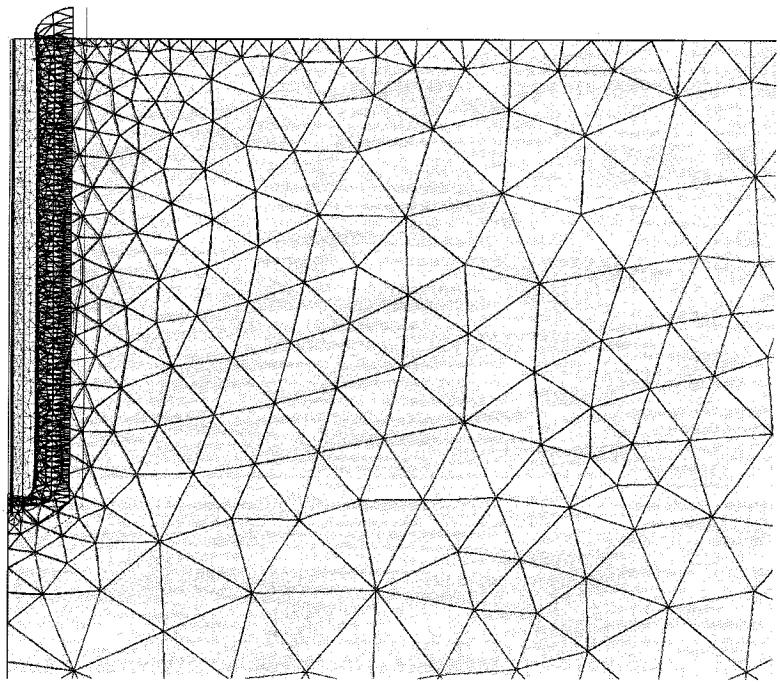

(a) Cavity Expansion

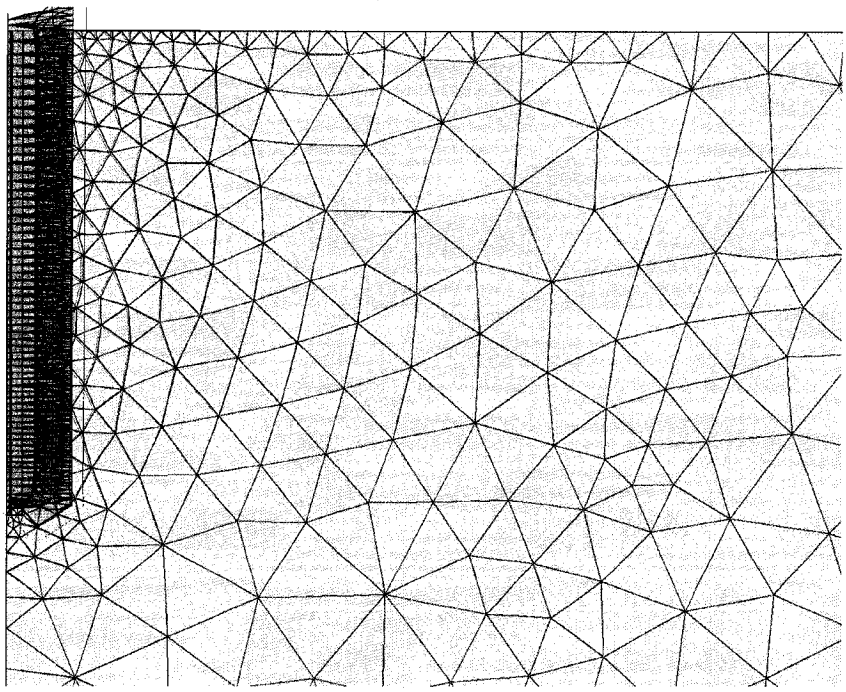

(b) Unloaded Pile

Figure 3.6 Typical undeformed/deformed mesh for a 6m-pile length.

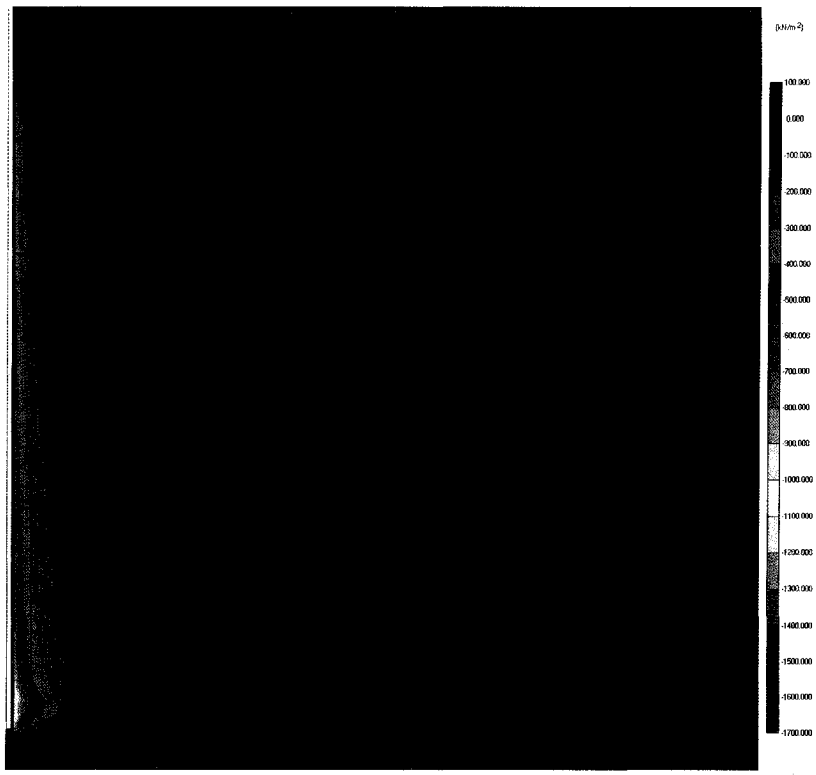

(a) Horizontal stresses

(b) Vertical stresses

Figure 3.7 Distribution of horizontal and vertical stresses around the pile's shaft.

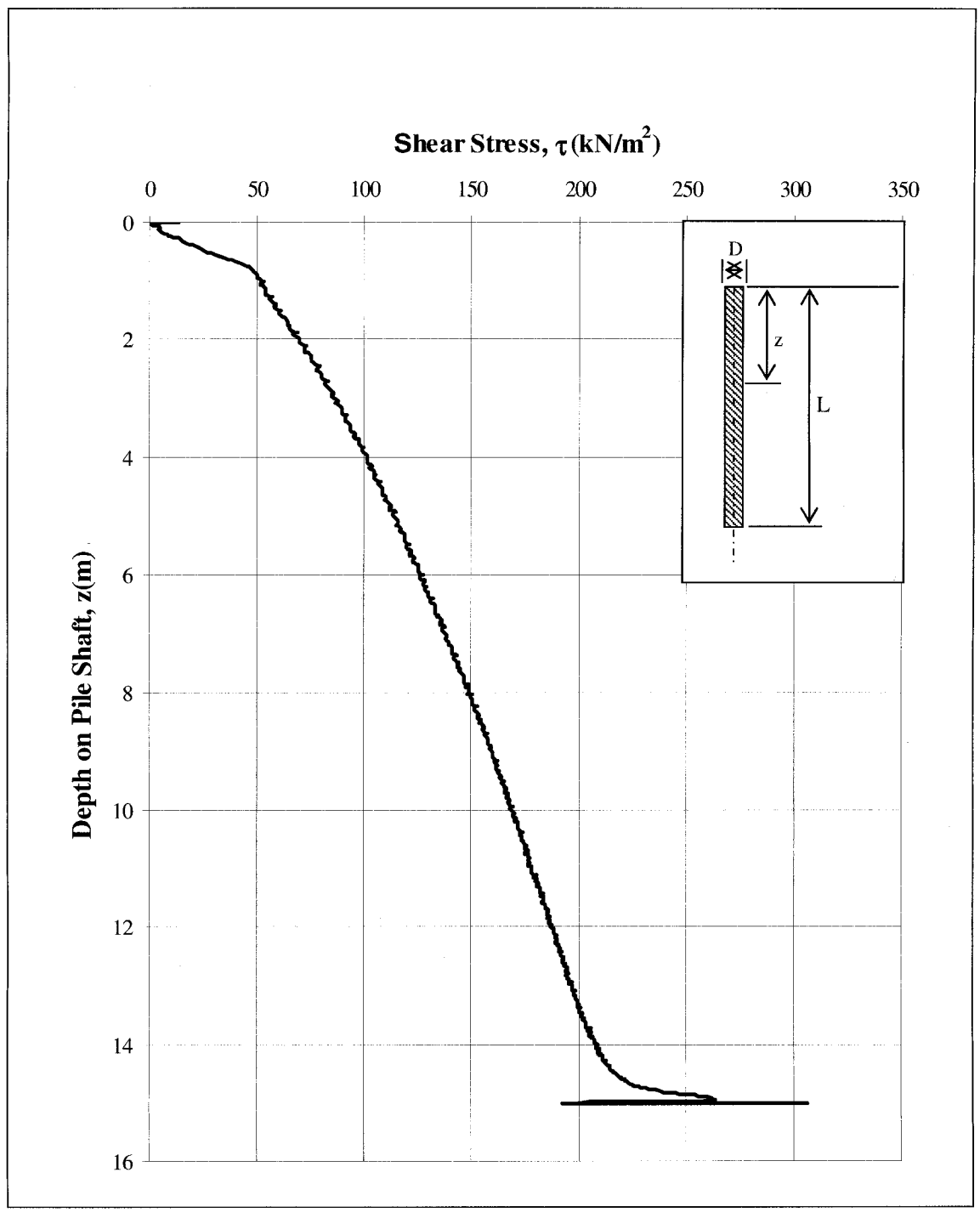

Figure 3.8 Typical shear stress distributions on the pile's shaft.

Figure 3.9 presents the effective horizontal pressure acting on the pile's shaft before and after pile installation. It can be noted from this figure that the horizontal stresses in the soil mass increased significantly due to pile installation. This increase was due to the radial compaction, which took place during the cavity expansion. It should be also noted from this Figure (3.9) that the horizontal stresses were decreasing directly below the pile's tip up to a level less than the initial value before the pile installation. This decrease is due to the tensile stresses that took place in the soil mass as a result of the radial displacement. This decrease in the horizontal stresses will eventually increase during the loading and the downward movement of the pile.

Figure 3.10 presents the effective vertical stresses in the soil mass near the pile's shaft before and after the pile installation. It can be noted from this figure that the vertical stresses increase near the soil surface due to the heave that occurs on the surface as a result of the lateral displacement of the soil. At the tip level, a sudden reduction in the vertical stress occurs for the same reason mentioned for the horizontal stresses. This reduction in the vertical stress will eventually vanish during loading the pile.

Figure 3.11presents typical stress-strain curves for elements along the pile's shaft. It can be noted from this Figure that elements, which were located deep in the soil gained more strength than that at or near the ground surface. This is due to the increase in the confining pressure (σ_z) at lower depths.

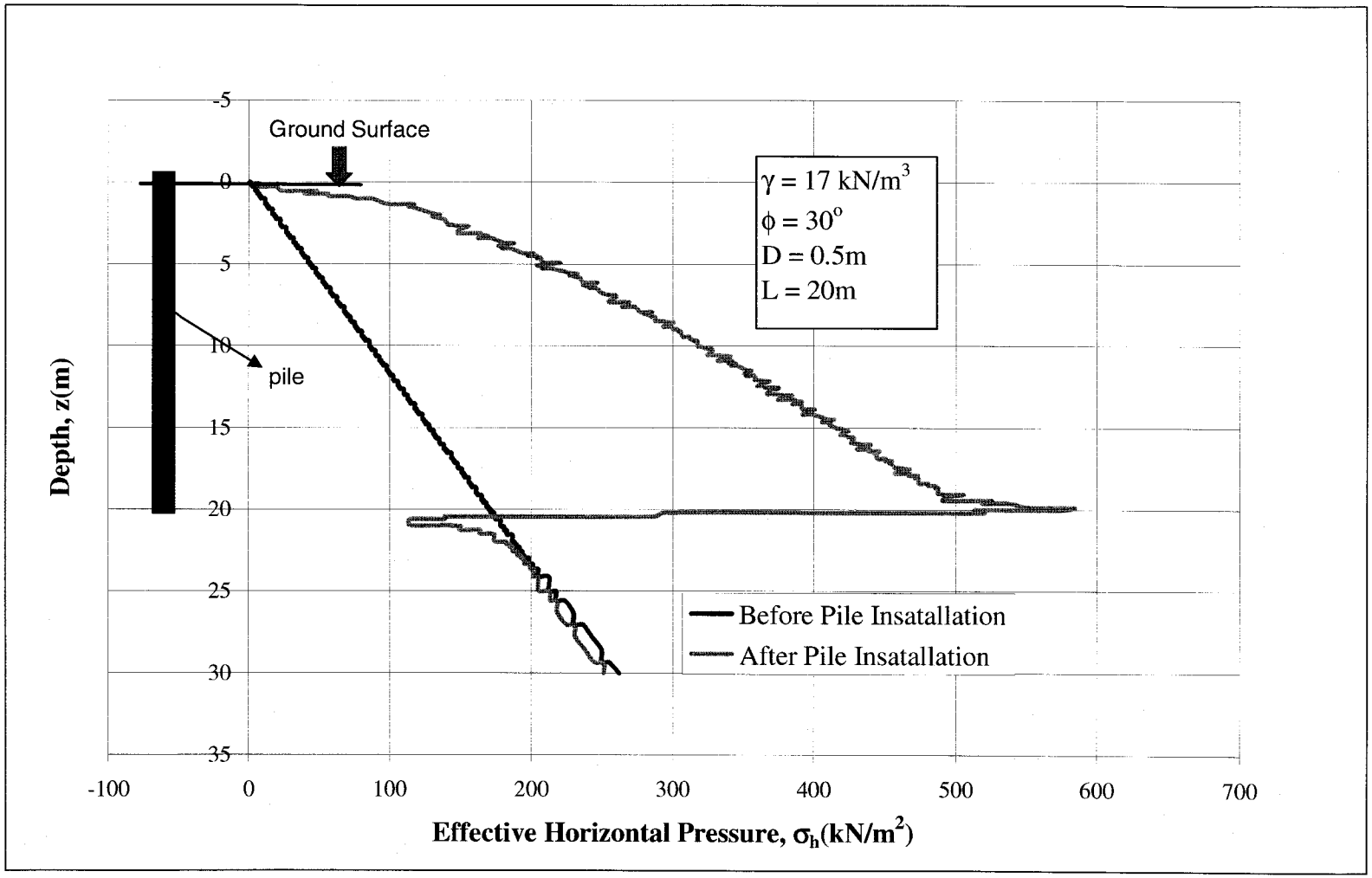

Figure 3.9 Effective lateral pressure due to pile installation.

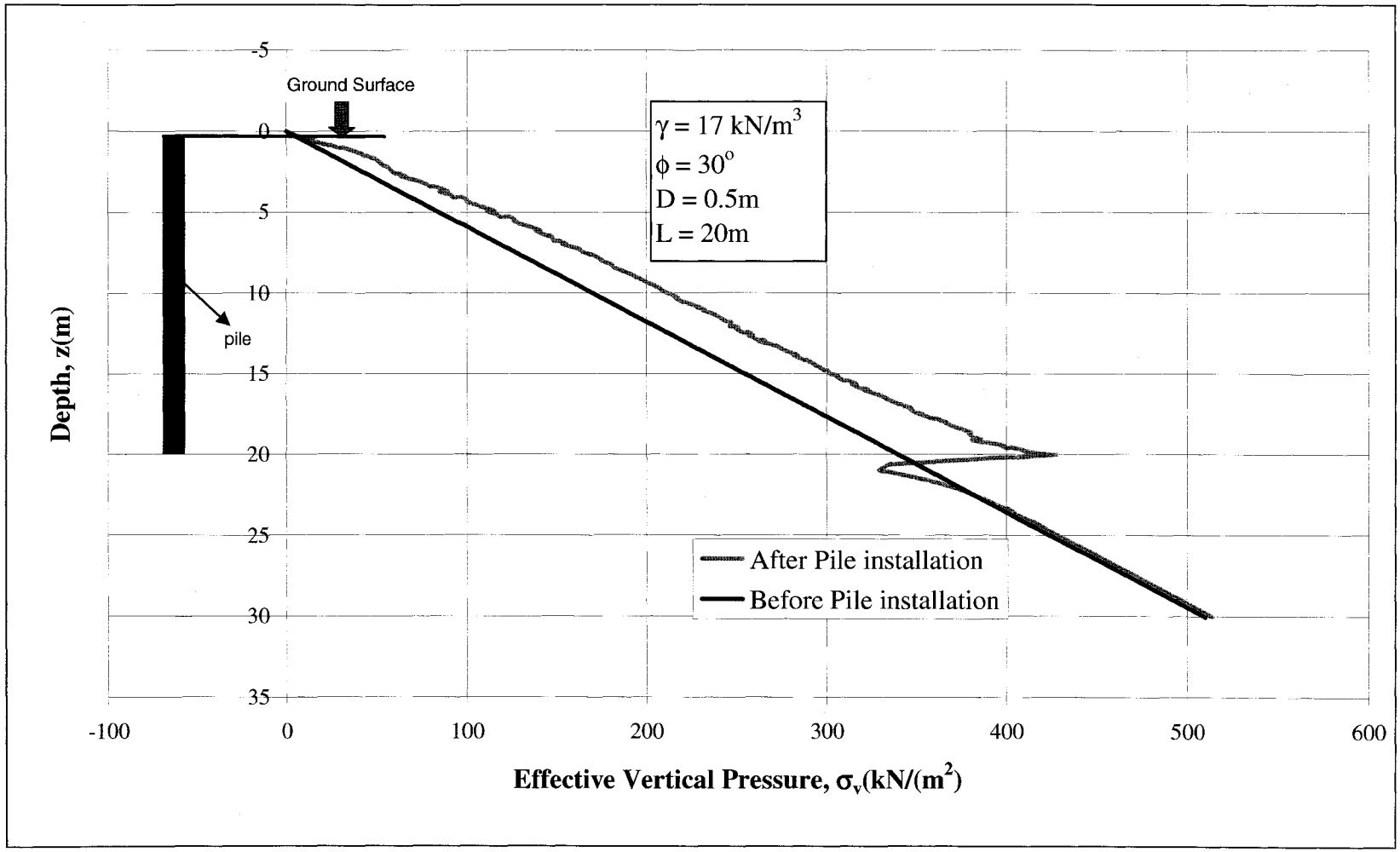

Figure 3.10 Effective vertical pressure due to pile installation.

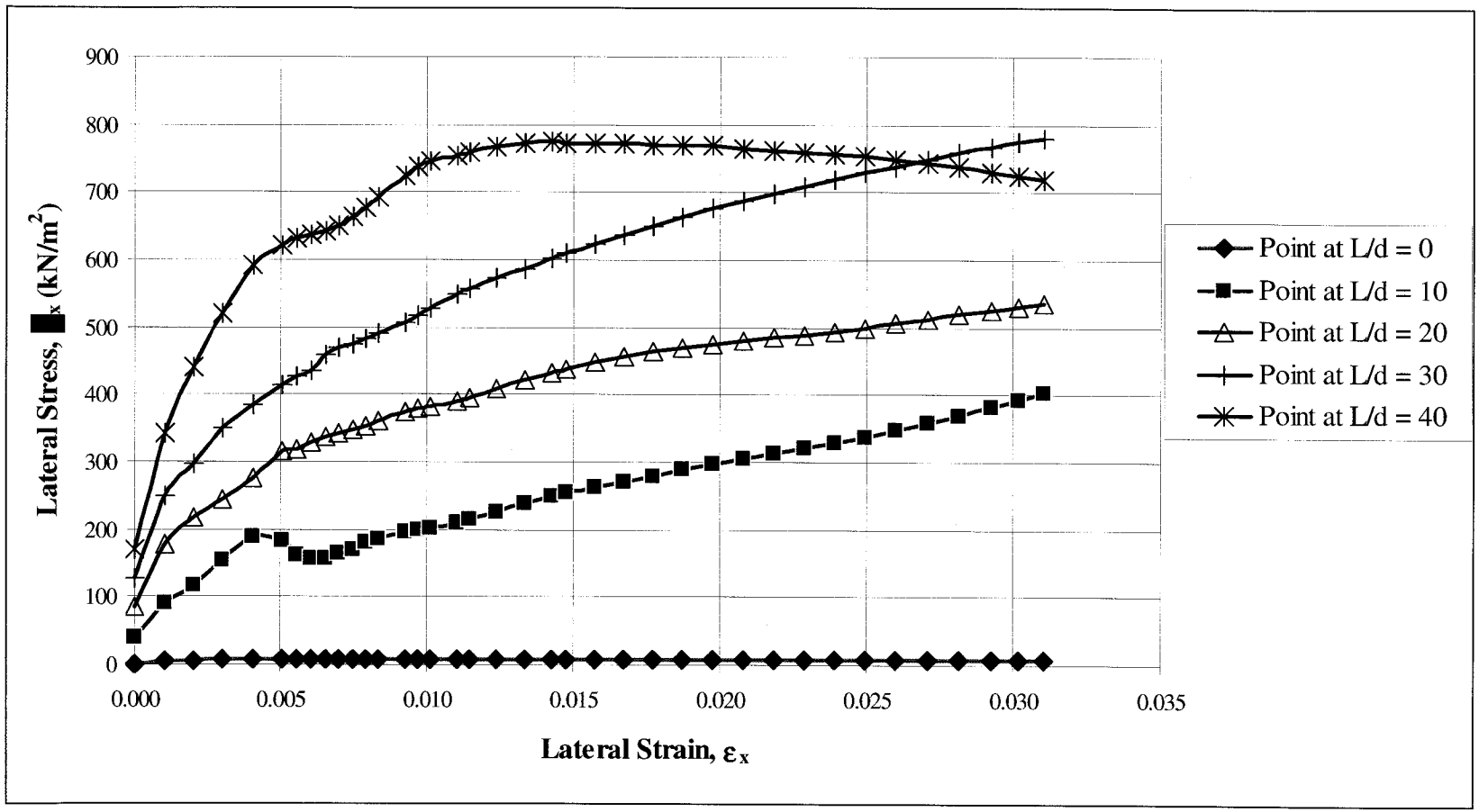

Figure 3.11 Stress-Strain relationships along the pile length.

3.4.3 Failure Mechanism

The failure pattern will be determined from the numerical model analysis results. The failure pattern is mainly developed due to the relative displacement of the soil particles in the soil. This movement is due to two major stages:

1- Installation stage

2- Loading stage

The main deformation that took place in the soil during installation was the lateral movement of the soil, which generated the earth pressure needed to develop the shaft resistance. This pattern was considered the zone of influence generated from the pile installation. To study the zone around the pile, a typical result from the numerical test is presented in Figure 3.12 showing the failure pattern along the pile length. By taking for example the test data from model No. 14 (ϕ = 35 and δ/ϕ = 0.6). The relative shear stress distribution around the pile is presented after installation, which indicates the proximity of the stress points to the failure envelope. The relative shear stress, τ_{rel} (F.S.) is defined as:

$$\tau_{rel} = \tau / \tau_{max} \qquad (3.2)$$

Where τ is the maximum value of shear stress (i.e. the radius of the Mohr stress circle). The parameter τ_{max} is the maximum value of shear stress for the case where the Mohr's circle is expanded to touch the Coulomb failure envelope. From the results it was found that the zone of influence takes a conical shape due to the cavity produced during the pile driving. In this phase it was assumed that soil around the pile will be in a passive condition.

It can be reported herein that the zone of influence is not only produced during loading the pile but also developed during the pile installation stage. The present numerical model is capable to generate this zone of influence during both pile installation and loading.

To easily visualize the effect of diameter on the zone of influence, the data from a range of pile diameters varying from 0.15m to 0.50m is presented in Figure 3.13 in terms of z/L to represent the pile length versus x/D in a non dimensional form. From the numerical analysis it was found that the volume in this zone is affected by the amount of displacement that happens in the sand mass, this was translated in a way that the increase in the pile diameter increases the volume of the failure pattern which will lead to a higher value for the coefficient of earth pressure "K_s" as noted in the previous section. It is of interest to find from this result that the relation between the zone of influence and the pile diameter is linear since the ratio x/D is almost constant along the pile length for all pile diameters. From here it was possible to replace these zone of influence by one general pattern which can represent the installation of any pile what ever its length or diameter. This typical pattern will help in developing the theoretical model in the next chapter.

The effect of length on the location of the zone of influence for a range of pile length was plotted in Figure 3.14. For a given type of soil it was found that zone of influence for long piles (15m, 20m) are the same and not affected by the length but for a short pile it was found that it goes more further away from the pile axes.

Figure 3.15 shows the effect of the soil strength on the zone of influence. It is clear that the angle ϕ has a non linear effect on the zone of influence. If we assume that there is a constant relation between the zone of influence and the pile diameter and length

then our only variable will be the soil strength. The zone of influence covers a larger volume when the pile is driven in dense sand with high value of ϕ, this will lead to higher resistance during the pile driving until it reaches to a limit where the pile couldn't be driven. This limit will depend on the pile material and geometry (length & diameter).

After understanding the behaviour of the zone of influence and how it is affected by the pile geometry and the soil strength, its geometry will be defined to be used in the next chapter for developing the analytical model. As concluded from the analysis that when the zone of influence is plotted in a non dimensional form, the variation of its pattern location is constant with the pile length and diameter and the only variable will be the angle of shearing resistance "ϕ" as noted in Figure (3.15). By observing the pattern it was possible to be idealized by dividing it into three sections as shown in Figure 3.16. The upper and the lower section will be covering the shaft area and the base section covers the tip of the pile. The cone at the base will have a half angle ($\theta_1 = \pi/4 - \phi/2$) according to Mayerhof's theory. It can be noted from the numerical result for the pattern, the distance from the pile tip to the midpoint of the pile can be idealized by a straight line "cb" having an angle ($\theta_2 = \pi/4 - \phi/2$) with the horizontal. The upper section which covers the upper half of the pile length "ab" will be idealized by a curve tangent to the line "bc" and tangent to the ground surface. From the numerical results presented previously an idealization for the curve in the upper part reviled that it can be described by a logarithmic spiral curve (Figure 3.16), where it can be formulated in the following form:

$$z/L = b\, e^{a\, x/D} \qquad (3.3)$$

Where a and b are constants.

In chapter 4, the three sections will be defined in details to be utilized in determining the pile capacity based on the installation effect by utilizing the failure plane. From the above it was clear that the zone of influence contributes to the pile capacity after being driven since the deformation in the soil generates an earth pressure on the pile's shaft. This pressure will determine the shaft capacity of the pile.

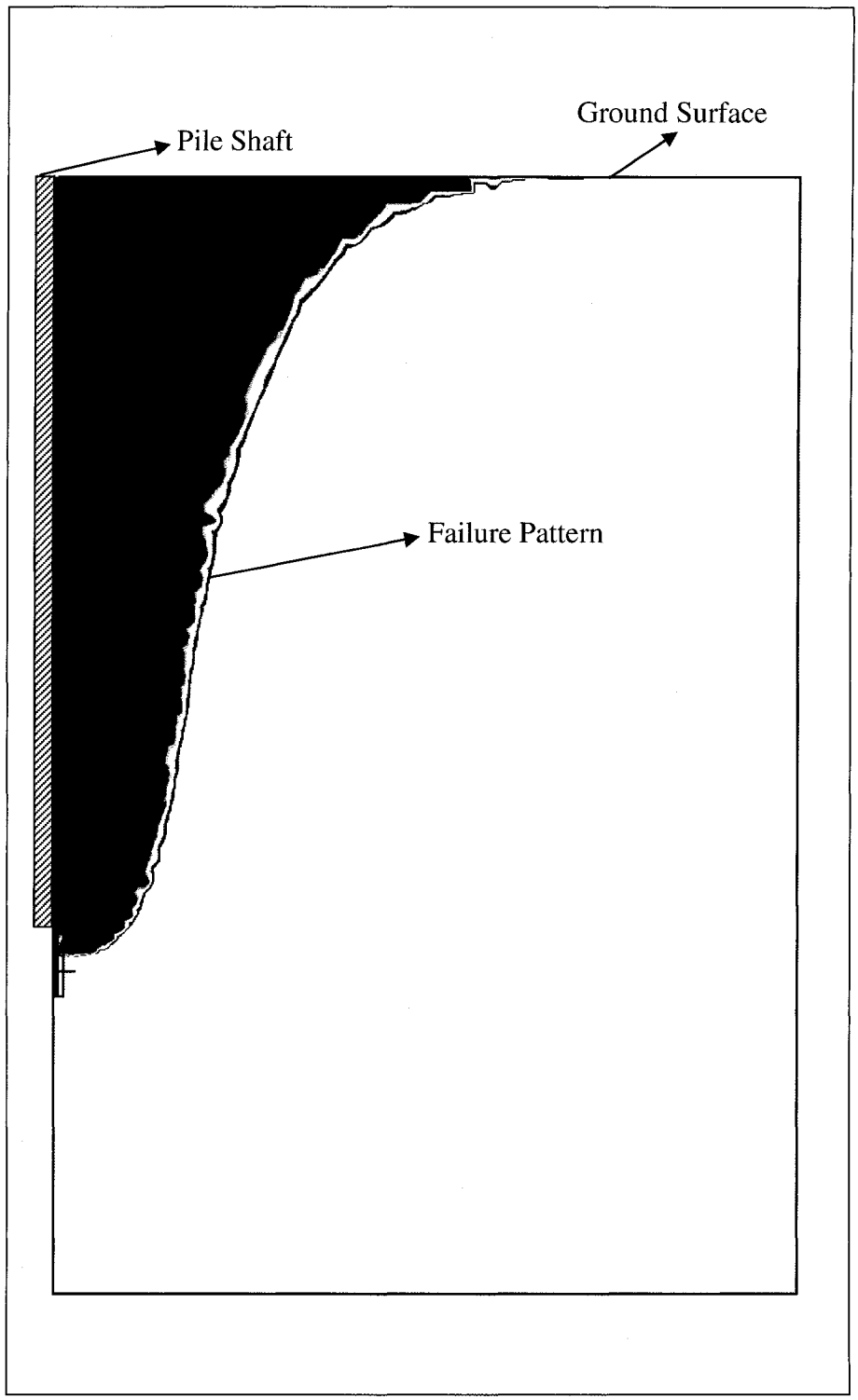

Figure 3.12 Failure pattern for a driven pile in sand.

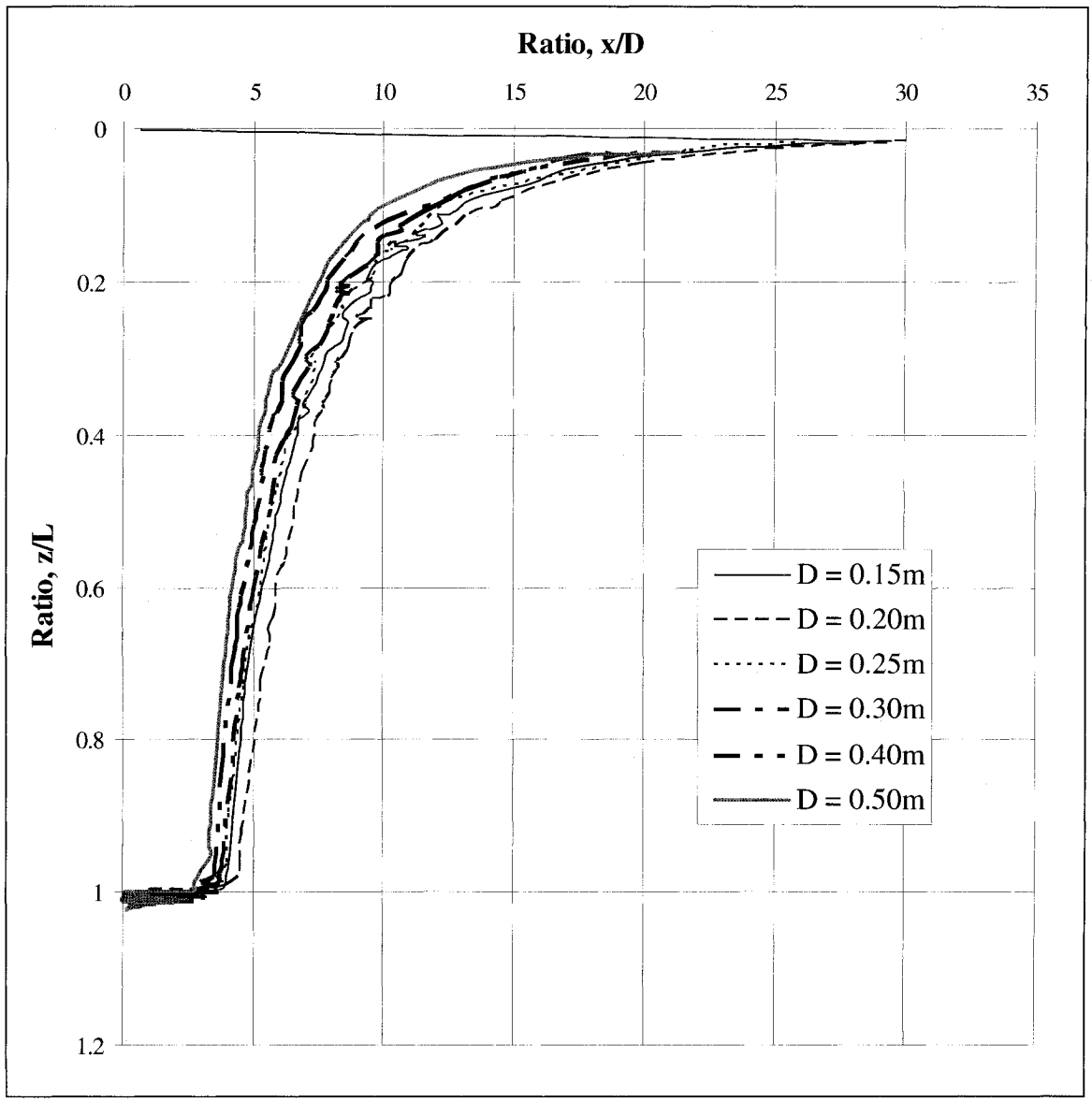

Figure 3.13 Zone of influence for a 15m pile length driven in sand with angle of shearing resistance $\phi = 35$.

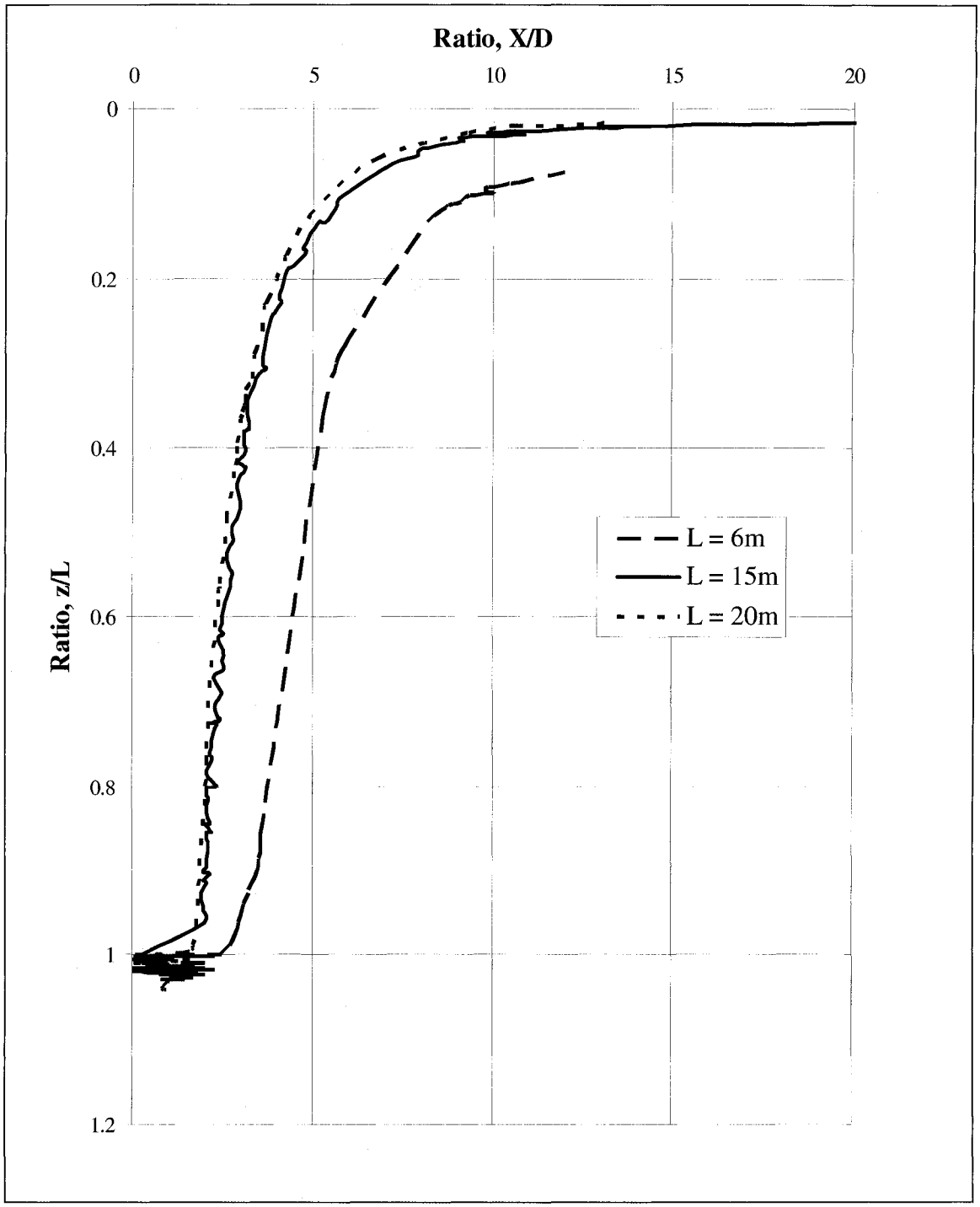

Figure 3.14 Zone of influence for 6, 15, 20m Pile length driven in sand with angle of shearing resistance $\phi = 30$.

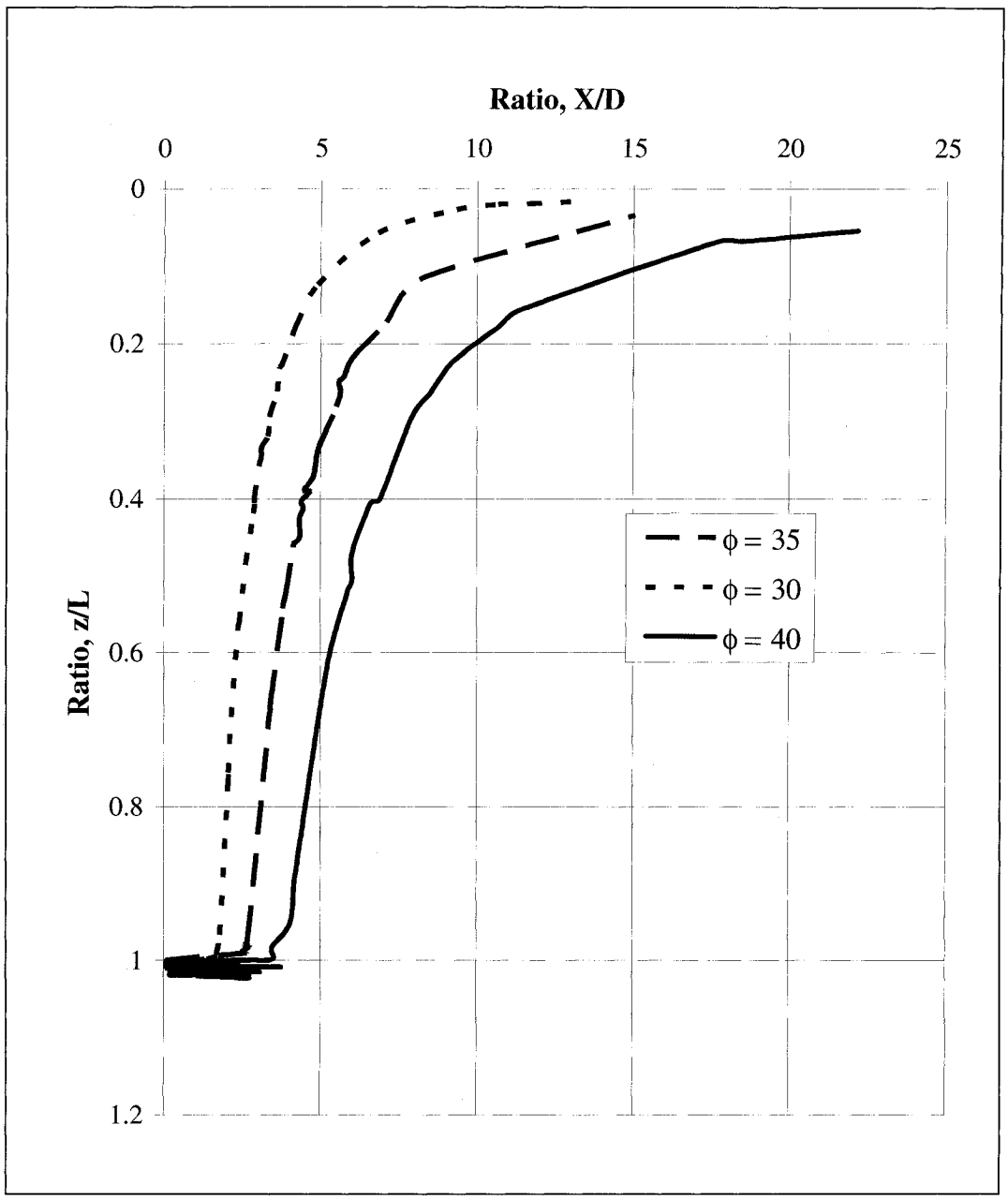

Figure 3.15 Zone of influence location in different soil Strength.

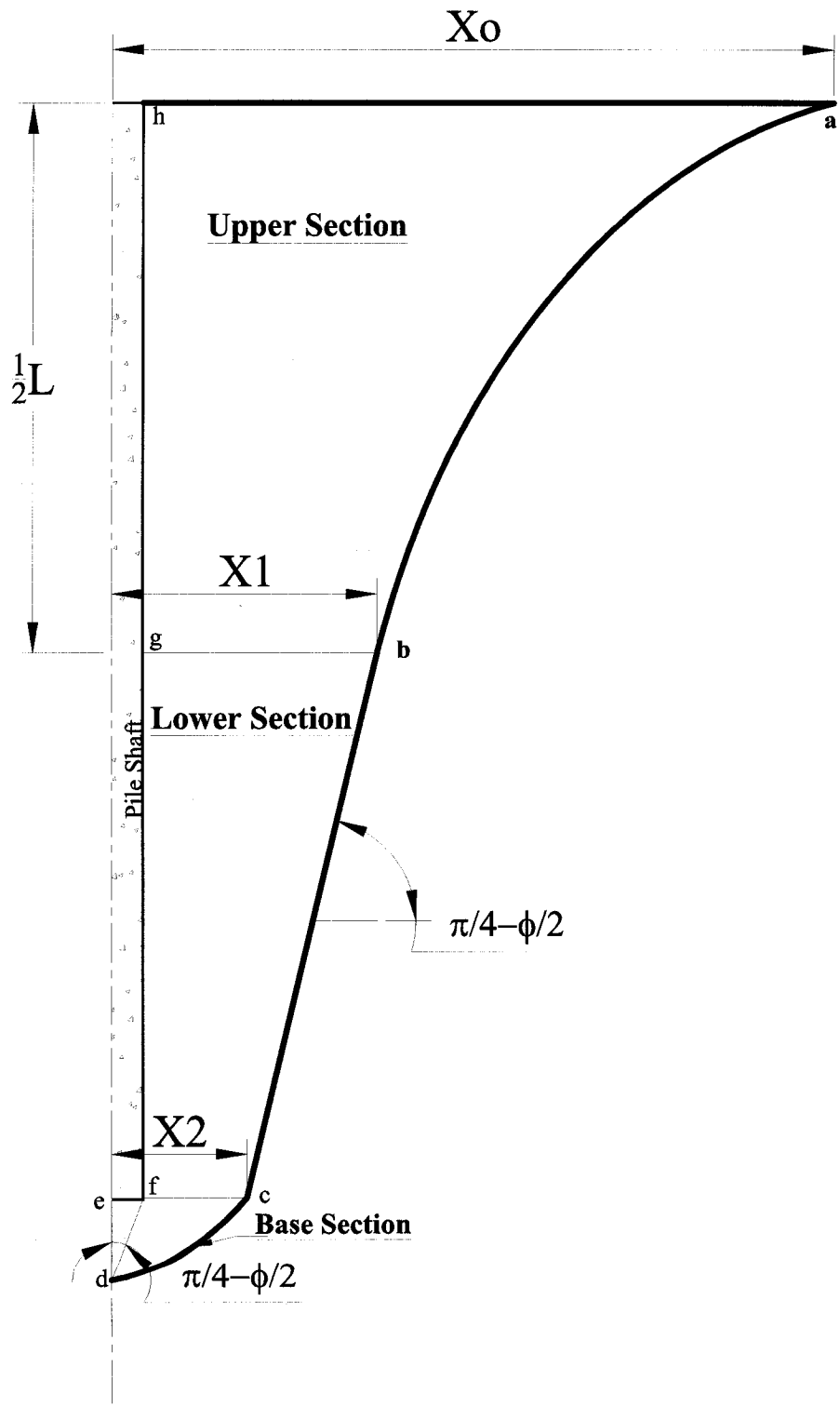

Figure 3.16 Sketch of the zone of influence of a single pile.

3.4.5 Distribution of Coefficient of Lateral Earth Pressure

From the produced horizontal and vertical stresses on the pile's shaft, the coefficient of earth pressure (K_s) was calculated along the pile's shaft. Figure 3.17 presents typical distribution of the coefficient of earth pressure (K_s) along the pile's shaft. It can be noted from this Figure that the K_s distribution increases near the pile head and then decreases with depth, then increases again near the pile's tip due to arching effects, which takes place during the pile driving and loading. It can be noted further that the values of K_s are higher than that of the coefficient of earth pressure at rest (K_o) due to the cavity expansion developed in the soil, which demonstrates superiority of driven piles as compared to bored piles under the same condition. The corresponding overconsolidation ratios OCR were calculated as follows:

$$OCR \approx (K_s / K_p)^2 \qquad \text{(Brooker and Ireland's (1965))} \qquad (3.4)$$

Where

K_p = Coefficient of passive earth pressure [$K_p = \tan (45 + \phi/2)^2$].

The deduced values of the OCR are given in Figure 3.18. It is important to note that a value of OCR > 1 shows the level of overconsolidation in the sand mass around the pile's shaft.

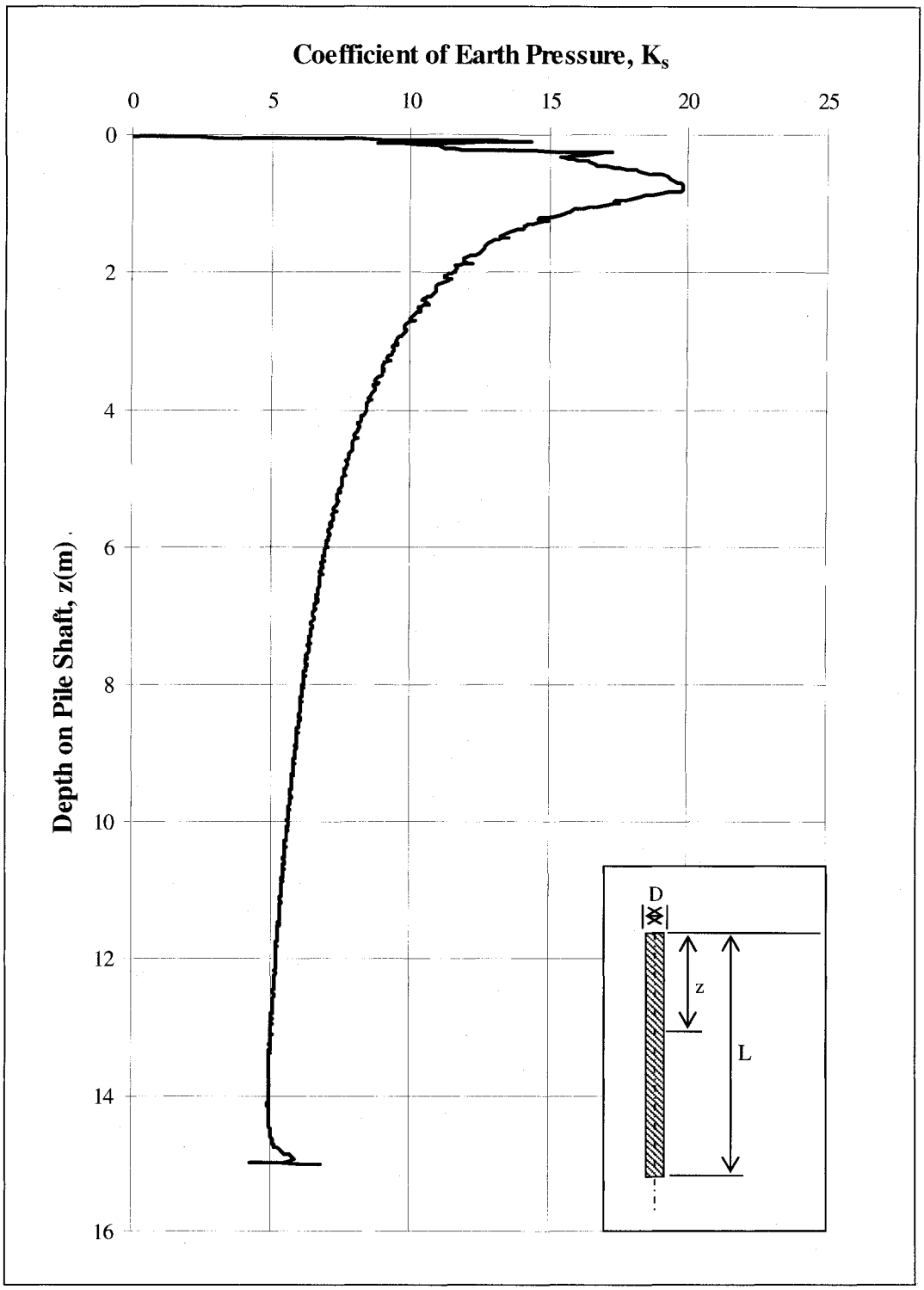

Figure 3.17 Distribution of the Coefficient of earth pressure along the pile's shaft.

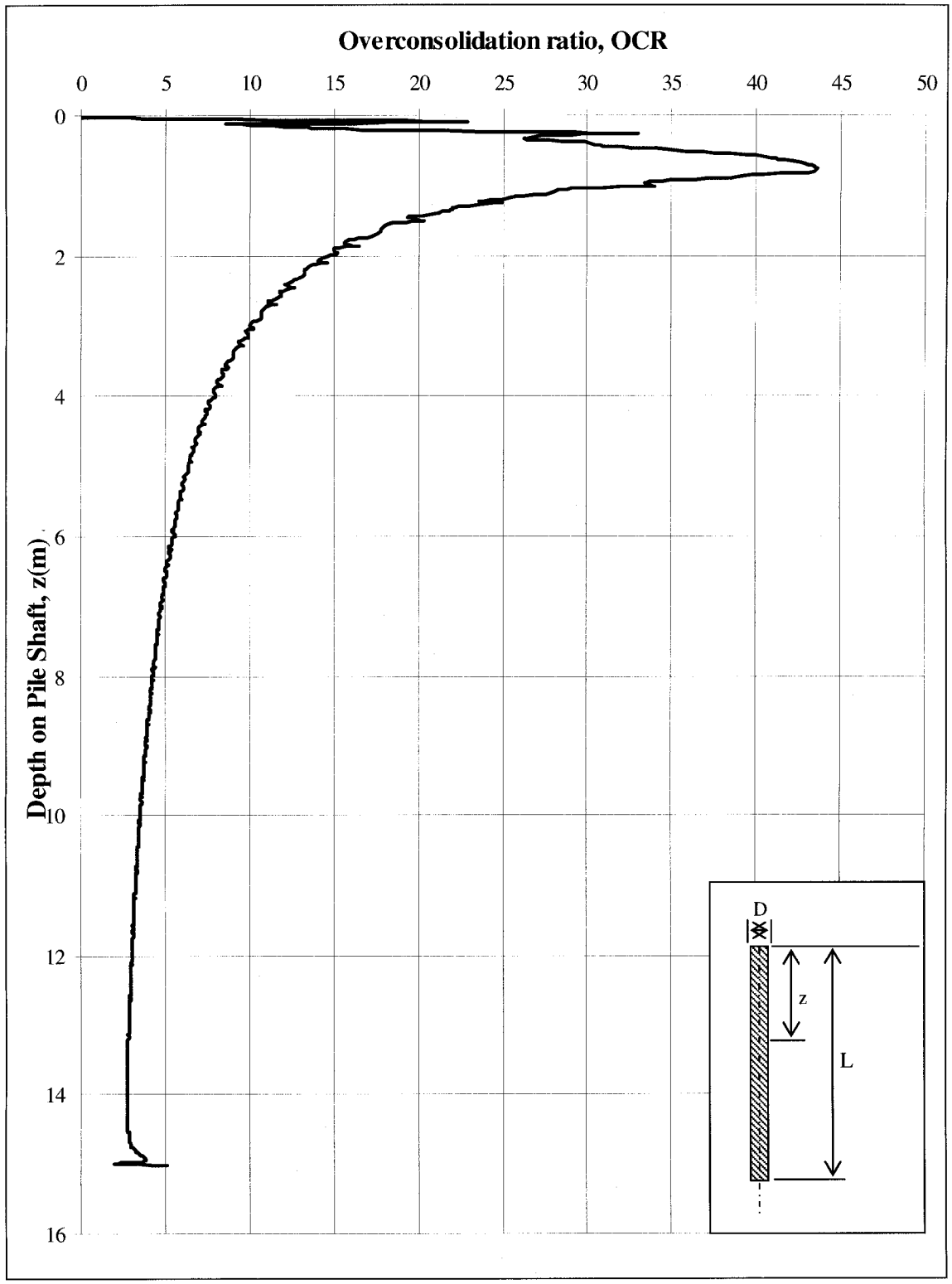

Figure 3.18 Distribution of the Overconsolidation ratio along the pile's shaft.

3.5 Sensitivity Analyses

After validating the numerical model, the model was then used to generate data to examine the parameters seemed to govern the behaviour of driven piles in sand these include: are the soil angle of shearing resistance, pile diameter, pile length and the roughness of pile shaft surface. Table 3.4 presents the numerical testing program and typical results on a wide range of pile lengths and diameters driven in sand having an angle of shear resistance $\phi = 35^{o}$. The ultimate pile capacity is evaluated by identifying the point of maximum curvature on the load - settlement curve. In this analysis, 24 pile models were developed and divided into three groups. 216 numerical tests were performed within the range of the soil and the pile parameters presented in Tables 3.1 and 3.2.

Table 3.4 Typical test result ($\phi = 35^0$).

Test No.	Pile Length, L (m)	Pile Diameter, D (m)	Slenderness Ratio, L/D	Ultimate Pile Capacity, Q_u (kN)
1	6	0.15	40.00	377
2		0.20	30.00	471
3		0.25	24.00	559
4		0.30	20.00	660
5		0.35	17.14	679
6		0.40	15.00	735
7		0.45	13.33	792
8		0.50	12.00	848
9	15	0.15	100.00	1571
10		0.20	75.00	2199
11		0.25	60.00	2325
12		0.30	50.00	2513
13		0.35	42.86	2639
14		0.40	37.50	2890
15		0.45	33.33	3047
16		0.50	30.00	3242
17	20	0.15	133.33	2425
18		0.20	100.00	3054
19		0.25	80.00	3412
20		0.30	66.67	3682
21		0.35	57.14	4222
22		0.40	50.00	4543
23		0.45	44.44	4857
24		0.50	40.00	5127

3.5.1 Effect of Angle of Shearing Resistance

The angle of shearing resistance (ϕ) has a significant role in formulating the behaviour of driven piles. In this investigation 72 tests were conducted on loose, medium and dense sands. Figure 3.19 shows the lateral earth pressure acting on the pile's shaft. It can be noted from this Figure that the lateral earth pressure acting on the pile's shaft increases with the increase of the angle of shearing resistance of sand (ϕ). Furthermore, this increase is not linear and it increases at a higher rate due the increase of ϕ. It was also

noted that piles driven in loose sand could mobilize the friction fully with less amount of pile movement; however in case of dense sand, more movement is required to mobilize the full friction on the pile's shaft. Figure 3.20 presents a pile subjected to a partial and full mobilization of the shaft resistance. It can be noted from this figure that the case of partially mobilized shaft resistance would confirm the presence of the critical depth in piles driven in sand. While if the load on the pile continued to increase, the level of the mobilization will continue to increase and it may reach its maximum limit where the shaft resistance is fully mobilized, where no critical depth was observed in this case. It can be then concluded that the shear resistance should be measured after the full mobilization of the friction on the pile's shaft, otherwise the results and accordingly the conclusion can misleads judgments. Also, it should be noted that, the pile material may fail before the shaft resistance reaches its full mobilization in the case of piles driven in dense sand. This may explain the contradictory reports found in the literature about the critical depth for piles driven in cohesionless soil.

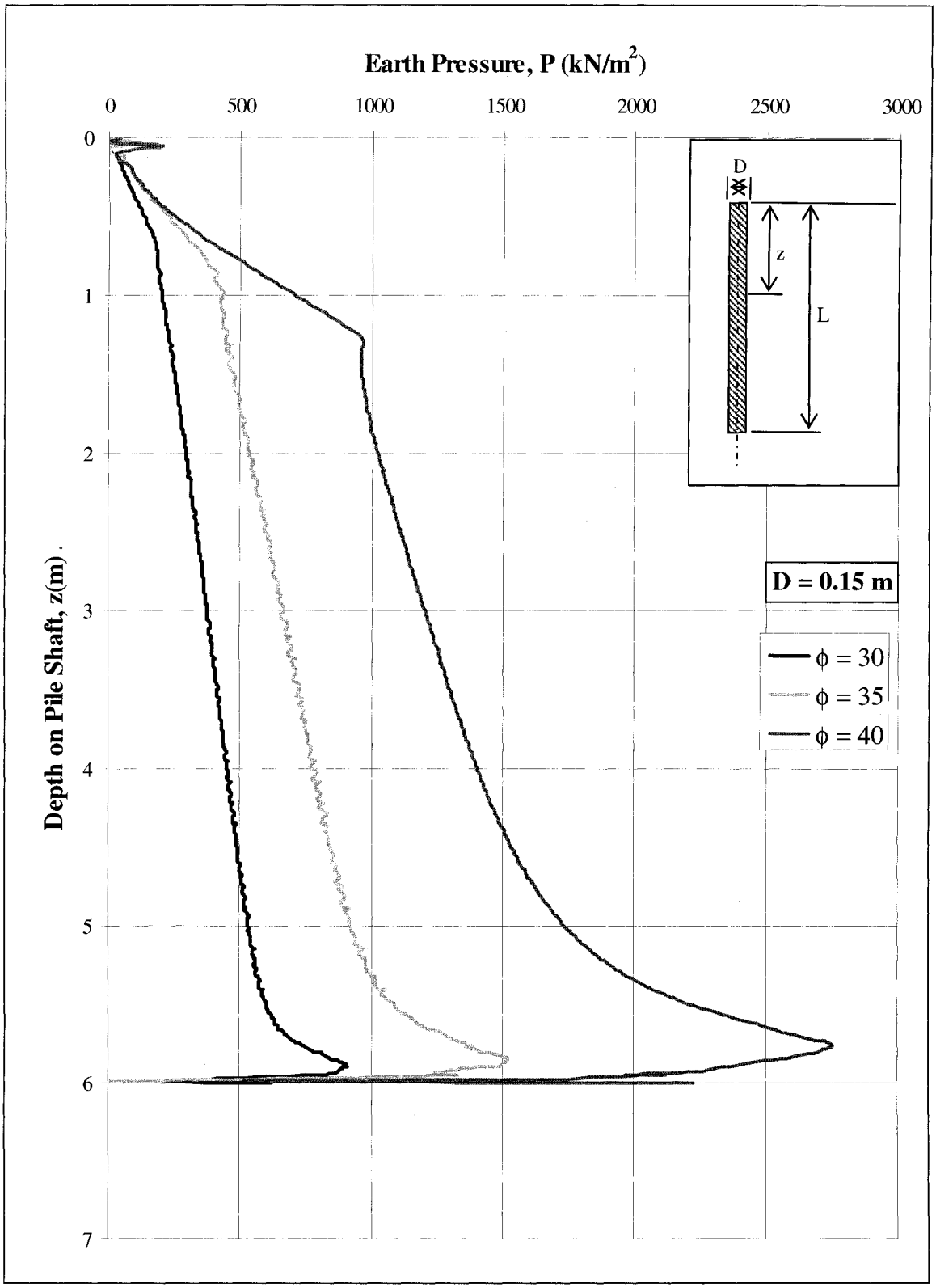

Figure 3.19 Earth pressure acting on the pile length.

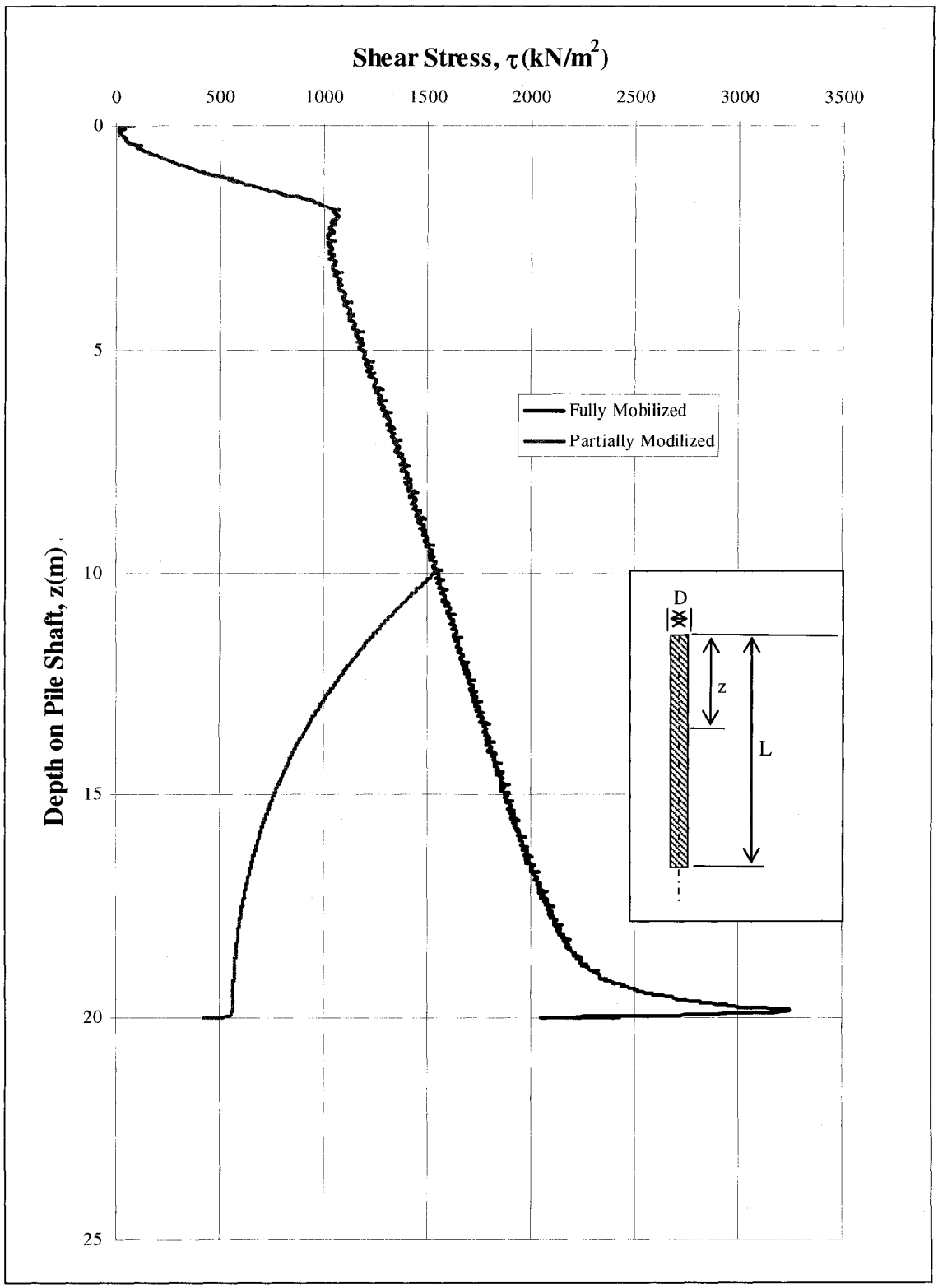

Figure 3.20 Full and partial mobilization of the shear stress on the pile's shaft.

3.5.2 Effect of Pile Diameter

The pile diameter has an important effect on the capacity and the distribution of stresses along the pile's shaft. Figure 3.21 presents the distribution of the earth pressures on the pile's shaft. It can be noted that the pressure diagram can be divided into three zones:

1- Zone 1, which starts from the pile head and ends slightly below.

2- Zone 2, which follow zone 1 and covers the mid-section of the pile.

3- Zone 3, which located below zone 2 and ends at the tip of the pile.

The extent of each zone depends on the pile diameter, pile length and the soil friction angle ϕ.

Figures 3.22 and 3.23 present typical shear stress and earth pressure distributions along the pile's shaft. It can be noted from these Figures that zone 1 is very distinct and well defined in the 6m piles; furthermore, the distribution showed a straight-line pattern. Figure 3.24 present the length of this zone for a given pile diameter and angle of shearing resistance ϕ. It can be noted from this figure that zone 1 extends to longer depths in the soil due to an increase in the pile diameter and the angle of shearing resistance.

It should be mentioned here that in zone 1 high level of dilations occur due to the low confining pressure near the ground surface. Furthermore, the higher the radial displacement of the sand the deeper this zone goes. By comparing Figure 3.23 for a 6m-pile length and Figure 3.25 for a 15m pile length it can be concluded that zone 1 is mainly governed by the angle of shearing resistance (ϕ) of the sand and pile diameter (D) but the pile length has no role in defining this zone. The following empirical formula is proposed to estimate the length of zone 1.

$L_1 = \phi(4.3D + 0.65)$ Where: ϕ is in radians (3.5)

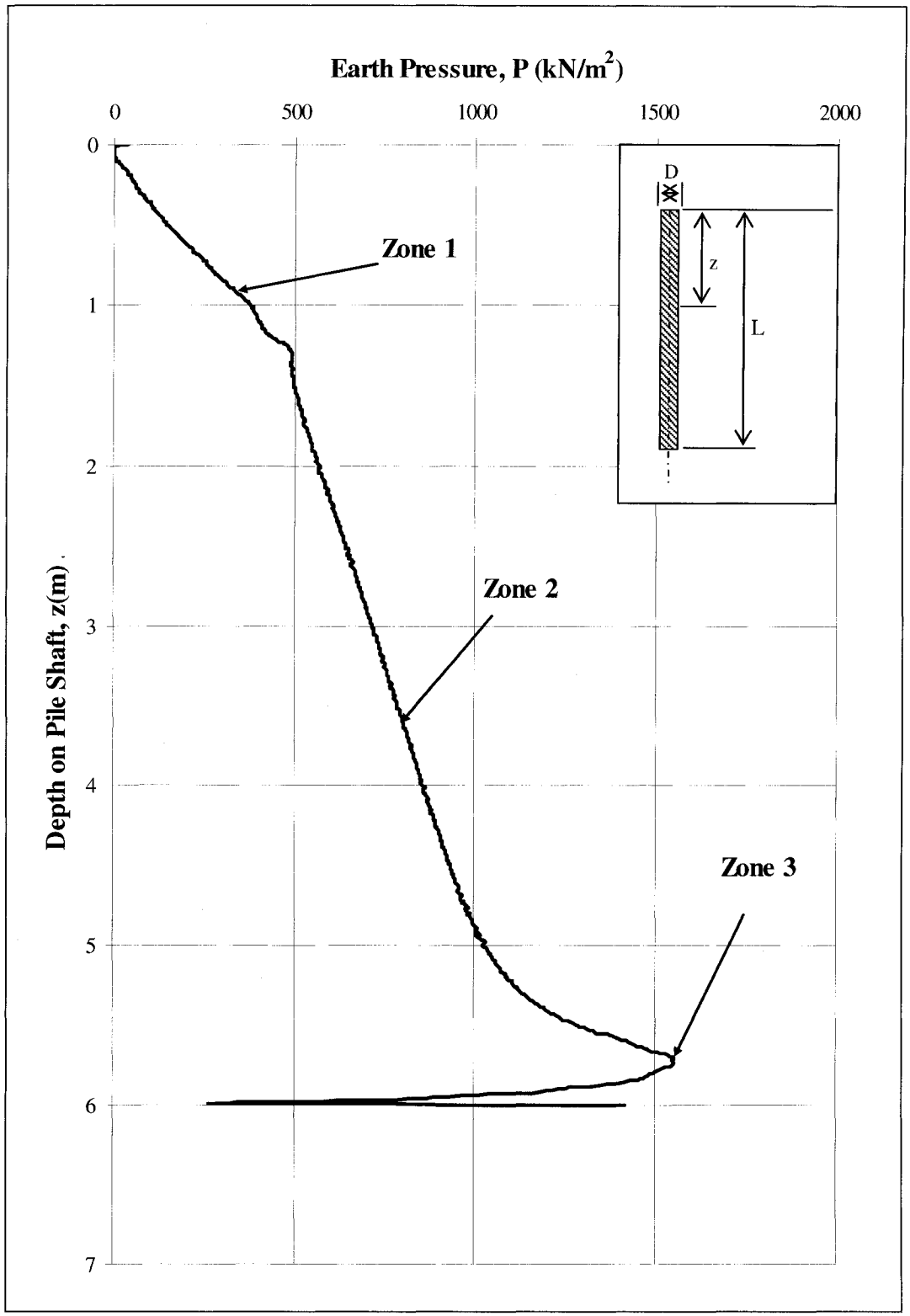

Figure 3.21 Location of stress zones.

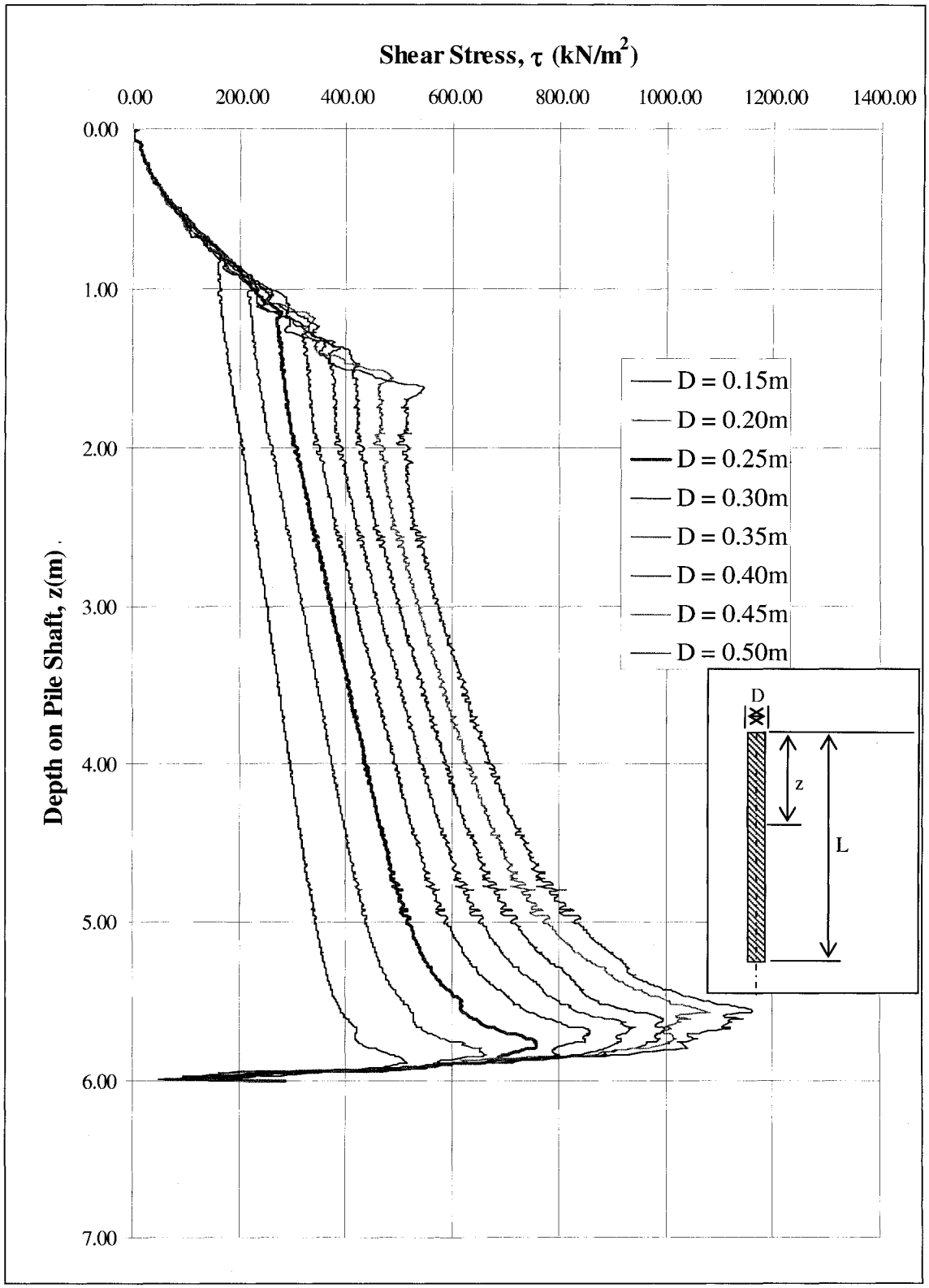

Figure 3.22 Shear stress distribution along the pile length (L=6m and $\phi = 35^{o}$).

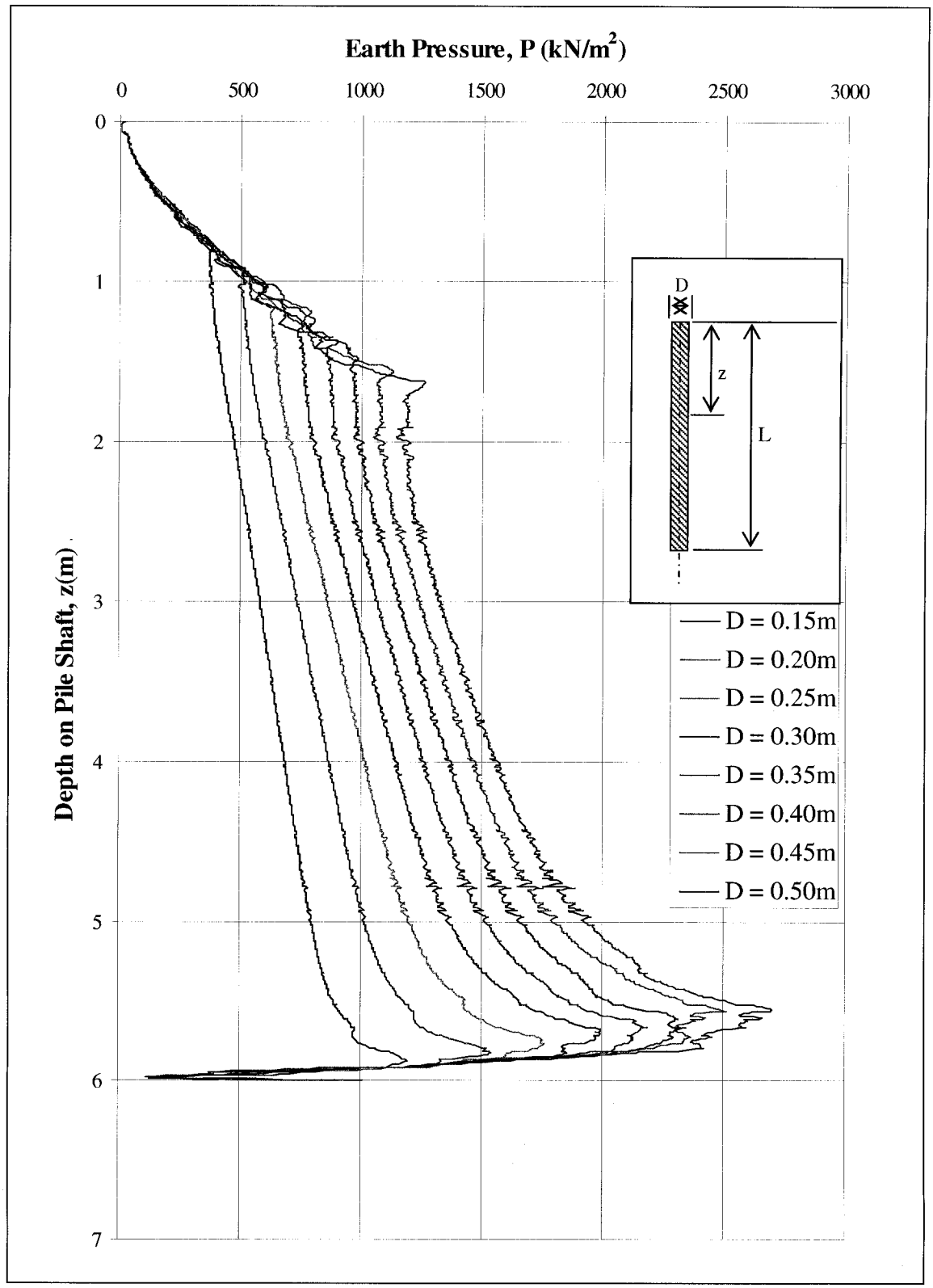

Figure 3.23 Earth pressure distribution along the pile length (L=6m and $\phi = 35^{\circ}$).

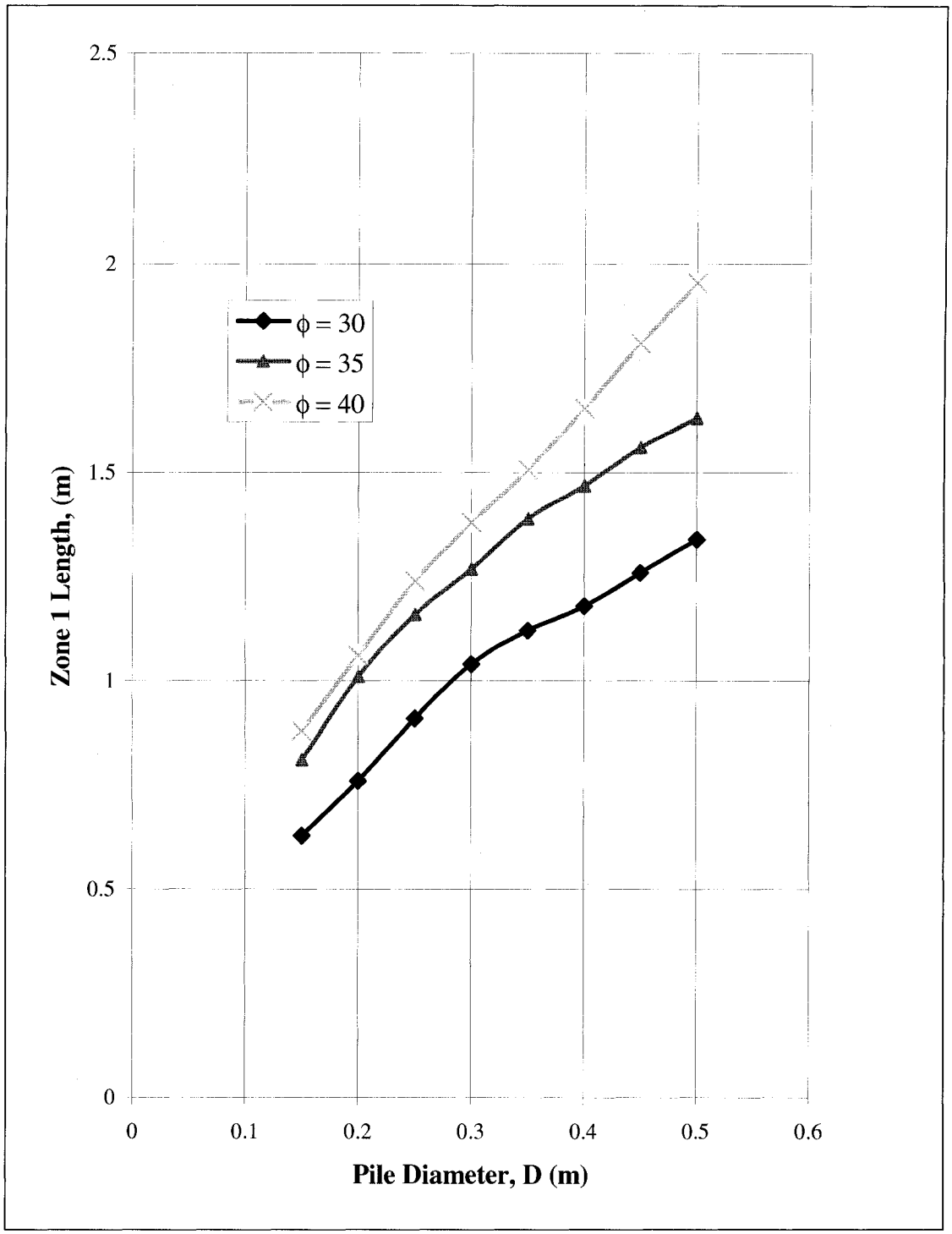

Figure 3.24 length of Zone (1) versus pile's diameter.

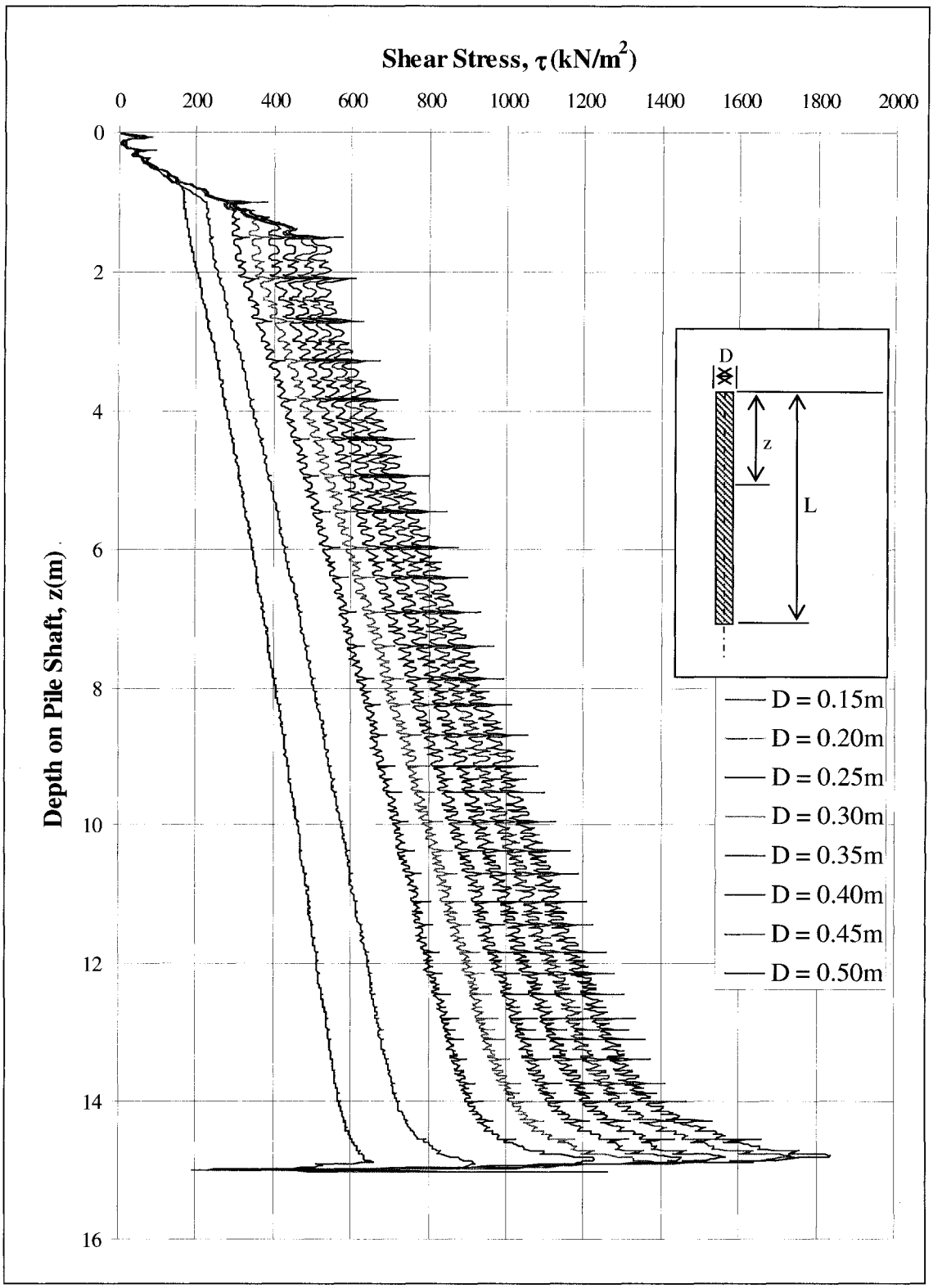

Figure 3.25 Shear stress distribution along the pile length (L=15m and $\phi = 35^{\circ}$).

Figures 3.26, 3.27 and 3.28 present the variation of the coefficient of earth pressure along the pile length for a range of pile diameters. Each figure represents the variation in a specific sand type, which were indicated by the angle ϕ. It can be noted that the coefficient of earth pressure (K_s) reaches very high values for the 6m piles. This can be explained by the fact that the earth pressure at this zone is much higher than the overburden pressure. It can be noted that the value of K_s reached to a maximum value of 20 at the end of zone 1 for the case of pile of 0.5m in diameter, driven in sand having of $\phi = 30^o$; while it reaches a value of 45 for the case of $\phi = 35^o$ and a value of 83 for $\phi = 40^o$. Similar values were observed for longer piles (see Figure 3.29). As noticed the values of the K_s are higher than the value of K_p for the case of normally consolidated sand. This indicates that the overconsolidation of the sand mass takes place due to the radial displacement produced during the pile installation and accordingly, the interlocking between pressure soil particles. The following formula was developed in this investigation to evaluate the coefficient of earth pressure in this zone:

$$K_{s1} = 0.6\, z\, e^{5\tan\phi} + 5\tan\phi + 6 \qquad \text{Where:} \qquad 0 \le z \le L_1 \qquad (3.6)$$

Figure 3.30 presents graphically the values of the coefficient of earth pressure versus (L_1/D) at zone 1. From this chart the average coefficient of earth pressure for zone 1 can be determined for a range of ϕ values. Figure 3.31 presents the change in OCR along the pile length. It can be noted that the OCR was not affected by the increase of the pile length; similar to the coefficient of earth pressure since both values are interrelated to each other. It can be further reported that zone 1 is a highly disturbed zone due to pile installation. Accordingly, the pile diameter is the only parameter, which plays an important role in defining the depth of this zone in the soil mass.

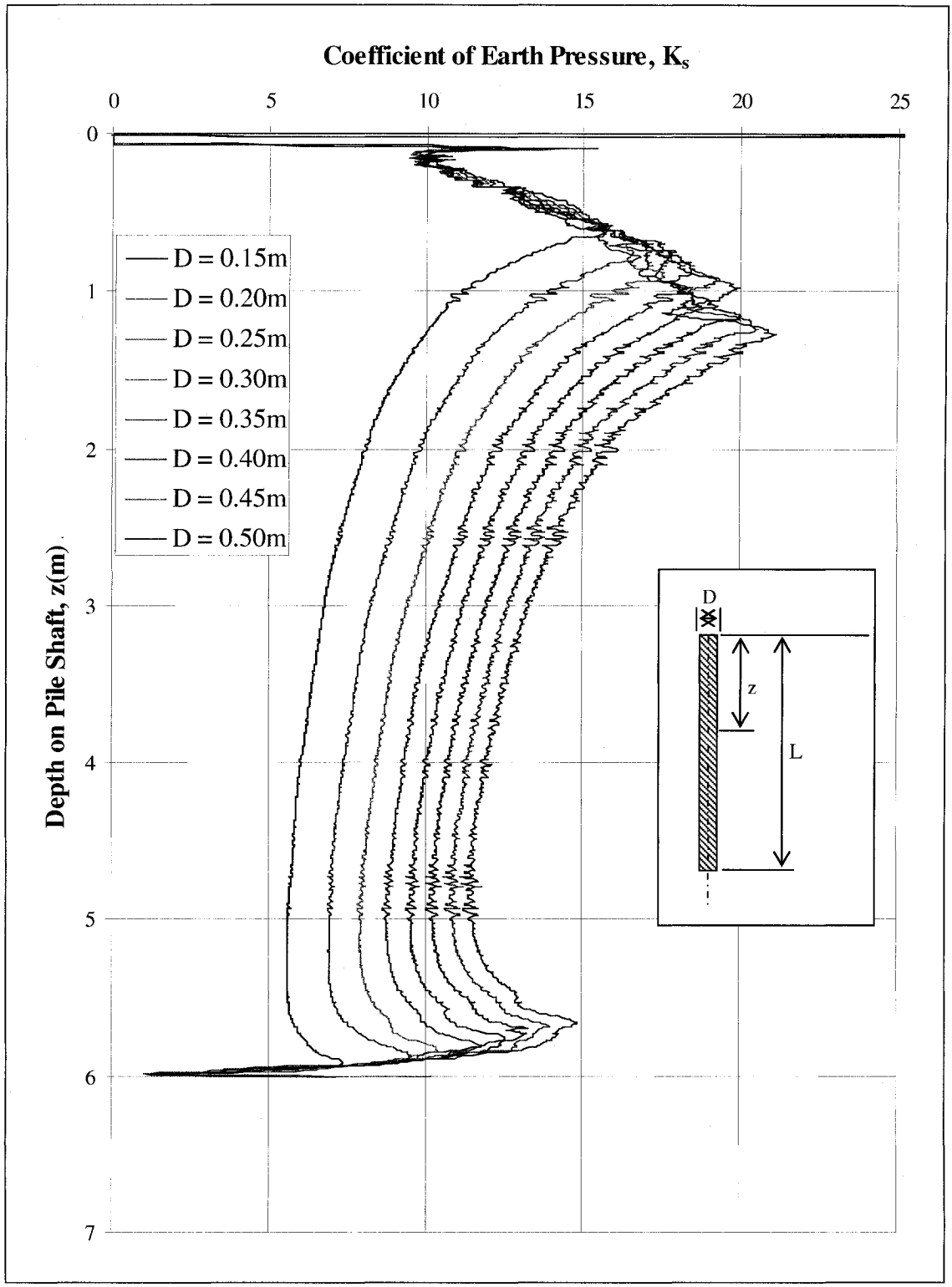

Figure 3.26 Coefficient of earth pressure distribution along the pile length (L= 6m, $\phi = 30^{\circ}$)

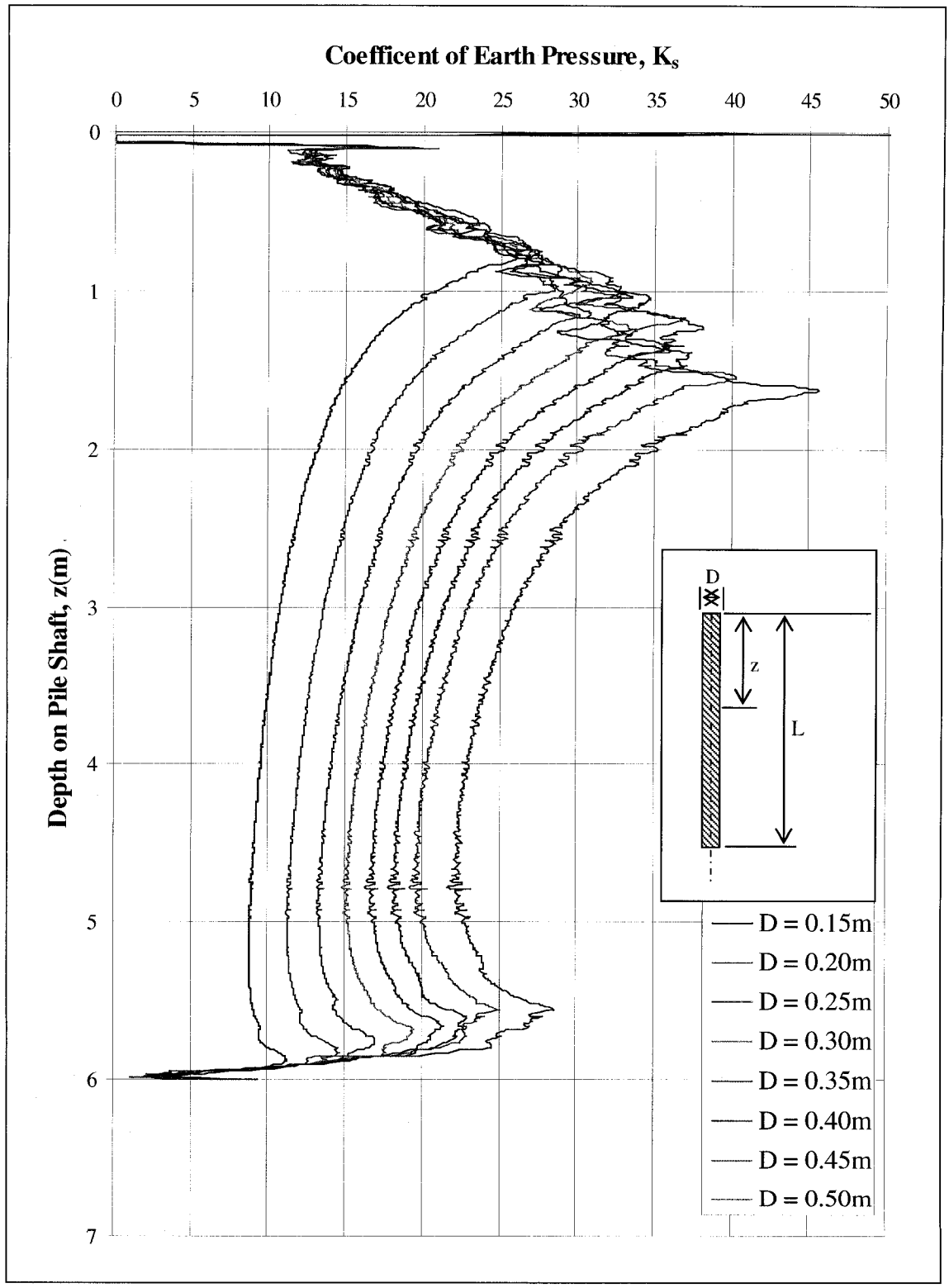

Figure 3.27 Coefficient of earth pressure distribution along the pile length (L= 6m, $\phi = 35^{\circ}$).

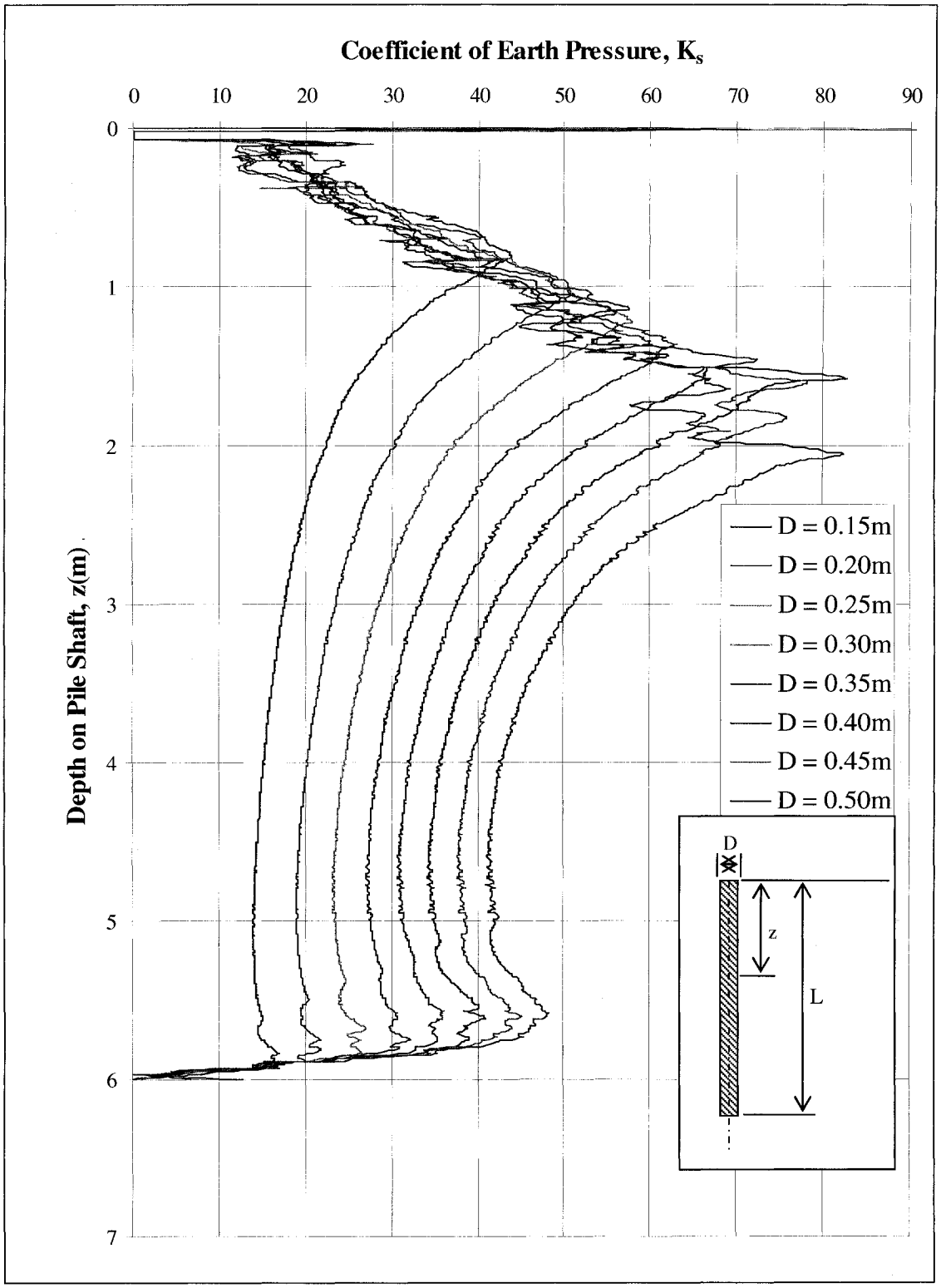

Figure 3.28 Coefficient of earth pressure distribution along the pile length (L= 6m, ϕ = 40°).

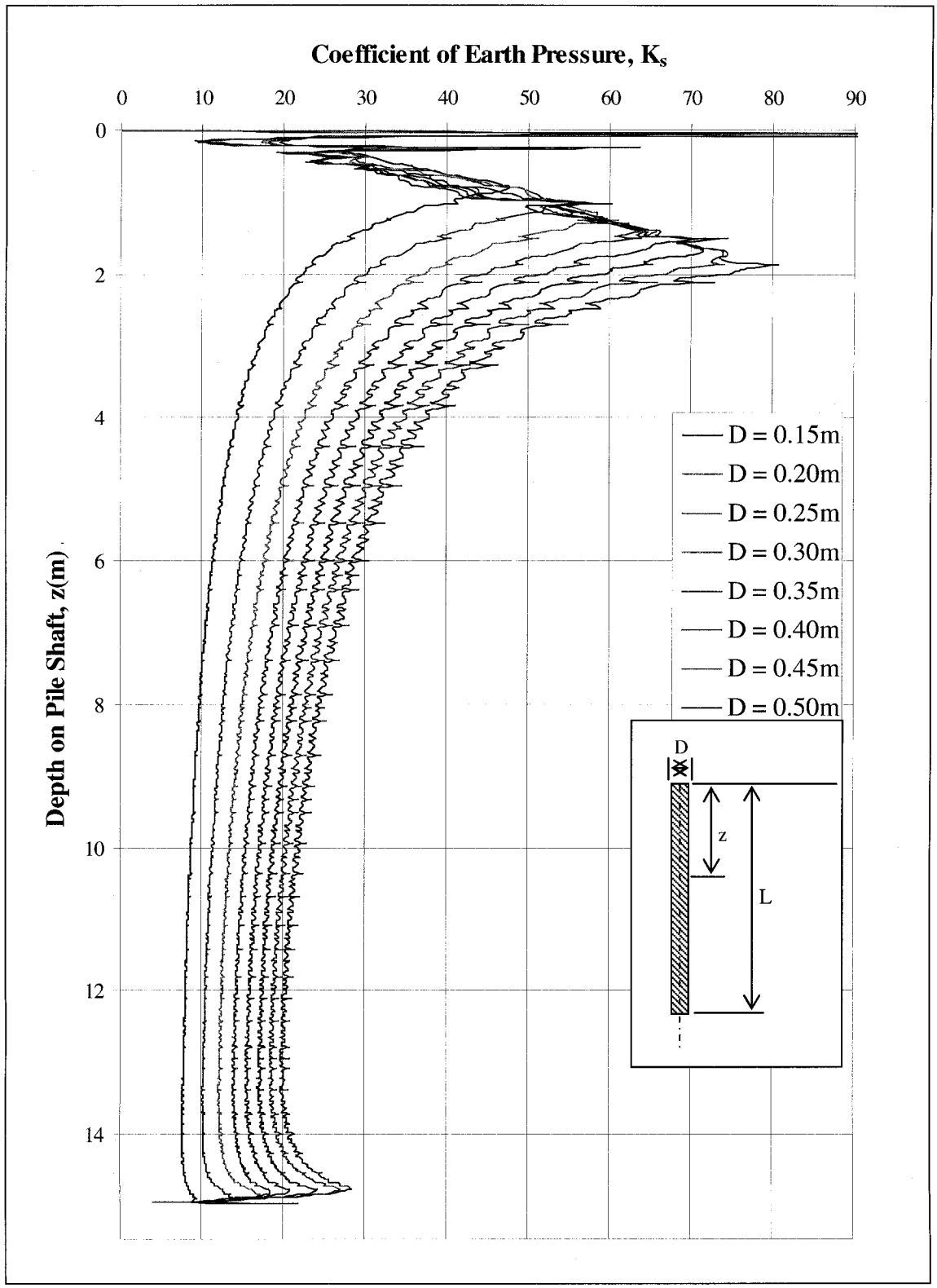

Figure 3.29 Coefficient of earth pressure distribution along the pile length ($L = 15m$, $\phi = 40^{\circ}$).

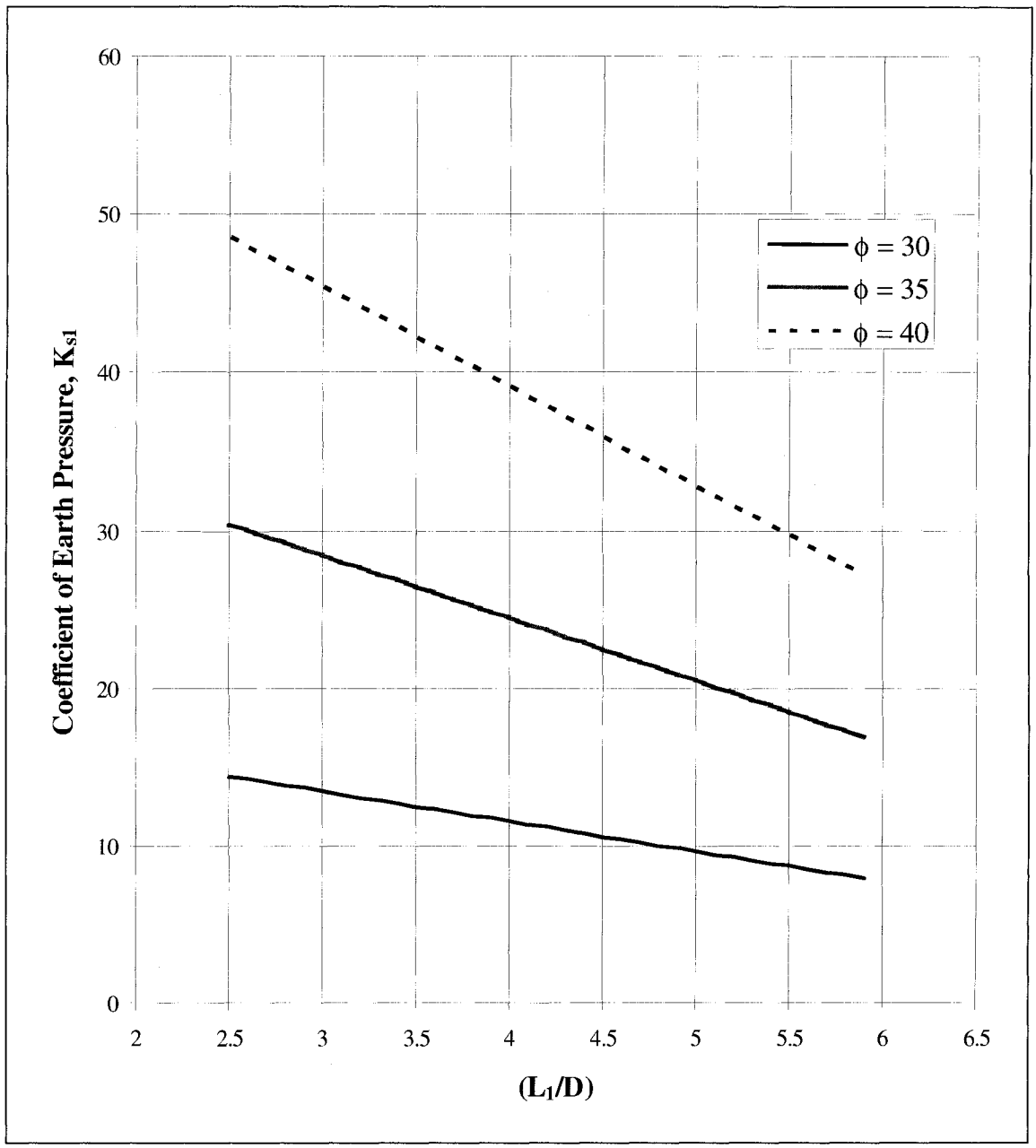

Figure 3.30 Coefficient of earth pressure in zone (1).

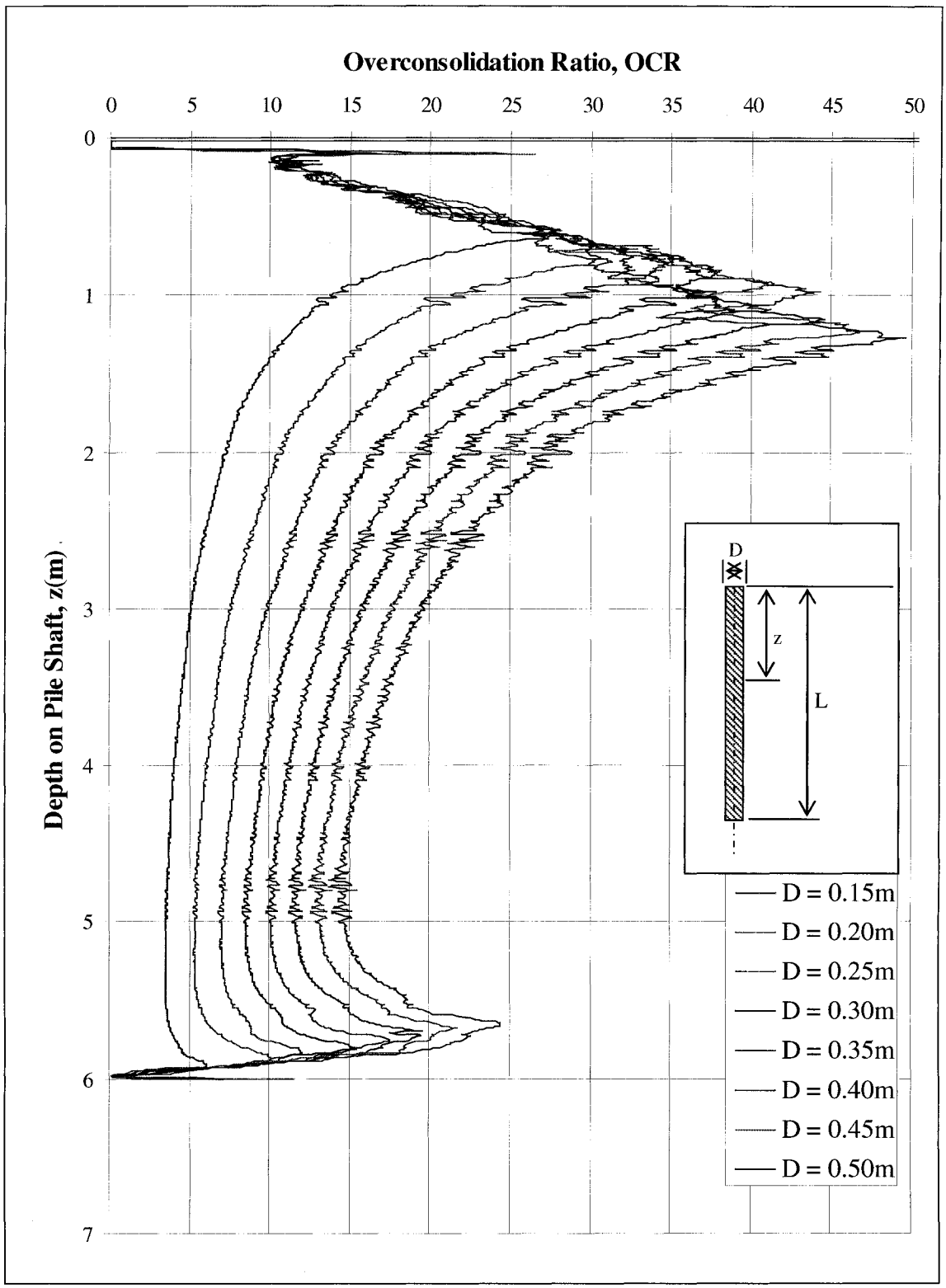

Figure 3.31 Overconsolidation ratio (OCR) along the pile length (L = 6m, $\phi = 30^{\circ}$).

The distribution of the earth pressure and the shear stress along the pile length in zone 2 presented in Figures 3.32 and 3.33, respectively. It can be noted that in zone 2 the earth pressure and the shear stresses increase linearly along the pile length (see also Figure 3.22 and 3.23). This can be explained by the fact that the soil was unable to dilate as in zone 1 due to the high confining stresses resulting from the overburden pressure where the soil does not reach to its critical state. Furthermore, in this zone the overburden pressure increases with depth to a value closer to the primary stress due to the high earth pressure produced by the radial displacement. Zone 2 is more pronounced in longer piles and it is not affected by the pile head and the tip zones (i.e. zone 1 and zone 3). The increase in the earth pressure due to the pile's diameter is clearly recognized in this zone. It is also noted that the critical depth was not observed herein, to the contrary to what has been reported in the literature. This can be explained, as the critical depth was determined according to the case of partially mobilized friction on the pile's shaft, while it is well established that the shaft resistance reaches full mobilization at the ultimate capacity of the pile (Franke 1993). Furthermore, due to the increase in the earth pressure on the pile's shaft, the critical depth may be pushed deeper and can be found at a greater depth, where it will not be recognized. It is also noted that the effect of the pile's diameter beyond 0.35m is little or none. From the coefficient of earth pressure distribution along the pile length in the mid zone presented in Figure 3.34, it can be noted that a linear increase in the earth pressure is reflected on the values of the coefficient of earth pressure. This can be explained by the fact that the movement of the sand particles in this zone is uniform along the pile's depth, which will result in a constant ratio between the earth pressure and

the overburden pressure. This constant ratio will be achieved in longer piles, where the value of Ks tends to be fixed for these piles. It can be also noted from Figure 3.34 that the average value of the coefficient of earth pressure in this zone is less than that of the previous zone and the deeper the pile the less the value of K_s until it reaches a value close to the case of normally consolidated sand K_p.

Figures 3.35 to 3.37 is the variation of the OCR along the pile length for a range of pile diameters. The OCR decreases along the pile length tending to reach a constant value for long piles (20m) in loose sand $\phi = 30^o$. OCR range from 1 – 4.5 for 0.15 – 0.5m pile diameter respectively, for pile in medium $\phi = 35^o$ sand OCR = 2 – 8.5 and for $\phi = 40^o$, OCR = 4.5 – 16. In this investigation, the following formula is proposed to evaluate the K_s in zone 2:

$$K_{s2} = 250 \tan^4 \phi \left(\frac{D}{z}\right)^{0.7 \tan \phi + 0.02} \qquad (3.7)$$

Where :

$L_1 \leq z \leq L_2$

The length L_2 is affected by zone 3, accordingly, it will be determined based on the analysis for this zone.

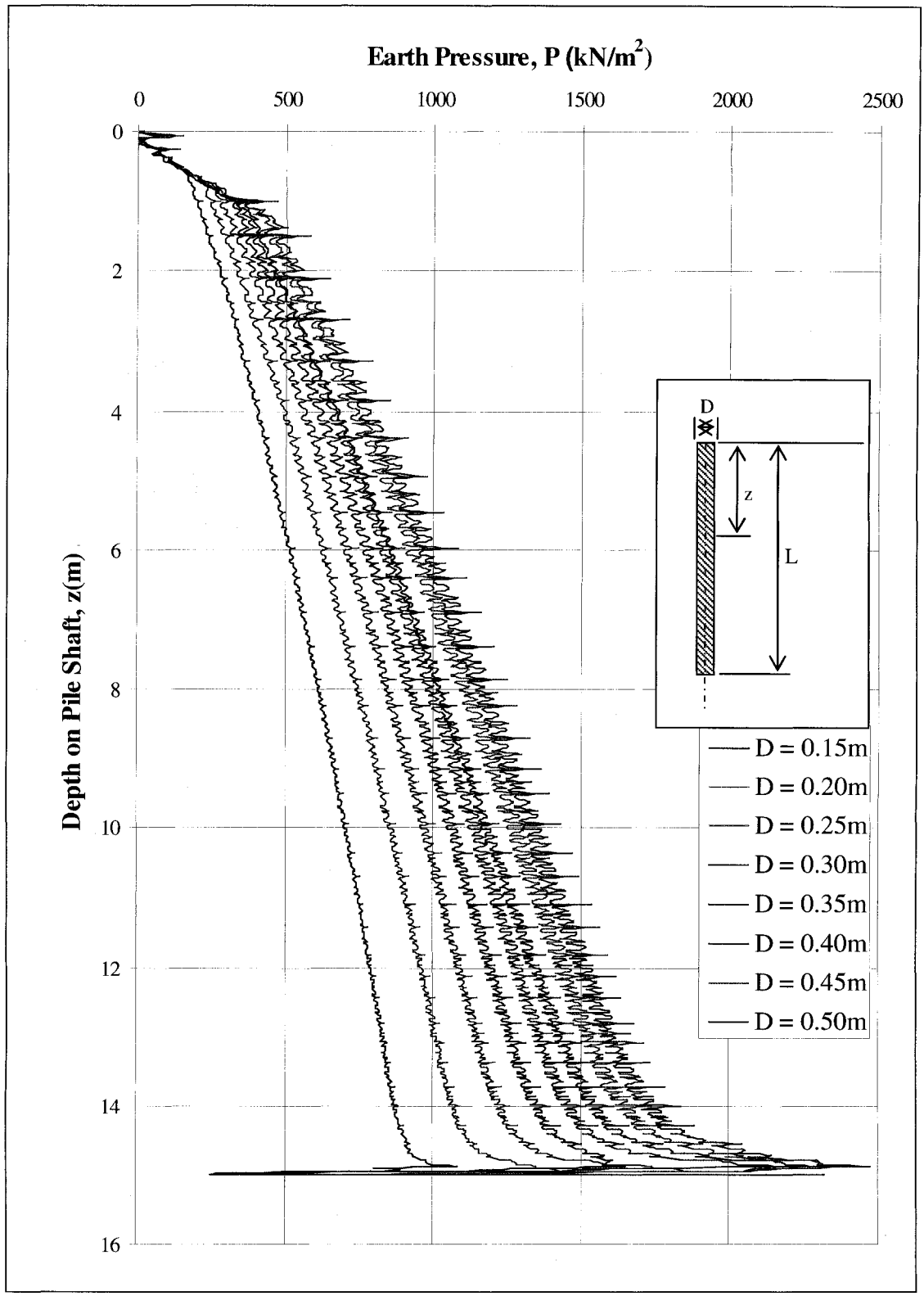

Figure 3.32 Earth pressure along the pile length (L = 15m, $\phi = 30^{o}$)

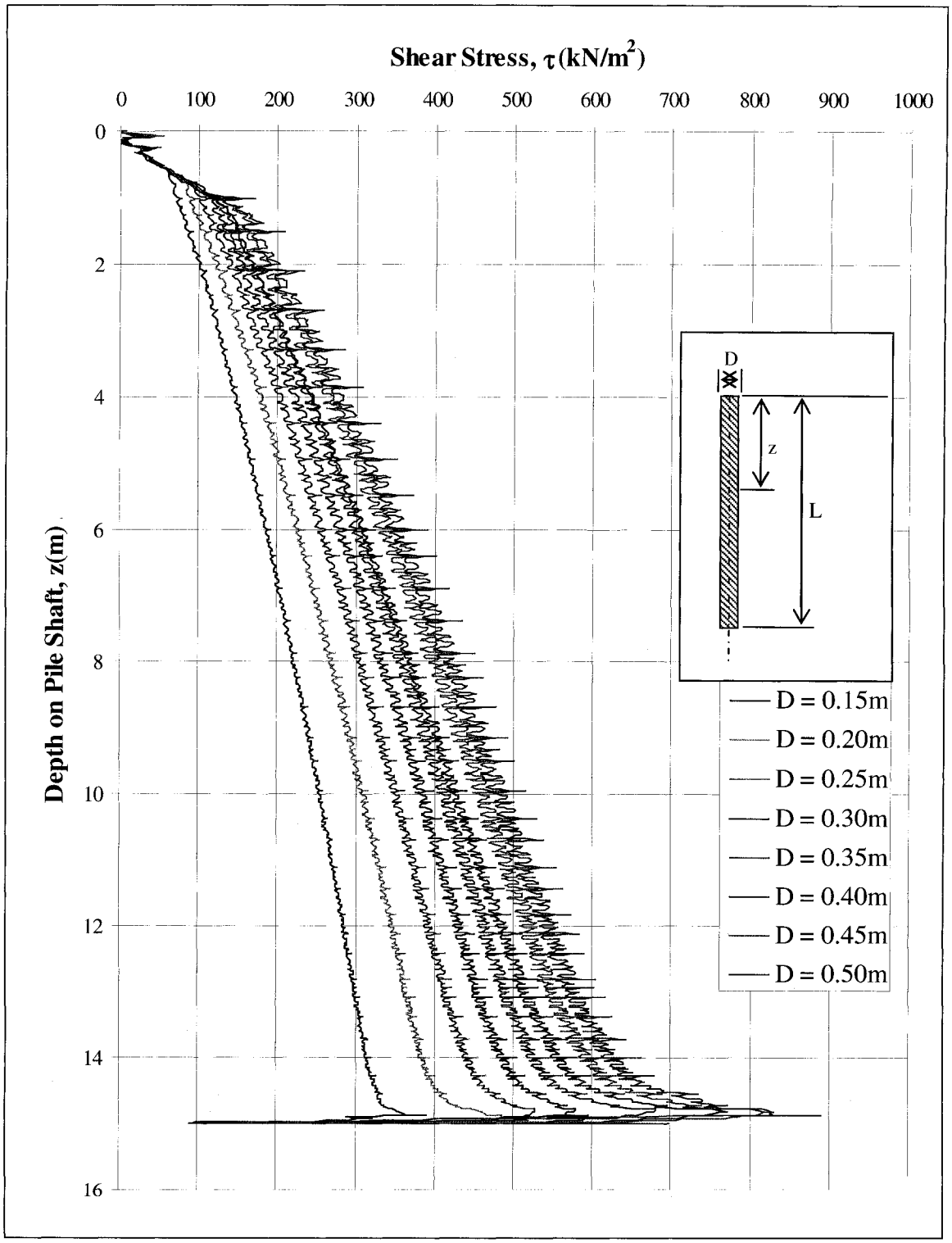

Figure 3.33 Shear stress along the pile length (L = 15m, ϕ = 30°).

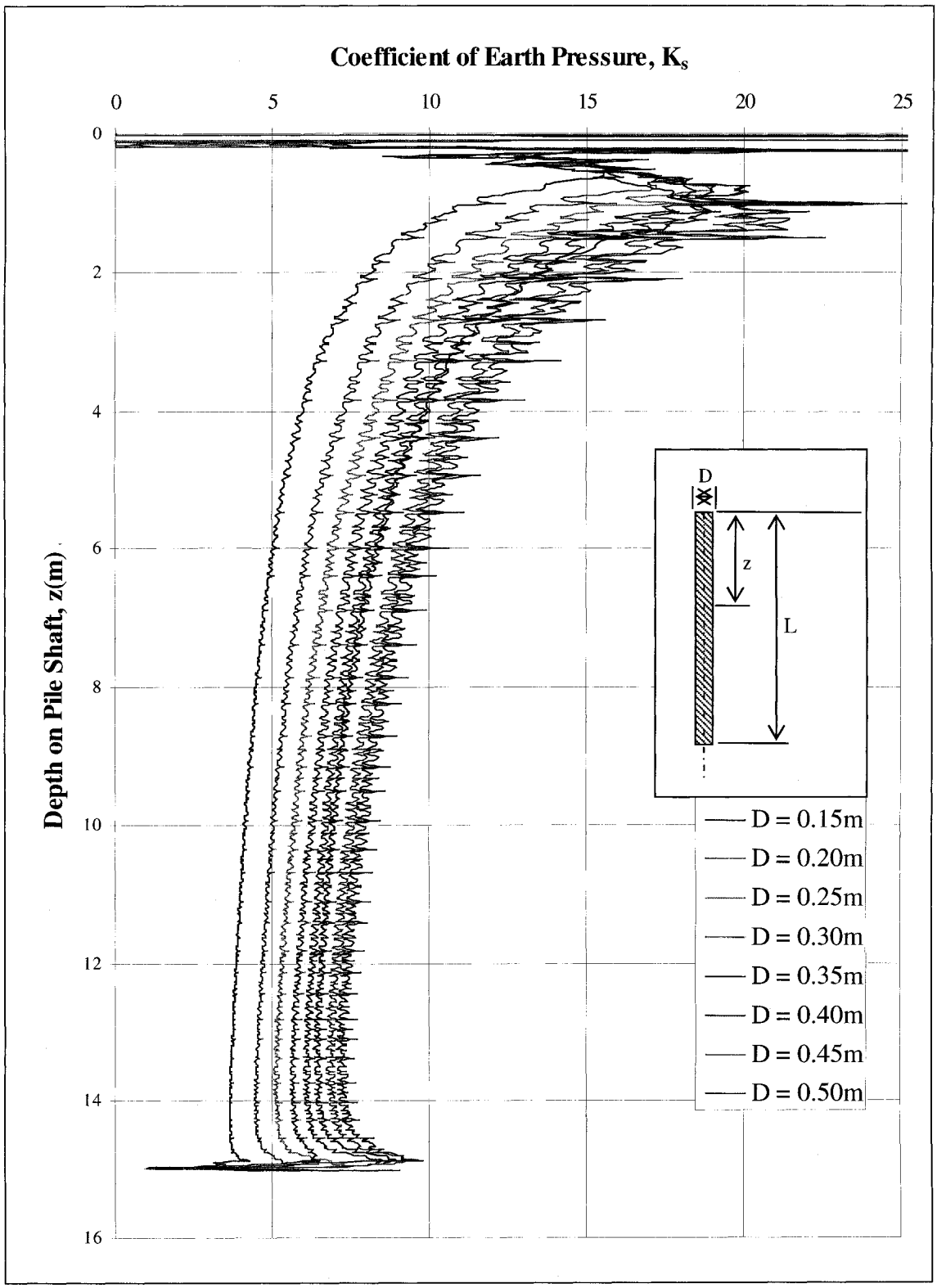

Figure 3.34 Coefficient of earth pressure along the pile length (L = 15m, $\phi = 30^{o}$).

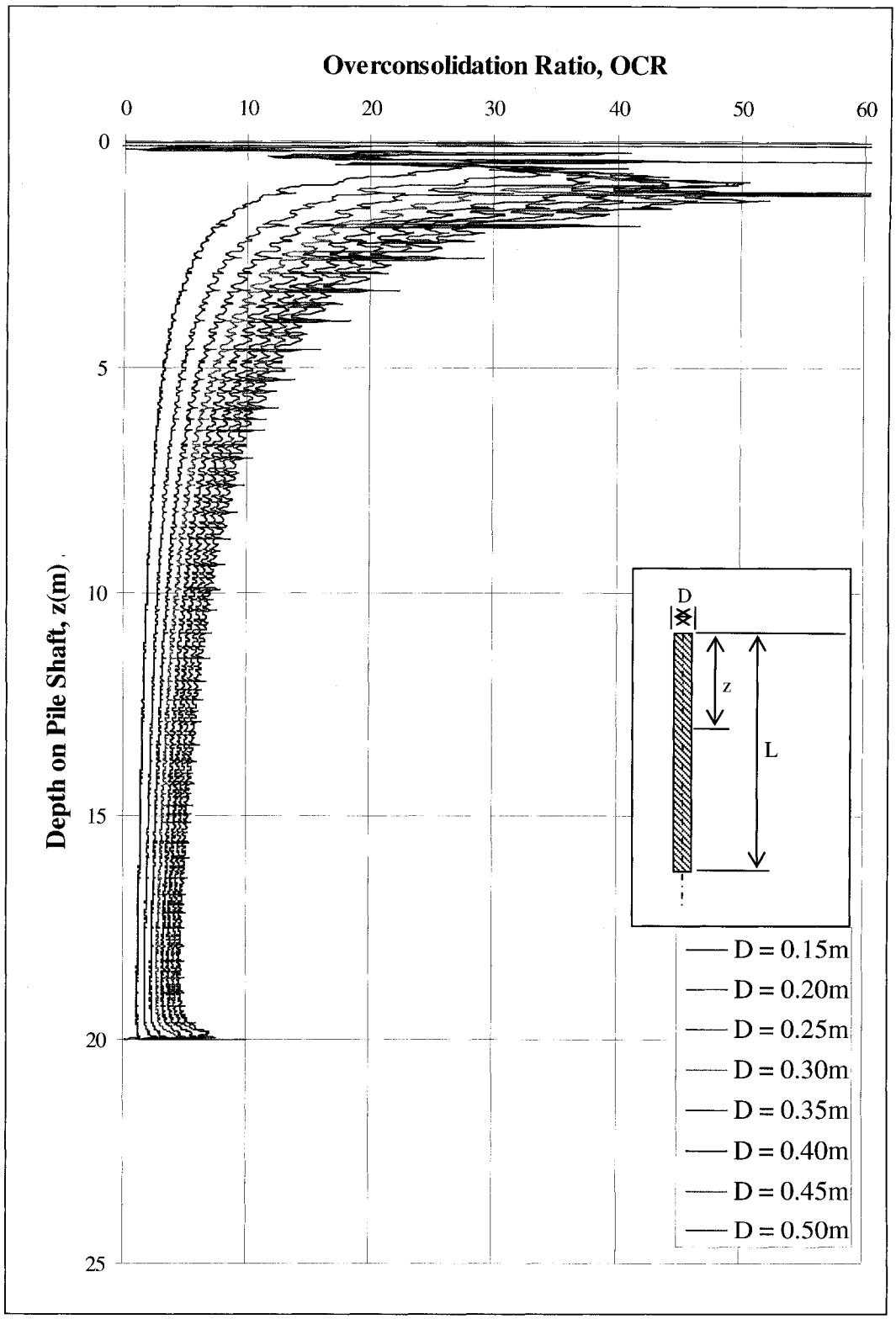

Figure 3.35 Overconsolidation ratio (OCR) along the pile length (L = 20m, $\phi = 30^{\circ}$).

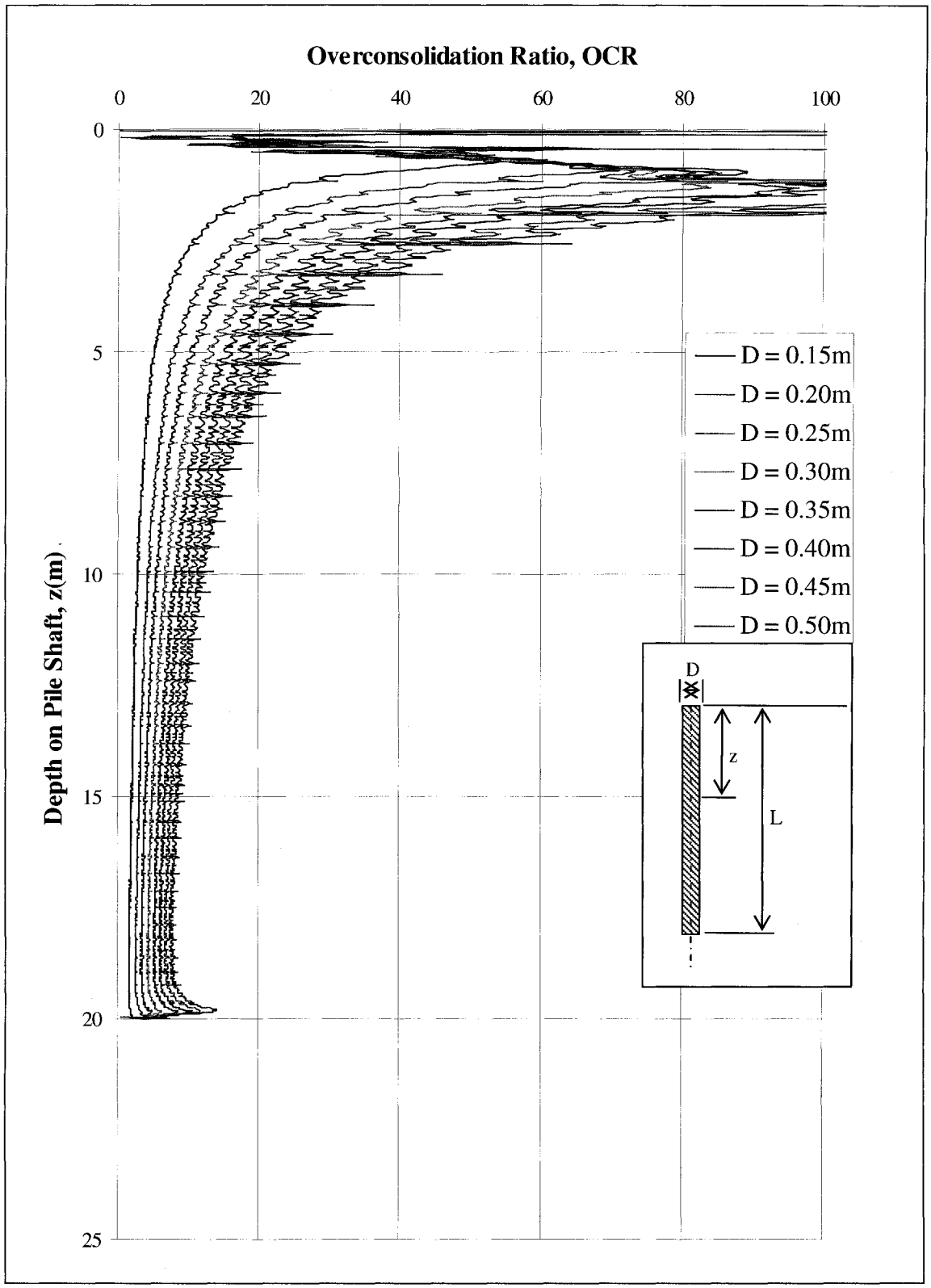

Figure 3.36 Overconsolidation ratio (OCR) along the pile length (L = 20m, $\phi = 35^{\circ}$).

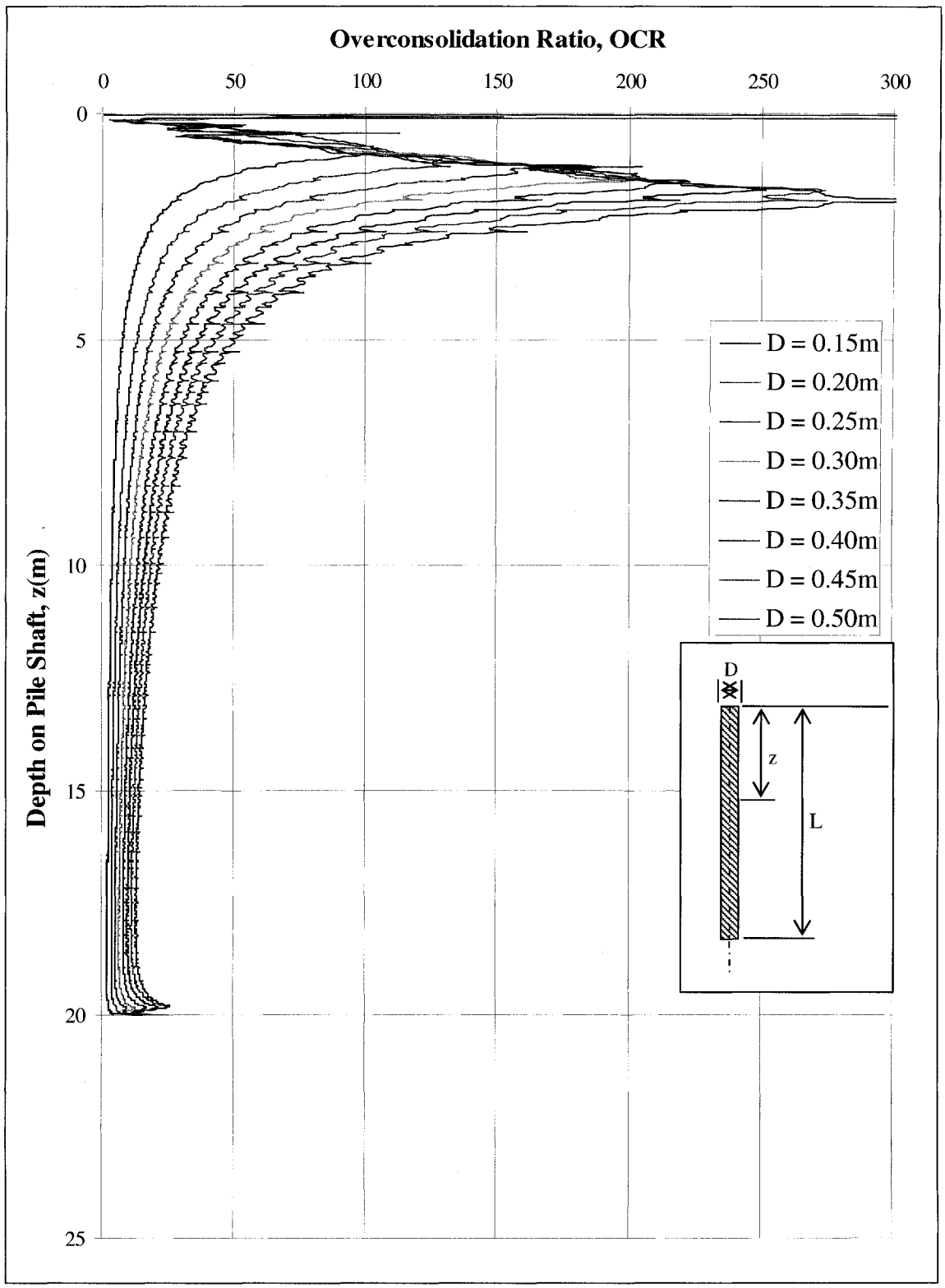

Figure 3.37 Overconsolidation ratio (OCR) along the pile length (L = 20m, ϕ = 40°).

Zone 3 is recognized by the sudden increase in the earth pressure at a rate higher than that of zone 2. The sudden increase in the earth pressure in this zone is mainly due to arching, which takes place below the pile tip, as a result of the downward movement of the pile.

The depth of zone 3 on the pile shaft depends on the pile movement and the radial displacement of the surrounding sand. Referring to Figure (3.22), it can be noted that this zone is hardly recognized for the 0.15m diameter pile, on the other hand it is well pronounced with the increase of the pile's diameter. Figure 3.38 presents the ratio between the depth of zone 3 with the pile's diameter (L_3/D) and the total pile length. It can be noted from this figure that the depth of zone 3 is reduced with the increase of pile length. This reduction is due to the increase of the overburden pressure up to a maximum value at the pile tip. An empirical formula is presented to define this zone taking into account the pile length and diameter and the angle of shearing resistance of the sand (ϕ):

$$L_2 = L - D\,[(0.02 - 0.1\tan(\phi))\,L + 6.5\tan(\phi) - 1] \qquad (3.8)$$

Referring to Figure 3.32, it can be noted that this zone is relatively small in long piles with $L/D < 15$, therefore it can be neglected in evaluating the pile performance. Referring to Figure 3.34, the coefficient of earth pressure, K_s increases in this zone, however, it never reaches a high value as occurred in zone 1. The OCR follows the same trend as K_s (see Figure 3.35 to 3.37). The variation of the coefficient of earth pressure versus the L/D ratio in zone 3 can be summarized in the chart at Figure 3.39, where the depth of this zone can be easily determined for any given pile/depth. It can also be formulated in the following expression:

$$K_{s3} = \frac{K_{sL2} - K_p}{L - L_2}(L\text{-}z) + K_p \qquad (3.9)$$

Where,

$L_2 \leq z \leq L$

$K_p = \tan^2(\pi/4 + \phi/2)$

After reaching the peek value, both K_s and the OCR decrease until they reach the values for the normally consolidated case at the pile tip.

Figure 3.40 presents a typical data generated from a 6m pile, where the unit average shear resistance versus the pile's diameter for values of ϕ. It can be noted that the diameter for pile driven in sand of higher value of the angle ϕ generate more shearing resistance than if the pile was driven in lower value of the angle ϕ. The reason is that for loose sand there are larger voids than dense sand so the increase in diameter will compact more the soil around the pile and most of the lateral movement is absorbed by the surrounding soil. It can be noted also that there is no much gain in the unit shaft resistance due to the increase in pile's diameter after a certain limit, beyond which the yielding of the soil takes place due to the cavity expansion. This is specially noticed in case of low soil strength ($\phi = 30$); as due to the increase of the pile diameter from 45cm to 50cm, the unit shaft resistance was increased by only 10%.

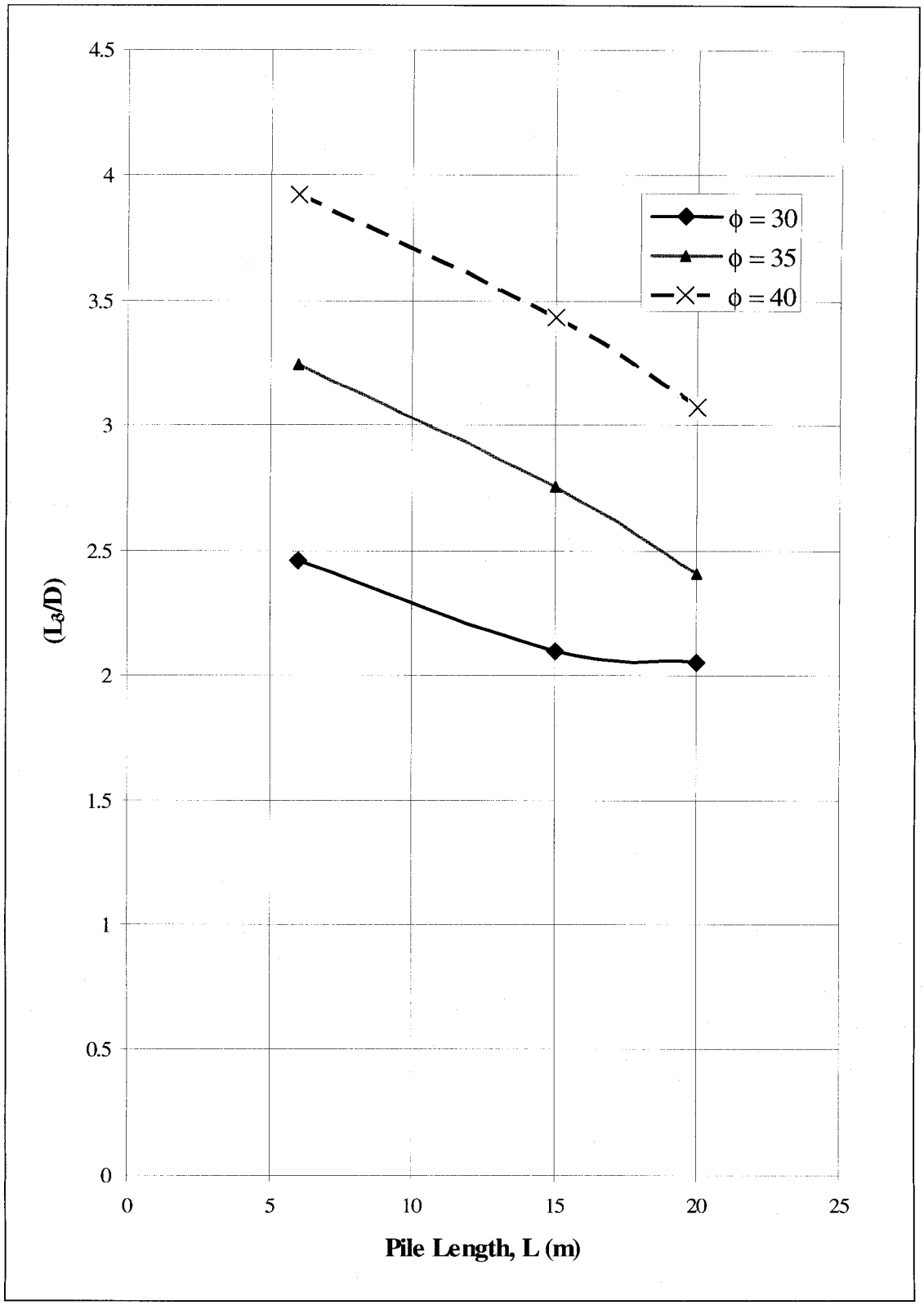

Figure 3.38 Length of zone 3 versus pile length.

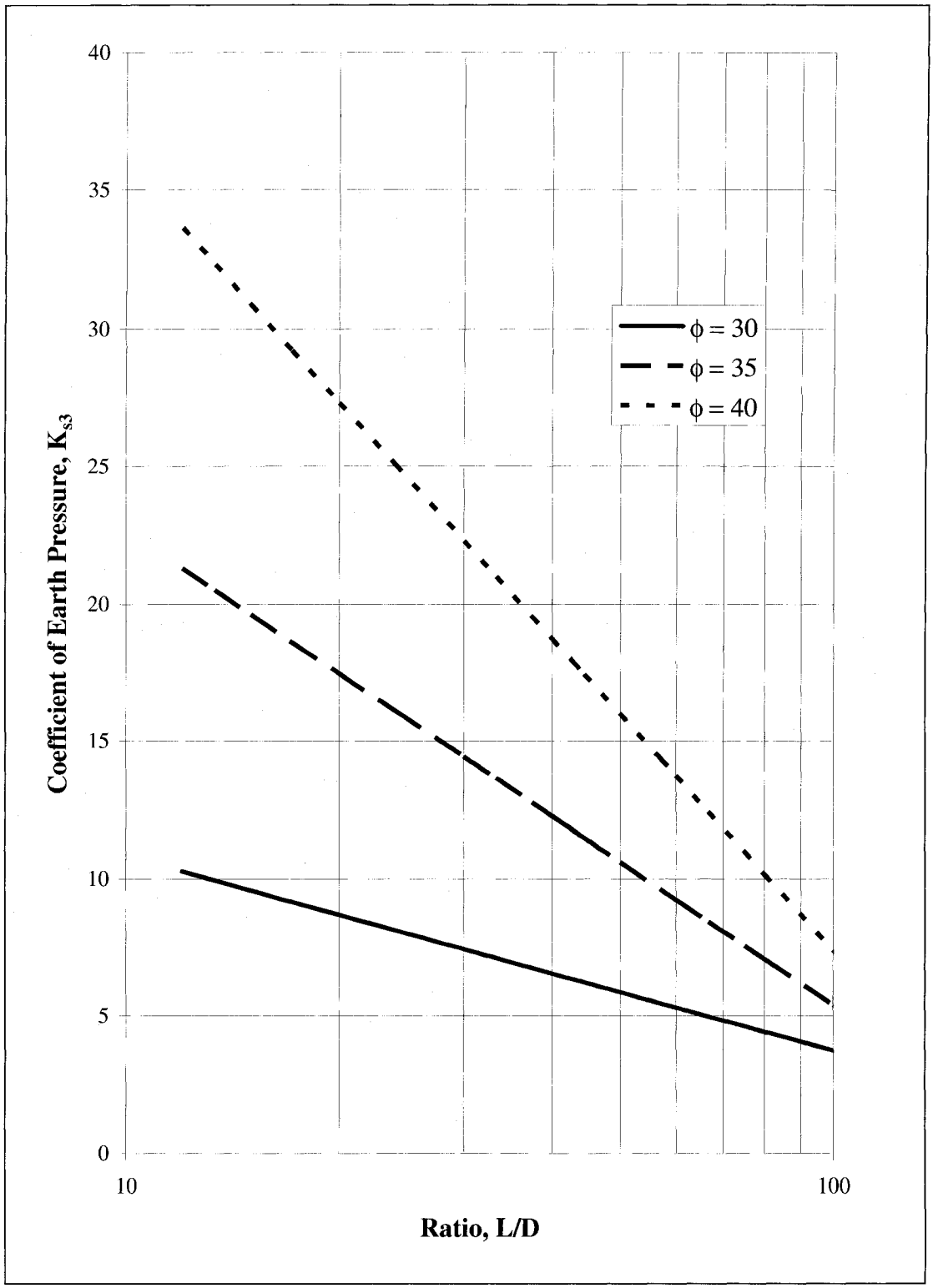

Figure 3.39 Coefficient of earth pressure versus L/D ratio in zone 3.

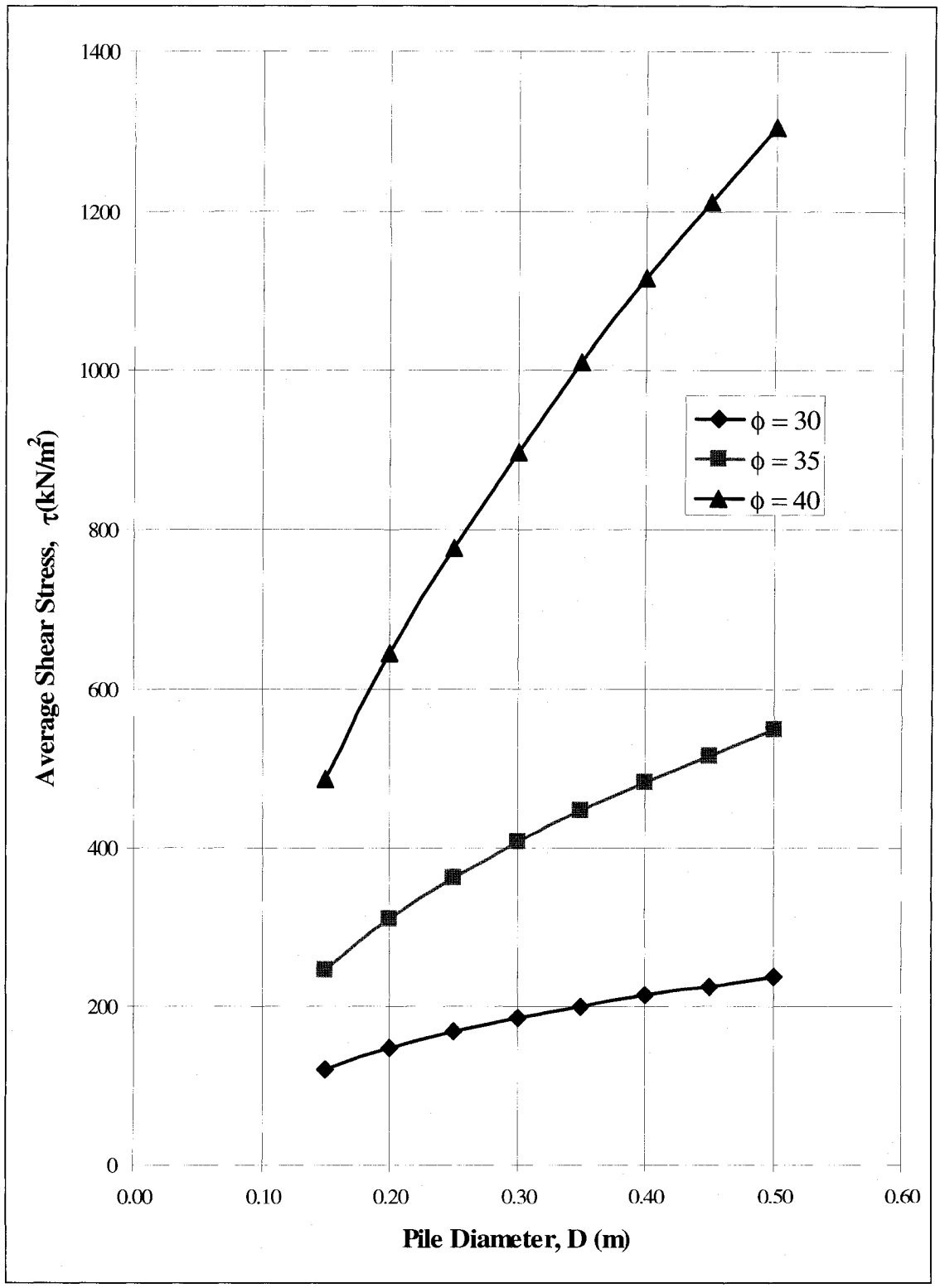

Figure 3.40 Pile's diameter versus the average shear stress on the pile's shaft.

3.5.3 Effect of Pile Length

The pile length is known as the major contributor to the pile capacity. Besides the facts that an increase in the pile length will increase the surface area of the shaft, it will also bring the pile tip to a deeper quite often-stronger soil layer. In deeper soil, the sand is more densified due to the increase of the overburden pressure.

Figures 3.41 to 3.43 present the average coefficient of earth pressure, K_s versus a range of pile's length. In general, it can be noted that the values of K_s decreases due to an increase of the pile length. This is mainly due to the increase in the overburden pressure. It can be also noted that the rate of decrease of K_s decreases along the pile length. This means that the average value of K_s remains approximately the same beyond a certain depth. From these results it can be noted that the coefficient of earth pressure reaches a maximum value at the ground surface and decreases to a constant value at large depths, due to the high overburden pressure where the interlocking between the soil particles increases. For example, it can be realized that there is no much change in the value of K_s if a pile has diameter less than 0.2m and goes longer than 15m in sand of $\phi = 35^{\circ}$.

Figures 3.44 and 3.45 present the average OCR versus a range of pile's length. It is indicated from these figures that the average OCR decreases with the increase of pile length. It is noted that the average OCR is high for short piles this is due to the high OCR near the ground surface because of the low overburden pressure and high vertical stresses due to soil displacement and the particles upward movement due to the cavity produced from the pile driving. The deeper the pile goes into the soil, zone 1 and zone 3 become apart from each other as shown in previous section. This leads to minimize their effect on the over all average of the OCR average distribution on the pile shaft. This indicates that

zone 1 and zone 3 have more effect in short piles than that in long piles. Generally, from this analysis it can be concluded that the appearance of the critical depth as noted by several researchers (Vesic 1964 & 1970) and (Meyerhof 1951 & 1975) was not observed in this investigation. On the other hand this observation was confirmed by (Fellenius 1995), (Altaee et al. 1993) & (Kulhawy 1984). This is because the critical depth can be observed as a result of incomplete friction mobilization on the pile shaft. If however, a full mobilization takes place the presence of critical depth will vanish. Another possibility could be due to the large deformation, which may take place in the soil due to the pile installation, and accordingly, it will push the critical depth to deeper layers, beyond the pile length. This issue needs to be examined experimentally to come to a clear and firm judgment taking into account the residual stresses resulted from the pile driving and not resetting the gauges to zero before loading the pile.

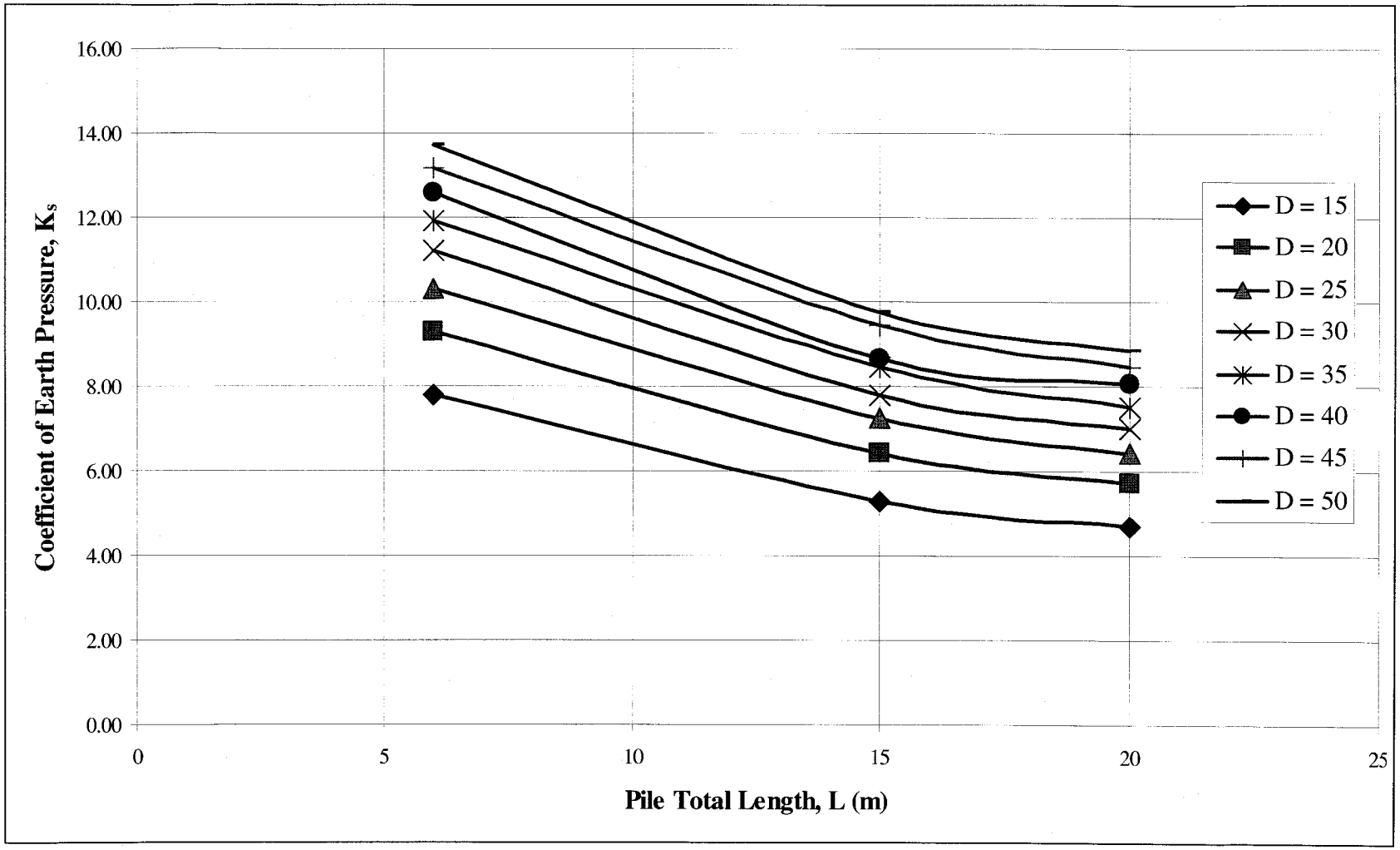

Figure 3.41 Average coefficient of earth pressure versus pile length - $\phi = 30^{o}$.

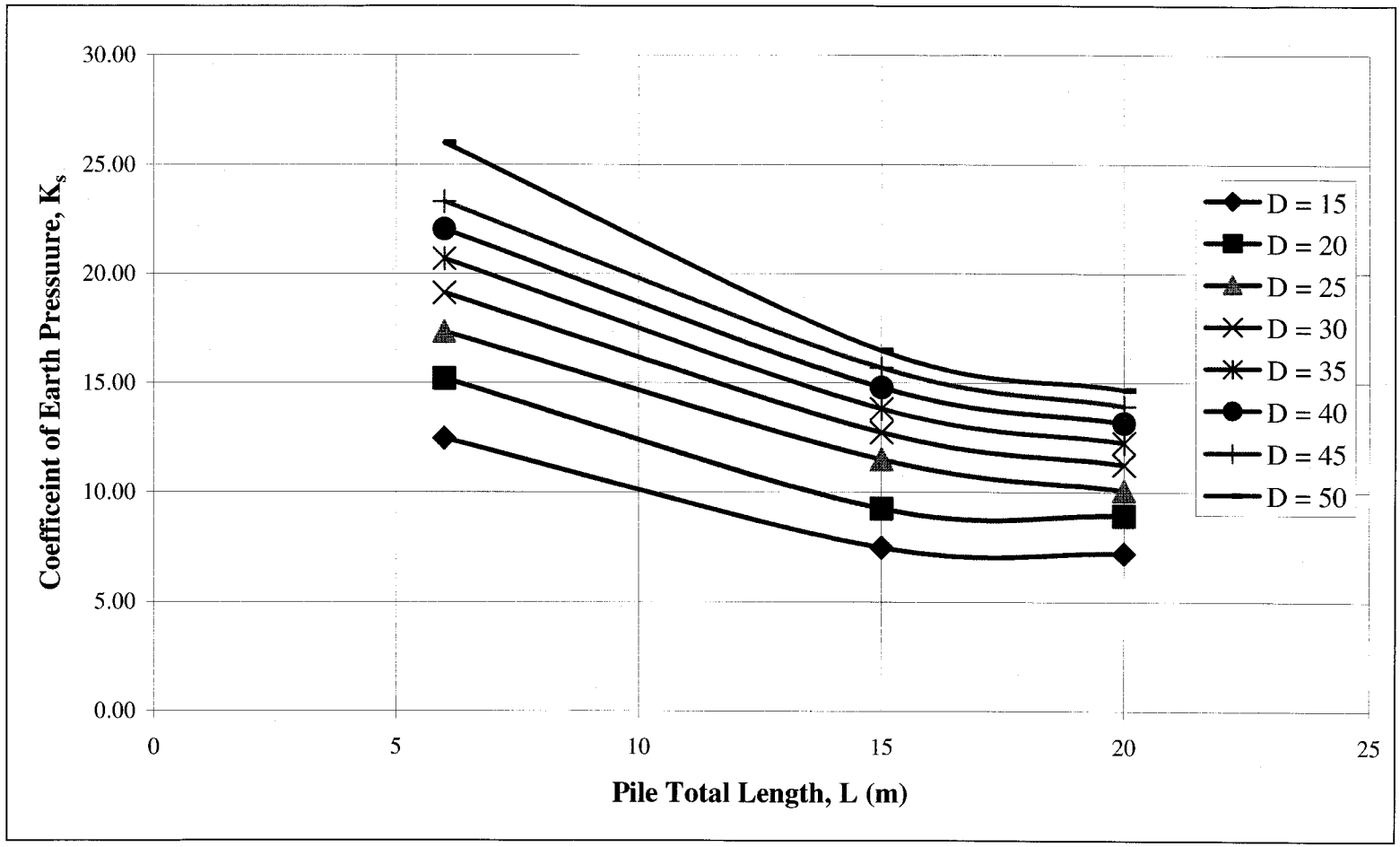

Figure 3.42 Average coefficient of earth pressure versus pile length - $\phi = 35^{o}$.

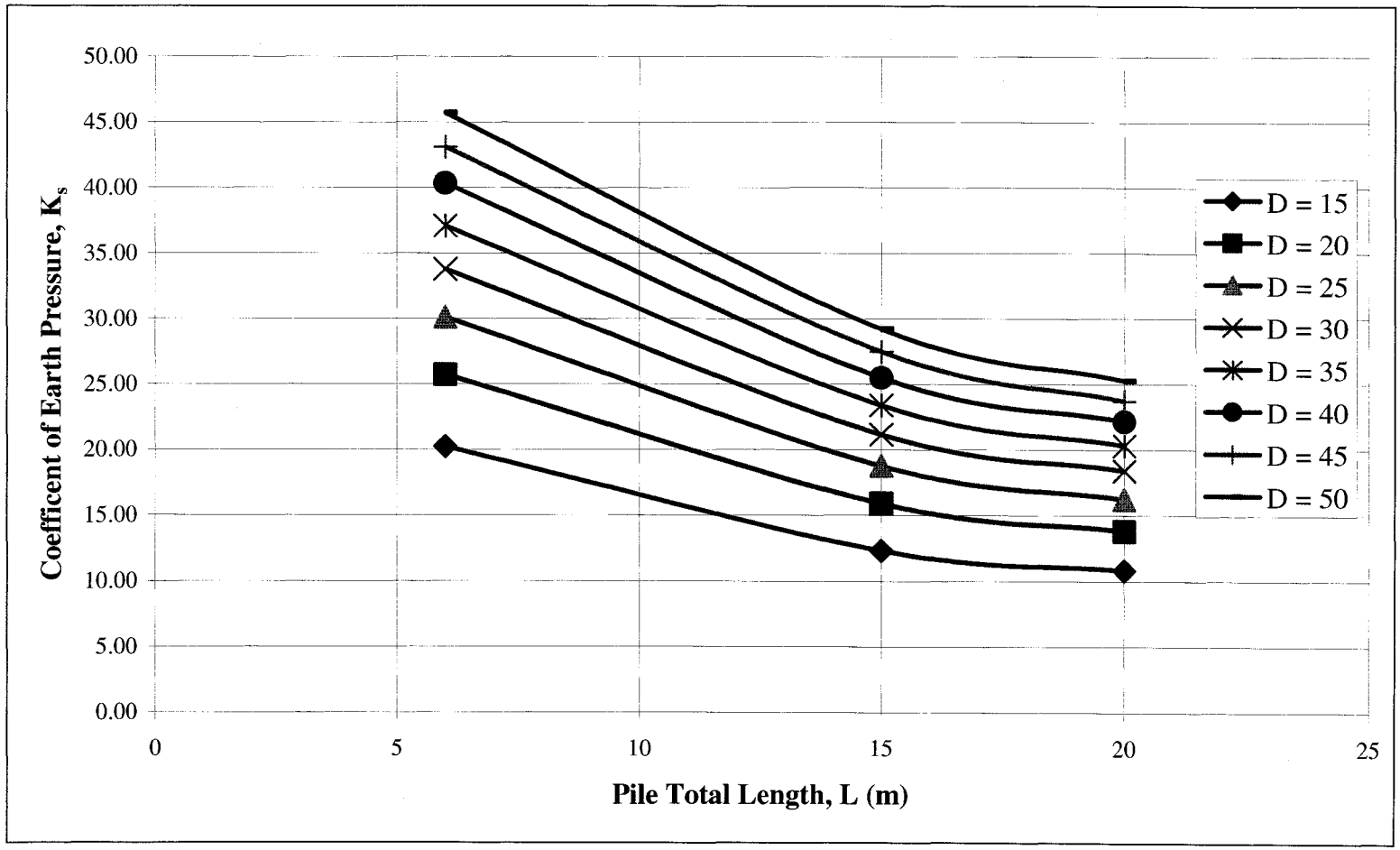

Figure 3.43 Average coefficient of earth pressure versus pile length - $\phi = 40^{o}$.

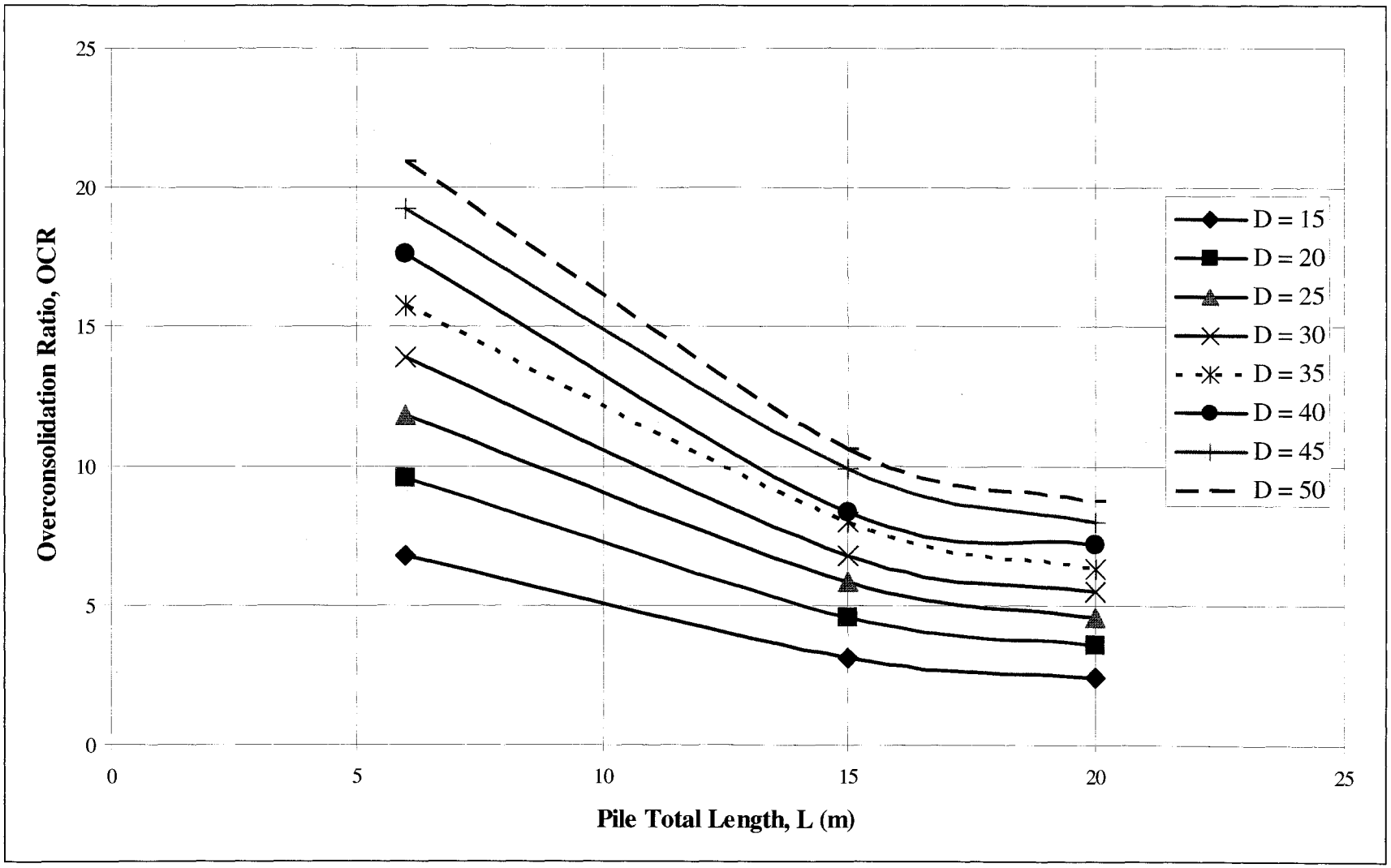

Figure 3.44 Average overconsolidation ratio versus pile length - $\phi = 30^{o}$.

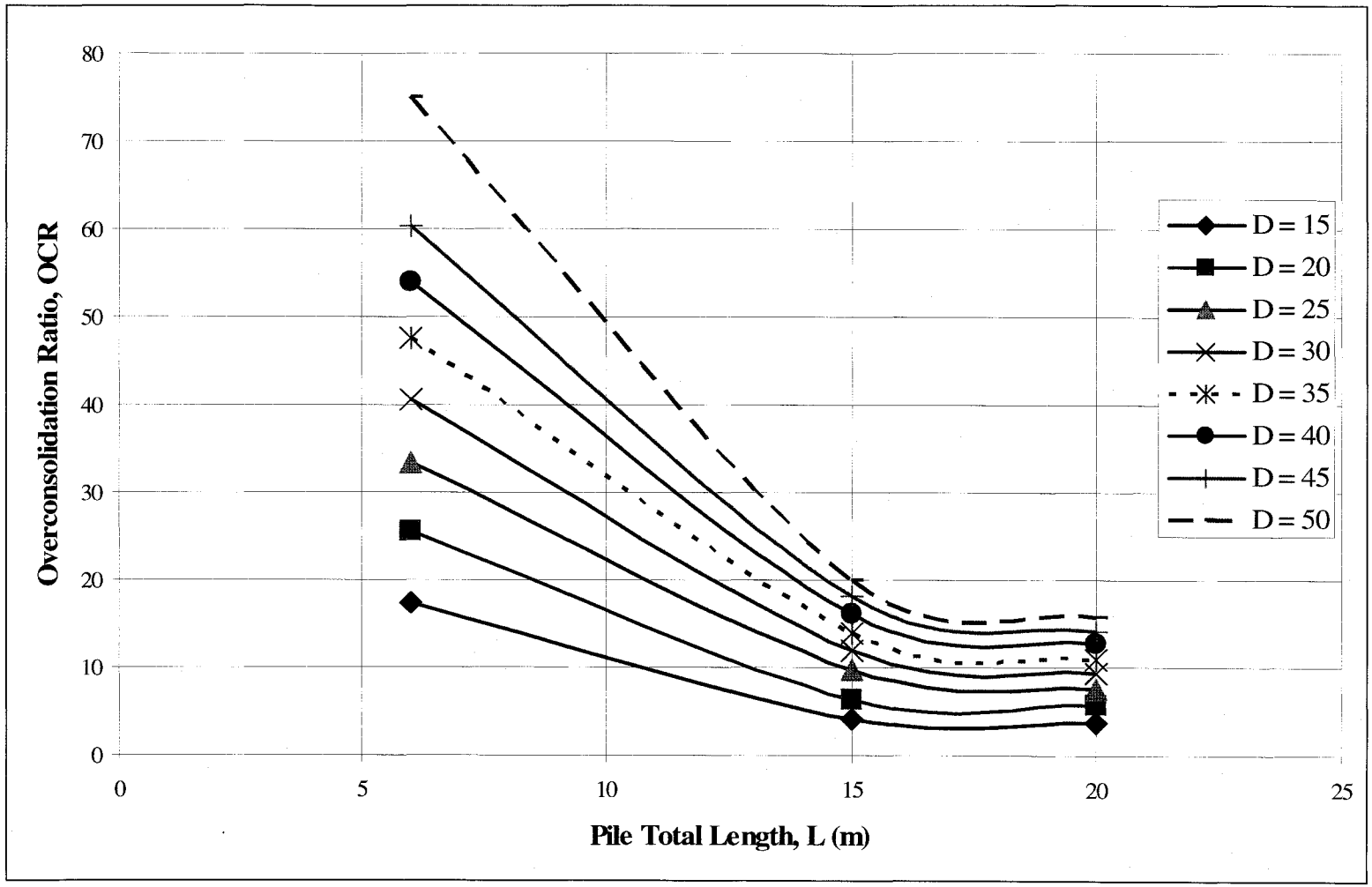

Figure 3.45 Average overconsolidation ratio versus pile length - $\phi = 35^{o}$.

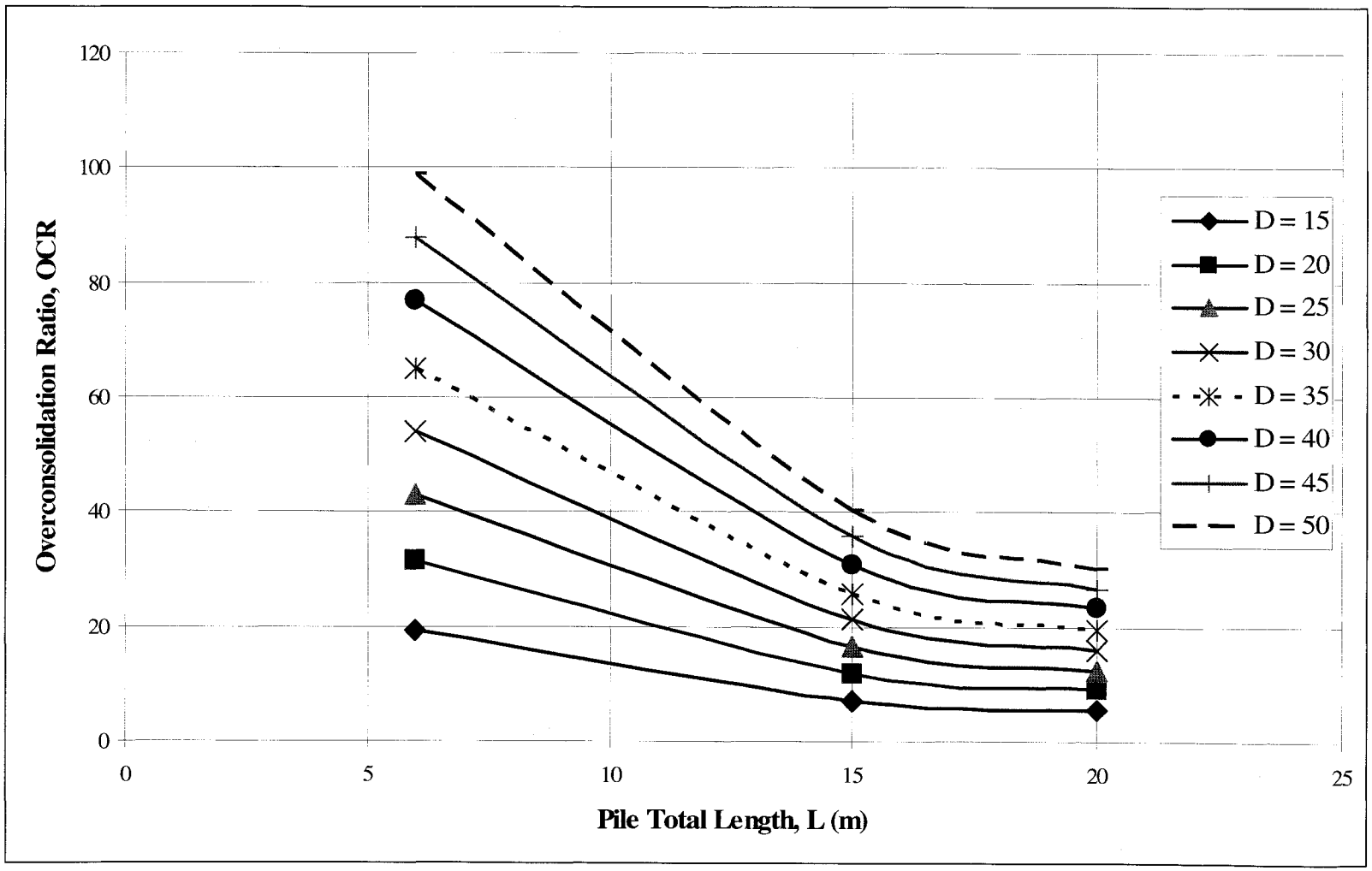

Figure 3.46 Average overconsolidation ratio versus pile length - $\phi = 40^{o}$.

3.5.4 Effect of Roughness of Pile's Shaft Surface

The pile/soil interface was modeled using a special type interface element. Three different δ/ϕ values were used in this investigation to study the effect of the pile roughness on the surrounding soil and accordingly on the pile performance. Figure 3.47 presents the shear stress along the pile's shaft for different degree of roughness of the pile's shaft represented by the ratio δ/ϕ. It can be noted that the shear stress increases on the pile shaft with the increase of δ/ϕ. Figure 3.48 represents the pile surface roughness versus the earth pressure acting on its shaft. It can be noted from this Figure that the ratio δ/ϕ does not contribute to the values of the coefficient of earth pressure and accordingly to the OCR. This phenomenon contradicts the theory of earth pressure for rough walls (Caquot and Kerisel, 1949). This is due to the downward and lateral movements of the soil, which is associated with the pile installation. The earth pressure will be determined herein on the light of the failure mechanism, which will provide an explanation for the evaluation of the coefficient of earth pressure acting on the pile's shaft as an independent parameter from the shaft friction. From Figure 3.49 it is possible to obtain the average coefficient of earth pressure for driven pile, knowing the angle of shearing resistance ϕ and the ratio L/D. From this chart, it is possible to determine the coefficient of earth pressure developed on the pile's shaft due to its installation.

Figure 3.50 presents the state of stresses around the pile in terms of the value of the OCR along the pile's shaft, as a result of the horizontal displacement caused by pile installation. From this chart it can be concluded that the sand around the pile is subjected to residual stresses caused the process of pile installation. From the chart, it can be noted

that for higher values of ϕ and same L/D value the overconsolidation value reaches to higher values on the logarithmic scale. The reason behind this result is that the voids between the sand particle for dense sand is minimum which gives no room for the particles to rearrange its location to achieve a more relaxing state of stresses. Also by installing bigger pile diameter (<L/D) in loose to medium sand will lead the sand close to the pile shaft to occupy most or all the voids. When the voids are being fully occupied by the sand particle stresses will start to build up, which will lead to higher values for the coefficient of earth, pressure and in order to higher value of OCR.

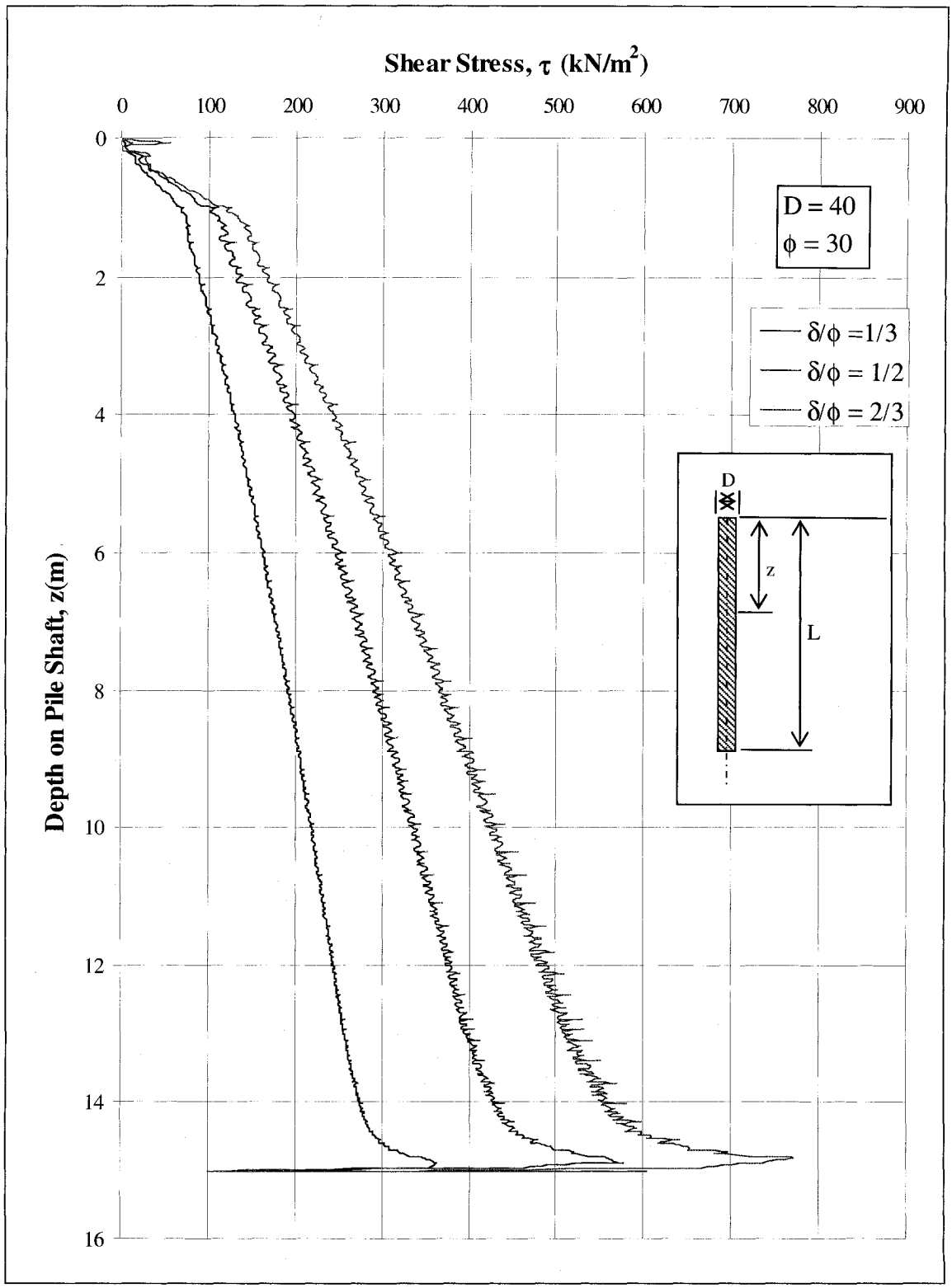

Figure 3.47 Shear stress versus pile length

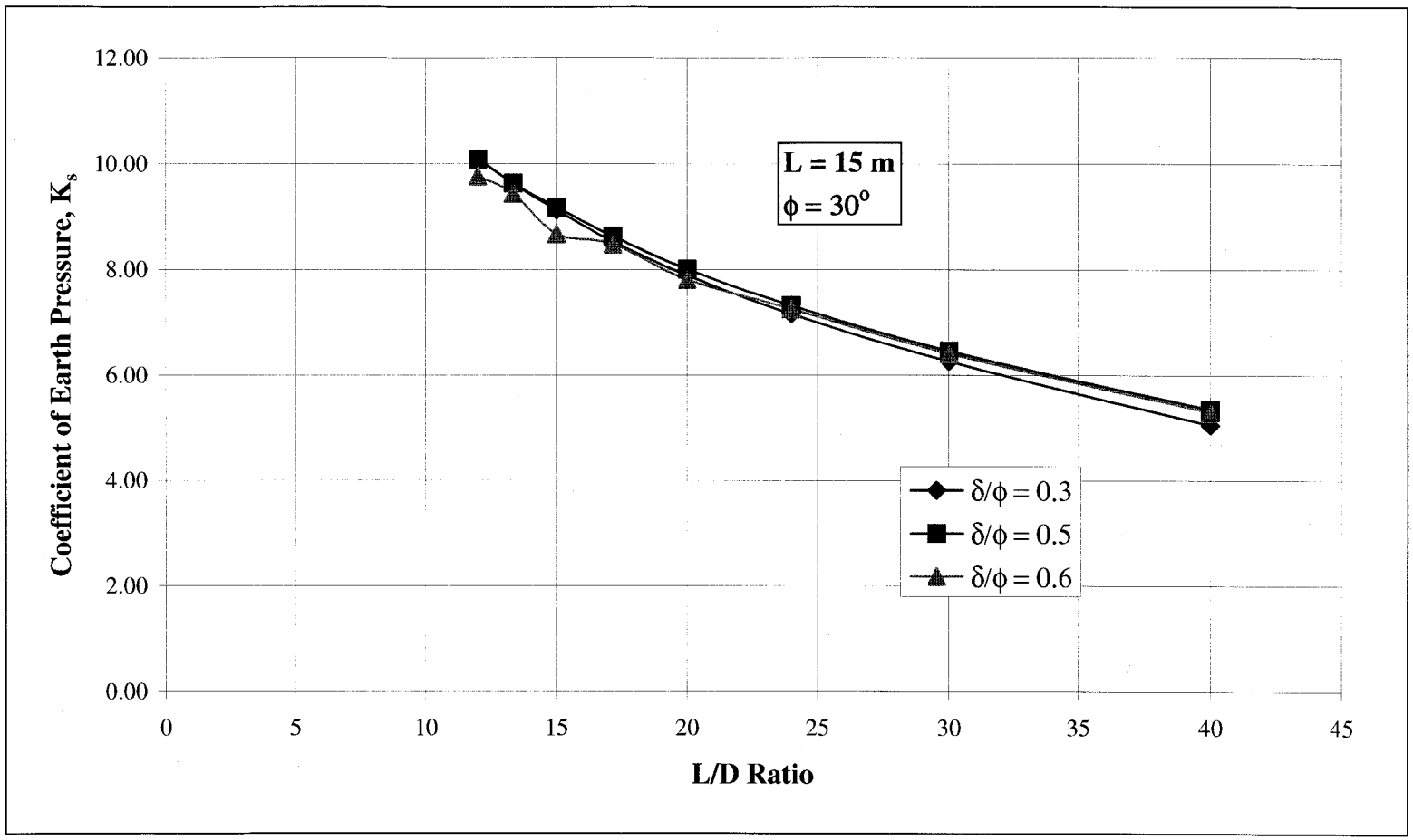

Figure 3.48 Coefficient of earth pressure, K_s versus L/D ratio

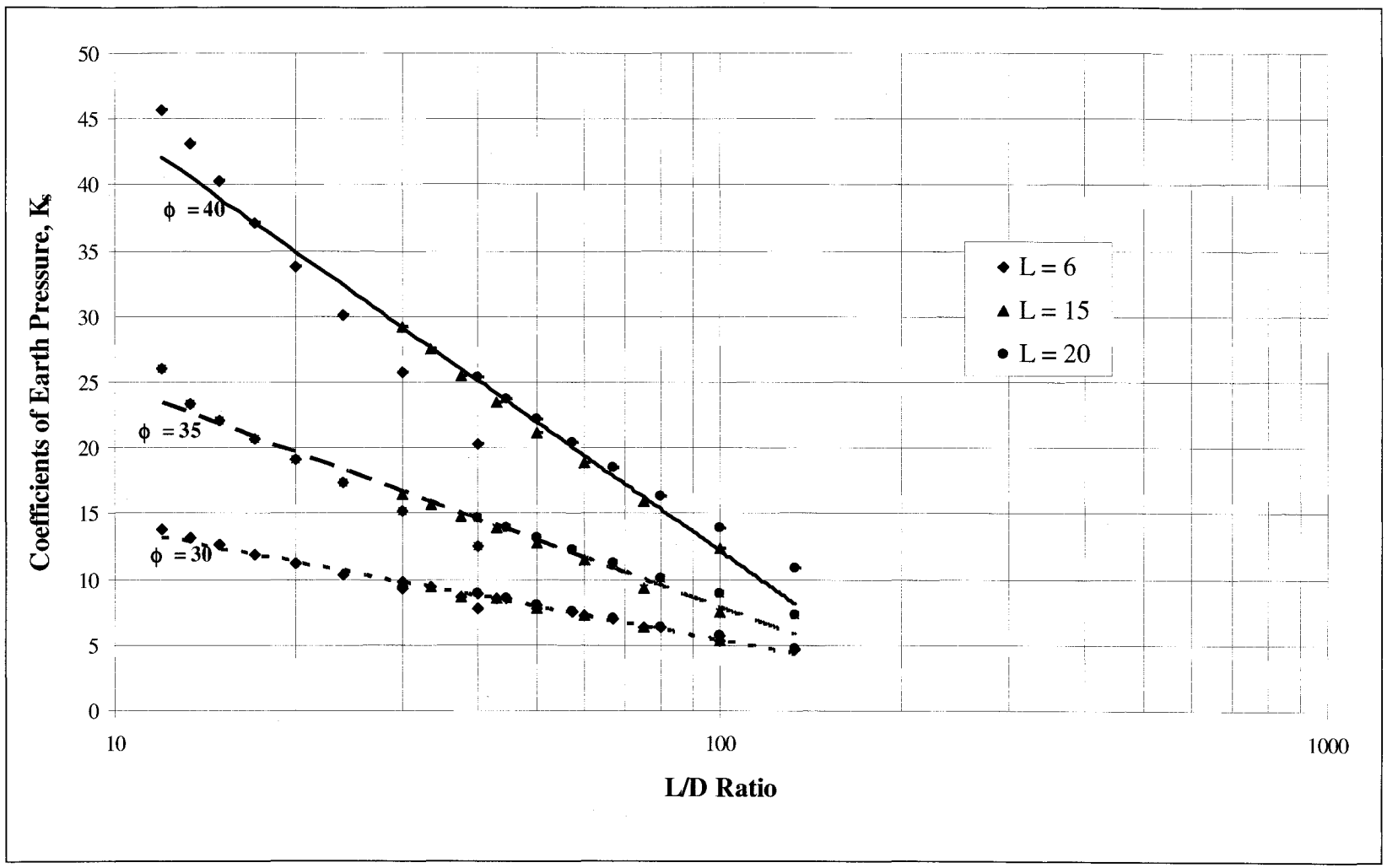

Figure 3.49 Coefficient of earth pressure versus L/D

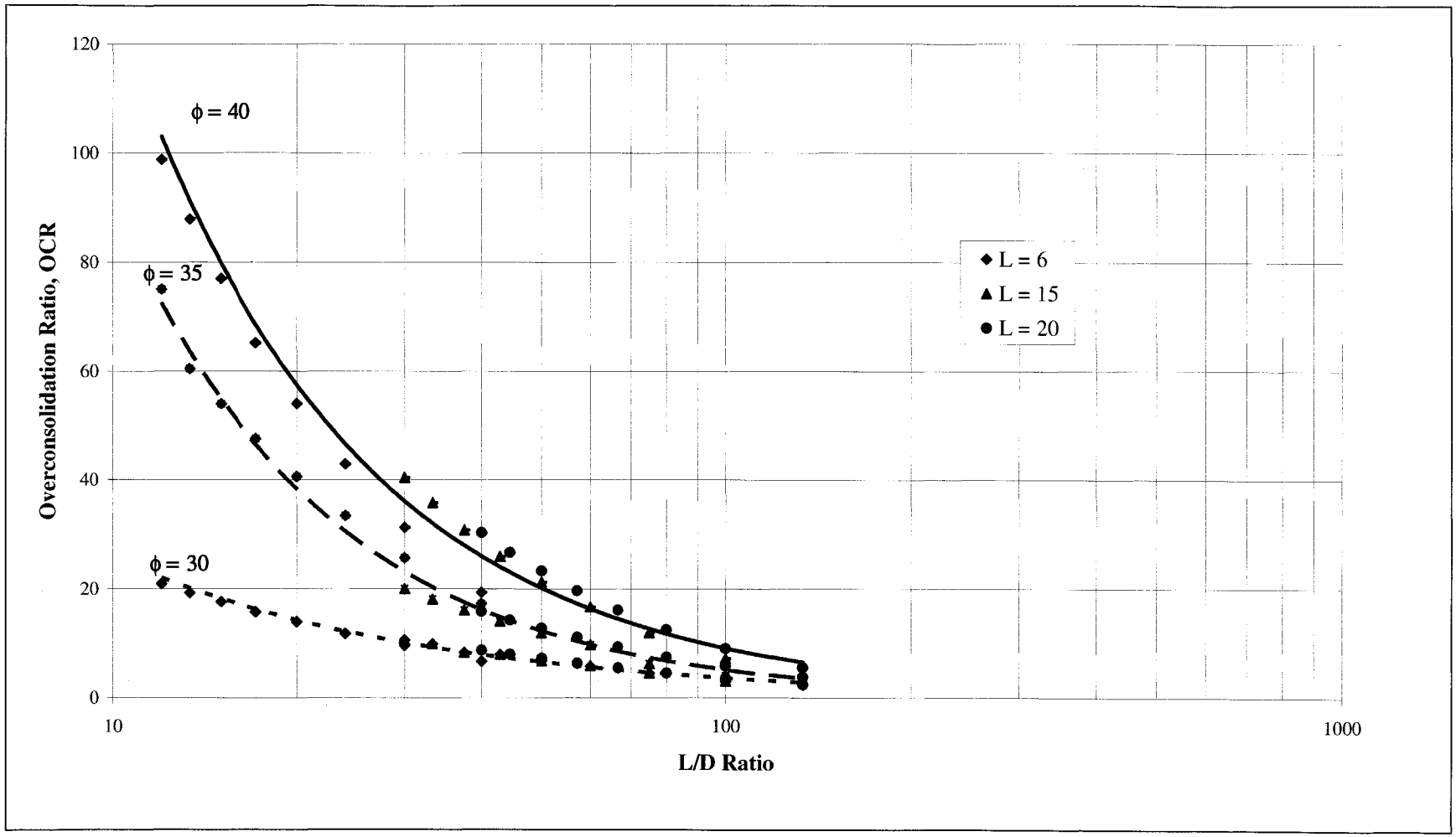

Figure 3.50 Overconsolidation ratio versus L/D

3.6 Effect of Pile Installation on Group Action

3.6.1 Horizontal Strain

The objective of this study was to evaluate the soil behaviour to the pile installation process at different zones. Figure 3.51 presents the horizontal displacements measured at selected horizontal sections along the pile shaft. It can be noted from this figure that the effect of pile installation is uniform along the entire depth of the pile except near the tip. This is due to the fact that at the tip zone, the soil is subjected to both horizontal and vertical movements, resulted from the downward movement of the pile. This movement causes arching effect around the pile's tip (Robisky et al. 1964). It can be noted from Figure 3.52 that large piles in diameter affect a larger area than that of smaller piles. To put this in a general relation Figure 3.53 is introduced. From this chart it will be fair to say that for a pile driven in a soil having an angle of shearing resistance of 30, whatever the diameter is, that after 4D from the pile axis the effect of installation is minimum. From Figure 3.54 it is possible to note the effect of installation in different sand strength starting from sand having an angle of shearing resistance of 30^{o} to a maximum of 40^{o}. Figure 3.55 summarizes the horizontal displacement resulted from driven piles. By knowing the value of ϕ the value of R/D can be estimated where R is the radius of the zone where beyond it there is no pile driving effect.

3.6.2 Vertical Strain

Figure 3.56 presents a comparison between the horizontal and vertical displacement along a horizontal section in the soil mass. It can be noted that the vertical displacement is relatively smaller than that of the horizontal displacement. Thus, it can be concluded

that the horizontal displacement is dominating and significant as compare to the vertical displacement. In this analysis, the location of section produced minimum displacement in the soil mass was defined. This data was used to generate a chart presented in Figure 3.55 to assist designer to establish the spacing between piles in pile groups and soil improvement applications.

3.6.3 Pile Group Calculation

From the above analysis it was possible to utilize the numerical results in producing a method to predict the pile group capacity. From the theory of cavity expansion it is known that a particle of soil "x" located at a distance r_o from the pile axis moves to a distance "r" after pile installation where a change in radial stresses on this particle "σ_r" will be resulted and a change of horizontal stresses on the pile shaft "σ_R" will occur (Clemente and Sayed 1991).

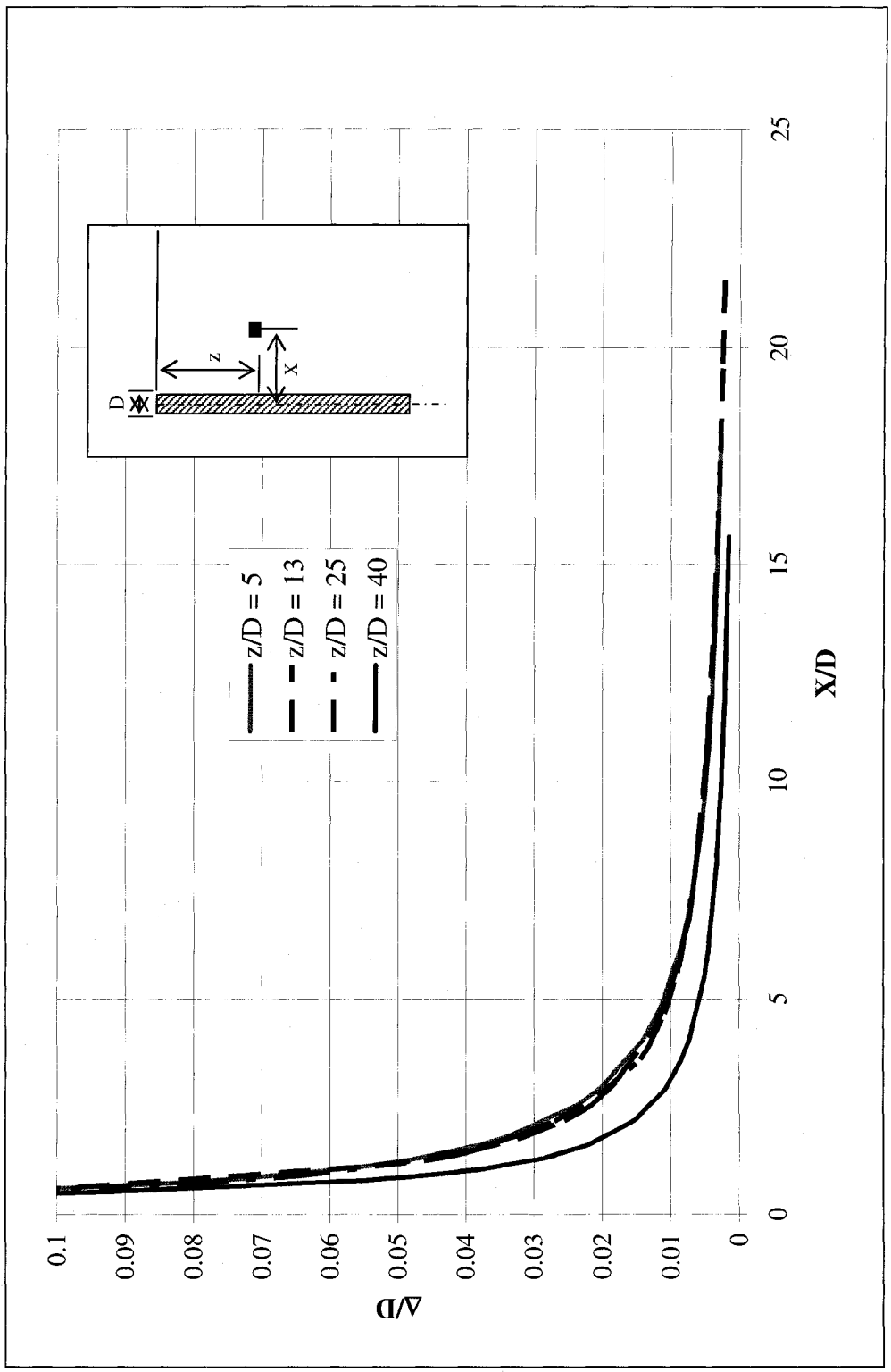

Figure 3.51 Soil displacement along horizontal cross sections (6m pile).

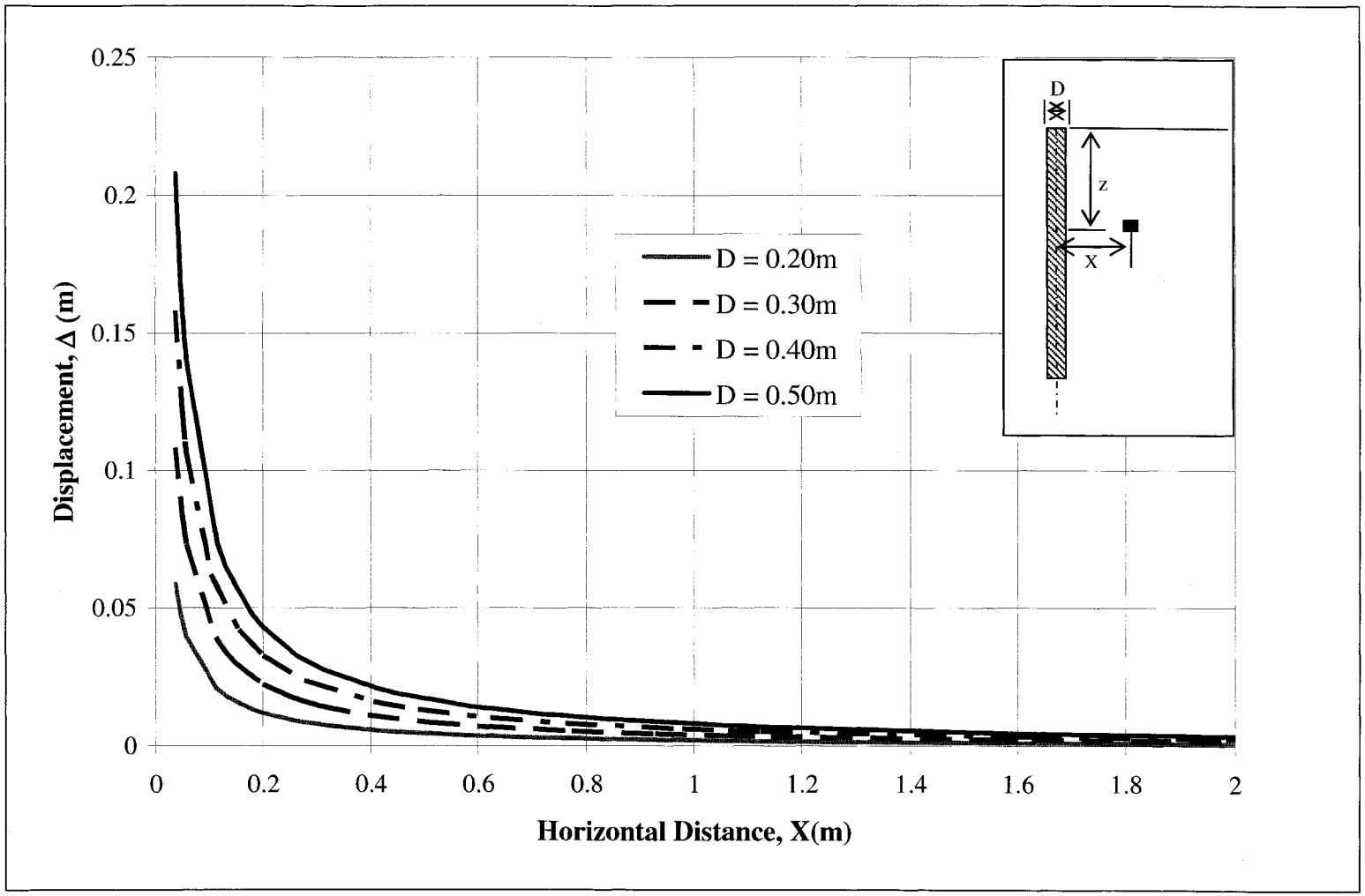

Figure 3.52 Soil displacement along a horizontal cross sections (ϕ = 30).

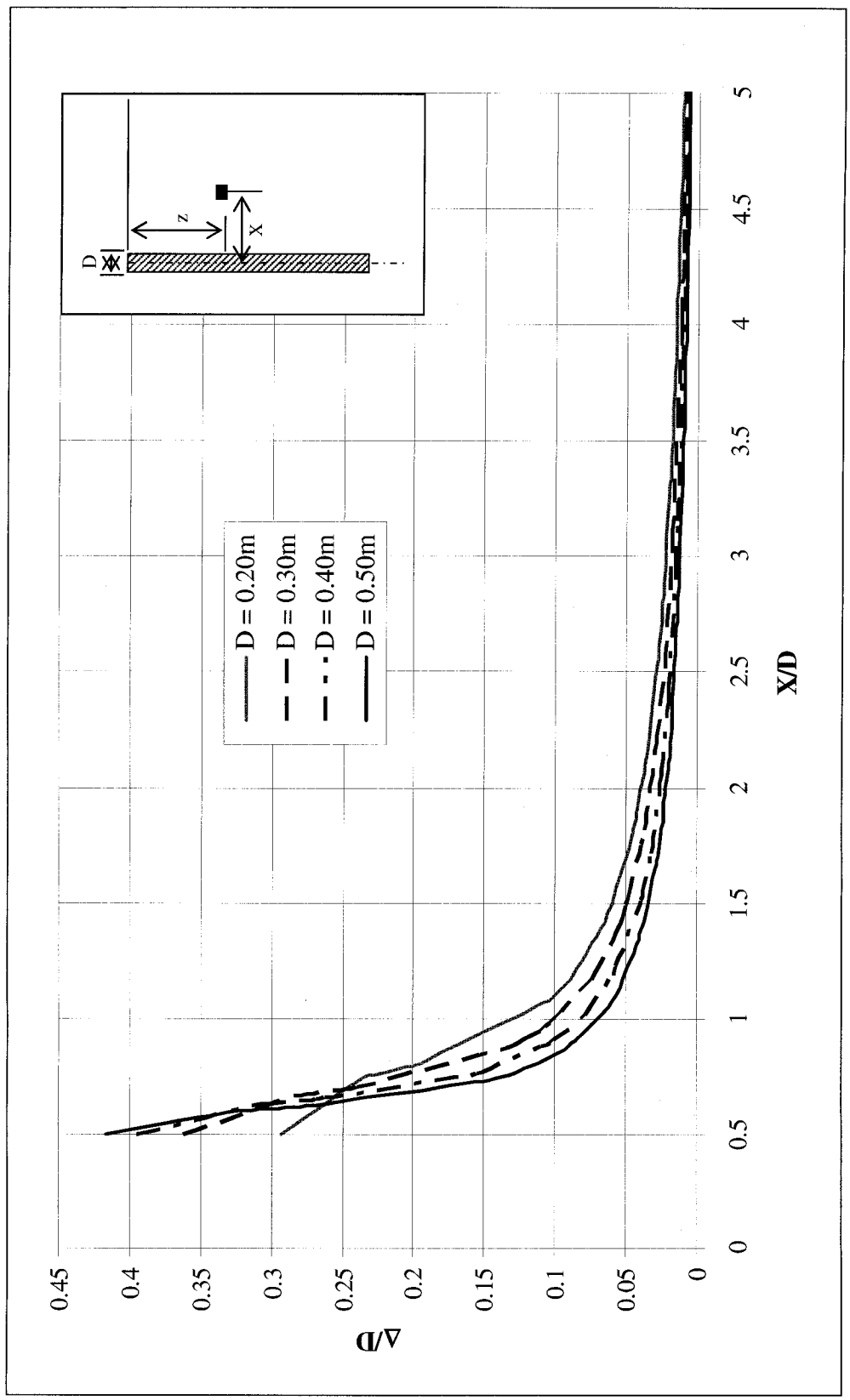

Figure 3.53 Soil displacements along a horizontal cross sections versus pile's diameters ($\phi = 30$).

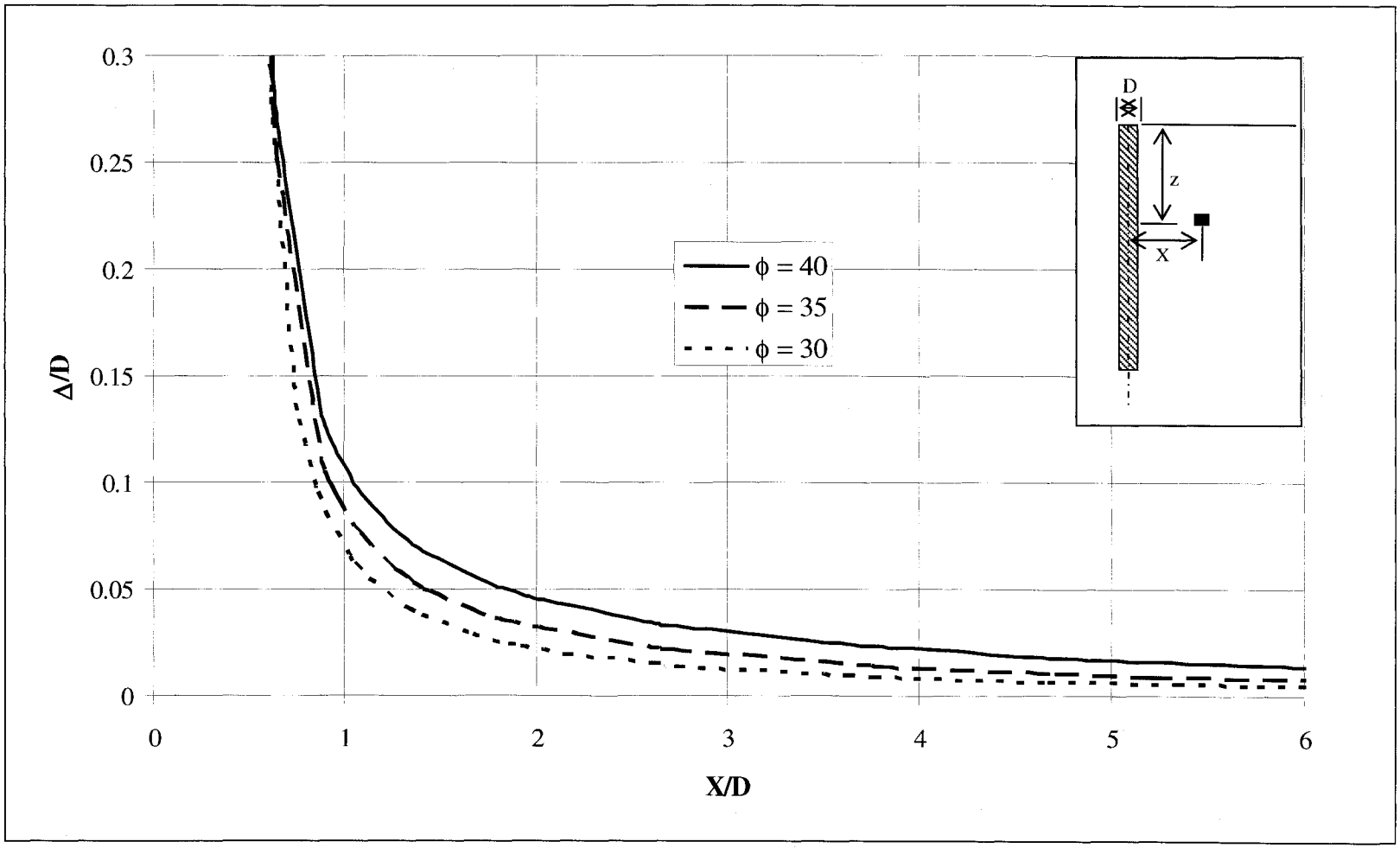

Figure 3.54 Soil displacements along horizontal cross sections for different soil strength.

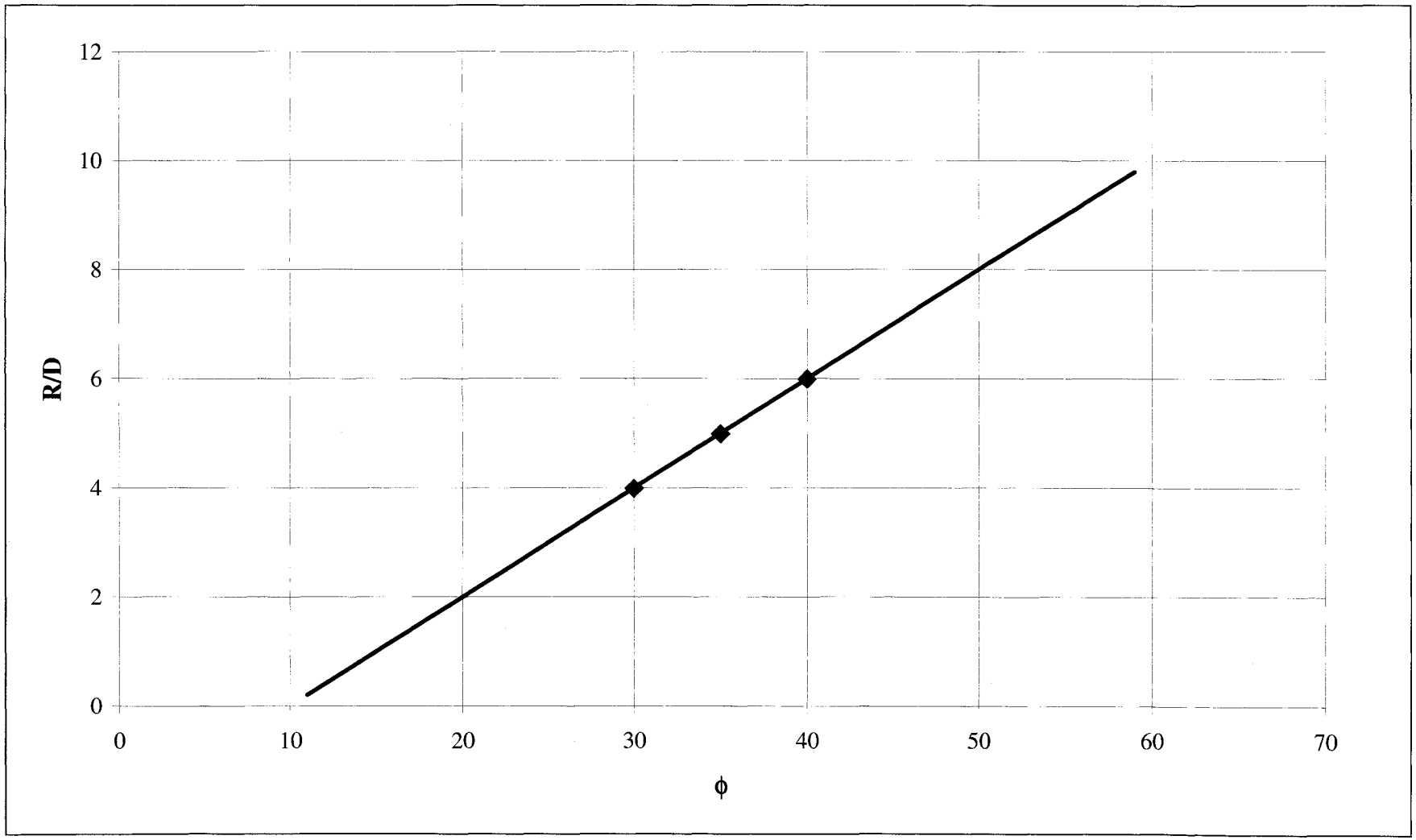

Figure 3.55 Radius of influence versus the angle of shearing resistance, ϕ.

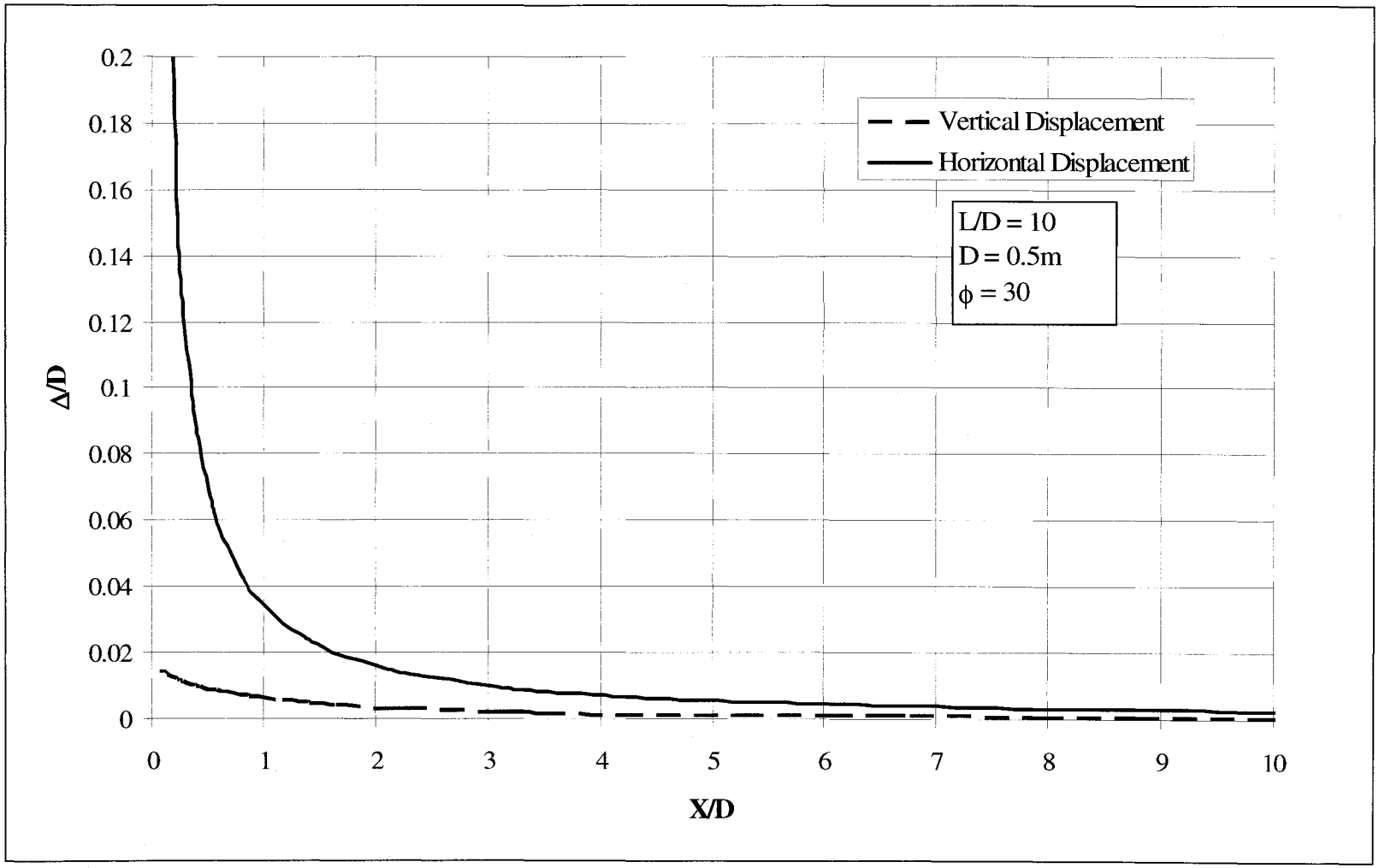

Figure 3.56 A comparison between the amount of Horizontal displacement and vertical displacement.

Where:

$$\sigma_R = (K_s - K_o)\,\sigma_v \qquad \sigma_v = \gamma L \qquad (3.10)$$

By plotting the ratio σ_r/σ_R versus r/R where R is the pile radius, a non dimensional chart was produced as presented in Figure 3.57. In this case r is considered the distance between the pile axis and the neighbouring pile. The ultimate group load capacity in this case could be calculated from:

$$Q_g = \sum_{i=1}^{n}\left[(K_s\sigma_v + \Delta\sigma_r)\tan(\delta)A_s + Q_t\right]_i \qquad (3.11)$$

Where "n" is the number of piles in the group, Q_t is the ultimate pile tip capacity of individual piles in the group. $\Delta\sigma_r$ is the increase of horizontal stresses caused from the neighbouring pile as shown in Figure 3.58. For example a pile located in middle of the group (surrounded by four piles) then $\Delta\sigma_r = 4 * \sigma_r$ but if it is located at the corner of the group (Surrounded by two piles) Then $\Delta\sigma_r = 2 * \sigma_r$ and so on. So $\Delta\sigma_r$ can be calculated as follows:

$$(\Delta\sigma_r)_i = \sum_{\substack{k=1 \\ k\neq i}}^{n}(\sigma_r)_k \qquad (3.12)$$

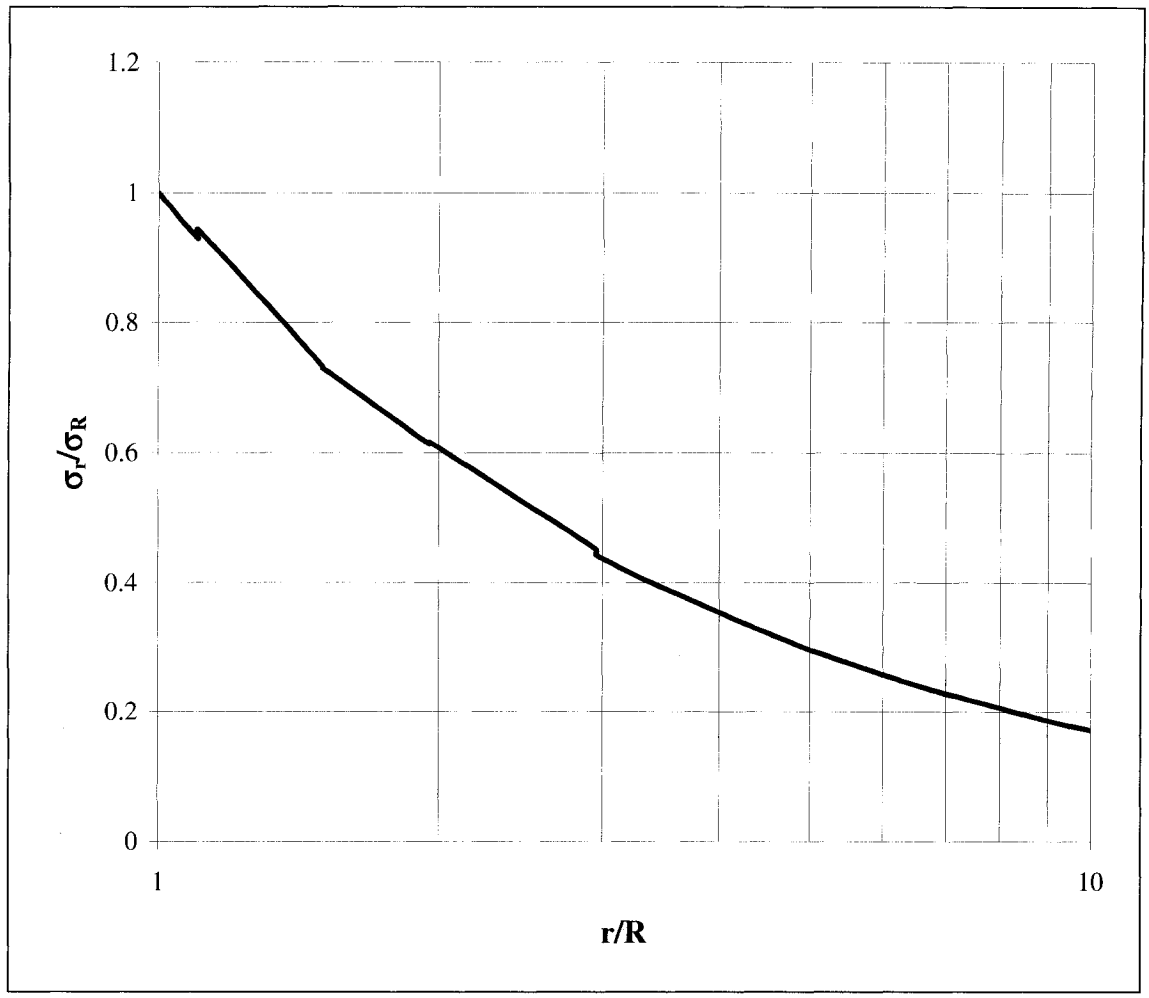

Figure 3.57 Ratio σ_r/σ_R versus r/R.

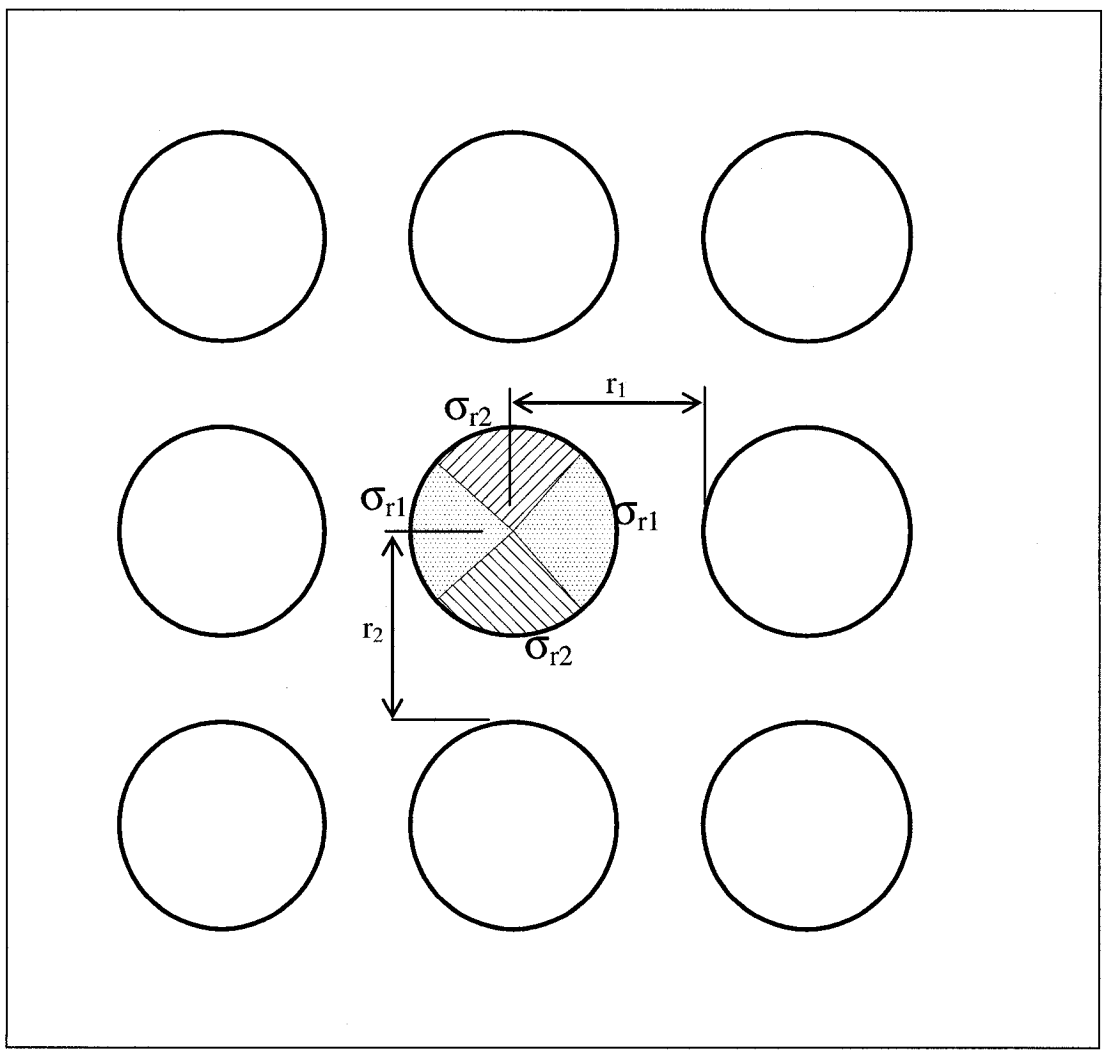

Figure 3.58 Pile group arrangement

3.7 Superiority and Limitations of Driven piles

In this section analysis was performed to demonstrate the superiority of driven piles over the bored pile. Figure 3.59 presents the numerical model for the case of bored pile. The size of the mesh and the boundary conditions were taken similar to that of the driven pile to maintain consistency. The pile material elements filled a hole, which has a diameter equal to pile diameter. The constitutive laws of the soil and the pile material were the same as for the case of driven piles. The pile was then pushed into the soil (Controlled displacement) to failure.

The difference between bored and driven piles can be well investigated by comparing the change in shear stress along the pile length as can be presented in Figure 3.60. The shear stress generated on a bored pile is much less than that of driven piles which gives the driven pile higher capacity compared to the bored pile having the same length and diameter and placed in the same sand medium. On the other hand the high shear stress on driven piles will limit its length especially in medium to dense sand. To find out why driven piles generate higher shear stress on its shaft than that of bored piles a study on the earth pressure is applied taking into account the geometry of the pile (length and diameter) and the sand property (angle ϕ).

The earth pressure acting on the pile is highly affected by the insitu stresses in the surrounding soil. From the previous analysis of driven piles it was found that the value of K_s was within the passive zone, which gives a high indication how the insitu stresses are disturbed due to the driving of the pile. Bored piles are known to cause no displacement to the soil, and accordingly, the coefficient of earth pressure is assumed to be at the rest state. The change in earth pressure along the pile length is presented by K_b/K_o in Figure

3.61. Where K_b is the coefficient of earth pressure along the bored pile length and K_o is the coefficient of earth pressure at rest. It can be noted that there is no significant change in earth pressure along the pile length whether it is long pile (20m) or short pile (6m) other than slight increase near the ground surface which doesn't have any effect on the shear resistance due to the low overburden pressure in this area. Usually in the site the value of K at the surface is higher than that in the ground due to high over consolidation ratio which generated due to loading the pile since the soil particles are free to move and they tend to move downward with pile.

Figure 3.62 presents the variation of value K_b/K_o along the pile length for a range of pile diameters. As presented earlier driven pile diameter is directly proportion to the earth pressure and contributes to the shaft resistance. Bored pile showed no effect from increasing the pile diameter. This is because there is no lateral displacement for the soil particles due to installing the pile. The soil around the bored pile is kept theoretically in its original place after the pile is in place.

Figure 3.63 presents the variation of value K_b/K_o along the pile length for a range of angle ϕ. Similarly it can be noted that bored piles in sand do not contribute to any changes in the insitu stresses.

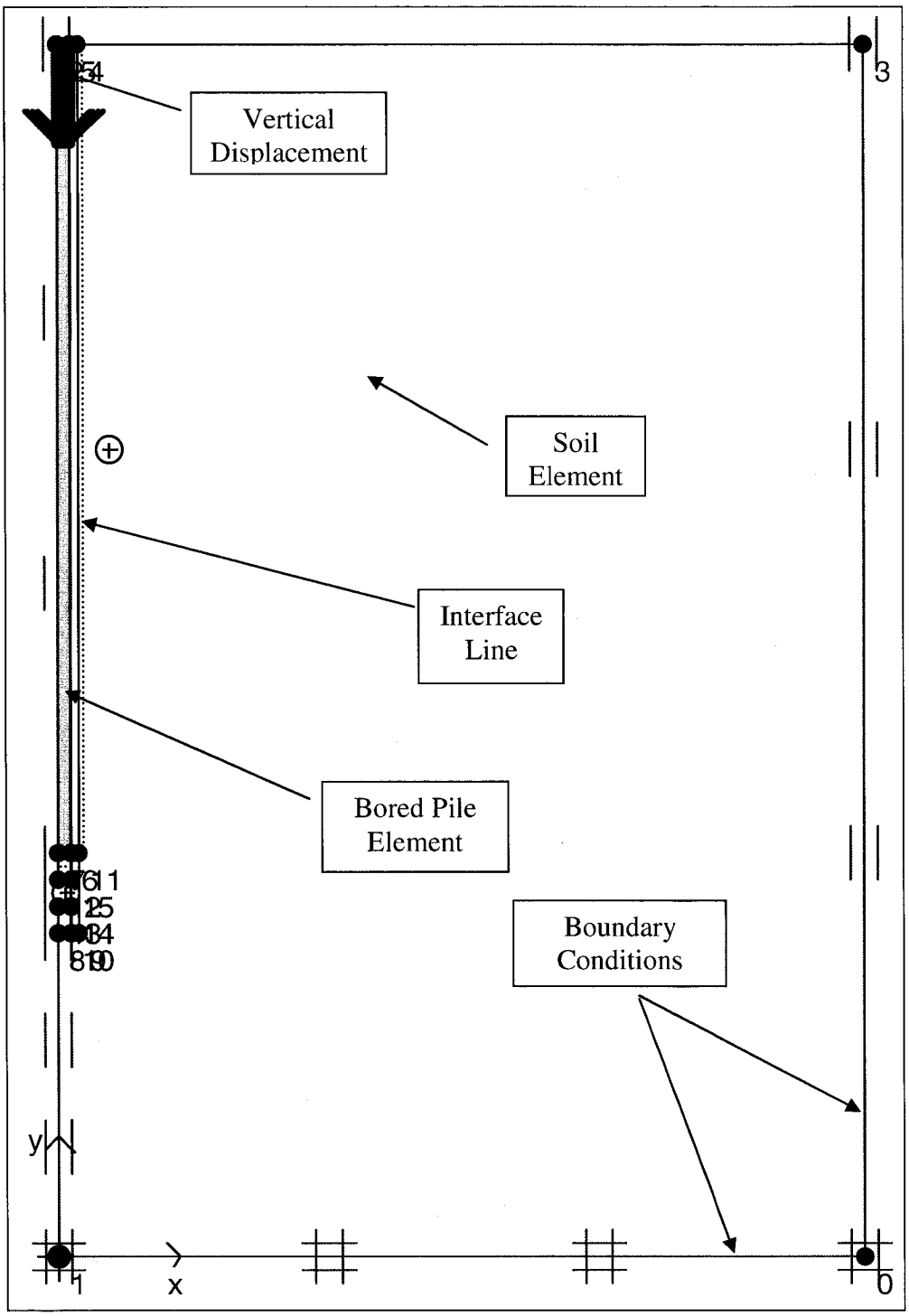

Figure 3.59 Bored Pile Model.

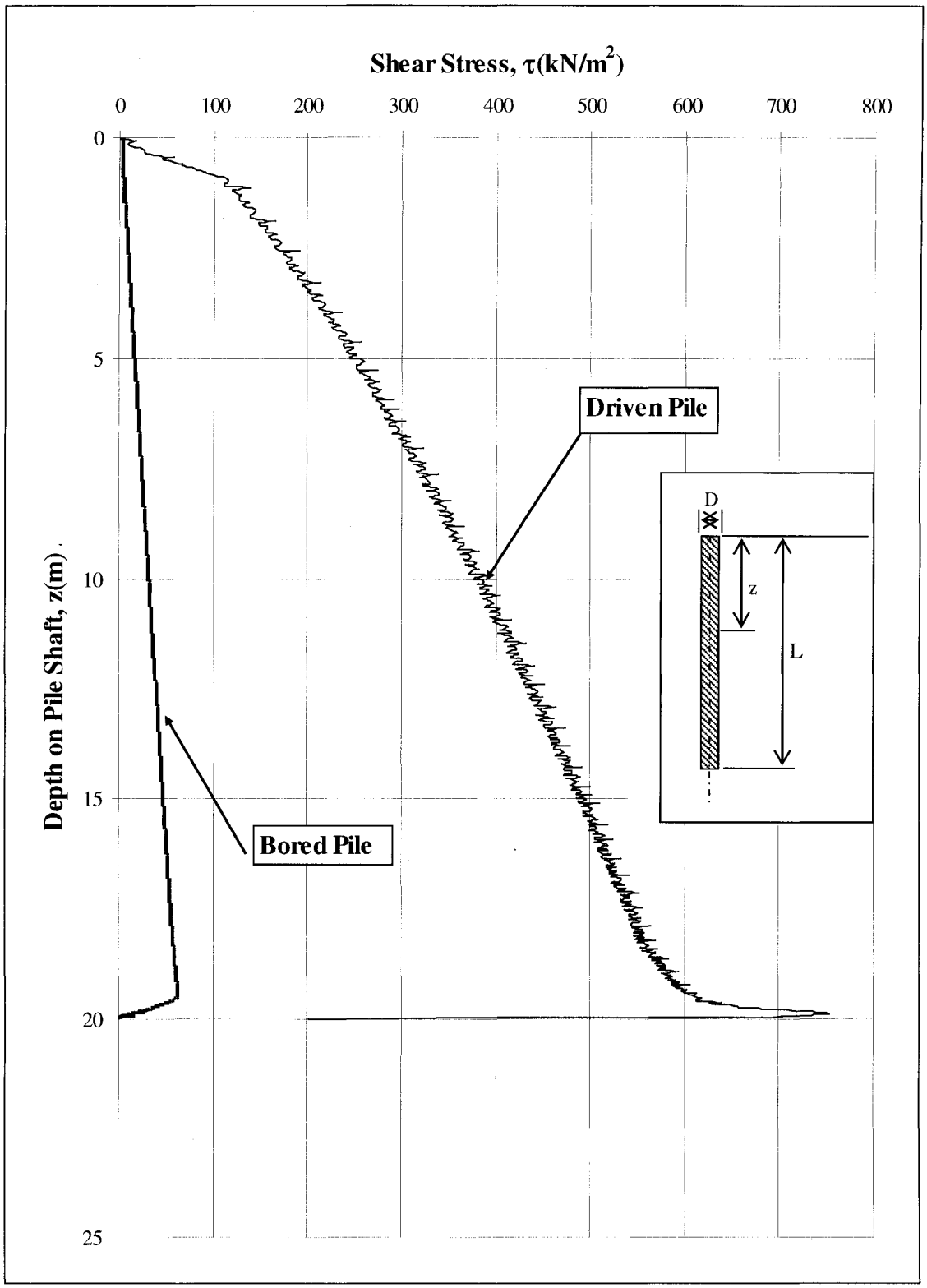

Figure 3.60 Shear stress for a bored and a driven pile (D= 0.30m, $\phi = 30^{o}$).

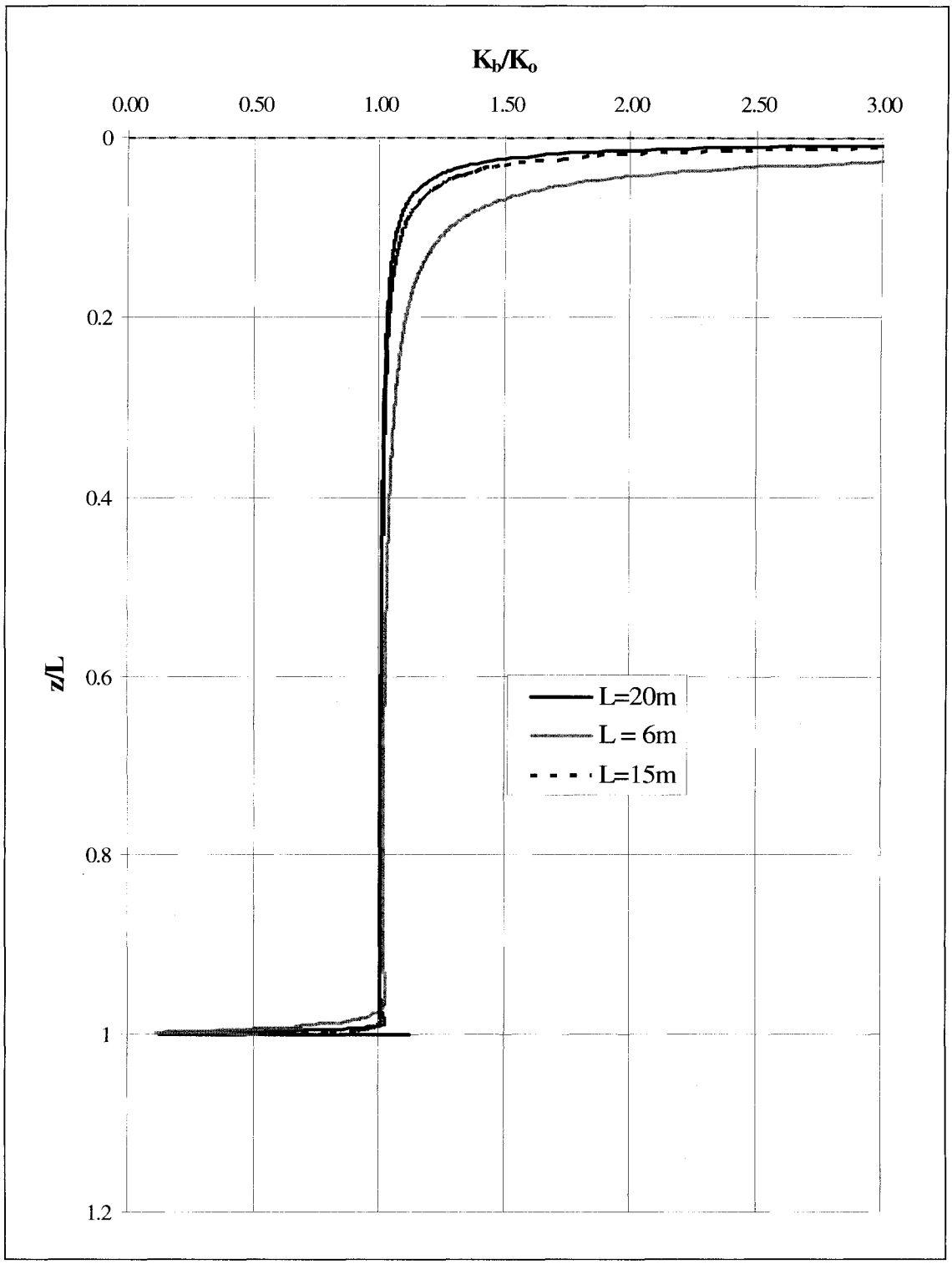

Figure 3.61 Typical distribution of ratio K_b/K_o with respect to z/L.

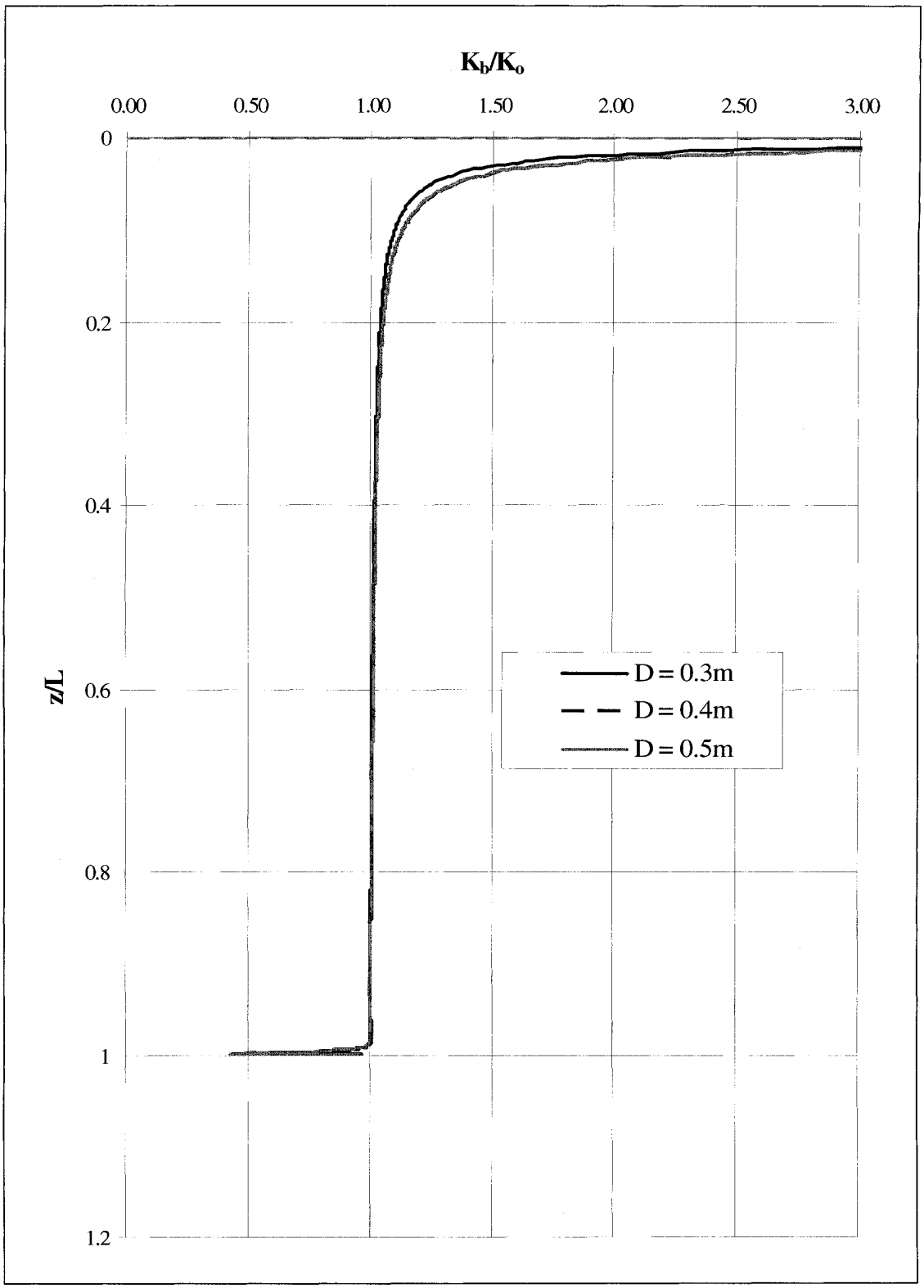

Figure 3.62 Typical distribution of ratio K_b/K_o with respect to z/L.

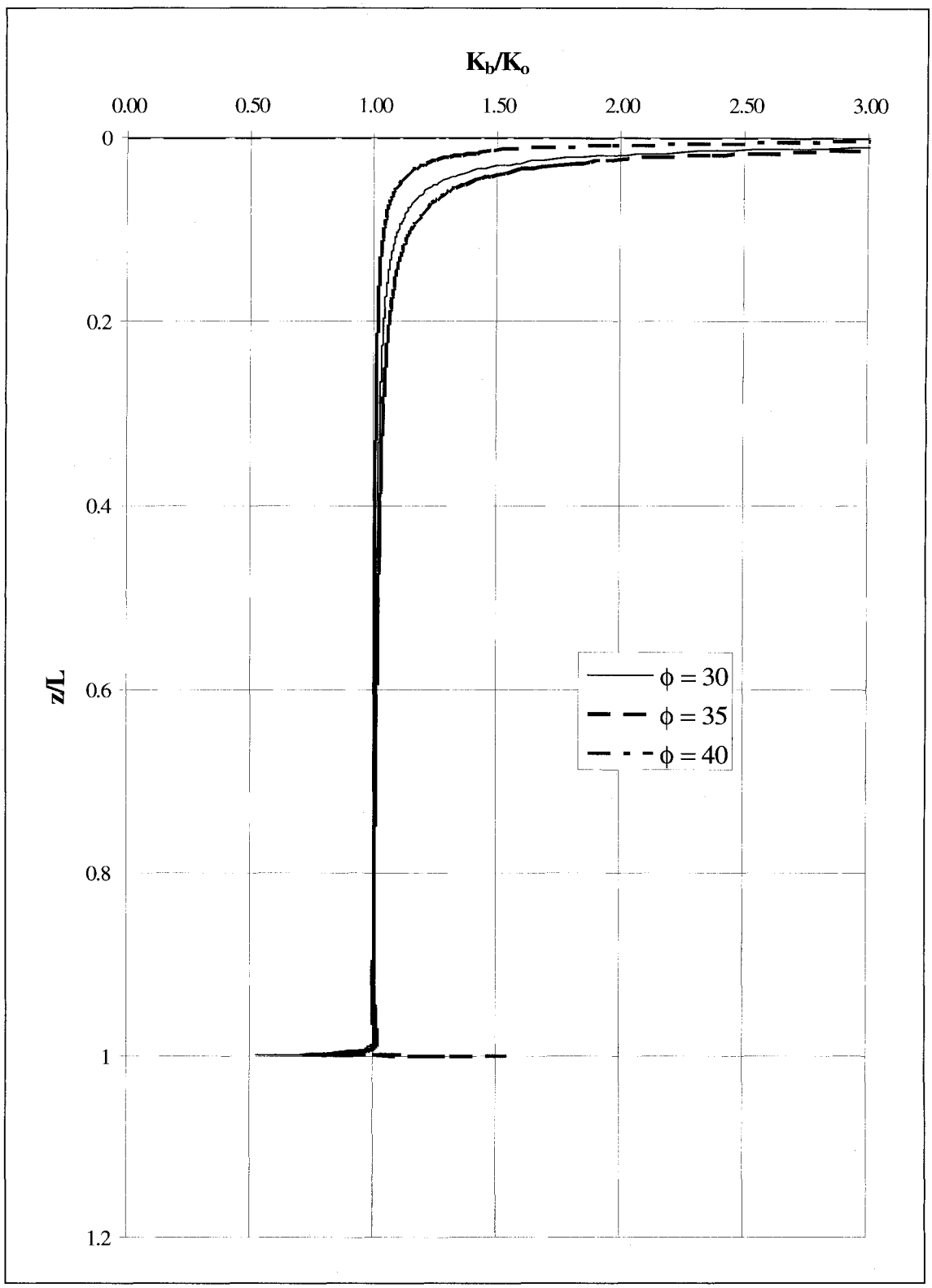

Figure 3.63 Typical distribution of ratio K_b/K_o with respect to z/L.

As it shown above that the insitu stresses around bored piles are not affected by the pile length, diameter and sand type. Although driven piles have some advantages over bored pile but still there is limitation for using them in practice.

Based on the above analysis, it was possible to give a limitation of driving piles in sand based on the following:

1. The pile diameter
2. The pile length
3. The pile material
4. Surface roughness of the pile surface (δ/ϕ)
5. The angle of shearing resistance of sand

From analyzing the results generated from the numerical model charts were created in Figure 3.64 to 3.66 showing the maximum L/D could be achieved for a given pile diameter and angle of shearing resistance ϕ. These charts give guidance for selecting and predicting the refusal depth of piles during their installation. Driven piles used in construction are mainly made of two materials either concrete or steel. Concrete piles are much weaker than steel piles when it comes to driving in sand. In general, the strength of concrete used in driven piles does not exceed 50MPa. The charts produced are based on this strength to show limitations for driving concrete piles in sand taking into account the above factors.

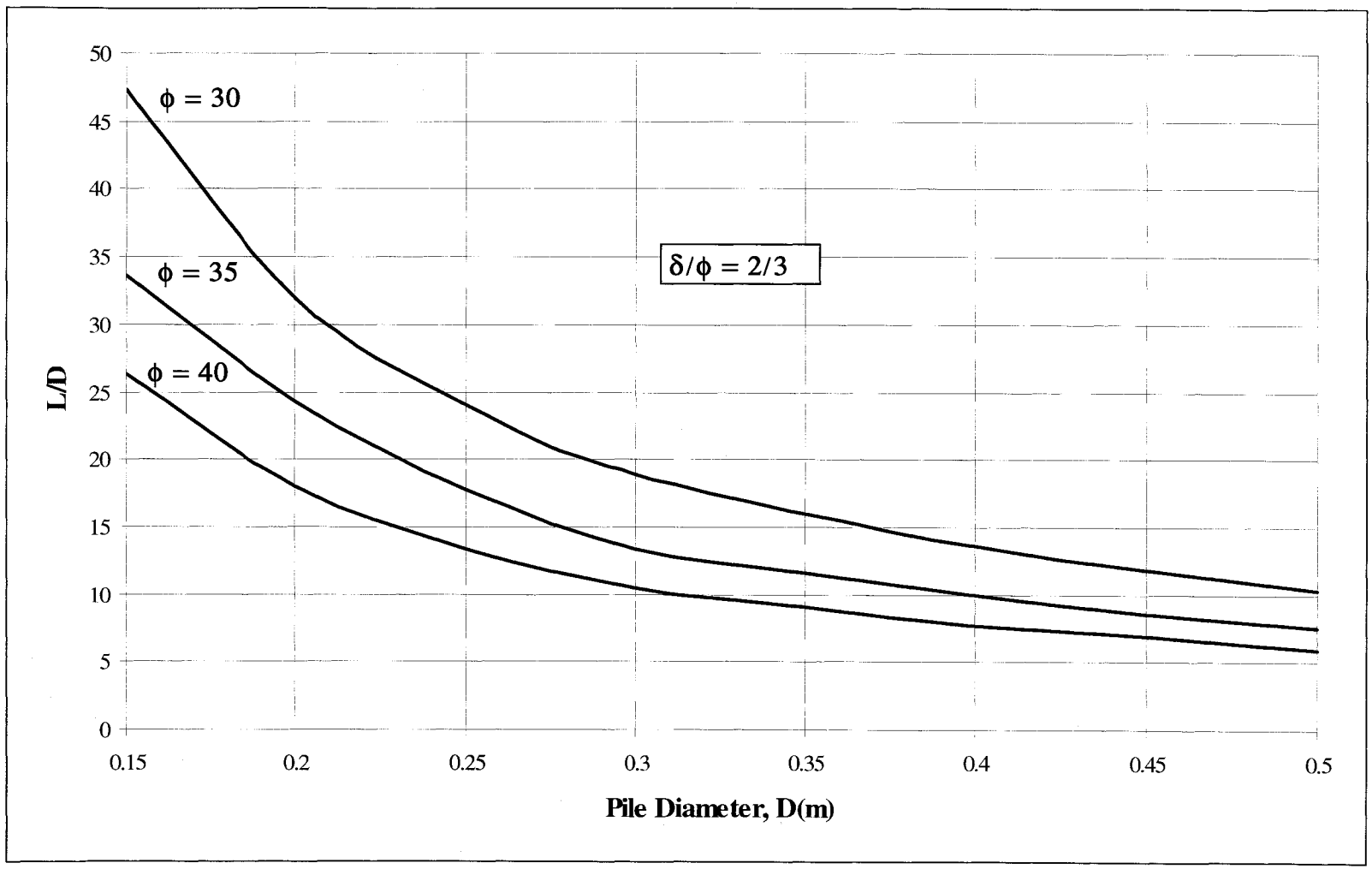

Figure 3.64 Pile driving limitation chart for $\delta/\phi = 2/3$ ($f_c = 50MPa$).

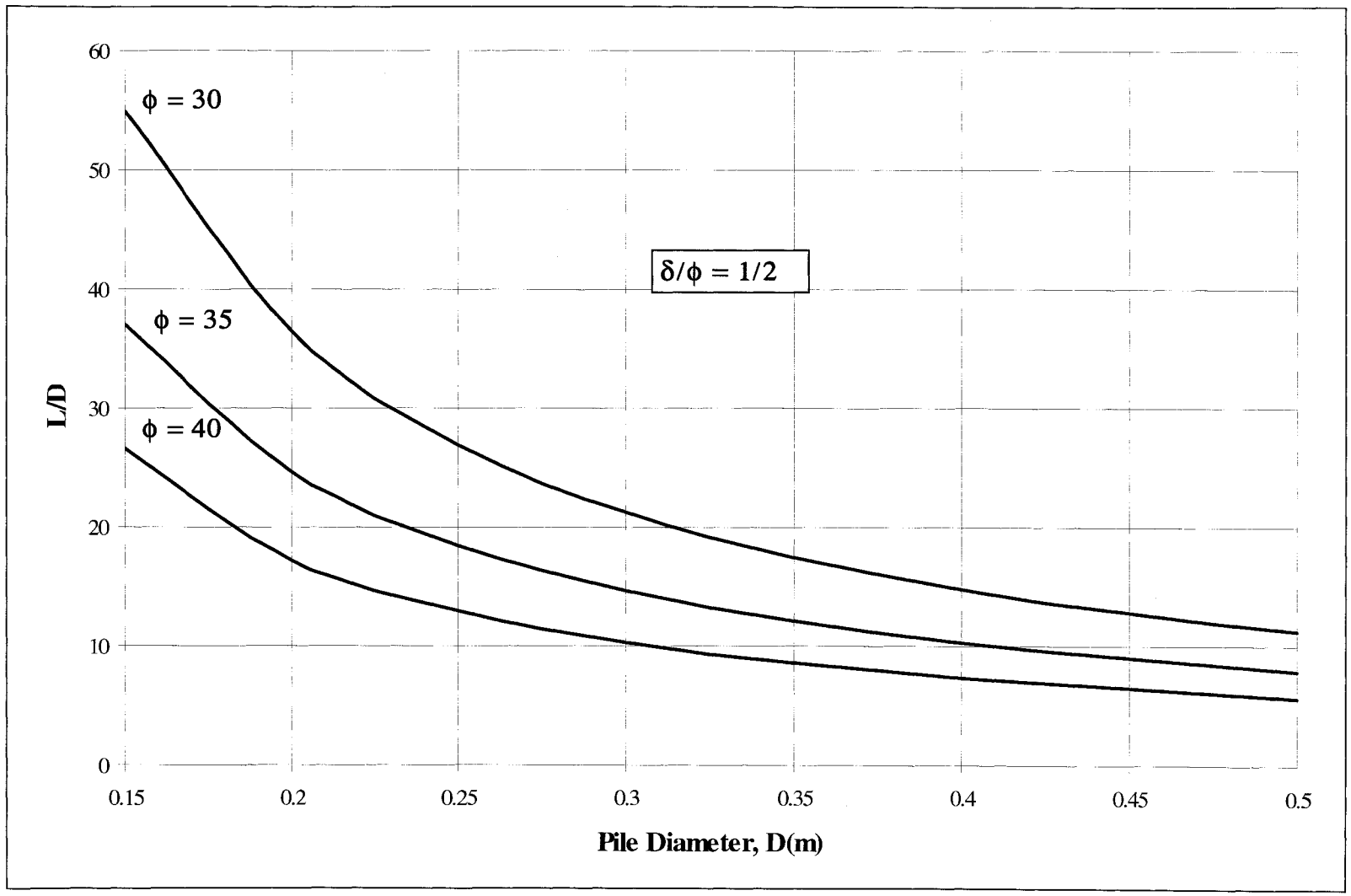

Figure 3.65 Pile driving limitation chart for $\delta/\phi = 1/2$ ($f_c = 50MPa$).

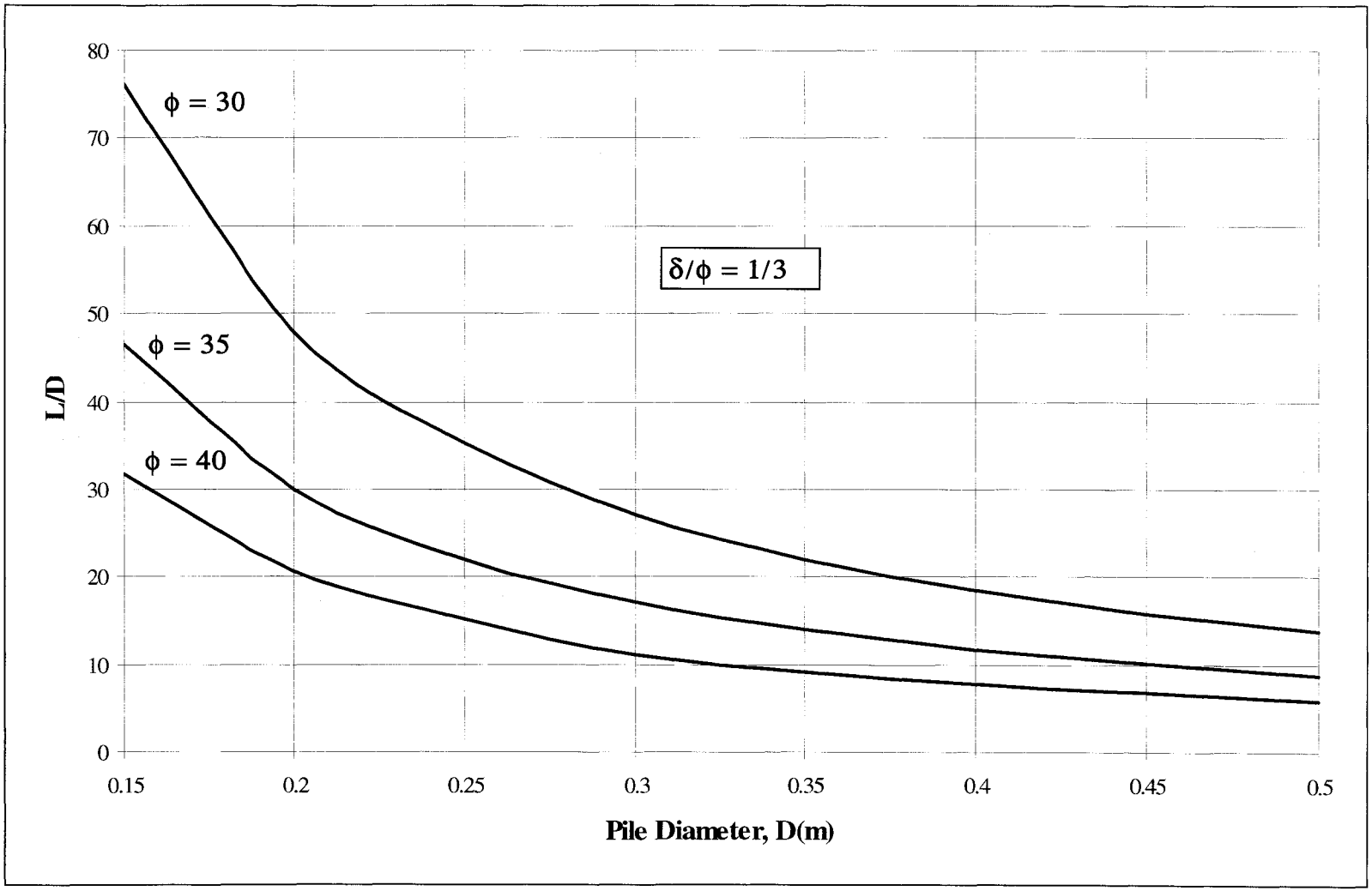

Figure 3.66 Pile driving limitation chart for $\delta/\phi = 1/3$ ($f_c = 50MPa$).

From these charts it is possible to predict the location of the refusal depth for a range of pile diameters starting from 0.15m – 0.50m having a surface roughness range from δ/ϕ = 1/3 – 2/3 driven in sand having an angle of shearing resistance from 30 – 40 degrees. From the charts it is evidence that when the diameter of the pile increases the shallower depth of the pile will be reached, and the more smoother the pile's shaft the deeper the pile can be installed and finally the higher the soil strength the pile length will significantly reduced until a limit where shallow foundation will be more suitable and economical. It is also clear from the chart that piles having a 0.5m pile diameter can be taken as a maximum in terms of unit pile capacity q_u after that the increase of the pile diameter has no major effect since the earth pressure generated from the cavity expansion due to installation reached its ultimate value. If the designer finds that the precast concrete pile will not satisfy the loading condition then the next alternative is to switch to steel shafts, which have a higher capacity reaching 300MPa based on the wall thickness and outer diameter. For higher values of L/D then the buckling, which will occur in long piles will govern the choice of the pile geometry. This could be done in a separate study since it is not in the scope of the current investigation.

The charts indicated above provide a guideline for driven pile selection based on diameter and length according to the soil condition available in site, it is also possible to control the surface finish of the precast concrete during fabrication to determine the surface roughness of the pile.

CHAPTER 4
ANALYTICAL MODELS

4.1 General

The deduced failure pattern and influence zones from the results of the numerical model were idealized herein. In this chapter, analytical models will be developed to simulate the pile installation process and the loading condition. Accordingly, the theory developed incorporates the parameters, which were overlooked in the previous theories.

4.2 Analytical Models

The pile capacity, Q_u is made of two components, one is generated from the friction along the pile's shaft, which is called the shaft resistance, Q_s and the second component is generated from the base resistance, Q_t. Thus:

$$Q_u = Q_s + Q_t \tag{4.1}$$

Although the two components are interdependent on each other (Hanna & Nguyen, 2002 and 2003), quit often designer evaluates each component separately.

4.2.1 Analytical model based on zone of influence

The observed zone of influence from the numerical model developed in the present investigation consisted of an inverted bell shape around the pile axis is used in this chapter to develop an analytical model (Figure 4.1). This zone constitutes the failure mechanism, which will take place around the pile's shaft at the ultimate point. By applying the limit equilibrium method of analysis, the ultimate capacity of the pile can be determined, which takes into account the pile installation and loading conditions. The observed failure mechanism was idealized in a dimensional format in this chapter as follows (Figure 4.2):

1. The upper section (a-b), which was created from logarithmic spiral curve, which is tangent to the ground level and terminates at the middle of the pile length.
2. The lower section (b-c), which was created from a straight line making an angle ($\theta = \pi/4-\phi/2$) with the horizontal and is tangent to the logarithmic spiral at the upper section and ends at the tip level.
3. The base section is an integrated part of the model plane and it effects the dimensions of the lower and uppers sections. The base section is created from a cone wedge (edf) having a tip angle ($\pi/2-\phi$) (Meyerhof 1951) and a logarithmic spiral connecting (d-c).

The zone of influence plane revolves around the pile axis creating an axisymmetrical stress condition. The geometry of the plane is defined starting from the base section ending at the ground surface as follows:

$$(df) = r'_o = \frac{D}{2\cos(\pi/4+\phi/2)} \qquad (4.2)$$

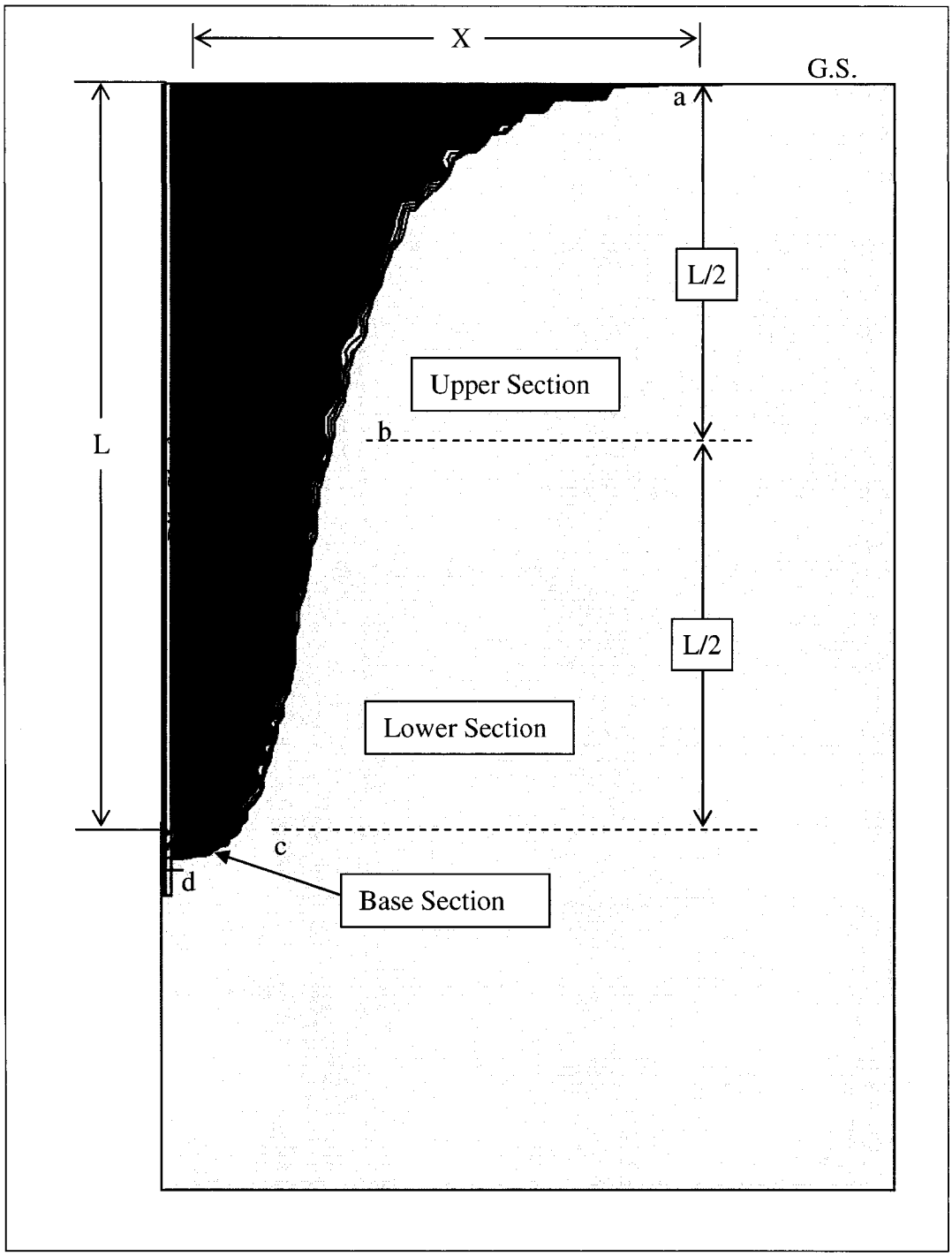

Figure 4.1 Observed zone of influence from the numerical test results.

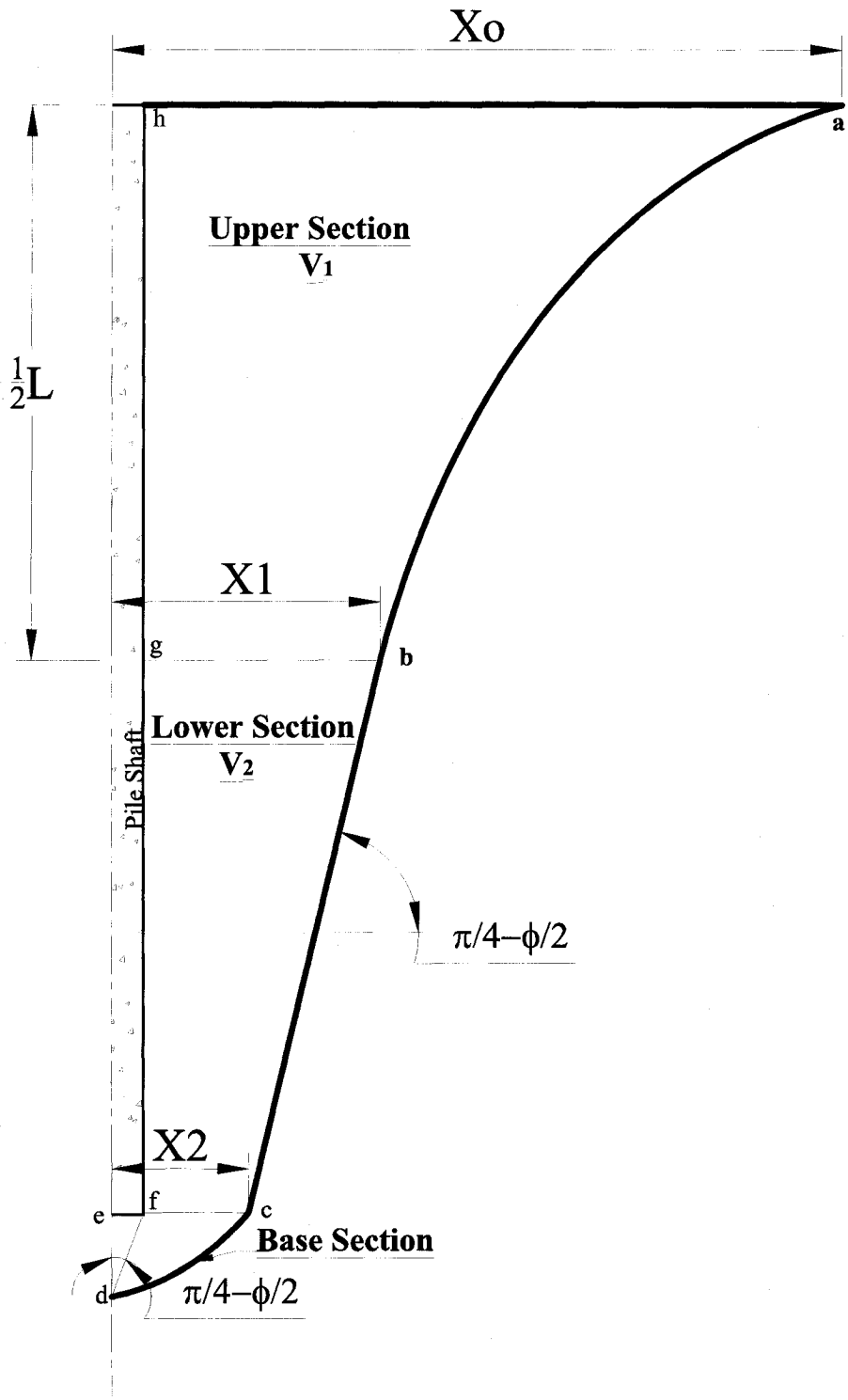

Figure 4.2 Sketch of the proposed zone of influence around a single pile in sand.

The equation representing the log-spiral curve is given as follows:

$$r_w = r'_o \, e^{\omega \tan\phi} \tag{4.3}$$

Where:

r_ω = radius of log-spiral at an angle ω

$$X_2 = r'_o \, e^{(3/4\,\pi - \phi/2)\tan\phi} + D/2 \tag{4.4}$$

Substitute (4.2) in (4.4) then:

$$X_2 = \frac{D}{2}\left(\frac{e^{(3/4\pi-\phi/2)\tan\phi}}{2\cos(\pi/4+\phi/2)}+1\right) \tag{4.5}$$

Considering the plane (c-b); a straight line having an angle ($\theta^* = \pi/4-\phi/2$), then:

$$X_1 = X_2 + 1/2L \tan(\pi/4-\phi/2) \tag{4.6}$$

Since the upper section is taken as a logarithmic spiral tangent to line (c-b) and tangent to the ground surface then it can be defined as follows (referring to Figure 4.3):

$$X_o = X_1 + X'' + X''' \tag{4.7}$$

X_1 can be determined from Eq (4.6).

$$X'' = r_1 \sin(\alpha_2) \tag{4.8}$$

Where:

$$r_1 = r_o \, e^{\alpha 1 \tan\phi} \tag{4.9}$$

r_o can be defined as follows:

$$½\,L = r_2 \cos(\alpha_3) - r_1 \cos(\alpha_2) \tag{4.10}$$

$r_2 = r_o \, e^{\alpha 4 \tan(\phi)}$ put $\alpha = e^{\alpha 4 \tan(\phi)}$

$r_1 = r_o \, e^{\alpha 1 \tan(\phi)}$ put $\beta = e^{\alpha 1 \tan(\phi)}$

$$L_1 = \alpha \, r_o \cos\alpha_3 - \beta \, r_o \cos\alpha_2 \qquad L_1 = ½\,L \tag{4.11}$$

Then

$$r_o = L_1 / (\alpha \cos \alpha_3 - \beta \cos \alpha_2) \quad (4.12)$$

Furthermore,

$$\alpha_2 = \theta - \phi \quad (4.13a)$$

$$\alpha_1 = \pi - \alpha_2 \quad (4.13b)$$

$$\alpha_3 = \phi \quad (4.13c)$$

$$\alpha_4 = \alpha_1 + \alpha_2 + \alpha_3 \quad (4.13d)$$

X″ can be calculated by substituting Eqs (4.11) & (4.12) in (4.8)

$$X''' = r_2 \sin \phi \quad (4.14)$$

Substituting the values of X″ and X‴ in Eq. (4.7):

$$X_o = X_1 + r_1 \sin (\alpha_2) + r_2 \sin \phi \quad (4.15)$$

The center of the logarithmic spiral connecting (b-c) can be located as follows

Horizontally from the pile axis = $X_1 + X''$ (4.16)

Vertically from the ground surface = $L_1 + r_1 \cos (\alpha_2)$ (4.17)

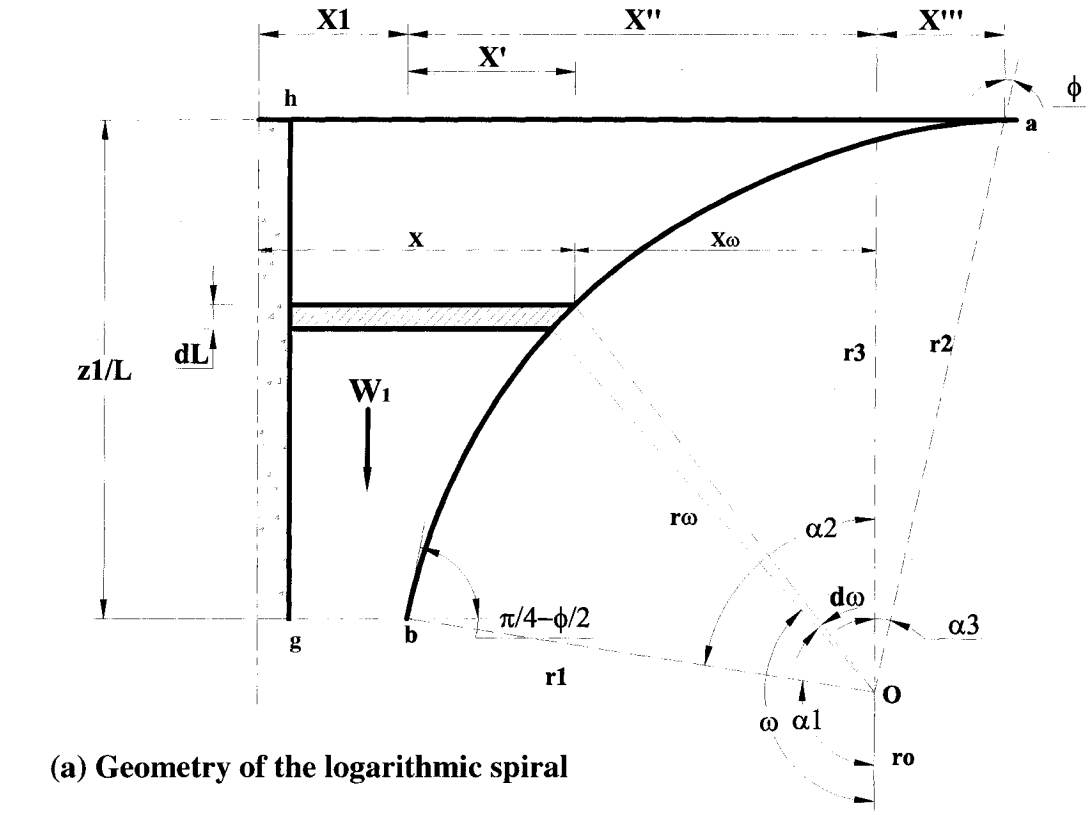

(a) Geometry of the logarithmic spiral

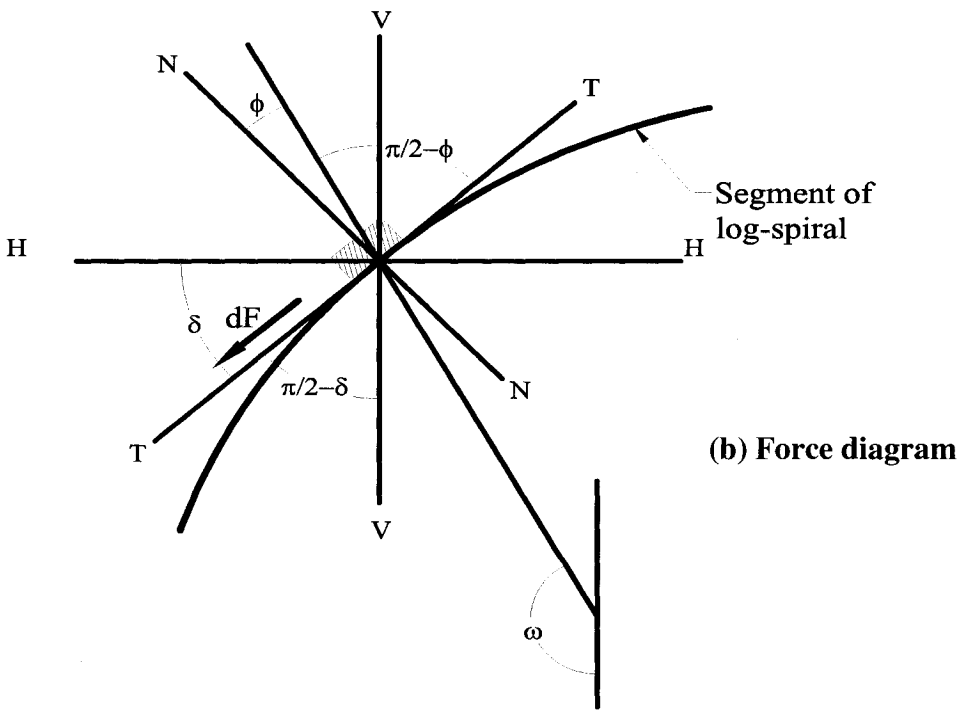

(b) Force diagram

Figure 4.3 Geometrical properties of zone of influence of the upper section.

4.2.2.1 Shaft Resistance:

The shaft resistance is usually calculated as follows:

$$Q_s = P_{sav} \tan(\delta) \tag{4.18}$$

Furthermore:

$$P_s = \tfrac{1}{2} \gamma L K_s A_s \tag{4.19}$$

Where

γ = Effective unit weight of soil

L = Pile length

A_s = Pile shaft surface area

K_s = Coefficient of earth pressure

Referring to Figure (4.3)

$$dL_1 = r_o e^{\omega \tan \phi} (\sin \delta / \cos \phi)\, d\omega$$

Knowing: $\delta = \pi - \omega + \phi$

$$dL_1 = r_o e^{\omega \tan \phi} (\sin (\omega - \phi) / \cos \phi)\, d\omega \tag{4.20}$$

The horizontal component of the shearing force acting on the failure mechanism will constitute the earth pressure acting on the pile's shaft.

$$P_{h1} = \int_0^{2\pi} \int_0^{L_1} dF_1 . dL . d\theta' \tag{4.21}$$

Where:

P_{h1} = the horizontal earth pressure

F_1 = the horizontal component of the shearing resistance acting on the rupture surface

L_1 = pile length of the upper section

θ' = angle of rotation around the pile axis

The variation of shear stress along the rupture surface was determined using Kotter's differential equation. This equation expresses the relationship between the resultant stress acting on the rupture surface at the critical state of limit equilibrium, and the radius of curvature of this surface.

The following simplifying assumptions were considered:

1. The sand is at the state of equilibrium; that is Mohr-Coulomb failure criterion is satisfied ($\tau = \sigma_n \tan \phi$) where τ and σ_n are shear stress and normal stress respectively.

2. The case of plane stress condition is considered; i.e. the stresses acting on the rupture surface depend on two coordinates in a semi-infinite mass, namely, the depth of a given point and the distance of that point from the pile's axis.

3. As the problem of pile capacity is a three-dimensional axisymmetrical problem in physical reality, a solution can be obtained by integrating the resulting stresses from the plane stress condition around the axis of the pile.

Thus, Kotter's differential equation for case of shaft resistance can be written in the following form:

$$\frac{d\tau}{d\delta} + 2\tau \tan\phi = \gamma \sin\phi . \sin(\delta + \phi) . \rho \qquad (4.22)$$

Where:

τ = shear stress along the rupture surface

δ = angle between the horizontal and the rupture surface

ρ = radius of curvature of rupture surface

In case of log-spiral rupture surface ρ is given by the following expression:

$$\rho = r_o e^{\omega \tan\phi}\left(\sqrt{1+\tan^2\phi}\right) = \frac{r_\omega}{\cos\phi} \tag{4.23}$$

From the geometry of the rupture surface shown in Figure (4.3b) δ can be evaluated by using this formula:

$$\omega = \pi/2 - \delta + \delta + \pi/2 - \delta + \phi \tag{4.24}$$

Thus:

$$\delta = \pi - \omega + \phi$$

Differentiating with respect to ω, then $d\delta = -d\omega$

Equation (4.22) can be written in the following form:

$$\frac{d\tau}{d\omega} - 2\tau\tan\phi = -\gamma.r_\omega.\tan\phi.\sin(\omega - 2\phi) \tag{4.25}$$

Solving Eq. (4.25) to find τ leads to:

$$\tau = e^{(2\omega\tan(\phi))}C + e^{\omega\tan(\phi)}.\gamma.r_o\cos(\omega - 3\phi)\sin(\phi) \tag{4.26}$$

Since $\tau = 0$ when $\omega = \alpha_4$

Then

$$C = \frac{\gamma\, r_0 \cos(3/4\,\pi - 3/2\phi).\sin(\phi)}{\alpha} \tag{4.27a}$$

$$\alpha = e^{\alpha_4\tan(\phi)} \tag{4.27b}$$

The horizontal component of the shearing resistance (F_1) acting on the failure surface can be calculated by considering the shearing resistance acting on an elemental area on the surface of the log-spiral (Figure 4.3b).

$$dF_1 = \tau\ \text{cosec}\ (\phi)\ \sin(\delta+\phi)\ X\ dL\ d\theta' \tag{4.28}$$

The horizontal distance "X" from the pile axis to the failure surface can be determined as

follows:

$$X = X' + X_1 \tag{4.29}$$

Where:

X = radius of revolution of element circular area (x/D)

X′ = distance between log-spiral and bottom end of upper section (x′/D)

$$X' = X'' - X_{\omega} \tag{4.30}$$

$$X_{\omega} = r_{\omega} \cos(\omega - \pi/2) \tag{4.31}$$

$$X' = X'' - r_{\omega} \cos(\omega - \pi/2) \tag{4.32}$$

Substitute the values of r_1 and r_{ω} in Eq. (4.32) from which the value of X can be calculated from Eq. (4.29)

$$X = r_o \beta \sin(\alpha_2) - r_o e^{\omega \tan(\phi)} \cos(\omega - \pi/2) + X_1 \tag{4.33}$$

Substitute the values of τ, X and sin δ from Eqs. (4.20), (4.26) & (4.27) in (4.28). The earth pressure for driven single pile is given by the following equation:

$$P_{h1} = \int_0^{2\pi} \int_{\alpha_1}^{\alpha_4} \frac{\tau}{\sin\phi} . \sin(\delta + \phi) . \frac{r_o e^{w \tan(\phi)}}{\cos(\phi)} X . d\omega . d\theta' \tag{4.34}$$

Due to the formula length resulted from this integration it is presented in Appendix 1.

The earth pressure generated from the upper section (abgh) and the lower section (bcfg) formulates the shaft resistance. Thus, the weight of the soil wedge "abcfgh" is determined as follows.

$$W_s = W_1 + W_2 \tag{4.35}$$

$$W_2 = \gamma V_2 \tag{4.36}$$

$$V_2 = \pi \int_{z_1}^{L} (X_1 - X_2)^2 dz - \frac{\pi D^2}{4} (L - z_1) \tag{4.37}$$

Where

D = Pile diameter

X_1 & X_2 = radius of revolution of elemental circular area for the end of upper and lower sections respectively.

$$X_1 = X_2 + L_2 /\tan(\theta) \tag{4.38}$$

From (4.37) and (4.38) the integration will lead to the following equation:

$$V_2 = \pi/3\, LD^2(1-\frac{z_1}{L})(X_1^2 + X_2X_1 + X_2^2) - \frac{\pi D^2}{4}L_2 \tag{4.39}$$

where $z_1/L = 0.5$

The determination of the earth pressure acting on the pile's shaft requires the evaluation of the shear stresses acting on the failure surface. The failure wedge in the soil mass is made of a trapezoidal wedge as "bcfg" as shown in Figure (4.4). The forces acting on the wedge are:

1- Weight of the wedge W_2.

2- Weight of surcharge coming from the upper section W_1.

3- Passive force developed during the pile installation P_{h2}.

4- The resultant of the shear and normal forces along the potential failure surface "bc".

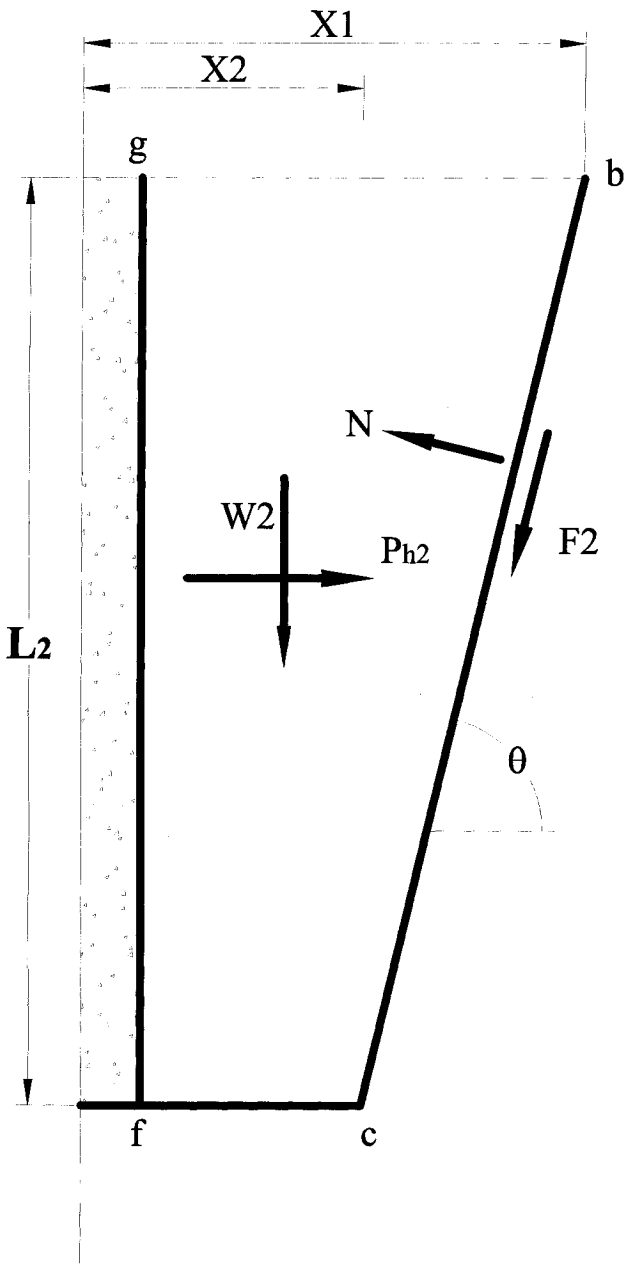

Figure 4.4 Geometrical properties of the mid section.

For equilibrium of the wedge "bcfg" the horizontal force, P_{s2} is calculated as follows:

$$P_{h2} = (W_1 + W_2)(\cos\theta \sin\theta + \cos^2\theta \tan\theta) \quad (4.40)$$

Where θ was assumed to have a value of $\pi/4 - \phi/2$.

W_1 is the weight of the soil in the volume (V_1) of the breaking out sand mass in the upper section (abhg), which can be calculated by integrating an elemental circular area of radius of revolution (x) on the total length of this section (L_1). (Figure 4.2)

$$V_1 = \int_0^{L_1} \pi x^2 dL_1 - 1/4\pi D^2 L_1 \quad (4.41)$$

From equation (4.3), (4.20), (4.32) and (4.33), the integration of Eq. (4.41) yields the following equation:

$$V_1 = \pi \int_{\alpha_1}^{\alpha_4} \frac{z_1}{L} D^2 [\beta r_o \sin(\alpha_2) + r_o e^{\omega \tan\phi} \sin(\omega) + X_1]^2 \left[r_o e^{w \tan\phi} \sin\omega - r_o e^{w \tan\phi} \cos\omega \tan\phi\right] d\omega - 1/4\pi D^2 L_1 \quad (4.42)$$

The integration of this formula is presented in Appendix 2.

Thus;

$$W_1 = \gamma V_1 \quad (4.43)$$

After calculating the earth pressure developed from the upper section (P_{h1}) and the lower section (P_{h2}), it is possible to calculate the average earth pressure developed on the pile "P_{sav}" and thereafter the shaft resistance Q_s can be calculated from Eq (4.18):

$Q_s = P_{sav} \tan\delta$

Where:

δ = Angle of Friction between the pile shaft and soil.

P_{sav} can be formulated as follows:

$$P_{sav} = \frac{1}{2} \gamma L^2 \pi D K_s \quad (4.44)$$

It can be noted that from Eq (4.44) the coefficient of earth pressure "K_s" is a governing parameter in the determination of the earth pressure and accordingly the shaft resistance "Q_s". It is of interest to note that the resulting K_s value takes into account both the pile length and the pile diameter.

Figure 4.5 presents a comparison between the results of the present analytical model with those produced from the numerical model (see Figure 3.49). It can be noted that in general a good agreement can be found. However, for higher values of L/D (>70), the values of Ks are higher than that of the numerical model. This can be explained by the fact that the method of limit equilibrium does not take into account the driving effect. In section 4.2.2 the shaft resistance will be re-evaluated according to the stress zone of influence, which is a proposed method of analyses to takes into account the driving effect on the pile shaft.

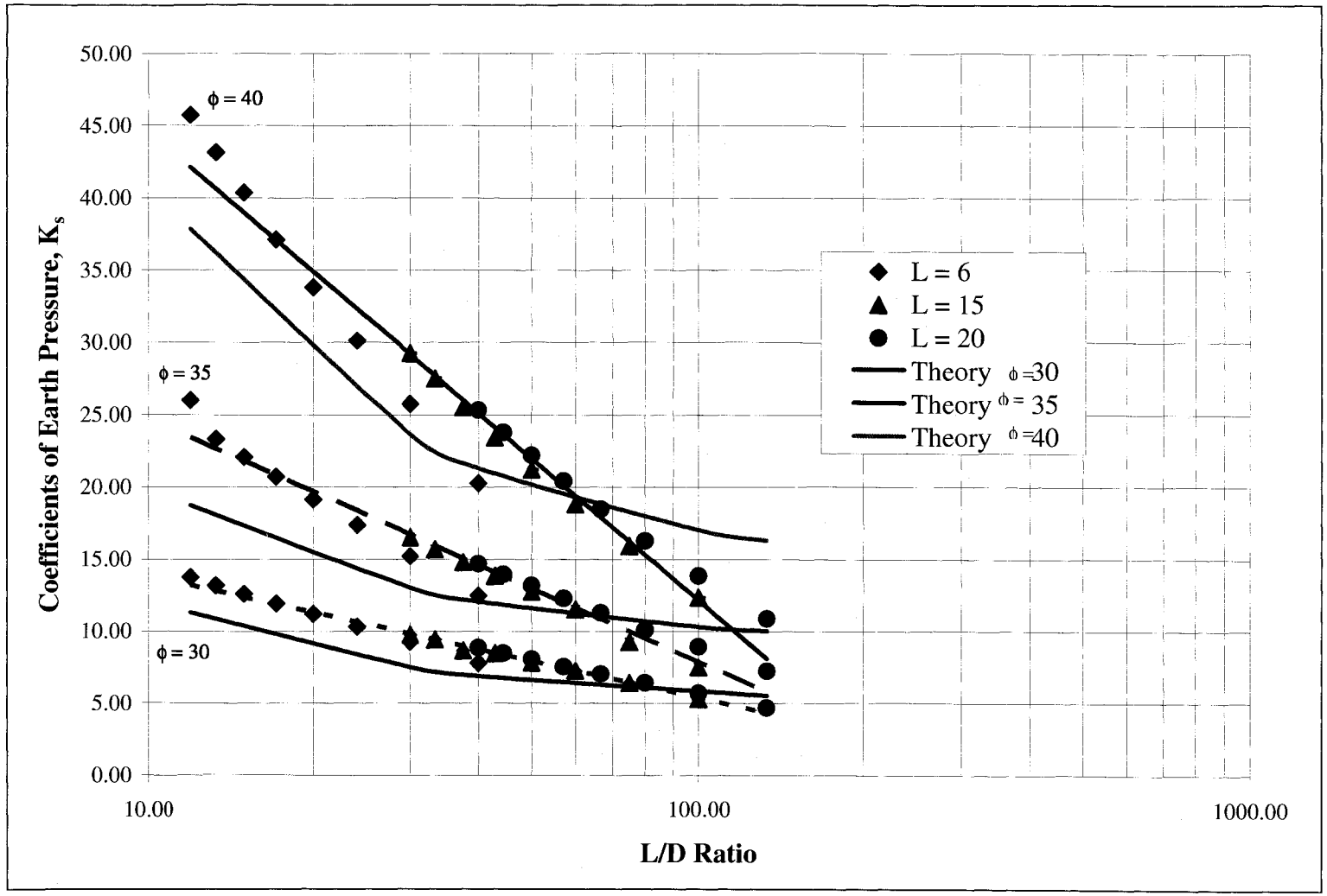

Figure 4.5 Comparison between the numerical and the theoretical values of the coefficient of earth pressure, K_s.

4.2.2.2 Tip Resistance

The tip resistance is generally evaluated as follows:

$$Q_t = q_o A_t N_q \tag{4.45}$$

Where:

q_o = effective vertical stress at the pile tip level

A_t = Base area of the pile

N_q = Bearing capacity factor

In the literature, the values proposed for N_q varied dramatically from one theory to another. This can be explained by the fact that namely due to the changes in the insitu stresses due to installation, which in turn affect the values of the OCR in the sand mass around the tip. Eventually, these changes were not taken into consideration in developing the existing theories.

Since the problem of vertical pile subjected to an axial load is symmetrical one, thus the calculations will be performed on a half of the pile. In this analysis, the failure surface generated around the pile's tip was assumed to be a logarithmically spiral, Figure 4.6. Then by applying the principle of limit equilibrium, the mechanism comprises two zones:

1- A triangular wedge, "fdc" moving down with the footing as a rigid body.

2- A logarithmic spiral wedge "cdf".

Consider the uniform surcharge pressure acting on "fc" results from W_1 and W_2. Such that:

$$q = \frac{W_1 + W_2}{\pi(\frac{D^2}{4} + X_2^2)} \tag{4.46}$$

Accordingly:

q_1 acting on "fd" can be evaluated based on the prandtl mechanism as:

$$q_1 = q\, e^{2\,\alpha'_2 \tan\phi} \tag{4.47}$$

The equilibrium of the vertical forces acting on the wedge "fdc" yields the following relation.

$$q_t B = qB \operatorname{cosec}(\alpha'_{1+}\phi)\, e^{2\,\alpha'2 \tan\phi} - 1/2\, \gamma B^2 \cot\ \alpha'_1 \tag{4.48}$$

$$q_t = q_1 \operatorname{cosec}(\alpha'_{1+}\phi)\, e^{2\,\alpha'2 \tan\phi} - 1/2\, \gamma B \cot \alpha'_1 \tag{4.49}$$

where $\alpha'_1 = \pi/4 - \phi/2$ (4.50a)

then: $\alpha'_2 = 3\pi/4 - \phi/2$ (4.50b)

It can be also written in this form:

$$q_t = q\, N_q - \tfrac{1}{2}\, \gamma B\, N_\gamma \tag{4.51}$$

Where:

$$N_q = \operatorname{cosec}(\alpha'_{1+}\phi)\, e^{2\,\alpha_{f2} \tan\phi} \tag{4.52}$$

The second part of Eq (4.51) can be neglected due to the small base of pile as compared to shallow foundation. The tip resistance can be then calculated as:

$$Q_t = \gamma L\, N_q\, A_t \tag{4.53}$$

The values of N_q was plotted versus the angle ϕ in figure 4.7 for practicing use . From this chart it can be noted that the value of N_q increases with the increase of the soil strength, which is represented by the angle of shearing resistance, ϕ.

The present theory is capable to determine the values of the two factors (K_s, N_q), which governs the ultimate capacity of the pile taking into account the effect of the pile diameter, length and the effect of installation.

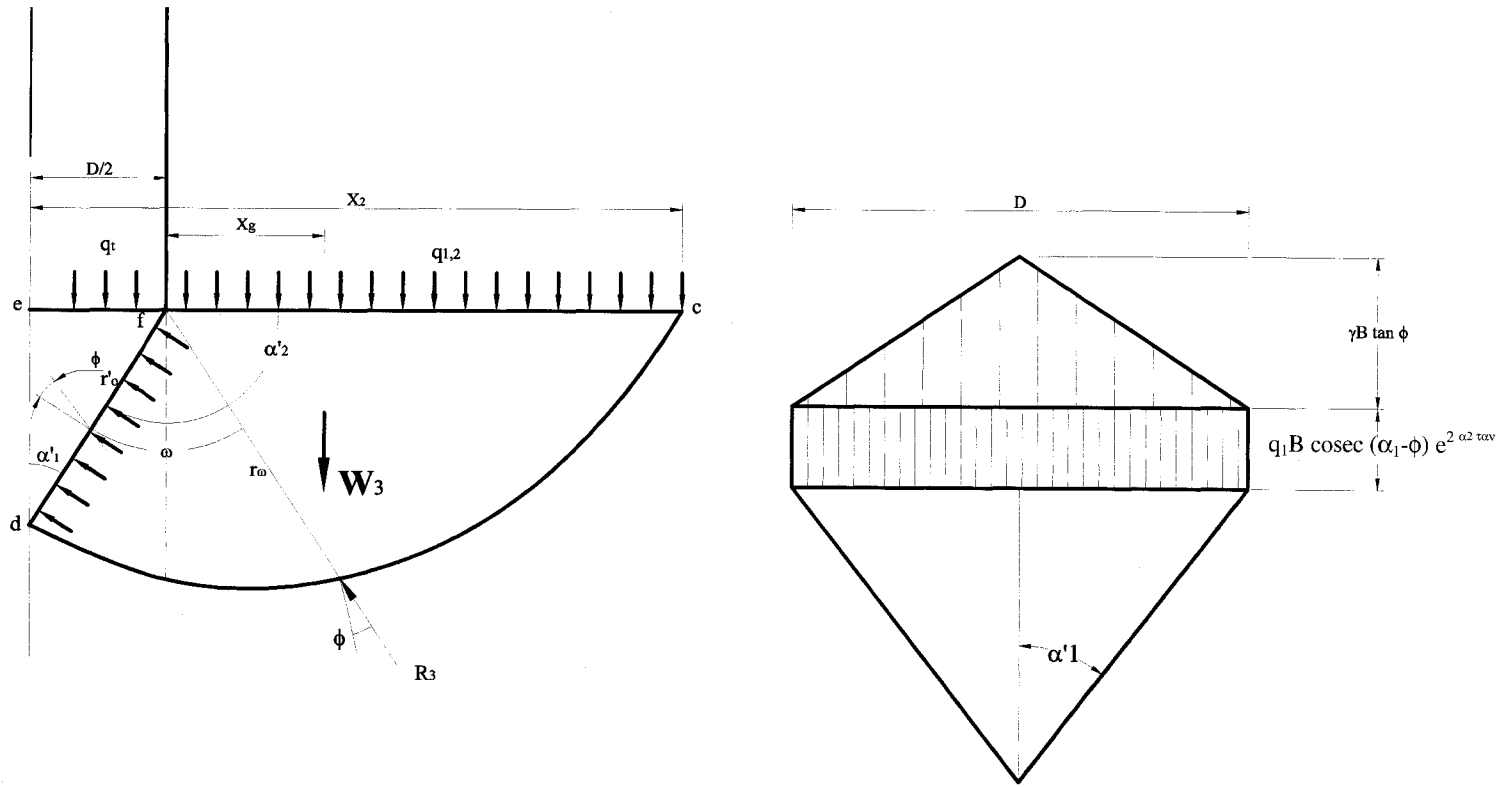

Figure 4.6 Geometry properties of the lower section.

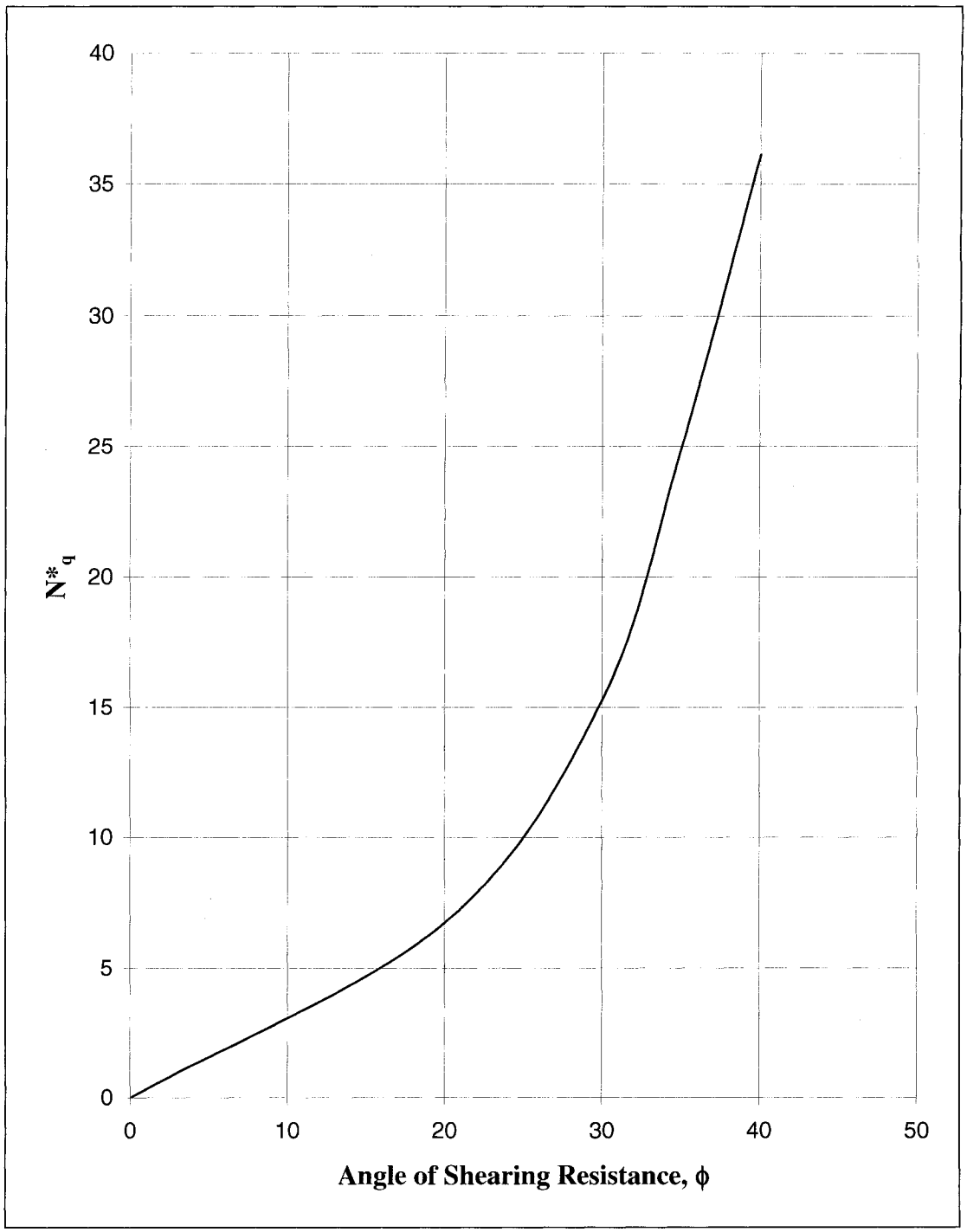

Figure 4.7 Design Chart for Bearing Capacity Factors, N_q.

4.2.2 Analytical model based on Stress Pattern

The stress pattern deduced from the numerical model developed in the present investigation was divided into three zones (zone 1, zone 2 and zone 3). The length of each zone was defined in terms of pile length, diameter and the angle of shearing resistance with the exception of zone 1, which was defined in terms of pile diameter and the angle of shearing resistance. Figure 4.8 presents a schematic sketch of these three zones. The horizontal stresses in each zone were evaluated using the coefficient of earth pressure for that zone. Thus, the shaft resistance will be formulated as follows:

$$Q_s = \sum_{i=1}^{3} P_{si} \tan\delta \tag{4.54}$$

Where:

P_{s1} : Earth pressure in zone 1

P_{s2} : Earth pressure in zone 2

P_{s3} : Earth pressure in zone 3

$$P_{s1} = \gamma\pi D \int_0^{L1} z K_{s1} dz \tag{4.55}$$

$$P_{s2} = \pi D \left[\int_0^{L_2 - L_1} (K_{s2}.\gamma.z + K_{q2}.q_1) dz \right] \tag{4.56}$$

$$P_{s3} = \pi D \left[\int_0^{L - L_2} (K_{s3}.\gamma.z + K_{q3}.q_2) dz \right] \tag{4.57}$$

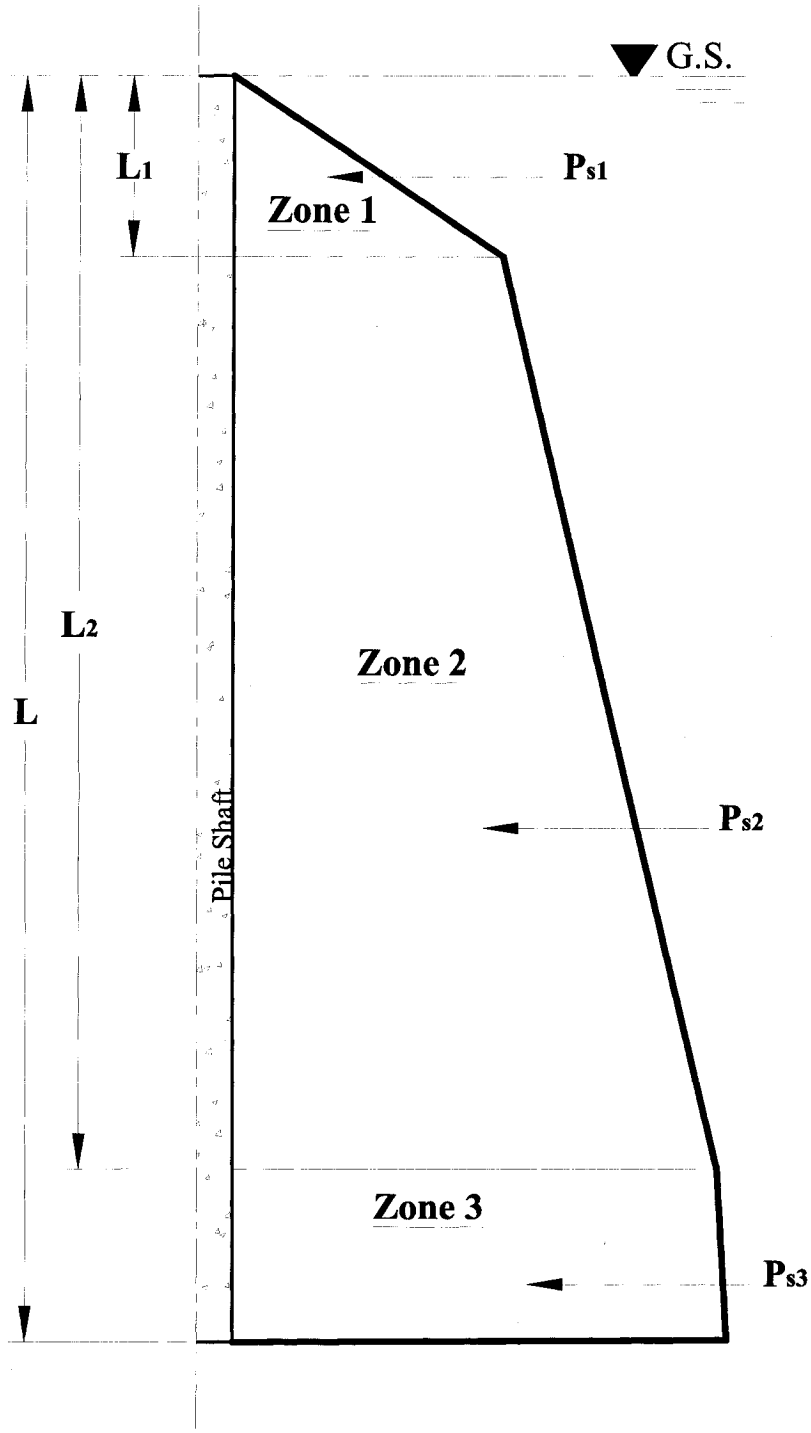

Figure 4.8 Sketch showing the horizontal stress distribution on the pile's shaft.

Where:

$$K_{qi} = \frac{K_{si}}{\cos(\beta - \lambda)}$$ (Costet and Sanglerat 1982)

β : angle of inclination of the sand surface to the horizontal ($\beta = 0$)

λ : angle of inclination of the pile to the vertical ($\lambda = 0$)

z : is the distance measured from the ground level to any point on the pile shaft.

therefore, $K_{qi} = K_{si}$

Furthermore,

q_1 : Surcharge pressure on zone 2 ($q_1 = \gamma.L_1$),

q_2 : Surcharge pressure on zone 2 ($q_1 = \gamma.L_2$)

The depth of the three zones and the corresponding earth pressures coefficients are calculated using Equations For convenience the empirical formulas to calculate the range of each zone and the coefficient of earth pressure produced in chapter 3 will be listed below:

Zone 1:

$L_1 = \phi(4.3D + 0.65)$ ϕ in radians (4.58)

$K_{s1} = 0.6\ z\ e^{5\tan\phi} + 5\ \tan\phi + 6$

it can be written as

$K_{s1} = a_1.z + b_1$ (4.59)

Where:

$a_1 = 0.6e^{5\tan\phi}$

$b_1 = 5\ \tan\phi + 6$

Zone 2:

$$L_2 = L - D[(0.02 - 0.1 \tan(\phi))\, L + 6.5 \tan(\phi) - 1] \tag{4.60}$$

$$K_{s2} = 250 \tan^4 \phi \left(\frac{D}{z}\right)^{0.7 \tan \phi + 0.02}$$

it can be written as

$$K_{s2} = a_2 . z^{-b2} \tag{4.61}$$

Where:

$$a_2 = 250 \tan^4 \phi (D)^{0.7 \tan \phi + 0.02}$$

$$b_2 = 0.7 \tan \phi + 0.02$$

Zone 3:

$$K_{s3} = \frac{K_{sL2} - K_p}{L - L_2}(L - z) + K_p$$

$$K_{s3} = b_3 - a_3 . z \tag{4.62}$$

Where:

$$a_3 = \frac{K_{sL2} - K_p}{L - L_2}$$

$$b_3 = \frac{K_{sL2} - K_p}{L - L_2} L + K_p$$

From Eq. (4.55)

$$P_{s1} = \pi D \gamma \int_0^{L_1} K_{s1} . z . dz = \pi D \gamma \int_0^{L_1} (a_1 z + b_1) z dz$$

so

$$P_{s1} = \pi D \gamma \left[\frac{a_1}{3} L_1^3 + \frac{b_1}{2} L_1^2\right] \tag{4.63}$$

From Eq. (4.56)

$$P_{s2} = \pi D\gamma\left[\int_0^{(L_2-L_1)} K_{s2}.z.dz + \int_0^{(L_2-L_1)} K_{s2}.L_1.dz\right] = \pi D\gamma\left[\int_0^{(L_2-L_1)} a_2 z^{1-b_2} dz + L_1 \int_0^{(L_2-L_1)} a_2 z^{-b_2} dz\right]$$

so

$$P_{s2} = \pi D\gamma \frac{a_2}{2-b_2}\left(L_2^{2-b_2} - L_1^{2-b_2}\right) \tag{4.64}$$

From Eq. (4.57)

$$P_{s3} = \pi D\gamma\left[\int_0^{(L-L_2)} K_{s3}.z.dz + \int_0^{(L-L_2)} K_{s3}.L_2.dz\right] = \pi D\gamma\left[\int_0^{(L-L_2)} (b_3 - a_3 z)z.dz + L_2 \int_0^{(L-L_2)} (b_3 - a_3 z)dz\right]$$

so

$$P_{s3} = \pi D\gamma\left[\frac{-a_3}{3}\left(L^3 - L_2^3\right) + \left(\frac{b_3}{2}\right)\left(L^2 - L_2^2\right)\right] \tag{4.65}$$

Thus the total earth pressure can be evaluated as follows.

$$P_s = P_{s1} + P_{s2} + P_{s3} \tag{4.66}$$

Substituting Eqs. (4.63), (4.64) and (4.65) in Eq. (4.66)

$$P_s = \pi D\gamma\left[\left(\frac{a_1}{3}L_1^3 + \frac{b_1}{2}L_1^2\right) + \left(\frac{a_2}{2-b_2}(L_2^{2-b_2} - L_1^{2-b_2})\right) - \left(\frac{a_3}{3}(L^3 - L_2^3) - \frac{b_3}{2}(L^2 - L_2^2)\right)\right] \tag{4.67}$$

The earth pressure along the pile is also defined as:

$$P_s = \gamma\pi D\int_0^L zK_s dz = \frac{1}{2}\pi D\gamma K_s L^2 \tag{4.68}$$

Where

K_s: average coefficient of passive earth pressure along the length of the pile

Equating Eqs. (4.67) and (4.68), the value of the average coefficient of earth pressure can be obtained as follows:

$$K_s = \frac{2}{L^2}\left[\left(\frac{a_1}{3}L_1^3 + \frac{b_1}{2}L_1^2\right) + \left(\frac{a_2}{2-b_2}(L_2^{2-b_2} - L_1^{2-b_2})\right) - \left(\frac{a_3}{3}(L^3 - L_2^3) - \frac{b_3}{2}(L^2 - L_2^2)\right)\right] \quad (4.69)$$

Applying with the value of K_s in Eq. (4.54), thus:

$$Q_s = \tan\delta . \sum_{i=1}^{3} P_{si} = P_s . \tan\delta \quad (4.70)$$

The values of the average coefficient of earth pressure, K_s determined from Eq. (4.69) were presented in graphical forms in Figure 4.9. Thus the value of P_s can be calculated and accordingly the Q_s.

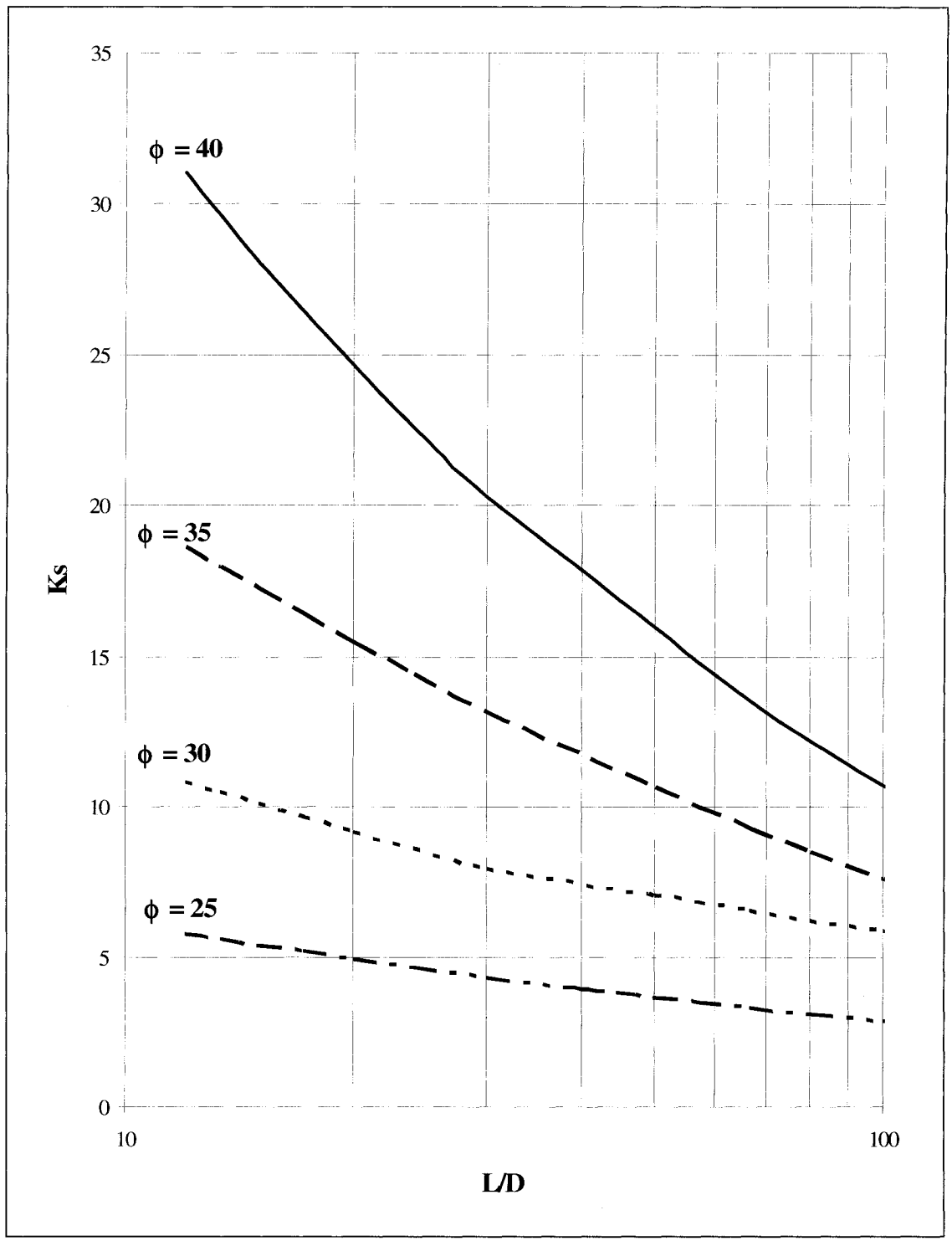

Figure 4.9 Design chart to evaluate K_s.

4.3 Validation of the theory developed

The present theories were validated by full-scale pile load tests, which are available in the literature. The measured capacity was compared with the theoretical values predicted by both theories developed in the present investigation; namely zone of influence method and the stress pattern method. The comparisons are presented in Table (4.1, 4.2). The discrepancies reported in some tests are due to the presence of ground water and the layered system of the soil strata. Otherwise, a good agreement can be achieved.

From comparing the stress zone method and the zone of influence method with the field tests, it can be noted that the theoretical model based on the zone of influence using the limit equilibrium method provided consistent results, which are higher than the field results (Figure 4.10). This is due to assumption of general mechanism acting on the pile without considering the local changes in the stresses acting on the pile's shaft. This is due to the fact that the limit equilibrium method, which was widely used in literature, did not take into account the driving effect on pile capacity. Furthermore, the comparison (Figure 4.11), which was based on the stress pattern method revealed good agreement.

Table 4.1 Pile load test data description and comparison with the zone of influence method.

ID	Penetration (m)	Diameter (m)	L/D	ϕ (Degrees)	Ks	N^*_q	γ_{eff} (kN/m^3)	Predicted Q_u (kN)	Measured Q_u (kN)	Variation (%)
Visic (1970) H-15	15.00	0.46	32.82	36	13	26	5.7	3572	3200	11.6
" H-14	11.97	0.46	26.19	39	19	30	5.8	3402	2630	29.4
" H-13	8.86	0.46	19.39	35	15	25	6	2064	1872	10.3
" H-12	6.13	0.46	13.40	34	13	23	6.4	1193	1533	-22.2
" H-11	3.01	0.46	6.59	31	15	16	7.9	422	411	2.6
Abe et al (1990)	16.50	0.31	54.10	25	4	10	12	1822	1735	5.0
Tavenas (1971) J-2	8.81	0.32	27.53	34	7	23	9.3	840	687	22.3
Coyle (1973)	8.69	0.45	19.31	34	10	23	10.3	2019	1690	19.5
Webster et al (1994)	13.80	0.61	22.62	30	7	16	10	3594	2200	63.4
Fellenius (1988) A4	37.00	0.32	114.55	32	4	16	5	4002	2260	77.1
" G1	43.00	0.23	188.60	32	3	16	6	3394	2936	15.6
M. Hussein (2002)	19.80	0.46	43.33	34	12	19	8	7805	7340	6.3
Beringen et al (1979) 1-c	7.00	0.36	19.61	35	15	35	10	2155	2440	-11.7
" 2-c	6.70	0.36	18.77	35	16	35	10	2626	3000	-12.5
Gurtowski & Wu (1984)	29.90	0.61	49.02	25	4	10	8	6853	4020	70.5
Mansour &Kaufman (1956) 5	13.70	0.43	31.64	25	4	10	8	1555	1470	5.8
" 6	19.80	0.48	41.08	25	3	10	8	3590	3470	3.5
" 7	19.80	0.46	43.33	28	5	15	9	4759	3109	32.1

Table 4.2 Pile load test data description and comparison with the stress pattern theory using (K_s) average.

ID	Penetration (m)	Diameter (m)	L/D	ϕ (Degrees)	K_s	N^*_q	γ_{eff} (kN/m^3)	Predicted Q_u (kN)	Measured Q_u (kN)	Variation (%)
Visic 1970 (H-15)	15.00	0.46	32.82	36	10	26	6	3325	3200	3.9
" (H-14)	11.97	0.46	26.19	39	14	30	6	2628	2630	-0.1
" (H-13)	8.86	0.46	19.39	35	11	25	6	1981	1872	5.8
" (H-12)	6.13	0.46	13.40	34	11	23	6	1450	1533	-5.4
" (H-11)	3.01	0.46	6.59	31	10	16	8	365	411	-11.2
Abe et al (1990)	16.50	0.31	54.10	25	4	10	11	1564	1735	-9.9
Tavenas (J-2)	8.81	0.32	27.53	34	12	23	9	947	548	72.9
Coyle (1973)	8.69	0.45	19.31	34	10	23	10	2065	1496	38.0
Webster et al 1994	13.80	0.61	22.62	30	5	16	10	2674	2200	21.5
Fellenius (1988) A4	37.00	0.32	114.55	32	6	16	5	4333	2260	91.7
G1	43.00	0.23	188.60	32	6	16	6	5460	2936	86.0
Mohamad Hussein (2002)	19.80	0.46	43.33	34	7	19	8	8133	7340	10.8
Beringen et al (1979) 1-c	7.00	0.36	19.61	35	14	35	10	2435	2440	-0.2
2-c	6.70	0.36	18.77	35	14	35	10	2702	3000	-9.9
Gurtowski & Wu (1984) A-c	29.90	0.61	49.02	25	2	10	8	4277	4626	-7.5
B-c	25.60	0.61	41.97	25	2	10	11	4547	4793	-5.1
Mansour &Kaufman (1956) 4	20.12	0.43	46.79	28	4	10	8	3440	3540	-2.8
" 5	13.70	0.43	31.64	25	3	10	8	1528	1470	3.9
" 6	19.80	0.48	41.08	25	3	10	8	3304	3470	-4.8
" 7	19.80	0.46	43.33	28	4	14	9	3246	3109	4.4
Mey et al. (1985)	18.00	0.91	19.69	27	3	13	10	5380	5080	5.9

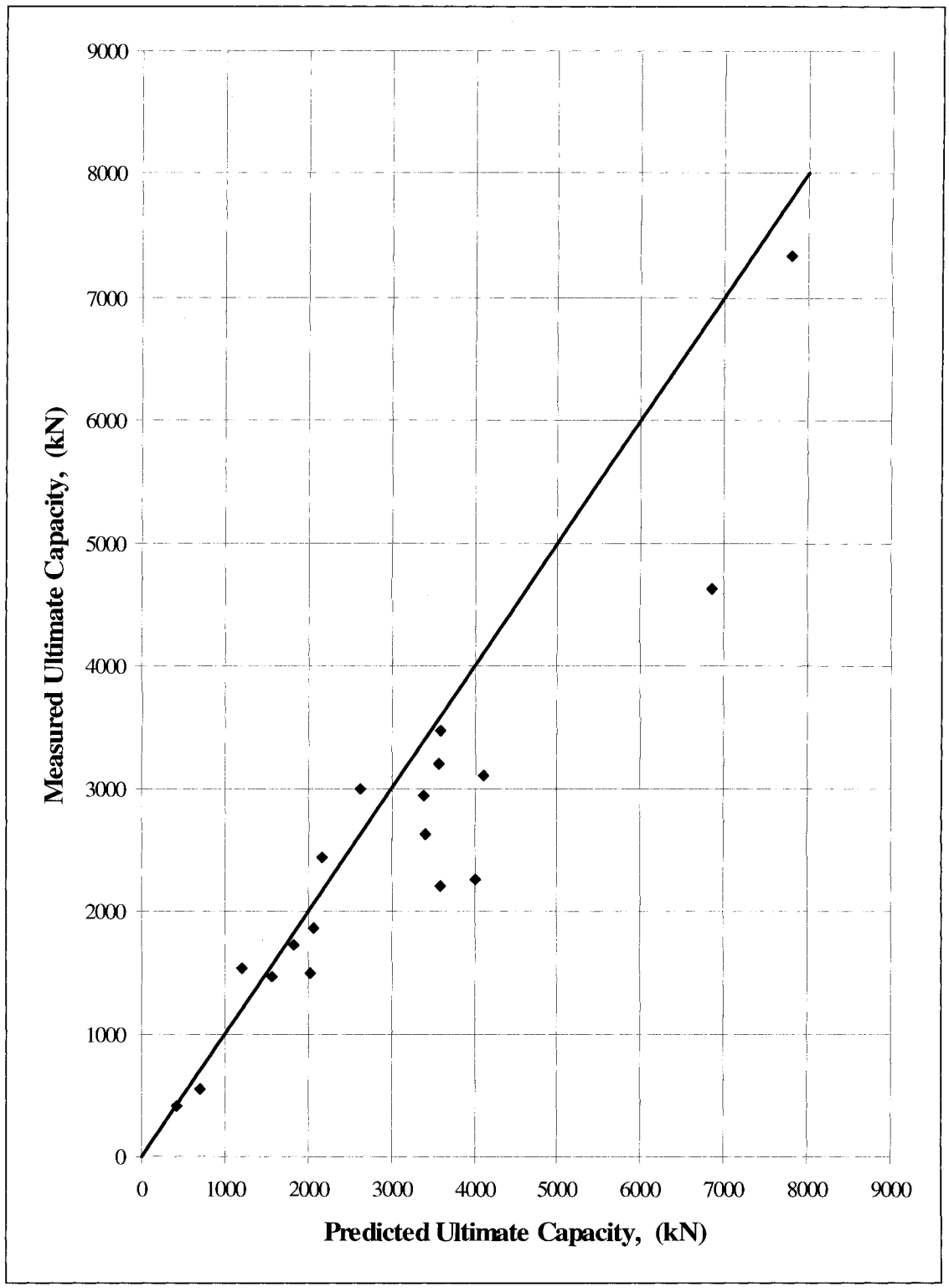

Figure 4.10 Predicted and measured pile ultimate capacity (zone of influence, Table 4.1).

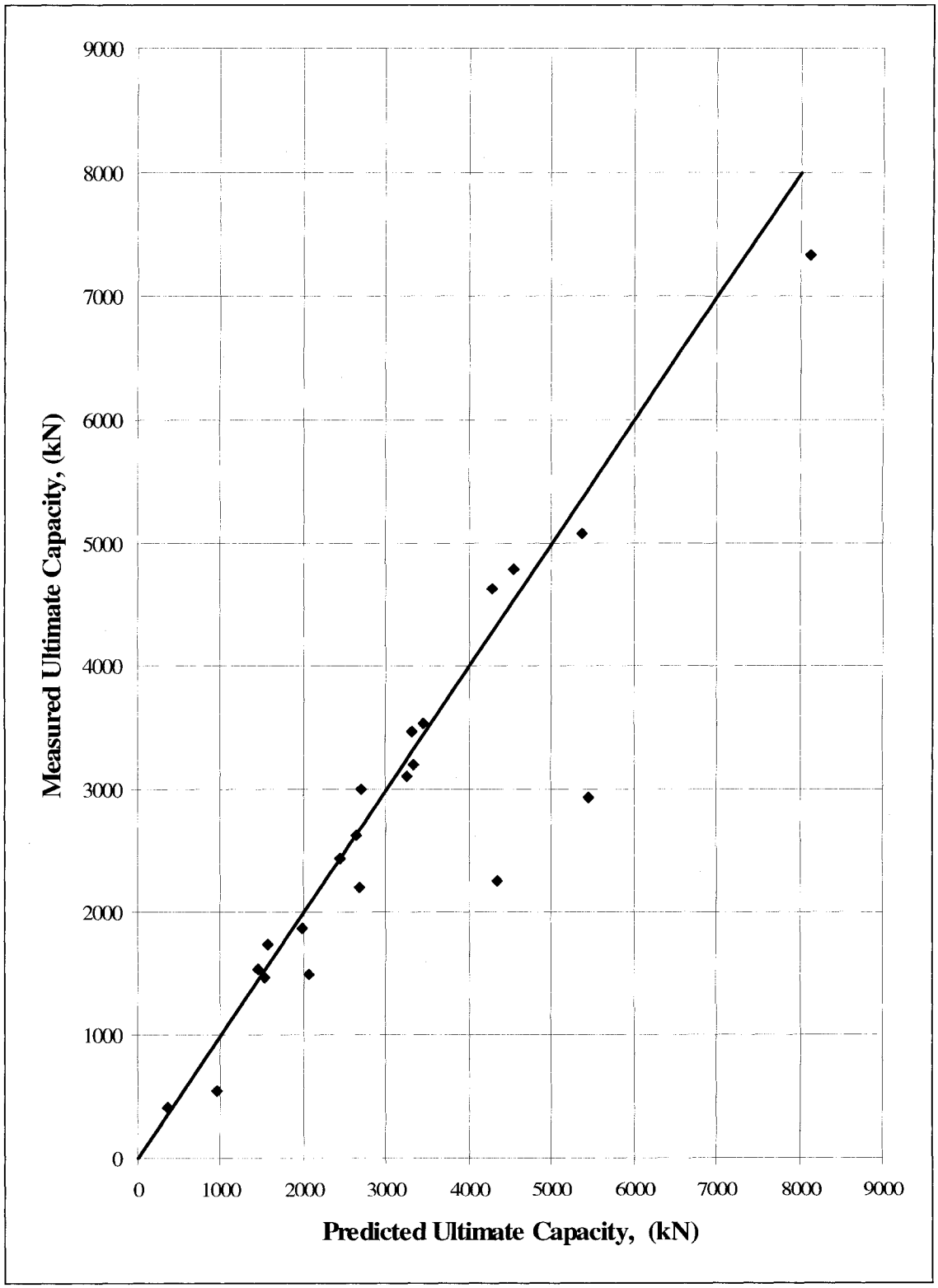

Figure 4.11 Predicted and measured pile ultimate capacity (Stress pattern, K_s for three zones, Table 4.2).

4.4 Design Procedure

Based on the present investigation, the recommended procedure to estimate the ultimate bearing capacity of a single vertical pile driven in sand may be summarized as follows:

1. Determine the angle of shearing resistance ϕ from the results of the triaxial test.
2. Knowing the value of ϕ determine the value of N_q from the design chart given in Figure (4.7).
3. Calculate the tip resistance Q_t for a given pile length and diameter using Eq. (4.53).
4. Determine the average earth pressure deduced for the three zones Eq. (4.68).
5. The values of K_s can be then predicted from the design charts in Figure (4.9)
6. Calculate the skin friction Q_s using Eq (4.70); employing the value of K_s determined in step 5 above
7. The Ultimate bearing capacity Q_u is then given by the sum of Q_t and Q_s.

The recommended procedure described above is subjected to the following limitations:

1. It is only applicable for rounded closed ended piles to generate the amount of lateral displacement in the sand mass producing the earth pressure predicted from the present theory.
2. It is only applicable for pile driven in dry homogenous sand.
3. For pile driven in overconsolidated sand deposits, the procedure results in a conservative estimate for pile bearing capacity. Further research into the effect of K_o on the shaft and tip resistance may lead to more economical design.

CHAPTER 5
CONCLUSIONS AND RECOMMENDATIONS

5.1 General

The conclusions drawn from the present investigation are summarized in this chapter. Suggestions for future work are also given.

5.2 Conclusions

1. A numerical model was developed to simulate the process of pile installation in sand. The theory of cavity expansion was adopted together with the finite element technique to develop this numerical model.
2. The numerical model is capable of evaluating the pile capacity and the insitu stresses around the pile's shaft during and after pile installation.
3. The results of the numerical model showed that for loose and medium dense sands, the level of overconsolidation in the sand mass increases during pile installation, and accordingly the earth pressure acting on the pile's shaft increases and further the capacity of the pile. The coefficient of earth pressure was found to be higher near the pile head and decreases along the pile length, then increases slightly near the pile tip.
4. The results of the numerical model showed that the earth pressure acting on the pile shaft depends not only on the angle of shearing resistance of the sand but also on the pile diameter.
5. The results of the numerical model showed that the critical depth may not exist in the case of driven piles in sand to the contrary for what was reported in the literature.

6. The pile roughness showed no significant effect on the value of the coefficient of earth pressure due to the full mobilization of the soil angle of shearing resistance for driven piles.
7. In the light of the results obtained in this investigation, interaction between individual piles was examined and recommendations were made to assign spacing between piles and to determined group capacity.
8. In the light of the results obtained in this investigation, a guideline was developed to assist practicing engineers to establish the limitations for driven piles in terms of pile diameter and length allowed for a given soil condition.
9. The results obtained in this investigation demonstrated the superiority of driven piles as compared to bored piles.
10. An analytical model was developed in this investigation utilizing the stress pattern and zone of influence deduced from the numerical model, which takes into account the effect of pile installation. The theory proved superior to the methods presented in the literature, which were developed based on the limit equilibrium method of analyses.
11. Design charts are developed and presented to evaluate the coefficient of earth pressure K_s based on pile's diameter, length and soil angle of shearing resistance.
12. Design charts are developed and presented to evaluate the bearing capacity factor N_q based on the theory of zone of influence.
13. Ultimate bearing capacity predicted by the proposed method agreed well with the field and laboratory test results available in the literature.

5.3 Recommendations for Future studies

Research on pile foundation driven in cohessionless soils requires more investigations, as follow:

1. Experimental investigation to be conducted to simulate the driving effect of piles.
2. Extend the current study to cover pile groups and the effect of pile installation on neighbouring pile.
3. Extend the current investigation to simulate the effect of pile installation on the tip component by utilizing the theory of spherical cavity expansion.
4. Dynamic simulation for pile driving in sand.
5. Extend the current study to piles driven in layered soil.
6. Extend the proposed model to cover cases of battered piles driven in sands.
7. Extend the current study to cover the effect of water table and/or degree of saturation.

REFERENCES

1- Abe, S., Likins, G. and Morgano, C. M. (1990), "Three case Studies on Static and Dynamic Testing of Piles", Geotecnical News, V8, No. 4, pp. 26-28.

2- Abu Kiefa, M. A. (1998), "General Regression Neural Networks for Driven Piles in Cohesionless Soil", J. Geotech. Engrg., ASCE, 124(12), pp 1177-1185.

3- Alsiny, A., Vardoulakis, I. and Drescher, A. (1992), "Deformation Localization in Cavity Inflation Experiments on dry sand", Geotechnique, v 44, n 2, pp 365-366.

4- Altaee, Amir and Fellenius, Bengt H. (1993), "Load Transfare For Piles In Sand And The Critical Depth", Canadian Geotechnical Journal, 30(3), pp. 455-463.

5- Armaleh, Sonia and Desai, C. S. (1988), "Load-Deformation Response of Axially Loaded Piles", J. Geotech. Engrg., ASCE, 113(12), pp 1483-1499.

6- Been, K., Crooks, H. A., Becker, D. E., and Jefferies, M. G. (1986), "The Cone Penetration test in sand: part I, State Parameter interpretation", Geotechnique, 36, No.2, pp 239-249.

7- Berden, L., Ismail, H., and Tomg, P.(1969), "Plane Strain Deformation of Granular Material at Low and High Pressures", Geitechnique v19 No.4, pp. 441-452.

8- Beringen, F. L., Windle, D. & Van Hooydonk, W. R. (1979), "Recent developments in the design and construction of piles", Inst. Of Civil Eng., London, pp. 213-225.

9- Bolton, M. D. (1986), "The strength and Dilatancy of Sand", Geotechnique, 36, No. 1, pp. 65-78.

10- Celement, Jose L.M. and Sayed, Sayed M. (1991), "Efficiency of Pile Group in sand", Geotechnical special publication, v1, n27, pp. 346-355.

11- Collins, I. F., Pender, M. J. and Yan, Wang (1992), "Cavity Expansion in sand Under Drained Loading Condition", Int. J. Numer. Anal. Meth. Geomech., 16, pp. 3-23.

12- Costet, J. and Sanglerat, G. (1982), "Cours Pratique de mecanique des sols.", Editions Dunod, Paris.

13- Coyle, H. M., Bartoskewitz, R.E. and Berger, W.J. (1973), "Bearing capacity prediction by wave equation analysis – state of the art", Research Report 125 – 8, Texas A&M University, College Station, Tex.

14- Das, B.M (1989). "Ultimate uplift capacity of piles and piles groups in granular soil", The International Conference on piling and deep foundations, London.

15- Feda, J. (1976). "Shaft resistance of piles", Sixth European Conference on Soil Mechanics and Foundation Engineering, Vienna.

16- Fellenius, B. H. and Altaee, A. A. (1995), "Critical Depth: How It Came into Being and Why it does not exist", Proc Instn. Civil Engrs. 113 pp. 107-111.

17- Fellenius, Bengt H., Riker, Richard E., O'Brien, Arthur J. and Tracy, Gerald R. (1989), "Dynamic and Static Testing in soil, Exhibiting Set-Up", J.Geotech. Engrg., ASCE, 114(7), pp. 984-1001.

18- Franke, E. (1993), "Design Of Bored Piles, Including Negative Skin Friction And Horizontal Loading", Proc., 2nd Int. Geotech. Seminar on Deep Foundation on Bored and Auger Piles, Van Impe, ed, Balkema, Rotterdam, The Netherlands, pp. 43-57.

19- Gurtowski, T. M. and Wu, M. J. (1984), "Compression load test on concrete piles in aluminum", Analis. and design of pile foundation, pp. 138-153.

20- Hanna, A. M. and Nguyen, T. Q. (2002), "An Axisymmetric Model for Ultimate Capacity of a single pile in Sand", Soils and Foundation, v42, n2 pp. 47-58.

21- Hanna, A. M. and Nguyen, T. Q. (2003), "Shaft Resistance of Single Vertical and Batter Piles Driven in Sand", J. Geotech. Engrg., ASCE, v129, n7, pp. 601- 607.

22- Hanna, A.M. and Saad, N. S. (2001), "Effect of Compaction Duration on the Induced Stress Level in a Laboratory Prepared Sand Bed," Geotechnical Testing J., ASTM, 24(4), pp. 430-438.

23- Hanna, T. H. and Tan, R. H. S. (1973), "The Behavior of Long Piles Under Compressive Loads in Sand", Canadian Geotechnical Journal, v10, n3, pp. 311-340.

24- Hussein, Mohamad H., Sharp, Michael R. and Knight, William F. (2002), "The use of Superposition for Evaluating Pile Capacity", Deep Foundation Conf. (ASCE) Orlando, FL. Pp. 6-21.

25- Kolar, V. and Nemec, I (1989), "Modeling of Soil - Structure Interaction", Elsevier.

26- Koltz, U., Coop, M. R. and Taylor, R. N. (2002). "An Assessment of Design Methods for Driven Piles in Sand", Proc. Of the Int. Deep Foundation Congress. ASCE, Orlando, Florida, pp. 1501-1517.

27- Kraft, Leland M. (1991), "Performance of Axially Loaded Pipe Piles in Sand", J. Geotech. Engrg., ASCE, 117(2), pp. 272-296.

28- Kulhawy, F. H. (1984), "Limiting tip and side resistance: fact or fallacy?", Proc. Symp. On Analysis and Design of Piles Foundations, R. J. Meyer, Editor, San Francisco, ASCE pp. 80- 89.

29- Ladanyi, Branko and Foriero, Adolfo (1998), "A Numerical Solution of Cavity Expansion Problem in Sand Based Directly on experimental Stress-Strain Curves", Canadian Geotechnical Journal, v34, n4, pp.541-557.

30- Mabsout, Mounir E. and Tassoulas, John L. (1994), " A Finite Element Model For The Simulation of Pile Driving", Int Jour. For Numerical Meth. in Eng. V37, pp. 257-278.

31- Mabsout, Mounir E., Reese, Lymon C. and Tassoulas, John L. (1995), "Sudy of Pile Driving by Finite-Element Method", J. Geotech. Engrg., ASCE, 121(7), pp. 535-543.

32- Mabsout, Mounir E., Sadek, Salah and Smayra, Toufic E. (1999), "Pile Driving By Numerical Cavity Expansion", Int. J. Numer. Anal. Meth. Geomech., 23, pp. 1121-1140.

33- Mansur, C. I. and Kaufman, R. I. (1956), "Pile test, low-still structure, Old River, Louisiana.", Trans. (ASCE) 123, pp. 715-743.

34- Mey, R., Oteo, C. S., Sanchez Del Rio, J. & Seriano, A. (1985). Field testing on Large driven piles. Proc. 11th int. Conf. Soil Mech., San Francisco 3, pp. 1559-1564.

35- Meyerhof G. G. (1951), "The Ultimate Bearing Capacity of Foundation", Geotechnique, 2(4) pp. 301-332.

36- Meyerhof G. G. (1976), "Bearing Capacity and Settlement of pile foundations", The Eleven Terzaghi Lecture, J. Geotech. Div. Am. Soc. Civ Engrs v102 pp. 195-228.

37- Mochtar, Indrasurya B. and Edil, Tuncer B. (1988), "Shaft Resistance of Model Pile in Clay," J. Geotech. Engrg., ASCE, 114(11), pp. 1227-1243.

38- Poulos, H. G. (1981), "Pile Foundation Subjected to Vertical Loading", Symposium on Geotechnical Aspects of Coastal and Offshore Structures, Bangkok, pp. 61-71.

39- Poulos, H. G. and Davis, E. H. (1980), "Pile Foundation Analysis and Design", John Wiley and Sons Inc., New York.

40- Rowe, P. W. (1962), "The Stress Dilatancy Relation for Static Equilibrium of an Assembly of Particles in Contact." Proc. R. Soc. A,269, 500-527.

41- Salgado, R., Mitchell, J. K. and Jamiol Kouski. M. (1997), "Cavity Expansion and Penetration Resistance in Sand", J. Geotech. Engrg., ASCE, 123(4), pp. 344-354.

42- Silvestri, Vincenzo (2003), "Limit Equilibrium Solution for Bearing Capacity of Strip Foundation on Sand", Canadian Geotechnical Journal, v40, pp. 351-361.

43- Tavenas, F.A. (1971), "Loading Tests Results on Friction Piles in Sand", Can. Geot. Jnl., No. 8, pp. 7-22.

44- Tsien, S.I.(1986), "Shaft Friction Resistance of Long pipe piles Driven Into dense sands", Paper OTC 5150 presented at the Annual Offshore Technology Conference.

45- Turner, William G. and Attwooll, William J. (2002), "Selection of Design Parameter for the I-15 Reconstruction Project", Deep Foundation Conf, Orlando FL, pp. 1471-1485.

46- Vesic, A. S. (1964), "Investigation of Bearing Capacity of Piles in Sand", Proc. N. Am. Conf. on Deep Foundation, Mexico City.

47- Vesic, A. S. (1972), "Expansion of Cavities in Infinite Soil Mass", J. Geotech. Engrg., ASCE, 98(3), pp. 265-290.

48- Vesic, A. S.(1970), "Tests on instrumented piles. Ogeechee River site", J. Soil Mech. Foundn. Engng Div. ASCE 96(2), pp. 561-584.

49- Webster, S. D., Hannigan, P. J., and Lawler, D. A. (1994), "Dynamic Pile testing for five mile bridge and tunnel crossing," Proceedings, International Conference on Design and Construction of Deep Foundations, Orlando, Fla., Vol. 3, pp. 1441-1454.

APPENDIX 1

$$P_{h1} = \int_0^{2\pi}\int_{\alpha_1}^{\alpha_4} \frac{\tau}{\sin\phi}.\sin(\delta+\phi).\frac{r_o e^{w\tan(\phi)}}{\cos(\phi)} X\,.d\omega.d\theta \tag{4.34}$$

$$\frac{1}{2\sin(2\,\phi)}\left(\pi\left(rc^2\,g\,D\,r\left(-\frac{e^{(3\,w\tan(\phi))}\cos(5\,\phi-w)}{9\tan(\phi)^2+1}-\frac{3\tan(\phi)\,e^{(3\,w\tan(\phi))}\sin(5\,\phi-w)}{9\tan(\phi)^2+1}\right)-\frac{rc^2\,g\,X\cos(3\,\phi)\left(e^{(w\tan(\phi))}\right)^2}{\tan(\phi)}\right.\right.$$

$$+2\,rc^2\,g\,X\left(\frac{2\tan(\phi)\,e^{(2\,w\tan(\phi))}\cos(5\,\phi-2\,w)}{4\tan(\phi)^2+4}-\frac{2\,e^{(2\,w\tan(\phi))}\sin(5\,\phi-2\,w)}{4\tan(\phi)^2+4}\right)$$

$$+4\,rc\_CI\,D\,\beta\,r\left(-\frac{e^{(3\,w\tan(\phi))}\cos\left(\frac{1}{2}\phi+w\right)}{9\tan(\phi)^2+1}+\frac{3\tan(\phi)\,e^{(3\,w\tan(\phi))}\sin\left(\frac{1}{2}\phi+w\right)}{9\tan(\phi)^2+1}\right)$$

$$+4\,rc\_CI\,D\,\beta\,r\left(-\frac{e^{(3\,w\tan(\phi))}\cos\left(\frac{5}{2}\phi-w\right)}{9\tan(\phi)^2+1}-\frac{3\tan(\phi)\,e^{(3\,w\tan(\phi))}\sin\left(\frac{5}{2}\phi-w\right)}{9\tan(\phi)^2+1}\right)$$

$$-rc^2\,g\,D\,r\left(-\frac{e^{(3\,w\tan(\phi))}\cos(\phi+w)}{9\tan(\phi)^2+1}+\frac{3\tan(\phi)\,e^{(3\,w\tan(\phi))}\sin(\phi+w)}{9\tan(\phi)^2+1}\right)$$

$$-rc^2\,g\,D\,r\left(-\frac{e^{(3\,w\tan(\phi))}\cos(\phi-w)}{9\tan(\phi)^2+1}-\frac{3\tan(\phi)\,e^{(3\,w\tan(\phi))}\sin(\phi-w)}{9\tan(\phi)^2+1}\right)$$

$$+rc^2\,g\,D\,r\left(-\frac{3\,e^{(3\,w\tan(\phi))}\cos(-3\,w+3\,\phi)}{9\tan(\phi)^2+9}-\frac{3\tan(\phi)\,e^{(3\,w\tan(\phi))}\sin(-3\,w+3\,\phi)}{9\tan(\phi)^2+9}\right)+\frac{rc^2\,g\,X\cos(\phi)\left(e^{(w\tan(\phi))}\right)^2}{\tan(\phi)}$$

$$-2\,rc^2\,g\,X\left(\frac{2\tan(\phi)\,e^{(2\,w\tan(\phi))}\cos(3\,\phi-2\,w)}{4\tan(\phi)^2+4}-\frac{2\,e^{(2\,w\tan(\phi))}\sin(3\,\phi-2\,w)}{4\tan(\phi)^2+4}\right)-\frac{rc\_CI\,D\,r\cos(\phi)\left(e^{(w\tan(\phi))}\right)^4}{\tan(\phi)}$$

$$+4\,rc\_CI\,D\,r\left(\frac{4\tan(\phi)\,e^{(4\,w\tan(\phi))}\cos(\phi-2\,w)}{16\tan(\phi)^2+4}-\frac{2\,e^{(4\,w\tan(\phi))}\sin(\phi-2\,w)}{16\tan(\phi)^2+4}\right)$$

$$\left.+rc^2\,g\,D\,r\left(-\frac{e^{(3\,w\tan(\phi))}\cos(w+3\,\phi)}{9\tan(\phi)^2+1}+\frac{3\tan(\phi)\,e^{(3\,w\tan(\phi))}\sin(w+3\,\phi)}{9\tan(\phi)^2+1}\right)\right.$$

$$
\begin{aligned}
&-rc^2\, g\, D\, r\left(-\frac{3\,e^{(3\,w\tan(\phi))}\cos(-3\,w+5\,\phi)}{9\tan(\phi)^2+9}-\frac{3\tan(\phi)\,e^{(3\,w\tan(\phi))}\sin(-3\,w+5\,\phi)}{9\tan(\phi)^2+9}\right)\\
&-\frac{rc^2\, g\, D\,\beta\, r\cos\left(\frac{3}{2}\phi\right)\left(e^{(w\tan(\phi))}\right)^2}{2\tan(\phi)}-\frac{rc^2\, g\, D\,\beta\, r\cos\left(\frac{9}{2}\phi\right)\left(e^{(w\tan(\phi))}\right)^2}{2\tan(\phi)}\\
&+rc^2\, g\, D\,\beta\, r\left(\frac{2\tan(\phi)\,e^{(2\,w\tan(\phi))}\cos\left(\frac{13}{2}\phi-2\,w\right)}{4\tan(\phi)^2+4}-\frac{2\,e^{(2\,w\tan(\phi))}\sin\left(\frac{13}{2}\phi-2\,w\right)}{4\tan(\phi)^2+4}\right)\\
&+rc^2\, g\, D\,\beta\, r\left(\frac{2\tan(\phi)\,e^{(2\,w\tan(\phi))}\cos\left(\frac{7}{2}\phi-2\,w\right)}{4\tan(\phi)^2+4}-\frac{2\,e^{(2\,w\tan(\phi))}\sin\left(\frac{7}{2}\phi-2\,w\right)}{4\tan(\phi)^2+4}\right)\\
&+\frac{rc^2\, g\, D\,\beta\, r\cos\left(\frac{1}{2}\phi\right)\left(e^{(w\tan(\phi))}\right)^2}{2\tan(\phi)}+\frac{rc^2\, g\, D\,\beta\, r\cos\left(\frac{5}{2}\phi\right)\left(e^{(w\tan(\phi))}\right)^2}{2\tan(\phi)}\\
&-rc^2\, g\, D\,\beta\, r\left(\frac{2\tan(\phi)\,e^{(2\,w\tan(\phi))}\cos\left(\frac{9}{2}\phi-2\,w\right)}{4\tan(\phi)^2+4}-\frac{2\,e^{(2\,w\tan(\phi))}\sin\left(\frac{9}{2}\phi-2\,w\right)}{4\tan(\phi)^2+4}\right)\\
&-rc^2\, g\, D\,\beta\, r\left(\frac{2\tan(\phi)\,e^{(2\,w\tan(\phi))}\cos\left(\frac{3}{2}\phi-2\,w\right)}{4\tan(\phi)^2+4}-\frac{2\,e^{(2\,w\tan(\phi))}\sin\left(\frac{3}{2}\phi-2\,w\right)}{4\tan(\phi)^2+4}\right)\\
&+8\,rc\_CI\,X\left(-\frac{e^{(3\,w\tan(\phi))}\cos(\phi-w)}{9\tan(\phi)^2+1}-\frac{3\tan(\phi)\,e^{(3\,w\tan(\phi))}\sin(\phi-w)}{9\tan(\phi)^2+1}\right)\Bigg)\Bigg)
\end{aligned}
$$

APPENDIX 2

$$V_1 = \pi \int_{\alpha_1}^{\alpha_4} \frac{Z_1}{L} D^2 [\beta r_o \cos(3/2\phi) + r_o e^{\omega \tan\phi} \sin(\omega) + X_1]^2 \left[r_o e^{w \tan\phi} \sin\omega - r_o e^{w \tan\phi} \cos\omega \tan\phi \right] d\omega \tag{4.42}$$

$$VI := \pi \left(X^2 rc \left(- \frac{e^{(w \tan(\phi))} \cos(w)}{\tan(\phi)^2 + 1} + \frac{\tan(\phi)\, e^{(w \tan(\phi))} \sin(w)}{\tan(\phi)^2 + 1} \right) - X^2 rc \tan(\phi) \left(\frac{\tan(\phi)\, e^{(w \tan(\phi))} \cos(w)}{\tan(\phi)^2 + 1} + \frac{e^{(w \tan(\phi))} \sin(w)}{\tan(\phi)^2 + 1} \right) \right.$$

$$+ \frac{1}{2} rc \beta^2 r^2 D^2 \left(- \frac{e^{(w \tan(\phi))} \cos(w)}{\tan(\phi)^2 + 1} + \frac{\tan(\phi)\, e^{(w \tan(\phi))} \sin(w)}{\tan(\phi)^2 + 1} \right)$$

$$- \frac{1}{2} rc \beta^2 r^2 D^2 \tan(\phi) \left(\frac{\tan(\phi)\, e^{(w \tan(\phi))} \cos(w)}{\tan(\phi)^2 + 1} + \frac{e^{(w \tan(\phi))} \sin(w)}{\tan(\phi)^2 + 1} \right)$$

$$+ \frac{3}{4} rc r^2 D^2 \left(- \frac{e^{(3 w \tan(\phi))} \cos(w)}{9 \tan(\phi)^2 + 1} + \frac{3 \tan(\phi)\, e^{(3 w \tan(\phi))} \sin(w)}{9 \tan(\phi)^2 + 1} \right)$$

$$- \frac{1}{4} rc r^2 D^2 \tan(\phi) \left(\frac{3 \tan(\phi)\, e^{(3 w \tan(\phi))} \cos(w)}{9 \tan(\phi)^2 + 1} + \frac{e^{(3 w \tan(\phi))} \sin(w)}{9 \tan(\phi)^2 + 1} \right)$$

$$+ \frac{1}{4} rc \beta^2 r^2 D^2 \left(- \frac{e^{(w \tan(\phi))} \cos(3\phi + w)}{\tan(\phi)^2 + 1} + \frac{\tan(\phi)\, e^{(w \tan(\phi))} \sin(3\phi + w)}{\tan(\phi)^2 + 1} \right)$$

$$+ \frac{1}{4} rc \beta^2 r^2 D^2 \left(- \frac{e^{(w \tan(\phi))} \cos(-3\phi + w)}{\tan(\phi)^2 + 1} + \frac{\tan(\phi)\, e^{(w \tan(\phi))} \sin(-3\phi + w)}{\tan(\phi)^2 + 1} \right)$$

$$- \frac{1}{4} rc \beta^2 r^2 D^2 \tan(\phi) \left(\frac{\tan(\phi)\, e^{(w \tan(\phi))} \cos(-3\phi + w)}{\tan(\phi)^2 + 1} + \frac{e^{(w \tan(\phi))} \sin(-3\phi + w)}{\tan(\phi)^2 + 1} \right)$$

$$- \frac{1}{4} rc \beta^2 r^2 D^2 \tan(\phi) \left(\frac{\tan(\phi)\, e^{(w \tan(\phi))} \cos(3\phi + w)}{\tan(\phi)^2 + 1} + \frac{e^{(w \tan(\phi))} \sin(3\phi + w)}{\tan(\phi)^2 + 1} \right) - \frac{rc \beta r^2 D^2 \cos\left(\frac{3}{2}\phi\right) \left(e^{(w \tan(\phi))} \right)^2}{2 \tan(\phi)}$$

$$+ \frac{1}{2} rc \beta r^2 D^2 \left(\frac{2 \tan(\phi)\, e^{(2 w \tan(\phi))} \cos\left(\frac{3}{2}\phi + 2w\right)}{4 \tan(\phi)^2 + 4} + \frac{2 e^{(2 w \tan(\phi))} \sin\left(\frac{3}{2}\phi + 2w\right)}{4 \tan(\phi)^2 + 4} \right)$$

$$+ \frac{1}{2} rc \beta r^2 D^2 \tan(\phi) \left(- \frac{2 e^{(2 w \tan(\phi))} \cos\left(\frac{3}{2}\phi + 2w\right)}{4 \tan(\phi)^2 + 4} + \frac{2 \tan(\phi)\, e^{(2 w \tan(\phi))} \sin\left(\frac{3}{2}\phi + 2w\right)}{4 \tan(\phi)^2 + 4} \right)$$

$$
\left) + \frac{1}{2} rc\, \beta\, r^2\, D^2 \left(\frac{2\tan(\phi)\, e^{(2 w \tan(\phi))} \cos\left(-\frac{3}{2}\phi + 2w\right)}{4\tan(\phi)^2 + 4} + \frac{2\, e^{(2 w \tan(\phi))} \sin\left(-\frac{3}{2}\phi + 2w\right)}{4\tan(\phi)^2 + 4} \right) \right.
$$

$$
+ \frac{1}{2} rc\, \beta\, r^2\, D^2 \tan(\phi) \left(-\frac{2\, e^{(2 w \tan(\phi))} \cos\left(-\frac{3}{2}\phi + 2w\right)}{4\tan(\phi)^2 + 4} + \frac{2\tan(\phi)\, e^{(2 w \tan(\phi))} \sin\left(-\frac{3}{2}\phi + 2w\right)}{4\tan(\phi)^2 + 4} \right)
$$

$$
+ \beta\, r\, D\, Xrc \left(-\frac{e^{(w \tan(\phi))} \cos\left(-\frac{3}{2}\phi + w\right)}{\tan(\phi)^2 + 1} + \frac{\tan(\phi)\, e^{(w \tan(\phi))} \sin\left(\frac{3}{2}\phi + w\right)}{\tan(\phi)^2 + 1} \right)
$$

$$
+ \beta\, r\, D\, Xrc \left(-\frac{e^{(w \tan(\phi))} \cos\left(-\frac{3}{2}\phi + w\right)}{\tan(\phi)^2 + 1} + \frac{\tan(\phi)\, e^{(w \tan(\phi))} \sin\left(-\frac{3}{2}\phi + w\right)}{\tan(\phi)^2 + 1} \right)
$$

$$
- \beta\, r\, D\, Xrc \tan(\phi) \left(\frac{\tan(\phi)\, e^{(w \tan(\phi))} \cos\left(-\frac{3}{2}\phi + w\right)}{\tan(\phi)^2 + 1} + \frac{e^{(w \tan(\phi))} \sin\left(-\frac{3}{2}\phi + w\right)}{\tan(\phi)^2 + 1} \right)
$$

$$
- \beta\, r\, D\, Xrc \tan(\phi) \left(\frac{\tan(\phi)\, e^{(w \tan(\phi))} \cos\left(\frac{3}{2}\phi + w\right)}{\tan(\phi)^2 + 1} + \frac{e^{(w \tan(\phi))} \sin\left(\frac{3}{2}\phi + w\right)}{\tan(\phi)^2 + 1} \right)
$$

$$
- \frac{1}{4} rc\, r^2\, D^2 \left(-\frac{3\, e^{(3 w \tan(\phi))} \cos(3w)}{9\tan(\phi)^2 + 9} + \frac{3\tan(\phi)\, e^{(3 w \tan(\phi))} \sin(3w)}{9\tan(\phi)^2 + 9} \right)
$$

$$
+ \frac{1}{4} rc\, r^2\, D^2 \tan(\phi) \left(\frac{3\tan(\phi)\, e^{(3 w \tan(\phi))} \cos(3w)}{9\tan(\phi)^2 + 9} + \frac{3\, e^{(3 w \tan(\phi))} \sin(3w)}{9\tan(\phi)^2 + 9} \right)
$$

$$
- \frac{r\, D\, Xrc \left(e^{(w \tan(\phi))} \right)^2}{2\tan(\phi)} + r\, D\, Xrc \left(\frac{2\tan(\phi)\, e^{(2 w \tan(\phi))} \cos(2w)}{4\tan(\phi)^2 + 4} + \frac{2\, e^{(2 w \tan(\phi))} \sin(2w)}{4\tan(\phi)^2 + 4} \right)
$$

$$
\left. + r\, D\, Xrc \tan(\phi) \left(-\frac{2\, e^{(2 w \tan(\phi))} \cos(2w)}{4\tan(\phi)^2 + 4} + \frac{2\tan(\phi)\, e^{(2 w \tan(\phi))} \sin(2w)}{4\tan(\phi)^2 + 4} \right) \right)
$$